UNIVERSIDAD POLITÉCNICA DE MADRID
Escuela Técnica Superior de Ingenieros de Telecomunicación

Ultrathin solar cells based on transition–metal dichalcogenide semiconductors

TESIS DOCTORAL

Presentada para optar al título de Doctor por:

Carlos Bueno Blanco
Grado en Ingeniería de Tecnologías Industriales y Máster en Ingeniería Industrial

Madrid, 2024

UNIVERSIDAD POLITÉCNICA DE MADRID
Escuela Técnica Superior de Ingenieros de Telecomunicación

Doctorado en Energía Solar Fotovoltaica

Ultrathin solar cells based on transition–metal dichalcogenide semiconductors

TESIS DOCTORAL

Presentada para optar al título de Doctor por:

Carlos Bueno Blanco
Grado en Ingeniería de Tecnologías Industriales y Máster en Ingeniería Industrial

Bajo la dirección de:
Dra. Elisa Antolín Fernández

Madrid, 2024

Título: Ultrathin solar cells based on transition–metal dichalcogenide semiconductors

Autor: Carlos Bueno Blanco

Programa de Doctorado: Energía Solar Fotovoltaica

Dirección de tesis:

Dra. Elisa Antolín Fernández, Profesor Contratado Doctor I3, Escuela Técnica Superior de Ingenieros de Telecomunicación. (Directora)

Revisores externos:

Tribunal de tesis:

Fecha de defensa:

Esta Tesis ha sido parcialmente financiada por el Programa Propio de la Universidad Politécnica de Madrid.

A mi familia y los compañeros que me han acompañado en este viaje

"Quien no tiene metas, es poco probable que las alcance"

–Sun Tzu

"Exactas no semos nadie"

–Cándida Retortillo Barroso

Agradecimientos

Este trabajo no es solo obra del autor y su directora, si no que cada página, cada resultado, cada conclusión o hallazgo tiene gran parte de todas aquellas personas que han estado a lo largo de estos cinco años ayudando directa o indirectamente. Ya sea un comentario para ofrecer una idea, el arreglar una fuga de agua que te paraliza un proceso, comprar un componente clave para un equipo, un código que parecía no tener solución o simplemente el poder disponer de los materiales de laboratorio en condiciones. Todas estas cosas son las que al final han hecho posible el escribir este documento. Por eso quiero recalcar que esta no es mi tesis doctoral, es la de todos aquellos que la han hecho posible.

Esta tesis tiene gran parte de trabajo de mi directora Elisa Antolín, a quien agradezco el trabajo de supervisión durante estos cinco años, por guiarme en mis inicios y por la paciencia a la hora de corregirme en los fallos que mentiría si dijese que solo he cometido una vez. También agradecer a Simon Svatek que me ha ayudado en las tareas del laboratorio, en el optimizando de los códigos para los programas de medida y a mejorar mi forma de presentar los resultados.

Me gustaría también agradecer a los miembros y exmiembros del grupo de Estudios Fundamentales del Instituto de Energía Solar, en especial a los técnicos Irene Artacho y Miguel Gómez por resolver los mil y un problemas de laboratorio y velar por que todo esté en óptimas condiciones. También quiero mencionar a los otros doctorandos con los que he compartido grupo, Marius Zehender, Mario Martínez, e Inés Durán, con los que he tenido el placer de trabajar codo con codo en múltiples ocasiones y me han ayudado a que los problemas que surgen durante la tesis se hayan hecho menos cuesta arriba.

Quiero destacar, sobre todo, que estos cinco años no han sido solo de investigación si no que el ambiente en el cual he desarrollado mi trabajo ha sido un ambiente enriquecedor por las personas que me han rodeado. Entre todos hemos compartido vivencias, quedadas, casas rurales, partidos de baloncesto, nuestras charlas de "Loosers", y en definitiva no solo hemos crecido como investigadores, sino también como personas. Por eso quiero agradecer también a todas esas personas con las que he compartido estos años en el IES, Sally Bo–Kyung, Luisja, Fran, Víctor, Pablo Martín, Alba, Norman, Alicia, Álvaro, Alfonso, Nacho, Pablo Fernández, Aitana,

Dani, Almudena, Ricardo. Todos ellos y algunos que me dejo, son unos excelentes profesionales y mejores compañeros aún.

Me he dejado a algunas personas a las que me gustaría mencionar especialmente. Clara Sánchez, por darnos su visión desde la experiencia del mundo de la investigación y ser una referencia durante estos años. Luis Cifuentes, por los consejos en el laboratorio y también por qué no, por los chistes (alguna vez más acertados que otras) que hacían más amenos los largos días de procesado. A Miguel Gómez que ha sido muchas veces un salvavidas en los temas de laboratorio cuando parece que los equipos quieren dejar de funcionar, siempre dispuesto a echar una mano. A Javier Macías, por compartir vivencias dentro y fuera del despacho y por ser más que un compañero de trabajo y un "partner", un gran amigo.

Quiero dar las gracias a mi familia, a mis padres, José Luis y Ana María por la educación que me han dado y escucharme especialmente los días que llegaba a casa enfadado con el mundo, por enseñarme que no hay nada sencillo y la importancia del esfuerzo. A mi hermano Marcos, que es gran responsable de que esta tesis exista pues, me supo guiar cuando aún era un adolescente con las ideas poco claras de que hacer en el futuro. Quiero mencionar a mi abuela Cándida, quien siempre ha cuidado de mí y me recuerda la importancia de la sencillez y la modestia. Y por último y creo que la persona más importante a la que tengo que agradecer, a Marina, por acompañarme siempre, ser mi mayor apoyo y tener esa capacidad de sacarme un pensamiento positivo y afrontar el día a día con más fuerza cuando las cosas parece que nunca salen bien.

Abstract

Transition metal dichalcogenides (TMDC) have attracted interest in optoelectronic applications because of their outstanding properties. The discovery of graphene by Andrey Gueim and Konstantin Novosiolov has boosted the research on materials with similar structures as TMDCs. Since then, numerous research groups have explored the properties of TMDCs aiming to develop a new generation of optoelectronic devices including solar cells.

The structure of TMDCs consists of atomic layers bonded by van der Waals forces allowing the exfoliation of materials. Exfoliation enables the obtention of nanometric thick layers and the fabrication of ultrathin devices by stacking several layers. Moreover, it has been demonstrated that these materials are compatible with large–area fabrication processes.

In the literature, there are several examples of the use of TMDCs in photovoltaic devices forming either heterojunctions or homojunctions mainly made of WSe_2 and MoS_2. However, both types of cell architecture suffer from low open–circuit voltages in comparison to the band gap of semiconductors, low fill factor and poor spectral response despite the high absorption coefficient of TMDCs.

This Thesis presents a detailed study of the use of TMDC in ultrathin solar cells addressing four issues. The fabrication and understanding of solar cells based on MoS_2 homojunctions, the analysis and optimisation of their optical properties, the electronic characterisation of the surface and bulk in substitutionally doped MoS_2, and the proposal and study of TMDC solar cells for semitransparent windows.

The fabrication and characterisation of MoS_2 solar cells take previous results from our research group as a starting point. The objective is to demonstrate the potential of MoS_2 homojunctions and the understanding of the mechanisms that hinder their light–power conversion. We present a proof–of–concept device with a high open–circuit voltage of 1.02 V under concentrated light that demonstrates the remarkable photoconversion of MoS_2 solar cells. Besides, we present a comprehensive study of the mechanisms that jeopardise the performance of devices which are caused by the presence of photoactive parasitic diodes at the metal/semiconductor interfaces.

The analysis of optical properties is done through homemade software designed for multilayered structures. We propose different structures of TMDC solar cells that maximise light absorption enhancing light interference effects in ultrathin structures. We remark the possibility of achieving a high absorptance by boosting the zeroth–order interference mode in 1D optical cavities.

The characterisation of the parasitic contacts and the optical model enable the design of solar cells with improved efficiency. We demonstrate how to make ohmic contacts to MoS_2 by correctly choosing metals and by developing a fabrication method that yields an optimised metal/semiconductor interface. We present a device with a 3.82% light–power conversion under the AM1.5G spectra. This value is the highest efficiency reported for MoS_2–homojunction based devices and one of the highest in TMDC–based solar cells.

Finally, we propose the use of TMDCs in semitransparent windows. The difficulties of conventional technologies in providing colour–neutral transmitted spectrums along with the balanced absorption of TMDC endorse the use of TMDC–based semitransparent devices. TMDC semitransparent devices balance the light–power conversion and the quality of the transmitted spectra. Analysing a case of study, we demonstrate through a rough approximation that implementing TMDC–based semitransparent windows could yield a fair save in energy consumption of large buildings.

Resumen

Los dicalcogenuros de metales de transición (TMDC) son de gran interés en aplicaciones optoelectrónicas por sus interesantes propiedades. El descubrimiento del grafeno por parte de Andréy Gueim y Konstantín Novosiólov impulsó la investigación sobre materiales con una estructura similar como los TMDC. Desde entonces, numerosos grupos de investigación exploran las propiedades de los TMDC para desarrollar una nueva generación de dispositivos optoelectrónicos, entre ellos, células solares.

La estructura de los TMDC consiste en capas unidas por fuerzas de van der Waals que hacen que sean fácilmente exfoliables. Esto permite la obtención láminas de espesor nanométrico y la construcción de dispositivos ultradelgados a través de su apilamiento. Además, estos materiales son compatibles con técnicas de fabricación de láminas de área grande.

En la literatura encontramos diferentes ejemplos de aplicación de los TMDC, principalmente el MoS_2 y el WSe_2, en dispositivos fotovoltaicos, formando heterouniones o homouniones. No obstante, ambas arquitecturas presentan valores bajos de la tensión de corto circuito en comparación con los valores de la banda prohibida de los semiconductores, factor de forma reducido y baja respuesta espectral a pesar del elevado coeficiente de absorción de los TMDC.

Esta Tesis presenta un estudio en detalle sobre el uso de los TMDC en células solares ultrafinas que aborda cuatro puntos, la fabricación y caracterización de células solares de homouniones de MoS_2, el estudio y optimización de las propiedades ópticas de células solares ultrafinas de TMDC, la caracterización electrónica en superficie y volumen del MoS_2 con dopaje sustitucional y el estudio y propuesta de la aplicación de los dispositivos en ventanas semitransparentes.

La fabricación y caracterización de las células MoS_2 inicia a partir de resultados anteriores de nuestro grupo de investigación. El objetivo es demostrar el potencial de las homouniones de MoS_2 y comprender los mecanismos que dificultan la conversión de la luz en energía eléctrica. Presentamos un dispositivo de prueba de concepto con una alta tensión de corto circuito de 1.02 V bajo luz concentrada demostrando el potencial de fotoconversión de las células de MoS_2. Además, presentamos un estudio de los mecanismos que afectan negativamente al rendimiento de los dispositivos, causados por la presencia de contactos parásitos fotoactivos en las interfaces metal/semiconductor.

El estudio de las propiedades ópticas se realiza con un software de desarrollo propio para estructuras multicapa. Proponemos diferentes estructuras de célula solar de TMDC que maximizan la absorción de la luz gracias a fenómenos de interferencia en estructuras ultrafinas. Destacamos en especial la posibilidad de conseguir estructuras con una elevada absortancia potenciando del orden cero de interferencia en cavidades ópticas 1D.

La caracterización de los contactos parásitos y el modelado óptico permite el diseño de células de mejor rendimiento. Demostramos cómo obtener contactos óhmicos en células de MoS_2 seleccionando correctamente los metales y desarrollando un método de fabricación que optimiza la interfaz entre metal/semiconductor. Presentamos un dispositivo con una eficiencia del 3.82% bajo el espectro AM1.5G, la eficiencia más alta reportada en homouniones de MoS_2 y uno de los valores más altos en células solares de TMDC.

Por último, planteamos el uso de TMDC en ventanas semitransparentes. Las dificultades de las tecnologías convencionales para obtener espectros de color neutro unido a la equilibrada absorción del espectro luminoso por parte de los TMDC abren la puerta a la aplicación de estos dispositivos. Los dispositivos de TMDC semitransparentes equilibran la conversión de luz en energía eléctrica y la calidad del espectro transmitido. A través de un caso de estudio demostramos en un cálculo aproximado que su implementación puede proporcionar un ahorro energético considerable en edificios de grandes dimensiones.

Contents

List of acronyms

AM1.5G	Air mass 1.5 global spectrum
AFM	Atomic force microscopy
ANSI	American national standard institute
APT	Average phototopic transmission
ARL	Anti–reflective layer
BIPV	Building integrated photovoltaics
CNL	Charge neutrality level
CRI	Colour rendering index
CSIC	Centro Superior de Investigaciones Científicas
CVD	Chemical vapour deposition
CVT	Chemical vapour transport
DMSO	Dimethyl sulfoxide
EQE	External quantum efficiency
EVA	Ethyl–vinyl acetate
FF	Fill factor
FP	Fabry–Perot
IQE	Internal quantum efficiency
ITO	Indium–tin oxide
IPCC	Intergovernmental Panel on Climate Change
IR	Infrared
KPFM	Kelvin–probe force microscopy
MBE	Molecular beam epitaxy
MIGS	Metal–induced gap states
PCE	Power conversion efficiency

PDMS	Polydimethylsiloxane
PLL	Phase–locked loop
PPC	Polypropylene carbonate
RMS	Root mean square
SCR	Space charged region
SPD	Spectral power distribution
TE	Transverse electric mode
TM	Transverse magnetic mode
TMDC	Transition metal dichalcogenides
UV	Ultraviolet
WEO	World Energy Outlook
WF	Work function

List of symbols

ε	Relative electric permittivity (adim.)
ε_0	Vacuum dielectric constant (C^2 / (N·m^2))
θ	Angle of propagation (º)
λ	Wavelength (nm)
μ	Carrier mobility (cm^2/V·s)
ρ	Resistivity (Ω·cm)
σ_c	Roughness square mean (nm)
φ_M	Metal work function (eV)
φ_{SB}	Schottky barrier height (eV)
χ	Semiconductor electronic affinity (eV)
A	Absorptance (adim.)
$CCT(K)$	Correlated colour temperature (K)
c	Speed of light in vacuum constant (m/s)
d	Thickness (nm)
DPA	Diffuse power absorption (W/(m^2·nm))
e	Electron charge (C)
E^+_{iR}	Electric field propagating in the positive direction (V/m)
E^-_{iR}	Electric field propagating in the negative direction (V/m)
E_c	Conduction band (eV)
E_{CNL}	Charge neutrality level (eV)
E_F	Fermi level (eV)
E_G	Band gap (eV)
E_v	Valence band (eV)
f	Frequency (s^{-1})

h	Planck constant (eV/s)
H^{+}_{iR}	Magnetic field propagating in the positive direction (A/m)
H^{-}_{iR}	Magnetic field propagating in the negative direction (A/m)
I	Current (A)
$I_{i,i+1}$	Wave propagation matrix through a coherent interface (adim.)
$\overline{I_{i,i+1}}$	Wave propagation matrix through an incoherent interface (adim.)
Ir	Irradiance (W/m^2)
J	Current density (mA/cm^2)
J_0	Recombination current density (mA/cm^2)
J_D	Diode current density (mA/cm^2)
J_L	Illumination current density (mA/cm^2)
J_{SC}	Short–circuit current density (mA/cm^2)
k_B	Boltzmann constant (eV/K)
k_i	Extinction coefficient (adim.)
L	Coherence length (nm)
L_e	Diffusion length (nm)
L_i	Wave propagation matrix through a coherent layer (adim.)
$\overline{L_i}$	Wave propagation matrix through an incoherent layer (adim.)
N_A	Number of acceptor species (cm^{-3})
N_i	Complex refractive index (adim.)
N_D	Number of donor species (cm^{-3})
n	Diode ideality factor (adim.)
n_c	Carrier density (cm^{-3})
n_i	Refractive index real part (adim.)
n_{int}	Intrinsic carrier population (cm^{-3})
P	Poynting vector (W/m^2)
R	Reflectance (adim.)
$R_{\square}$	Sheet resistance ($\Omega_{\square}$)

R_H	Hall coefficient (cm^3/C)
R_S	Series resistance ($\Omega \cdot cm^2$)
R_P	Shunt resistance ($\Omega \cdot cm^2$)
S	Wave propagation transfer–matrix in a coherent structure (adim.)
$\bar{S}$	Wave propagation transfer–matrix in an incoherent structure (adim.)
S_e	Surface recombination velocity (cm/s)
S_p	Pinning factor (adim.)
$T(K)$	Temperature (K)
T	Transmittance (adim.)
U^+_{iR}	Square module electric field in the positive direction (V^2/m^2)
U^-_{iR}	Square module electric field in the negative direction (V^2/m^2)
V	Voltage (V)
$V_{built-in}$	Built–in potential (eV)
V_{CPD}	Contact potential difference (V)
V_{OC}	Open–circuit voltage (V)
W_{OC}	Band gap–voltage offset (eV)
w_{SCR}	Space charge region width (nm)
x_n	N–material neutral zone width (nm)
x_P	P–material neutral zone width (nm)
$\bar{x}(\lambda)$	X colour–matching function (adim.)
$\bar{y}(\lambda)$	Y colour–matching function/photopic function (adim.)
$\bar{z}(\lambda)$	Z colour–matching function (adim.)
Z_0	Vacuum impedance (Ω)

List of Figures

List of Tables

Chapter 1

Introduction

1.1. Global context of solar energy

The consumption of energy in the world is growing every year. Although the demand for energy in developed countries such as the European Union, United States or Japan is stabilised showing minimal variation since 2000, the economic growth and the transformation of regions such as China, India, the Middle East, and sub–Saharan Africa need to be pushed by a substantial increase in the energy production and the requirements of natural resources. Furthermore, the electrification of transport and industry will increase even more the electricity demand. The World Energy Outlook (WEO) 2022 estimates that the global electricity demand will rise from 24.7 PWh in 2021 to 30.6 PWh in 2030 and 43.6 PWh in 2050 according to the standard policies scenario [1]. Such an increase presents an enormous challenge conditioned also by the necessity of shifting the energy mix based on fossil fuels to low–carbon energy sources. Reports such as the Intergovernmental Panel on Climate Change (IPCC) warn about the necessity of reducing the emissions of greenhouse effect gases to keep the increase of global mean temperature under 1.5ºC [2]. In this context, solar photovoltaic energy appears as one of the principal powerhouses in the transition toward an economy less dependent on fossil fuels and able to accomplish the climate accords settled in the Paris Agreement.

Solar photovoltaics convert light into electricity. Solar cells absorb the photons from a light source to generate charge carriers that are extracted at the terminals of the device providing electric power. Photovoltaic energy is increasing its weight in the global energy mix, overcoming the records of photovoltaic production year by year. The considerable decrease in the price of the silicon modules to values of 0.18 €/W [3] is directly related to the exponential growth of photovoltaic capacity. Yearly photovoltaic capacity additions are expected to grow from 150 GW in 2021 to nearly 600 GW in 2050 to meet the expected electricity demand increase according to the net–zero emission scenario settled in the WEO [1]. Figure 1.1

shows the change in the amount of energy generated forecasted for 2030 according to the stated policies scenario, and it illustrates that solar photovoltaics will grow more than any power–generating technology with an expected increase of 3000 TWh.

The unprecedented growth in the capacity additions of solar photovoltaics is pushing device manufacturers to increase the production of solar modules. Nowadays, the market of photovoltaic modules is practically monopolised by monocrystalline silicon devices, representing approximately 84% of the production in 2021 [3]. Silicon offers the best solution for photovoltaics as it provides the best balance between fabrication costs and energy yield. Other technologies like multijunction solar cells made of III–V semiconductors show larger efficiencies than silicon, up to 47.1% for a single cell using concentrated light [3]. However, the cost differences between these highly efficient cells and silicon constrains the market of III–V solar cells to industries where the requirements of efficiency overcome the budget limits, such as the aerospace industry. It is expected that silicon will continue as the leading technology in the following years while new emerging technologies try to gain a fraction of the market filling those gaps where silicon may not be a reliable solution.

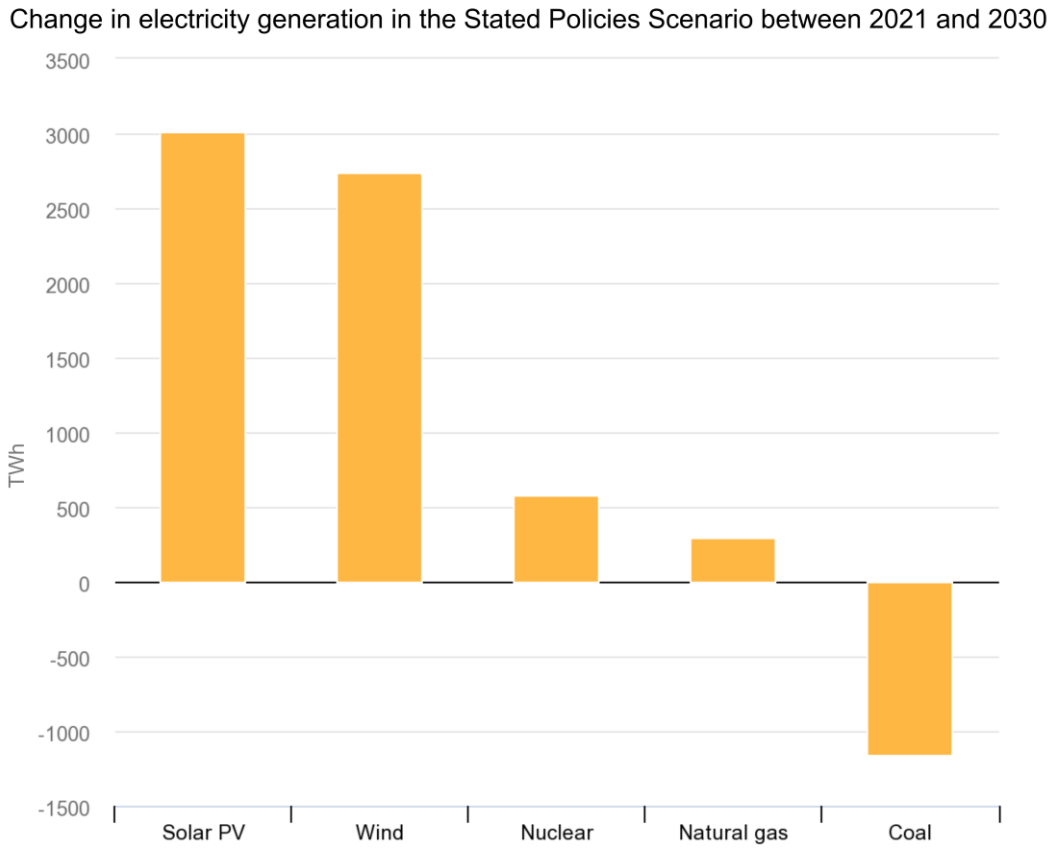

Figure 1.1. Expected variation of global electricity production according to the stated policies from 2021 to 2030. Chart extracted from IEA World Energy Outlook 2022 [4].

Silicon solar cells are widely used but show some potential problems. After decades of research, silicon solar cells approach the physical limit of energy conversion for this technology which is 29% [5]. The record in the efficiency of silicon solar cells is 26.81% [6], meaning that the range of improvement of this technology is limited. Additionally, most of the production of silicon solar modules is allocated in Asia, China mainland, where 74.6% of the solar modules of the world were produced in 2021 [7]. This fact raises questions about supply chain risks and bottlenecks that might threaten the energy transition of European countries. These reasons back the research and development of alternative technologies in the field of solar photovoltaics. Emerging technologies such as perovskites, organic and dye–synthesised solar cells are currently in development surpassing their records in efficiency year by year [8]. These technologies may not overcome silicon as the main material used in the photovoltaic industry but offer different characteristics that could be interesting in applications such as flexible photovoltaics, tandem devices, or semitransparent photovoltaics. Another advantage that may have the

diversification of the technologies used is the reduction of the supply chain issues aforementioned related to the production of silicon solar cells. Additionally, the photovoltaic industry faces the huge challenge of supplying the growing energy demand while phasing out more pollutant technologies such as coal, oil, or natural gas. This implies not only supplying the growing demand but also the substitution of the existing power plants that rely on the use of fossil fuels. Then it may not be reliable that this growth can be matched only by the conventional silicon modules, being necessary to explore new materials and devices that may be complementary to the already commercial solutions.

1.2. Layered materials

In 2004, Andréy Gueim and Konstantín Novosiólov rediscovered and isolated the graphene [9]. Graphene is an allotropic form of carbon that consists of a single layer of carbon atoms arranged in a hexagonal lattice. Graphene can be isolated from graphite, as it is composed of several graphene layers bonded through van der Waals forces. This finding was remarkable as until then, the existence of graphene in monoatomic layers had been discarded. Gueim and Novosiólov characterised graphene unveiling its outstanding properties as tensile strength, transparency, and electric conductivity. Thanks to this work, Gueim and Novosiólov were awarded the Nobel Prize in Physics in 2010, and their discovery opened numerous lines of research related to the application of graphene and materials with a similar layered structure (2D materials) in electronics and other disciplines.

Graphene is probably the most explored of the 2D materials existent, but the family of 2D materials embraces a wide variety of materials which include a considerable fraction of the elements in the periodic table. The possibilities that 2D materials offer are practically unlimited because of the existence of an extensive gamut of metals, semiconductors, and insulators. The interlayer van der Waals interactions allow 2D layered materials to be assembled creating a wide range of heterostructures or macro–ordered structures without constraints related to lattice matching and processing compatibility. Even more, the 2D geometry is highly compatible with current thin film manufacturing techniques in the semiconductor industry, enabling the integration of 2D materials with traditional electronic materials [10].

2D materials offer flexibility in the manufacturing of electronic devices, but their properties must be suitable to develop disruptive applications. Graphene is very popular thanks to its outstanding properties, reporting electrical mobilities up to 200000 $cm^2/V \cdot s$ at room temperature [10]. Nevertheless, the lack of an electronic bandgap hinders the application of graphene in the electronics industry. The necessity of overcoming this issue has stimulated research about other allotropic forms of carbon and 2D materials with a semiconducting character [11]. One group of materials where it is possible to find semiconductors is Transition Metal Dichalcogenides (TMDCs). Some of these materials present non–layered structures such as zincblende or wurtzite while most of them could be isolated in ultrathin layers as graphene. Layered TMDCs consist of a transition metal atom as Mo, W, Re, or Nb, colligated with two atoms of a chalcogenide as S, Se, or Te. The atom arrangement configuration yields two possible phase structures, a trigonal prismatic phase (2H) or an octahedral phase (1T) [12]. Which of the two arrangements is thermodynamically stable depends on the pair metal–chalcogen chosen. Atoms are connected forming layers whose thickness depends on the way that atoms are allocated and their size. These layers are attached among them through van der Waals forces (see Figure 1.2), making the exfoliation of the material relatively easy and enabling the isolation of slabs made of a few layers of material. If the exfoliation process is repeated several times, it could be possible to obtain a monolayer of material as illustrated in Figure 1.2.

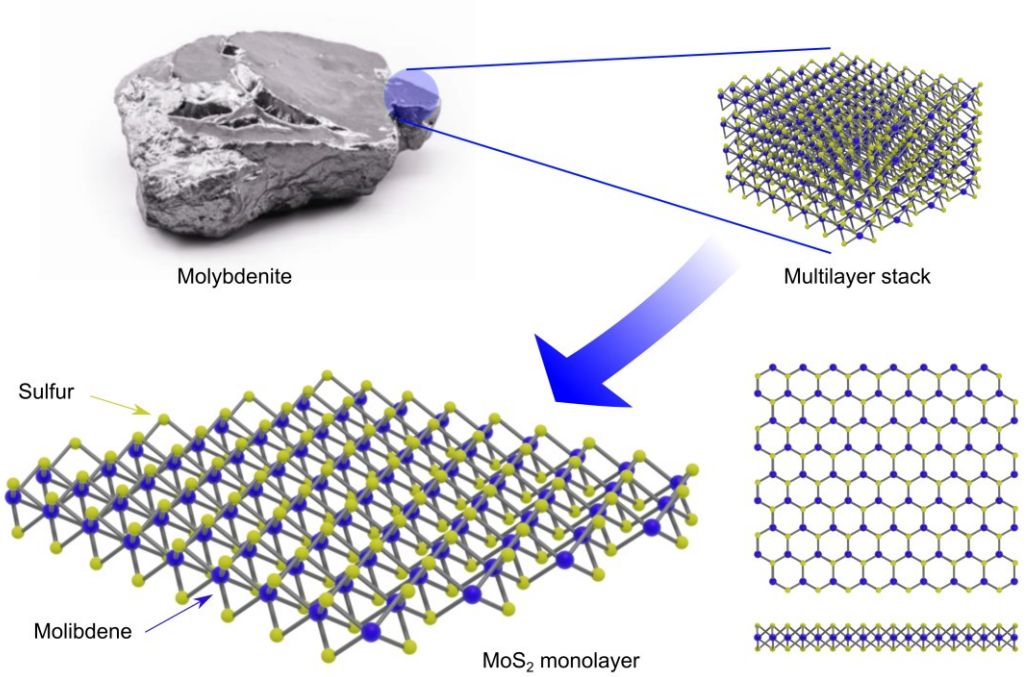

Figure 1.2. Layered structure of the molybdenite.

Among all the TMDCs there are semiconductors (MoS_2, WS_2, WSe_2), semimetals (WTe_2, $TiSe_2$), true metals (NbS_2, VSe_2), and superconductors ($NbSe_2$, TaS_2). The electrical properties of each one depend on the coordination and oxidation state of the metal atoms. The first studies about TMDCs were published in 1923 when Linus Pauling analysed the structure of molybdenite, a mineral mainly constituted of MoS_2 [13]. However, the first reports about the production of ultrathin MoS_2 layers date back to 1963 by Robert Frindt [14]. MoS_2 is a material widely used in the industry because of its tribological properties. It was traditionally used to fabricate lubricants and its use in electronics has been proposed in the last decade. Although the first attempts to unveil the electrical properties of TMDCs were set in the second half of the XX century, it was in the 2010s when the works about graphene published by Gueim and Novosiólov boosted interest in TMDCs. Since then, TMDCs and especially MoS_2 have attracted great attention because of their potential application in ultrathin optoelectronic devices. MoS_2 is the most studied of the TMDCs, and their properties have been a frequent subject of discussion since the first characterisation of the few–layer regime published by Mak et *al.* [15]. Since then, the application of TMDCs and especially MoS_2 in electronic circuits and devices promises the advent of a new technology that completely changes the conception of electronic devices reaching the nanometric scale.

Some of the TMDCs such as MoS_2 can be found in nature, but it is possible to fabricate them via existing deposition processes. TMDCs can be synthesised by chemical vapour deposition processes [16] where the precursors are mixed in stochiometric proportions. Both, high–quality nature crystals and synthetic crystals can be used to obtain layers of TMDCs. Mechanical exfoliation is the most popular way to create prototypes because of its easiness. Bulk crystals can be peeled using adhesives, and devices can be built by stacking several layers of material. However, this method is not scalable because of the reduced area of the flakes exfoliated and the haphazard nature of the material exfoliation. Despite the size restriction of mechanical exfoliation, this method is widely used to build proof–of–concept devices. To obtain devices with larger areas, molecular beam epitaxy (MBE) or chemical vapour deposition (CVD) can grow TMDC layers. Between both processes, CVD is preferable as it does not require ultrahigh vacuum and it is relatively easy to integrate into industrial processes. For instance, MoS_2 can be grown by sulphurisation of predeposited Mo [17] or MoO_3 [18]. TMDCs can be also grown by metal–organic CVD using gases as precursors [19]. Another alternative in the pursuit of large–area devices is the use of liquid precursors where TMDCs are diluted. Such precursors can be spun over substrates and then baked to obtain layers with a diameter of 6 inches [20]. These processes that yield large–area devices are crucial to achieve a scalable production of materials. Without them, it would not be possible to transform the proof–of–concept devices fabricated in a laboratory into commercial devices.

1.3. Solar cells based on layered materials

Among the potential applications that TMDCs offer, there is their use to create photovoltaic devices, taking advantage of their strong light–matter interaction and their potential low cost [21]. As mentioned in Section 1.1, the photovoltaic market is practically monopolised by silicon modules, with a lower fraction of thin–film technologies (CIGS, CdTe), III–V devices (used mainly for aerospace applications), and multiple emerging technologies pushing to fill the remaining gaps left by conventional technologies. Although this context is very competitive, TMDCs offer some interesting features that make them a reliable option for the future of photovoltaics.

TMDCs are relatively abundant in the Earth's crust [22]. Their main elements W or Mo are present in a larger volume than Cd, In, or Te which are used in inorganic thin film devices. Some of them can be found in rocks as the MoS_2 in molybdenite. TMDCs show outstanding optical properties. Their high absorption coefficient implies that TMDCs–based devices can absorb a large amount of light with minimal thickness requirements, even with few layers of material [23]. Additionally, TMDCs have a tuneable thickness–dependent band gap [15]. For instance, MoS_2 bandgap increases from the 1.29 eV of the bulk material [24], to 1.89 eV when considering a single atomic layer [15]. Another important feature is their self–passivated structure which makes them very stable and reduces surface recombination, which is an advantage when considering their application in solar cells [23].

Their strong light–matter interaction, their semiconductive character and their self–passivated structures make TMDCs optimal candidates for the development of a new generation of solar cells. In recent years, photovoltaic devices based on van der Waals junctions made of TMDCs have demonstrated remarkably high photocurrents even in ultra–low thicknesses, [23,25], holding out the promise of TMDCs being non–toxic and chemically stable absorbers that will enable highly efficient ultrathin solar cells. These devices have attracted significant attention as ultrathin and flexible alternatives to conventional III–V photovoltaic devices. Although the technology of TMDC–based solar cells is still in its early stages, there is a compelling argument that efficiencies approaching 20% may be attainable in the forthcoming years [26]. Although photoactive devices in the monolayer regime have been reported in the literature [27–30], thicker devices are preferred to increase light absorption and facilitate current transport. In the literature, there is an extensive range of solar cells made of different combinations of MoS_2, $MoSe_2$, ReS_2, $ReSe_2$, WS_2, and WSe_2 [31–34]. The most common approach towards these cells is based on MoS_2–WSe_2 heterostructures, which yield solar–to–electric power conversion efficiency (PCE) of below 3% with simulated sunlight. The highest efficiency published for a TMDC–based solar cell date from 2022 for a device made of WSe_2, with a PCE of 5.1% [35].

The reported values of PCE for van der Waals solar cells are still far from commercial and even emerging technologies. Nonetheless, this concept of solar cells has been widely explored since the middle of the last decade and promising results have been achieved. These devices are expected to show a similar learning curve to already established photovoltaic technologies, and the efficiencies

reported will grow year by year. TMDCs appeal to the industry of self–powered and aerospace vehicles because of the potential increase in specific power (power produced per unit of mass) and the mechanical properties of their layered crystalline lattice. The thickness reduction of TMDC–based devices along with their optical properties would enable the fabrication of semitransparent devices. These semitransparent devices could be used in innovative applications such as photovoltaic windows where conventional technologies struggle to be applied. Therefore, this family of semiconductors can be employed in the fabrication of ultrathin crystalline absorbers, possibly leading to lower costs (low–temperature fabrication) and opening the path to new photovoltaic applications as illustrated in Figure 1.3.

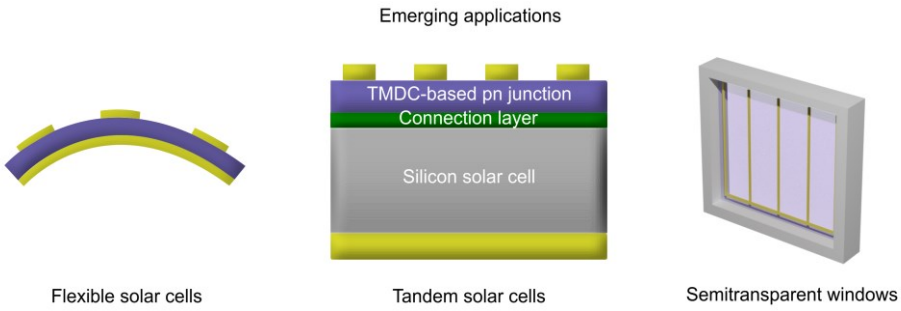

Figure 1.3. Proposed applications of the TMDC–based solar cells.

1.4. Scope of the Thesis

Layered Materials and especially TMDCs display outstanding properties that make them optimal candidates to create a new generation of optoelectronic devices. The wide variety of materials available offers almost unlimited possibilities, but this technology is still in its early stages, and there are several issues to solve before developing the first commercial devices. The properties of TMDCs have been deeply studied but the implementation of these materials in electronic devices still shows several barriers. The difficulties in obtaining ohmic contacts, the limited efficiency of the devices, the anisotropic characteristics of the materials, or the lack of scalable fabrication processes are some of the problems that hinder the consolidation of TMDCs as a reliable option in electronics. Besides, the

mechanisms that lead to poor performance of the devices are not completely understood.

The scope of this Thesis is to solve the questions that the application of these novel materials in photovoltaic devices raises. This objective embraces all the stages in the study of the use of TMDCs, especially the MoS_2, in photovoltaic applications, from the fabrication and characterisation of the proof–of–concept device to the development of specific modelling tools to understand limitations and identify ways to improve the performance of devices. Additionally, another objective is to analyse the opportunities that these materials offer in the development of future commercial applications, identifying where TMDC–based solar cells could be considered a reliable alternative to the current photovoltaic technologies.

This Thesis is divided into nine chapters apart from the present one, that cover experimental and modelling tasks:

- Chapter 2 provides an overview of all the experimental methods carried out in the Thesis, from the fabrication of the devices to their electrical characterisation. The features of the prototypes fabricated will require the development of adapted set–ups to perform the characterisation of the devices.
- Chapter 3 presents a proof–of–concept device that demonstrates the potential of MoS_2 homojunction solar cells as well as a discussion about the limiting factors of these devices. We will show that the electrical contacts of TMDC–based devices play a crucial role and can influent severely the characteristics of the devices and how to unlock the potential of MoS_2–based devices.
- Chapter 4 focuses on the optical modelling of the devices. This chapter describes the mathematical model developed to evaluate the optical properties of TMDC–based structures considering their optical characteristics. During the document, the model will be referred to continuously as all calculations related to the optical properties of the structures will be performed with this model. Additionally, this chapter develops other modelling tools that will be used in Chapter 8.
- Chapter 5 focuses on the optimisation of absorption of TMDC–based structures using the model described in Chapter 4. The optical properties are improved by reducing reflection losses and amplifying absorption through interference effects. In this chapter are presented optimised structures that would improve the efficiency of MoS_2–based structures.

- Chapter 6 will analyse the electrical characteristics of the materials used in the fabrication of MoS_2 solar cells. The use of ultrathin devices involves problems related to the sensitivity to the atmosphere or the substrates. We will show how the characteristics of the surrounding environment can alter the properties of the TMDCs.
- Chapter 7 redirects the discussion back to the fabrication and characterisation of MoS_2–solar cells, presenting a device that results from the conclusions extracted from the previous chapters. A better understanding of the behaviour of MoS_2 devices allows the fabrication of one of the most efficient TMDC–based solar cells reported to date.
- Chapter 8 presents a theoretical study about a possible future application of TMDC–based solar cells. The possibility of fabricating devices with few nanometres of thickness and their optical properties makes TMDCs suitable for semitransparent windows, which is one of the most interesting trends in the integration of photovoltaic devices in buildings.
- Chapter 9 presents the conclusions of every chapter and a section with the future lines of the works related to the results presented in this Thesis. Here there are explained some bullet points that are not covered in this document but may be key steps towards the realisation of the first TMDC–based devices suitable for the photovoltaic market.

Chapter 2

Experimental methods

2.1. Introduction

The fabrication processes of TMDC–based devices involve different techniques that range from complex methods such as the CVD of each layer forming the device to simpler procedures such as liquid phase deposition or mechanical exfoliation. All the devices presented in this Thesis are made of layered materials which were grown in bulk crystals by chemical vapour transport (CVT) and are then mechanically exfoliated to obtain material slabs of reduced thickness. This method implies some disadvantages as the reduced area of the semiconductors, but it provides high–quality materials and is a quick and easy way to fabricate experimental devices.

The fabrication of TMDC–based devices from mechanically exfoliated semiconductors requires more steps than just processing the semiconductors. Metallic contacts to the semiconductors are required to ensure they can be connected to the measurement instruments. Mechanical exfoliation of TMDCs yields tiny layers with a surface area of barely 100 μm^2 with random shapes, so the fabrication of these contacts involves the use of geometries that provide a proper connection of the semiconductor while facilitating the characterisation of the devices. Moreover, such a small area of the semiconductors not only hinders the assembling of the devices but also implies the use of optical instruments such as magnifying lenses for the fabrication and characterisation.

The characterisation of TMDC–based samples that we have performed combines the same techniques employed in conventional solar cells, such as current density–voltage *(J–V)* characterisation or external quantum efficiency (EQE) measurements, with material characterisation techniques such as atomic force microscopy (AFM) or Van der Pauw measurements. In every measurement, special care is necessary to control the current values, as they can sensibly alter the integrity of the materials. The limited values of current that devices can hold conditionate their electrical characterisation requiring customised set–ups adapted to the TMDC–based samples.

In this chapter, we present all the experimental procedures carried out for the devices introduced in the following chapters. We describe from the assembling of TMDC prototypes to the evaluation of their electrical and optical characteristics. The fabrication of every sample and the characterisation of each sample has been done at Instituto de Energía Solar in their Labcell and IBLAB facilities. Some of the measurements presented in the following chapters, particularly some included in Chapter 6, have been done externally at Centro Nacional de Microscopía Electrónica from Universidad Complutense de Madrid and Instituto de Micro y Nanotecnología from Centro Superior de Investigaciones Científicas (CSIC).

2.2. Fabrication of TMDC–based devices

2.2.1. Fabrication of metallic contacts

The fabrication of contacts can be done before the pn junction (which means that the semiconductors are transferred onto the electrodes) or once the pn junction has been placed on a substrate (which means that metal contacts are evaporated directly onto the semiconductor). The convenience of each method will be discussed in the following chapters. Different substrates have been used, transparent substrates such as glass and sapphire (Ossila [36]) and non–transparent as SiO_2(290 nm)/Si wafers (Siegert Warfers). In SiO_2/Si substrates, the thickness of the oxide layer should be thick enough to avoid its rupture during the measurements. This rupture would lead to a shunting effect that will distort the electrical characterisation of the devices. Glass can be used as a transparent substrate. Still, we found that, for example, MoS_2 flakes do not adhere well to the surface. Every substrate is cleaned before the evaporation process with acetone and isopropyl alcohol to remove any residue or debris on the surface prior to material deposition.

We use different strategies to fabricate the contacts to semiconductors. Simple testing devices are fabricated with an evaporation mask, while devices focused on creating a proof–of–concept device are fabricated using maskless photolithography. The use of maskless photolithography is a good alternative as practically unlimited options of contact morphology can be created. Metallic pads are patterned using maskless photolithography (SmartPrint by SmartForce) using a bilayer photoresist. This equipment exposes selectively some areas of the resist

to generate custom photolithography patterns. The exposed resist is removed using a 4:1 mixture of de–ionised water and AZ 400K developer. The underlying resist (LOR7B [37]) is more sensitive to ultra–violet (UV) light, so it develops an undercut below the overlying resist (Microchemicals AZ1512 HS [38]) enabling the production of perfectly flat metal surfaces after lift–off. After the removal of the exposed resist, high–purity metals (Kurt–Lesker) are deposited either by thermal evaporation (Cr, Au, Lurrun Vapour Station VS–5) or by sputtering (Pt, Vaksis PVD–MT/2M3T). Following the metal deposition process, the resist is removed using dimethyl sulfoxide (DMSO) while applying ultrasounds, so the result is a substrate with metallic contacts that follow the pattern drawn through the photolithography process. Further details about the fabrication process of the contacts will be discussed in Chapter 7. Metal pads are typically ~ 25 nm thick. Metals used for the electrical contacts are noble and do not require special handling after their fabrication except Cr. Cr oxidises rapidly, so immediately after Cr evaporation substrates are kept in an N_2 chamber to avoid oxidation (Cr pads are exposed to air for a total time < 10 mins, including all steps of fabrication, before they are covered with the van der Waals structure).

2.2.2. Bulk TMDC crystals

Doped MoS_2 crystals are fabricated by the CVT. CVT is a process where a liquid or solid substance reacts with a gas, forming vapour phase reaction products that undergo the reverse reaction in a different place of the system [39]. The fabrication of bulk crystals is carried out by Professor Der–Yuh Lin from the National Changhua University of Education, in Changhua, Taiwan. The fabrication method follows the procedure described by Wang et *al.* [40] (n–type, doped with Fe) and Suh et *al.* [41] (p–type, doped with Nb). For this Thesis, the use of materials grown by CVT is essential to obtain doped semiconductors. Moreover, the quality of the materials growth by CVT processes surpasses the quality provided by larger area fabrication methods. Thus, CVT growth crystals are suitable for exploring the possibilities offered by TMDCs. We will discuss in Chapter 3 the importance of the use of doped TMDCs to achieve acceptable performance in solar cell prototypes. We also use h–BN provided by Kenji Watanabe and Takashi Taniguchi from the National Institute for Materials Science in Tsukuba, Japan. Apart from the doped MoS_2 and the h–BN, other materials such as pristine MoS_2, p–doped MoS_2 and more h–BN bulk crystals are commercially available from HQ Graphene. Bulk and exfoliated crystals are stored in an N_2 atmosphere to prevent their degradation.

2.2.3. Van der Waals assembly

Van der Waals assembling is the process in which one or more TMDC flakes are picked and then transferred onto a substrate with or without metallic contacts. This approach is widely used to build laboratory samples as it offers ample throughput and relatively easy changes in layer sequences [42]. Among the assembling techniques used in the literature, the use of temporary carriers is a common practice to handle the semiconductors before deposition in a desired place, also called deterministic placement methods [43]. Some processes are carried out in wet conditions as the polymethyl methacrylate carrying layer method [44] or the wedging transfer method [45]. Other alternatives avoid the presence of water through the use of polymers with a low transition temperature [46]. Device samples fabricated in this Thesis follow two transfer techniques, the polydimethylsiloxane (PDMS) deterministic transfer technique described by Castellanos–Gómez et *al.* [47] and a variant of the hot–pick–up technique described by Pizzocchero et *al.* [48] which is also similar to the pick–up technique described by Wang et *al.* [49].

In the PDMS deterministic transfer method, semiconductor flakes are exfoliated from bulk crystals using adhesive tape (BT–150E–CM, Nitto) and then exfoliated again onto a PDMS stamp. The semiconductors are then transferred from the stamp onto the contacts by physical contact between the metal and the stamp. The transfer operates on the principle of viscoelasticity. The stamp exhibits characteristics of an elastic solid in the short term, yet it gradually flows over extended periods [50]. Besides, when PDMS is heated up to 45ºC its viscosity changes helping to release the materials attached to the stamp. This process is useful when only one material is placed onto the contacts because PDMS leaves a residual layer of adhesive on the surface of the flake. PDMS residues are hard to remove and will hamper the properties of TMDC stacks of several flakes, as residues of PDMS are stuck at the interface between the semiconductors and interfere with the electrical properties of the device.

To improve the cleanness and performance of the devices, we have implemented a variant of the hot–pick–up technique described by Pizzocchero et *al.* [48]. The semiconductor crystals are firstly exfoliated from bulk crystals using the Nitto–tape and then exfoliated onto a temporary carrier (SiO_2(85 nm)/Si wafer). To increase the amount of material transferred onto the SiO_2/Si carrier, we advise doing an oxygen plasma etching on the surface of the carrier before material

exfoliation. Polymer stamps are prepared, consisting of a glass slide onto which a drop of Sylgard® 184 PDMS is deposited and covered with polypropylene carbonate (PPC) (25% by weight in anisole, Merck). Stamps are prepared via oxygen plasma etching (Diener Electronics FEMTO) of the PDMS surface for three minutes and subsequent PPC deposition on PDMS. During the plasma treatment, the functional groups at the surface of the PDMS are activated and they can be linked to the PPC molecules. Once the PPC has been deposited, the stamps are placed on a hot plate at 55ºC to evaporate the solvent.

A schematic of our developed technique used to create a pn junction is depicted in Figure 2.1. The first flake is picked up by heating the carrier to 45 °C and bringing the stamp into contact with it (step 1). The stamp is then retracted and removes the flake from the substrate (step 2). This pick–up is repeated to build the pn junction on the stamp (step 3). To release the stack, the stamp is brought into contact with the substrate with the pre–patterned metallic pads and heated to 100 °C. At high temperatures, PPC turns into a viscous liquid releasing the stack on the substrate (step 4). This method guarantees that the interfaces forming the pn junction have not been in contact with any polymer. Note that the process can be repeated several times stacking more than two flakes of materials allowing multiple combinations. The assembly is made in air and all semiconductor surfaces are exposed to air for several minutes. PPC residues are removed from the upper surfaces using chloroform (step 5). Figure 2.2 shows two photographs of a pn junction which are the typical structure of the devices characterised through this Thesis: one image is macroscopic where only the metallic pads are appreciable, and the other was taken with a microscope showing the pn junction.

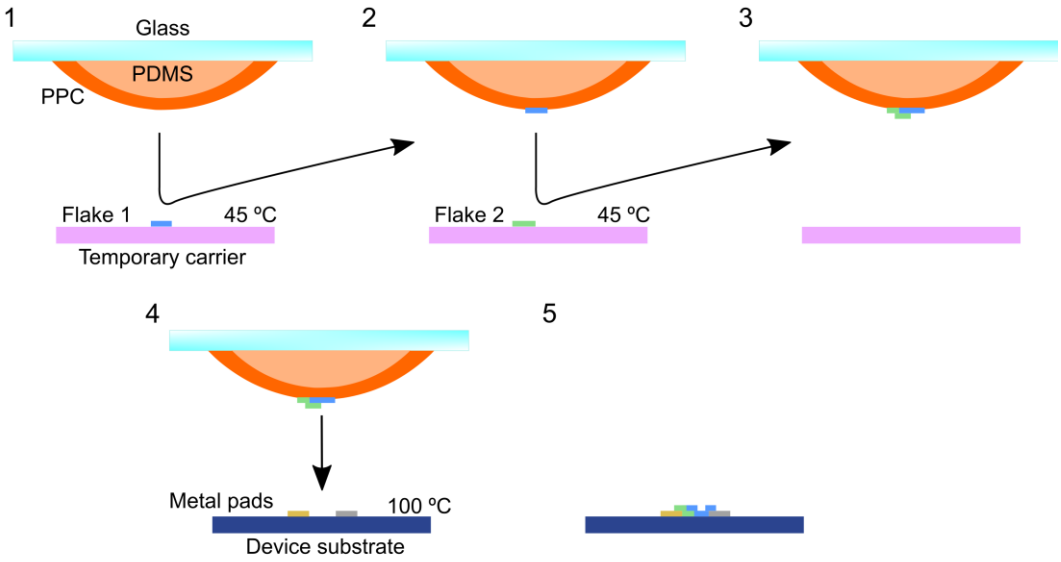

Figure 2.1. Steps in the Van der Waals assembly by the hot–pick–up technique.

The explained process of van der Waals cell assembly can be also done by substituting the PPC with commercial nail polish. This method has been successfully applied in the construction of van der Waals heterostructures [51]. The use of nail polish does not require the plasma treatment step, the application can be simply done by using a brush and the releasing stage requires lower temperatures (75ºC). The cleaning of the residues is done with less toxic chemicals, using acetone and isopropyl alcohol. Nevertheless, the use of nail polish involves some disadvantages such as a more difficult control of the releasing step and the detachment of the nail polish layer from the PDMS stamp.

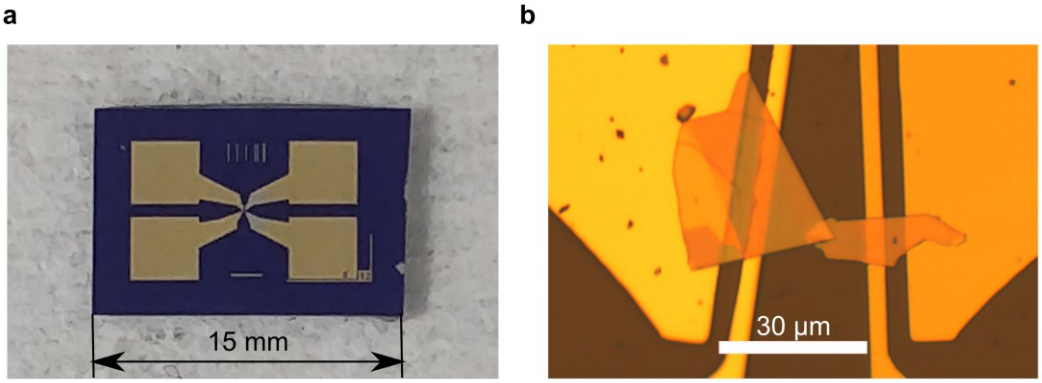

Figure 2.2. (a) Photography of the chip for the solar cell. (b) Micrograph of a MoS_2 pn junction.

2.3. Electronic and optoelectronic characterisation of devices

2.3.1. Current–density voltage measurements

J–V curves are recorded in the open air using a source–measure unit (Keysight B2901A or Keithley 2602A). Scan speed is ~ 85 mV/s. Apart from dark *J–V* characterisation, three light sources are employed for measurement under different illumination conditions:

- Solar simulator. We have used two different simulators. The first is a Xe–lamp–based solar simulator with air mass filters. The irradiance was finely adjusted to 100 mW/cm^2 by tweaking the distance to the sample platform using a calibrated Si photodiode (Thorlabs FDS1010 [52]). The second simulator is Wavelabs LS–2 solar simulator. It is based on an LED system of different colours that emulates the solar spectrum and is calibrated with the Antonometrics RC18 Series reference solar cell [53]. The temperature of the sample is maintained at 25ºC using a Peltier controller in each solar simulator.
- Green laser 500 mW laser diode with wavelength 525 nm (Thorlabs I520g1) for characterisation under high power (Figure 2.3). The illumination power density is controlled using a current source (Elektro–Automatik PS 2042–06). The sample is vacuum–hold to a copper heat sink whose temperature is controlled with a Peltier device so that it does not heat up during measurements.
- Broadband lamp with adjustable irradiance halogen lamp coupled to a microscope (Motic BA310 MET–H) with different magnifying lenses. The irradiance is calibrated using a NIST–traceable calibrated silicon detector (Newport STPVCERT).

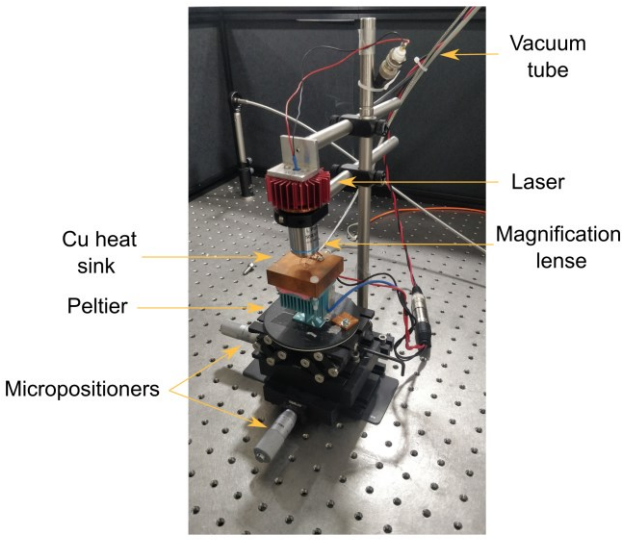

Figure 2.3. Green laser set–up for characterisation of TMDC solar cells under high power illumination.

2.3.2. Cryostat measurements

J–*V* measurements in a cryostat are useful as this equipment guarantees minimal effect from the external environment. Moreover, characterisation using a cryostat provides further insights into the effect of temperature on device behaviour and a more accurate evaluation of the electrical properties of devices. Our cryostat system (see Figure 2.4) consists of a double vessel connected to a vacuum pump (Pfeiffer Vacuum pump PM 103 583 AT) operating at a rotation speed of 1500 rpm. Once under vacuum conditions, the chamber is cooled down thanks to a helium–closed loop which is powered by an external compressor. The samples are placed on a holder located in the internal vessel of the system where temperatures down to 5 K can be reached. The vacuum between the internal vessel and the external vessel guarantees thermal isolation. The temperature of the internal chamber is regulated using a temperature controller (LakeShore 331). This machine regulates the current flow through a resistance placed inside the cryostat that generates heat by the Joule effect to counteract the cooling effect of the helium loop. Both vessels have windows that allow the illumination of the samples with an external light source. Samples are connected externally with a coaxial cable to a current source (Keysight B2901A).

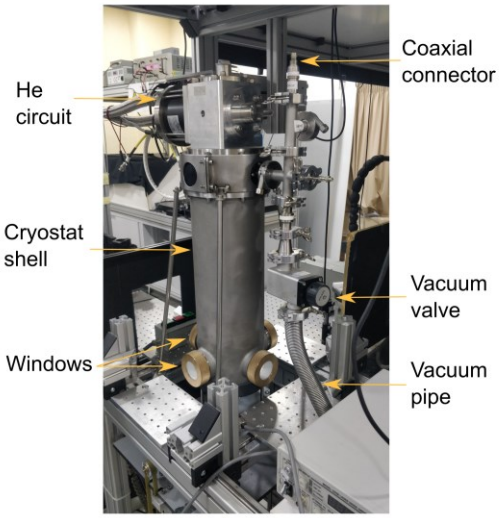

Figure 2.4. Cryostat system set–up for characterisation of TMDC solar cells at low temperatures.

2.3.3. Photocurrent maps

A photocurrent map is a visual representation that illustrates the spatial distribution of photocurrent across the surface of a device. This map indicates how efficiently different regions of the solar cell are converting incident light into electrical current. Our measurement set–up is presented in Figure 2.5. Photocurrent maps are measured using a diode laser with wavelength 505 nm (Thorlabs M505F3) focused with a 50x objective to obtain a spot of ~ 10 μm^2. Samples were mounted on a xy–stage moved with piezoelectric actuators (Thorlabs PIA25) controlled by a four–channel K–Cube piezo inertia motor controller (Thorlabs KIM101). The position of the sample and the laser spot are controlled using a digital camera. A Keysight B2901A source–measure unit is used to voltage bias the sample and record the current. Both, the motor controller and the Keysight are controlled with a homemade MATLAB software created to measure the current output of the sample at each point of the map.

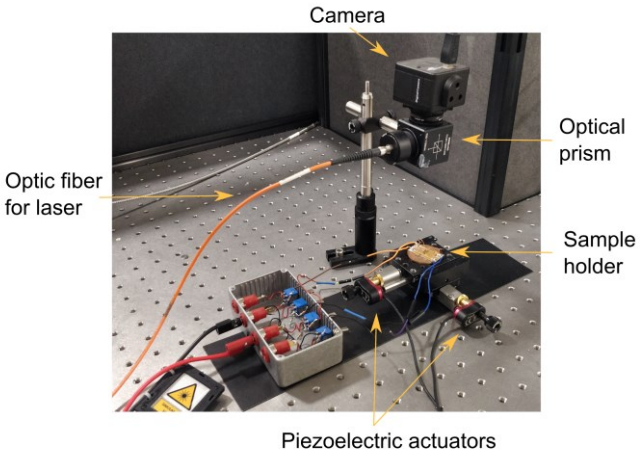

Figure 2.5. Photocurrent map measurement set–up.

2.3.4. External quantum efficiency (EQE) measurements

EQE measurements are carried out using a lock–in amplifier (Stanford Research SR830 DSP) equipped with a mechanical chopper and a low–current trans–impedance preamplifier (Stanford Research SR570 DSP) (Figure 2.6). The light source is a stabilised 100 W halogen lamp, focused on the sample using optical mirrors and the wavelength is selected by a grating monochromator (Cornerstone 260, Newport) equipped with order sorting filters. The spectral power density is determined using a NIST–calibrated silicon detector (Newport STPVCERT). The measurement process consists of measuring the photoresponse of the samples. Then, the calibrated detector is measured under the same illumination conditions. The photoresponse of the detector is compared to its EQE which is tabulated to determine the number of photons provided by the light source at each wavelength. Finally, the photoresponse of the sample is compared to the spectral characteristics of the illumination source to obtain the EQE of the sample.

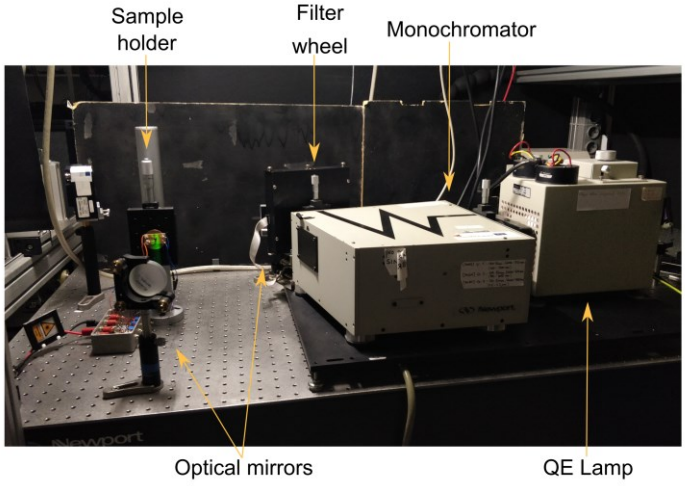

Figure 2.6. EQE measurement set–up.

2.3.5. Van der Pauw method for measurement of resistivity and Hall mobility

For Van der Pauw characterisation, samples are fabricated using the assembly procedure based on the direct transfer of the TMDCs from PDMS stamps. The geometry of metallic pads is designed individually for each sample to achieve point–like contacts. The first measurements were performed using the Ecopia Hall Effect Measurement System (HMS–3000) with a magnet of 0.55 T. However, the reduced size of the samples limits the maximum current that samples can hold under limits hardly attainable for the HMS–3000. This is especially problematic when measuring highly resistive samples.

HMS–3000 specifications datasheet states that this equipment can work in a range of current between 1 nA to 20 mA, and measure resistivities between 10^{-4} to 10^{7} Ω·cm. Nevertheless, we have found a lack of repeatability when measuring highly resistive samples with low currents (range of nA). In these cases, the current cannot be increased as sample integrity is risked because of their reduced size. To improve the accuracy of the measurements, our research group created a specific set–up that allows the measurement of these highly resistive materials. Figure 2.7 illustrates the set–up which consists of a current source (Keithley 6221), a voltmeter (Keithley 2182A), an Arduino controller and a sample holder. The Arduino controller switches the connection between the current source, the voltmeter, and the sample holder to perform all the characterisation measurements. Data is processed with homemade MATLAB software that

implements the equations of Van der Pauw to extract the parameters of the sample [54]. Further details about the equations implemented in this software are discussed in Chapter 6.

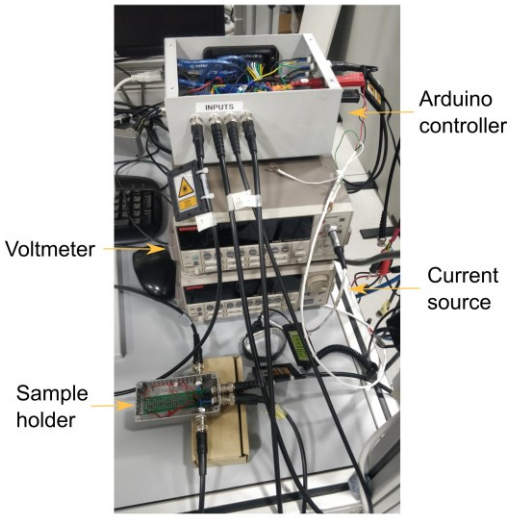

Figure 2.7. Set–up for the measurement of resistivity and Hall mobility using the Van der Pauw method.

2.4. Atomic and Kelvin–probe force microscopy (AFM and KPFM)

The haphazard nature of the exfoliation process to obtain TMDC layers precludes the accurate control of their thickness. Thus, AFM is essential to determine the thickness of the materials used in the TMDC–based samples fabricated. The AFM characterisation was done with different equipment. Some samples were measured internally at IES in the IBLAB facilities using a Multimode Nanoscope III A. in tapping mode. Data processing was carried out using Gwyddion software. Other samples were characterised externally at Centro Nacional de Microscopía Electrónica from Universidad Complutense de Madrid. Data processing in this case was carried out using Nanoscope Analysis 2.0 software.

KPFM is a non–contact variant of AFM whereby the work function (WF) of the surfaces can be measured at atomic and molecular levels. This technique yields the measurement of the WF and the topography of the samples simultaneously [55]. While measuring, the electrical connection between the KPFM tip and the sample occurs, leading to the generation of an electron flux that equalises their Fermi levels [56]. Consequently, a potential difference known as the contact potential

difference voltage (V_{CPD}) arises between the sample and the tip. This technique has been employed to evaluate the surface photovoltage provided by TMDC heterojunctions [57–59]. Further details about these measurements will be discussed in Chapter 6.

KPFM measurements in this Thesis were done at Instituto de Micro y Nanotecnología CSIC, conducted by Mónica Luna and Micaela Rodríguez Peña. The purpose of KPFM measurements was to determine the surface characteristics of the semiconductors and evaluate the evolution of the potential difference between the n–material and p–material in a pn junction under different illumination conditions. Simultaneous AFM and KPFM were implemented by operating in noncontact amplitude modulation mode with phase–locked loop (PLL) detection and electrostatic force gradient feedback [60]. In this configuration, two different modulations are applied to the cantilever: (1) a mechanical excitation at its resonance frequency (85 kHz) and (2) an electrical excitation at a lower frequency (7 kHz); and in addition, three simultaneous feedback are implemented: (1) topography feedback keeps the mechanical oscillation amplitude constant by regulating the tip−sample distance [61,62]; (2) a PLL nullifies the phase difference between the driving signal and the cantilever mechanical oscillation, keeping the oscillation at resonance by controlling the excitation frequency; (3) a bias voltage is applied to the tip to nullify the electrostatic force or force gradient [63].

The V_{CPD} between the tip and sample is obtained at each pixel, as described in the literature [64,65]. It has been used Nanotec Electrónica AFM and ATEC–EFM (Nanosensors) cantilevers, with a resonance frequency of 85 kHz and a force constant of 2.8 N/m. For the applied electrical excitation, the chosen amplitude was 1 V p–p at a frequency of 7 kHz.

The technique operates in non–contact mode. Topographic non–contact feedback relies on the attractive force between the tip and sample that decreases the oscillating amplitude of the cantilever as the tip approaches the surface, making possible noncontact imaging of the surface and simultaneous acquisition of topography and V_{CPD} data in a single pass [64–66]. Data was processed with the software WSxM (version 5.0) [67]. Experiments were performed in an N_2 atmosphere.

2.5. Handling recommendations of TMDC samples

TMDC devices fabricated during the experimental works of this Thesis consist of small–area semiconductors placed between metallic contacts. Due to their reduced area, electrical characterisation of the devices is done using small values of current, (in the range of microamperes and nanoamperes) in other to prevent device degradation or eventual destruction of the samples. This fact implies that special care in the manipulation of the devices is necessary to prevent accidental discharges that could be caused by static electricity that may build up in the body of the operator. Safe manipulation of the device requires these recommendations:

- Devices are manipulated using an antistatic wrist strap that prevents discharges from the operator to the device.
- Devices are measured using a cage system that can be connected or disconnected using a switch. This switch short–circuits the device assuring a safe connection to the measurement equipment.
- During electrical characterisation is necessary to avoid excessive bias or injected current. For example, during J–V measurements, a limit of current is chosen under 1 μA when measuring a device for the first time.

Chapter 3

Large open–circuit voltage in a MoS_2 homojunction

3.1. Introduction

The working principle of solar cells is based on the light absorption of materials and the generation of free charge carriers. These free charge carriers are drifted by the presence of the built–in potential ($V_{built-in}$) generated at the pn junction by the difference between the Fermi levels of the p–material and the n–material, so minority carriers at each side of the pn junction flow into the opposite side and can be extracted providing a photocurrent. When the solar cell is in the open–circuit state, free carriers generated under a steady illumination accumulate at the terminals of the pn junction generating a potential difference. This potential is called open–circuit voltage (V_{OC}) which is the maximum voltage provided by a photovoltaic device and represents the maximum energy that can be extracted under given illumination conditions.

The V_{OC} of a solar cell is dependent on the band gap of the materials forming the pn junction, which is the minimum energy of a photon required to induce the generation of an electron–hole pair in the material lattice. When light illuminates the solar cell, photons with larger energy than the material band gap can induce the generation of electron–hole pairs, which are then extracted, providing photocurrent. However, during the extraction process, energy losses occur due to different mechanisms, such as thermalisation losses caused by the loss of energy of charge carriers with energy greater than the material band gap, and recombination losses resulting from different processes like radiative recombination, Auger recombination, Shockley–Read–Hall recombination, and surface recombination.

To measure the energy losses of a device, the band gap–voltage offset is often used ($W_{OC} = E_G/e - V_{OC}$) [68,69]. W_{OC} has a lower limit because of the thermodynamic constraints related to thermalisation. This limit is approached when all parasitic loss mechanisms have been eliminated and only radiative recombination takes

place. The minimum W_{OC} value can be evaluated following the Shockley–Queisser detailed balance theory [70]. The typical value of W_{OC} lies between 0.24 and 0.30 V for E_G values between 1.1 and 1.9 eV for an illumination with the AM1.5G standard solar spectrum. Devices made of epitaxial III–V materials, such as GaAs, exhibit the lowest experimental W_{OC} with 0.31 V under the AM1.5G standard solar spectrum as they work close to the radiative limit [71]. In the case of silicon, the record one–sun W_{OC} is 0.38 V, determined by the Auger recombination inherent to this material [72]. Among emerging technologies, metal halide perovskites have reached the lowest W_{OC} with 0.44 V [73], while record organic solar cells exhibit higher values around 0.53 V [74].

TMDCs solar cells are expected to reach W_{OC} values similar to the already consolidated technologies. Developing effective doping processes for TMDCs can unlock the possibility of realising homojunctions that would provide larger photovoltage values than heterojunctions based on pristine materials. However, the realisation of efficient TMDCs solar cells not only depends on the quality of the semiconductors. The correct functioning of TMDC solar cells is subjected to the obtention of ohmic contacts to these materials.

In this Chapter, the results from our research team [75] and [76] are presented, along with a discussion about the main problems that hamper the performance of the TMDCs solar cells based on MoS_2 homojunctions, and the modelling of their *J*–*V* characteristics. We demonstrate that it is possible to extract a high V_{OC} of 1.02 V yielding a W_{OC} of 0.27 V for an illumination intensity of 4 W/cm^2. Besides, a comprehensive analysis of the principal mechanisms that hinder the performance of MoS_2 solar cells is presented. We will show that the ideality of the metal/semiconductor contacts used to extract the photogenerated current from the pn junction plays a significant role in the overall performance of the device.

3.2. State–of–the–art of TMDC solar cells

The isolation of graphene [9] has garnered attention towards research on this material and other materials with a layered structure. Layered materials display a wide range of properties, ranging from highly conductive materials like graphene to insulators like BN. Recently, the family TMDCs such as WS_2, WSe_2, MoS_2, $MoSe_2$, and $MoTe_2$ have started to gain momentum, being proposed in multiple optoelectronic applications. These materials have attracted the interest of the

scientific community because of their strong light–matter interactions, chemical stability, and easy manipulation [15,21,23,27,77]. Their layered structure allows them to be piled forming van der Waals structures, enabling multiple combinations of materials. This results in the possibility of assembling various device architectures without the lattice–matching constraints required in conventional solar cells.

Concerning the application of TMDCs in photovoltaic devices, their band gap is an essential property to consider. The band gap of these materials lies in the range from 1.0 to 2.0 eV [78], which is well–suited to the solar spectrum. This band gap is also comparable with the band gap of conventional semiconductors such as Si (1.1 eV), GaAs (1.4 eV), or CdTe (1.5 eV) [15,79]. Although most of the TMDCs exhibit an indirect band gap, their band gap varies with the thickness of the material. For instance, the band gap of MoS_2 increases from 1.3 eV to 1.9 eV when reducing the thickness to the limit of the monolayer [15]. Other properties such as refractive index are also thickness–dependent [80–82]. The change in the properties from bulk to few layers occurs when the number of stacked layers is lower than a certain limit. For example, it has been argued that the bulk properties are exactly reached when the semiconductor slab has a thickness of 13 atomic layers in the case of MoS_2 (~ 8 nm) [81] or 8 atomic layers in the case of h–BN (~ 3 nm) [83].

Regarding the aforementioned properties, TMDCs have been proposed as candidates for new models of ultrathin, light, and flexible [35,84] photovoltaic devices. In recent years, numerous publications about photovoltaic devices have demonstrated the potential of TMDC–based devices, using multilayers and monolayers. While monolayer devices display intriguing properties such as strong photoluminescence response or tuneable band gap [85], the use of multilayers is preferable when considering solar cells. This can be explained by several facts, for instance, a monolayer has two surfaces and no bulk in between, which presents the extreme case of surface science. This implies that monolayers are notably more reactive than even bilayers [86,87], so, many 2D crystals would corrode, decompose, or segregate, and hence cannot be useful in commercial devices [42]. Another reason to use multilayers is that despite the high absorption coefficient of TMDCs, light absorption in monolayers is limited by the thinness of the absorbing layer.

Solar cells based on TMDCs can be implemented thanks to the existence of both naturally n–type materials such as MoS_2 [88], and p–type materials like WSe_2 [89].

Reported solar cells based on van der Waals junctions of TMDCs utilise diverse structures, including Schottky devices, heterojunctions, and homojunctions. Heterojunctions are widely used as they combine intrinsic p–type and n–type materials to construct a pn junction. On the other hand, Schottky devices are based on metal/semiconductor junctions, where the difference between the Fermi level of the material and the Fermi level of the metal generates a potential barrier and a rectifying behaviour. Lastly, homojunctions rely on the use of previously doped materials to shift the Fermi Level of the semiconductor downwards (p–doping) or upwards (n–doping) allowing the utilisation of the same material with different doping levels to create a pn junction.

The most explored TMDC–based device is the heterojunction of MoS_2 and WSe_2, which exhibits W_{OC} values above 0.8 V for bulk devices and above 1 V for monolayer devices. The corresponding V_{OC} values are below 0.4 V for multilayer [25,33,34,90], (E_G 1.2–1.3 eV) and below 0.6 V for monolayer devices [27,28,91,92] (E_G 1.6–1.9 eV), even for illumination levels much higher than one–sun irradiance. Moreover, many of these devices show a pinned V_{OC} [25,33,34,93], which is a V_{OC} that does not increase with illumination intensity. It is remarkable that lateral junctions created on a TMDC flake through split–gating, selective chemical surface doping, or using a double Schottky barrier provide lower W_{OC}s than van der Waals devices. The W_{OC} values reported in these devices for bulk flakes are around 0.54 V [94,95] and 0.73 V for the case of monolayers [29,95]. Alternatively, Schottky devices have been explored, showing a W_{OC} of 0.92 V in a WSe_2–based solar cell [96]. It can be concluded that W_{OC} values of TMDC–based devices are far from the values achieved by conventional technologies. This fact suggests that the limitations of the van der Waals junction rather than the materials are likely the cause behind the low V_{OC} in TMDC solar cells.

3.3. The problem of the Fermi–level pinning

The performance of solar cells depends on their band diagram. The ideal maximum voltage that can be extracted from a solar cell is determined by the $V_{built-in}$ generated between the p–type and n–type material. Charge carriers are generated at the pn junction, but to extract electrical power from the solar cell, an adequate transport of carriers from the semiconductor to the electrical contact is crucial. The

realisation of the electrical contact involves the presence of an additional interface between the semiconductor and usually a metal that works as a contact.

When a semiconductor is put into contact with a metal, there is a band alignment where the Fermi level of the semiconductor reaches the same level as the WF of the metal. The metal/semiconductor contact causes a band bending at the interface generating a potential barrier at the junction whose height depends on the characteristics of both materials. This barrier is called the Schottky barrier, and according to the Schottky–Mott rule, its height (φ_{SB}) depends on the WF of the metal (φ_M) and the position of the bands of the semiconductor. Figure 3.1 shows the ideal case of what happens when an n–type semiconductor with a band gap E_G and electronic affinity χ is put into contact with two different metals. If the WF of the metal is larger than the electronic affinity of the semiconductor, electrons from the semiconductor will flow into the metal, depleting locally the semiconductor and generating a potential barrier at the interface defined by Equation (3.1). This is the case illustrated in Figure 3.1.a, so electrons cannot flow into the metal without enough energy to surpass the Schottky barrier. By contrast, if the WF of the metal is lower than the electron affinity of the semiconductor, the metal will donate electrons to the semiconductor. In this case, there is no potential barrier for electrons and an ohmic contact is achieved as it is depicted in Figure 3.1.b.

$$\varphi_{SB} = \varphi_M - \chi \tag{3.1}$$

Nevertheless, the Schottky–Mott rule is not realised in most of the experimental cases giving incorrect predictions of the Schottky barrier height [97]. This is caused because the Schottky–Mott rule is an idealisation of the interface between metal and semiconductor. There are several sources of defects that can affect the properties of the interface between metal and semiconductor. For instance, the surface is a defect of crystals because of the rupture of the continuity of the lattice that leads to the presence of dangling bonds [98]. The non–ideality of the surface is one of the main problems when developing contacts to semiconductors as the presence of defects causes the apparition of metal–induced gap states (MIGS) allocated in the band gap of the semiconductor generating the so–called charge neutrality level (CNL). When there is a CNL, the Fermi level of the metal is pulled towards the CNL, so the properties of the contact are no longer governed by the properties of the semiconductor but by the properties of its surface. Figure 3.1.c shows a scheme of how the CNL can lead to non–ohmic contacts even using a metal with an appropriate WF. The presence of defects at the surface causes the depletion of the semiconductor moving the bands upwards at the surface. The degree of

pinning can be measured by how far the measured Schottky barrier from the value predicted by the Schottky–Mott rule is. Equation (3.2) shows the expression of the Schottky barrier height considering the pinning factor S_p and the position of the CNL. S_p values range from 0 (completely pinned) to 1 (not pinned). For instance, strong Fermi–level pinning effects are well–known in conventional semiconductors: pinning factors of 0.3 for Si and 0.1 for GaAs have been measured [99].

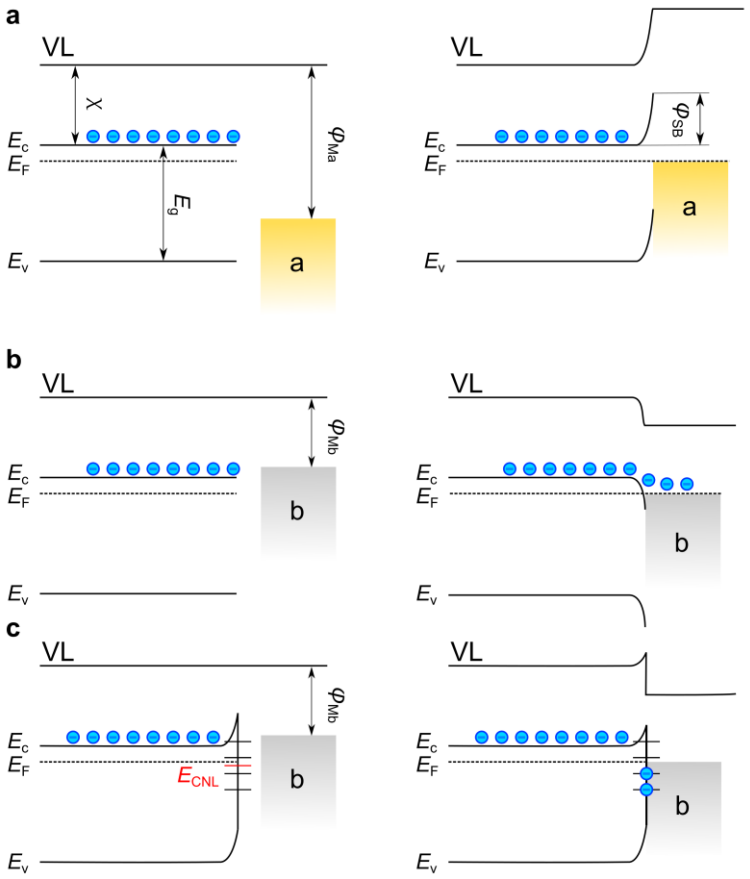

Figure 3.1. Band diagram of an n–type semiconductor contacted with metal. Case of an ideal Schottky contact (a) and an ohmic contact (b) according to the Schottky–Mott rule. (c) Case of Fermi level pinning induced by MIGS.

$$\varphi_{SB} = S_p(\varphi_M - \varphi_{CNL}) + (\varphi_{CNL} - \chi) \tag{3.2}$$

The deviation from the Schottky–Mott rule is inherent to conventional materials. This implies that ohmic contact cannot be realised by selecting a metal with a suitable WF. When there is no ohmic contact, the mechanisms of metal/semiconductor charge transport depend on the carrier population of the

semiconductor. When the carrier population is lower than 10^{17} cm^{-3}, the main mechanism is the thermionic emission over the Schottky barrier. This implies that carriers need an amount of energy to surpass the barrier and consequently flow into the metal. Conversely, if the carrier population is over 10^{19}, the width of the barrier shrinks, activating tunnelling transport [100]. Then, the obtention of tunnelling transport is a way to obtain ohmic contacts. Among the techniques that can be used to obtain ohmic contacts include depositing a thin layer of a highly–doped semiconductor material (such as a heavily doped n–type or p–type material) between the metal and the semiconductor. This procedure reduces the contact resistance by providing a more gradual transition in doping concentration from the metal to the semiconductor.

When considering TMDCs solar cells, these materials offer some advantages and disadvantages in comparison to conventional semiconductors when realising ohmic contacts. One advantage is their layered structure, which provides almost defect–free surfaces with the absence of dangling bonds and charge traps that theoretically would cause the Fermi–level pinning. Nevertheless, the realisation of ohmic contact to TMDCs also presents problems related to the Fermi–level pinning. For instance, values of a pinning factor of 0.1 have been reported for combinations of MoS_2 with different metals [95,101–103]. The origin of the Fermi–level pinning in TMDCs could be caused by different phenomena. First, the junction by van der Waals forces between metal and semiconductor generates a small barrier called the van der Waals gap. This is less problematic when considering multilayer structures showing lower contact resistance [104]. Second, TMDC surfaces are not fully free of defects [105–107], and they can alter the position of the Fermi level at the surface. Vacancies or discontinuities are present in the lattice of the semiconductor generating the presence of MIGS. For instance, it has been reported that chalcogen atoms can volatilise leaving vacancies at the surface of TMDCs [108]. Although there are different theories about the possible mechanism that induces the presence of MIGS, there is no consensus about the origin of the Fermi–level pinning in TMDCs. Therefore, the obtention of ohmic contacts to TMDCs is not trivial, and effective strategies of contact designing are required to solve this problem.

In conventional materials, the presence of the Fermi–level pinning can be overcome using heavily doped semiconductors at the contacts, thermal annealing, and diffusion layers. However, these techniques do not apply to TMDC devices. The use of diffusion layers in such thin devices (tens of nanometres) would lead to

significant distortion of the semiconductor lattice and compromise its properties. Moreover, the absence of effective doping schemes for TMDCs limits the use of heavily doped materials that could realise ohmic contacts by tunnelling transport. Although there has been some progress in doping 2D materials, most of these techniques rely on surface electrostatic doping, where a charged species on the surface results in the accumulation of electrons or holes in the semiconductor [109]. A strong pinning factor means that Schottky barriers at the metal/semiconductor interface cannot be eliminated by simply selecting a metal with an appropriate WF. Hence, the presence of the Fermi–level pinning in TMDCs must be addressed to improve the quality of the contacts and unleash the potential of solar cells based on TMDC materials.

3.4. Why using MoS_2 homojunctions

MoS_2 is the most studied TMDC. It can be found in nature as a mineral in the form of molybdenite. MoS_2 has been industrially used as a lubricant, but the isolation of graphene has helped to boost the interest in the use of MoS_2 in optoelectronic applications. MoS_2 has a hexagonal lattice structure, consisting of layers of molybdenum atoms sandwiched between two layers of sulphur atoms. MoS_2 shows a direct band gap of 1.9 V for monolayers and an indirect band gap of 1.3 for the bulk material [110]. This band gap value makes it an attractive material for applications in which the control of electronic properties is critical. Another important feature of MoS_2 is its strong light absorption along with the presence of excitonic peaks that enhance light absorption at ~600 nm and ~650 nm [15]. Both characteristics, the existence of a suitable band gap and its strong light absorption make MoS_2 appealing to solar cell devices.

MoS_2 is naturally an n–type semiconductor [88], and as we mentioned in Section 3.2, it is used together with WSe_2 in van der Waals heterostructures. However, the light–energy conversion in heterojunctions made of intrinsic materials is limited because of the reduced $V_{built-in}$ voltage at the pn junction. As an alternative, the development of doping methods to TMDCs would let the obtention of homojunctions which are more interesting from the electrical point of view, as the $V_{built-in}$ of these devices approaches the band gap of the material. Figure 3.2.a shows a schematic of the band diagram of a WSe_2/MoS_2 heterojunction made of intrinsic materials and Figure 3.2.b shows a MoS_2 homojunction made of doped

materials. The use of substitutionally doped crystals of MoS_2 allows the obtention of a larger $V_{built-in}$ so a larger V_{OC} could be extracted.

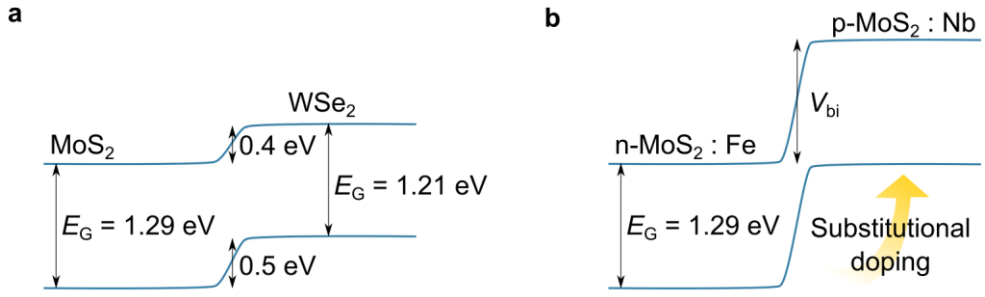

Figure 3.2. Ideal band diagram structure of (a) intrinsic MoS_2 and WSe_2 heterojunction and (b) a MoS_2 homojunction with substitutional doping.

Doping of TMDCs can be achieved by diverse procedures. For instance, plasma doping consists of using an ionised gas that modifies the carrier population of the TMDC by embedding gas atoms into the semiconductor lattice. The doping effects induced by various plasma species on MoS_2 have been studied in the literature, finding that F– and O–contained plasmas (e.g., O_2, SF_6, CF_4, and CHF_3) can result in prominent p–type transport characteristics in few–layer MoS_2 transistors [31]. Other techniques involve the use of chemical compounds such as benzyl–viologen that can be used with simple methods such as drop–casting. This method consists of the exposition of the semiconductor to the compound for twelve hours and subsequent removal of the compound using a solvent [111]. Recently, substitutional doping of MoS_2 has been achieved by growing the material by CVT [41]. During the process, niobium atoms replace the molybdenum in the material lattice. This is possible because of the similarity in the parameters of the lattice of NbS_2 and MoS_2, as well as the similar covalent radius of both atoms. The presence of Nb, which has one valence electron less than MoS_2 induces an effective p–doping of the material. The use of any of these doping techniques would help to the obtention of homojunctions that provide larger V_{OC} values and potentially a larger PCE. The use of CVT growth MoS_2 crystals to form MoS_2 homojunctions was first reported by our research team in 2017. This device consisted of a gate–tuneable homojunction that reported a maximum V_{OC} of 0.51 V under a gate bias of -30 V [112].

Although homojunctions are expected to provide a higher V_{OC} than heterojunctions, experimental devices had not shown a considerable improvement [112]. The best–

reported result is a V_{OC} pinned at 0.57 V [113]. We guess that the limited performance of the devices is associated with the bad performance of the metallic contacts. The strong Fermi–level pinning effect and the absence of effective strategies to obtain ohmic contacts result in the formation of rectifying contacts at the terminals of the device. The causes of the detrimental effect of the electrical contacts in TMDC–based solar cells are not completely understood. Therefore, it is essential to analyse how the performance of the device is jeopardised by the electrical contacts. This is a mandatory step in the pathway to the obtention of a well–functioning solar cell.

3.5. Results and discussion

3.5.1. Characterisation of MoS_2 homojunctions at low temperatures

Our first attempts at realising MoS_2 homojunctions followed the same procedure of our research team in [112], where a gate–tuneable MoS_2 homojunction achieved a maximum V_{OC} of 0.51 V under a gate–bias of -30 V. Flakes were exfoliated from fresh crystals using a Nitto–tape adhesive and deposited onto a chip with pre–patterned gold contacts using a PDMS stamp. In [112], although the photovoltaic effect in MoS_2 homojunctions was demonstrated, the PCE was still low (~ 0.5%), and the mechanisms that jeopardise the performance of the pn junction were not completely understood. We have surpassed the V_{OC} achieved in [112] with an architecturally identical MoS_2 device shown in Figure 3.3.a (inset). This device is identified as device A011. To perform a better characterisation of device A011, we have measured it at low temperatures inside a cryostat. There are several reasons for measuring solar cells in a cryostat. First, thermal noise is minimised. At room temperature, there is a significant amount of thermal noise generated by the electrons, which can interfere with the measurement. Secondly, the dark current is reduced. At higher temperatures, the dark current is typically higher, which can affect the accuracy of the measurements. Cooling the solar cell reduces the dark current, allowing for more accurate measurement of its electrical properties. Lastly, the performance of a solar cell is often affected by temperature–dependent effects such as carrier mobility and recombination rates. By measuring the solar cell at different temperatures, we can evaluate temperature–related effects and determine how they impact the performance of the device.

In Figure 3.3.a, *I–V* curves of device A011 are presented at different temperatures, in dark conditions, and in Figure 3.3.b under a He–Ne laser (Melles Griot 25 LHR 35 mW) illumination. At 50 K, the V_{OC} under laser illumination is 0.74 V, which becomes pinned thereafter. When reducing the temperature, the current density of the device decreases, which is expected by the reduction of its recombination current. However, this reduction of the current density becomes more significant when temperatures are lower than 70 K. At this point, the current is one order of magnitude lower compared to the dark *I–V* curves at higher temperatures. The reduction in the current density values observed may not be only explained by the lower recombination current, but also by additional phenomena occurring at the interface between metal and semiconductor. If there is a rectifying contact at the metal/semiconductor interface, it would work as a diode that is in the opposite orientation to the pn junction. Hence, the current given by the pn junction when it is forward–biased is limited by the reverse current of the diode at the contact which would be reverse–biased.

When decreasing the temperature, the reverse current of the diode from the contact will decrease too, therefore the current of the device will decrease apparently as a variable series resistance. This would explain the sharp decrease of the current density when reducing the temperature under 70 K. Furthermore, the presence of these rectifying contacts can explain the difference between the current values measured at the same temperature in dark and illumination conditions. If the metal/semiconductor interface is photoactive, the reverse current of the metal/semiconductor contact is increased by its photoactive behaviour so current density values of the pn junction under illumination are then limited by the photocurrent generated at the contacts. However, this difference also can be caused by a photoresistive effect of the materials forming the pn junction. These results suggest that the performance of device A011 is hindered by the quality of the metal/semiconductor contacts which could work as parasitic photoactive diodes but does not reveal the presence of these parasitic diodes.

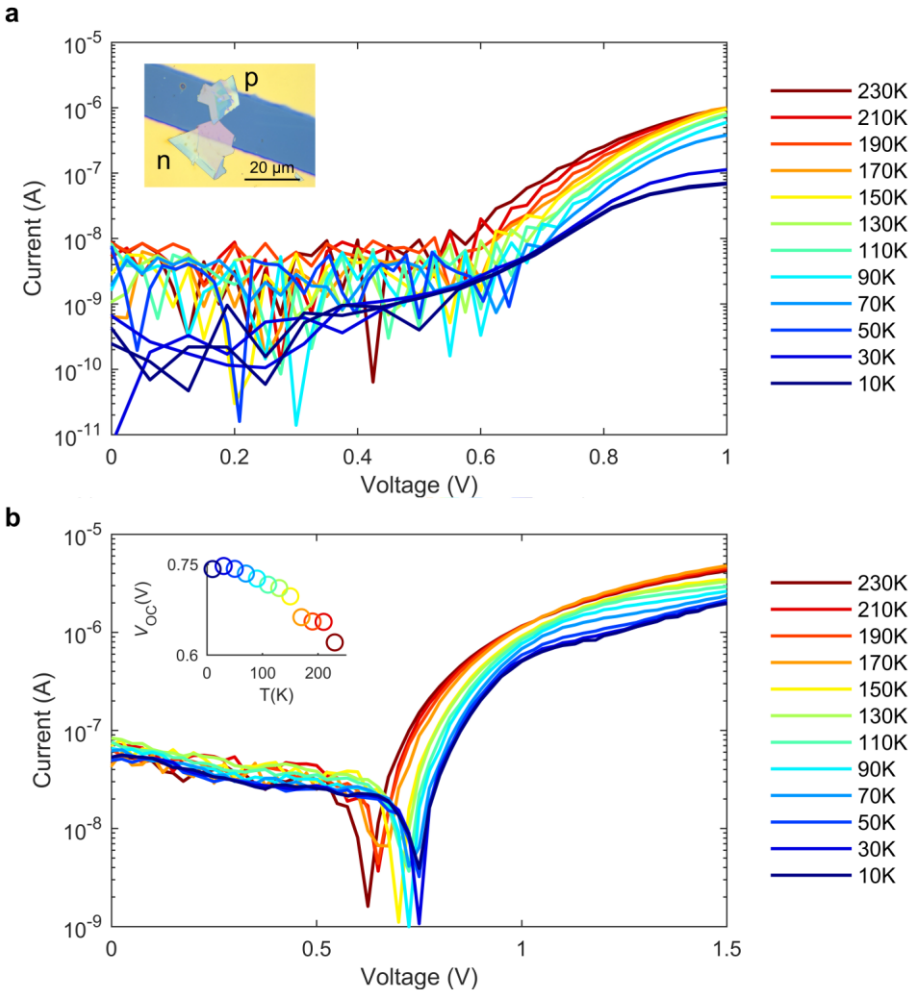

Figure 3.3. *I*–*V* characteristics of a MoS_2 homojunction at different temperatures, (a) (inset: device A011 micrograph) in dark conditions and (b) (inset: V_{OC} dependence with temperature) under the illumination of a He–Ne laser.

3.5.2. Characterisation of photoactive Schottky diodes

The presence of parasitic photoactive diodes at the metal/semiconductor junction is caused by the formation of a Schottky contact. As was explained in Section 3.3, when the difference between the WF of the metal and the bands of the semiconductor is positive, there is a potential barrier that charge carriers must surpass to flow. The height of this potential barrier depends on the characteristics of both, metal and semiconductor. Figure 3.4.a shows device A122 which consists of a p–MoS_2 flake placed between two Pd contacts. Pd WF values reported in the literature range from 5.2 eV [114] to 5.55 eV [115], so if the Pd WF had its largest value, it would be a reasonably suitable hole contact for MoS_2, whose valence band lies at 5.6 eV [24]. When measuring device A122 under illumination conditions, it

seems to show a nearly ohmic contact (Figure 3.4.b), but when light only illuminates one of the contacts a rectifying behaviour is detected. The J–V curves of device A122 can be modelled as two photoactive diodes which are oriented in opposite directions (inset in Figure 3.4.b). The current provided is limited by the reverse current of each diode plus its corresponding photogenerated current. When for example the bottom (blue) contact is illuminated and the device is forward biased (see inset in Figure 3.4.b), charges can pass through the blue diode but are blocked by the top (red) one. As the top (red) contact is in dark conditions, there is no illumination current, and the overall current flow is limited by the reverse current of the red diode. When the device is reverse–biased, current passes through the red diode, and it is limited by the photogenerated current at the bottom (blue) contact.

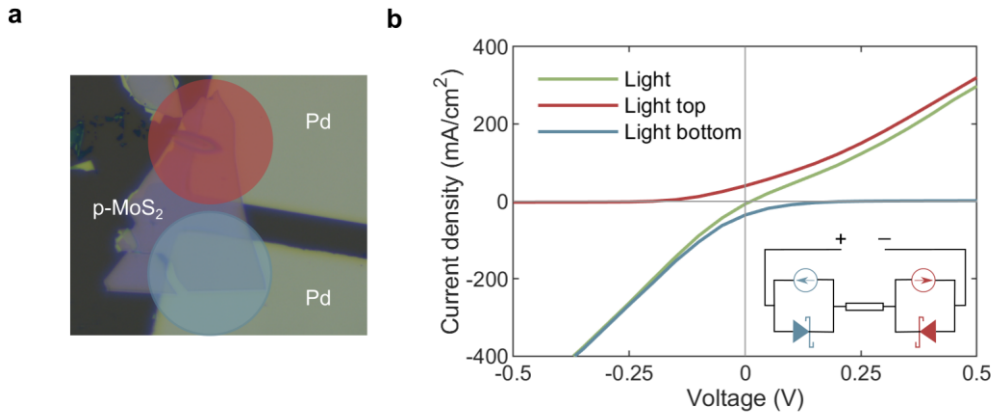

Figure 3.4. (a) Device A122 micrograph. (b) J–V curves. The green curve corresponds to the whole device being illuminated; the red curve has the light on the top side and the blue curve on the bottom side. (inset: equivalent electrical circuit).

The experiment of device A122 elucidates the behaviour exhibited by a Schottky contact formed between metal and semiconductor. We observe that when illumination is applied to solely one side of the device, a V_{OC} of nearly 0.2 V is attained under an equivalent illumination of 4 W/cm^2. If these p–MoS_2/Pd contacts were part of a pn junction device, the photovoltage generated at the metal/semiconductor interface would be deducted from the photovoltage provided by the pn junction. The parasitic effect of the metal/semiconductor contacts explains the substantial disparity in the values of the observed W_{OC} in preceding devices in contrast to conventional solar cells and the pinning effect observed in

some devices. Hence, the elimination of this photoactive trait is imperative for the attainment of optimal functionality in solar cell design.

3.5.3. Demonstration of large V_{OC} in MoS_2 homojunction solar cells

The previous attempts at MoS_2 homojunctions were characterised by the presence of photoactive metal/semiconductor contacts. As photoactive contacts can cause a reduction of the photovoltage provided by the homojunction, a solution may be the deposition of the metal contacts over the semiconductor to block the light and prevent photogeneration at the metal/semiconductor interface. This solution offers the possibility of designing tailored contacts for each flake and performing four–wire configuration measurements. The four–wire configuration arrangement ensures that the voltage is measured across the device terminals without including the resistance of the connecting wires. This set–up provides more accurate readings of the intrinsic resistance or voltage characteristics of the device, particularly in situations where low–resistance or high–precision measurements are crucial.

Figure 3.5.a shows the schematic of a MoS_2 homojunction, identified as A146, with a different structure in comparison to device A011 from Figure 3.3. Device A146 consists of one flake of p–MoS_2 (12 nm thick) and another of n–MoS_2 (120 nm thick) forming a pn junction. Material flakes are exfoliated from bulk crystals onto a Si/SiO_2 (90 nm) substrate. Then, following the pick–up technique described in Chapter 2, the pn junction is assembled on a new and clean Si/SiO_2 substrate using a PPC–covered stamp. The crystals were grown using CVT and have a high doping level of ~ 10^{19} cm^{-3} [41]. Both materials are contacted on the top with Ni/Au contacts using photolithography followed by a thermal evaporation process. Figure 3.5.b illustrates a micrograph of device A146. Figure 3.5.c shows the J–V characteristics of device A146 measured under broadband illumination with three different intensities, using a two–wire configuration. The V_{OC} grows when increasing the illumination power, not showing the pinning effect reported in other TMDC–based devices [25,33,34,93,113]. The V_{OC} reaches 0.68 V at the highest illumination intensity of 4 W/cm². This value of V_{OC} reported surpasses the highest values reported for heterojunctions (0.38 V) [25] and for MoS_2 homojunctions (0.57 V) [113] made of bulk materials. Still, it does not show the real voltage given by the pn junction. Despite blocking the light from the metal/semiconductor interface, the photoactive effect of the contacts is not fully eliminated. We guess that from the considerable difference in the series resistance among the J–V curves at different

illumination levels. This feature suggests that the current extraction through the metallic contact is still affected by a rectifying effect and limited by a photoactive response of the contacts.

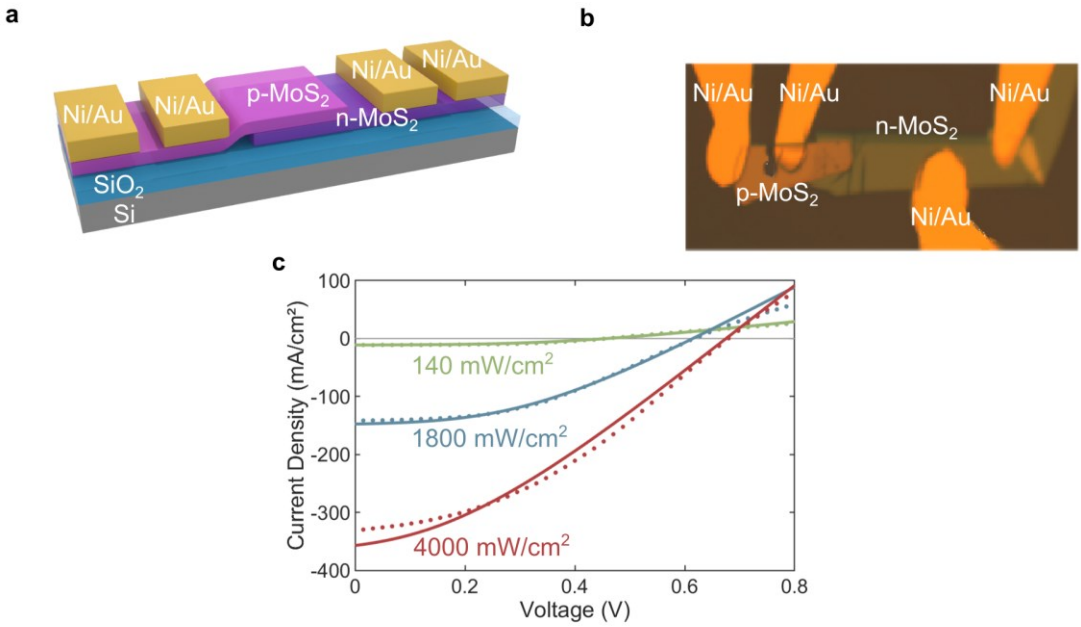

Figure 3.5. (a) Schematic of device A146. (b) Device micrograph. (c) Two–wire J–V characteristics are measured when the whole chip is illuminated with a broadband (halogen) spectrum with the irradiances given by the labels.

The behaviour of device A146 is unconventional because the presence of rectifying Schottky contacts at the metal/semiconductor interface has not been eliminated. This results in a non–ohmic series resistance having a detrimental impact on the fill factor (FF) of the device. As we mentioned in Section 3.3, in conventional solar cells, Schottky contacts between metal and semiconductor are avoided using different strategies such as diffusion layers or annealing treatments. In the case of TMDCs, the reduced thickness of the material layers hampers the use of the techniques used for conventional materials. These Schottky contacts not only have an impact on the FF and the series resistance, but they also have a detrimental effect on the V_{OC} draining the voltage generated at the pn junction. The shadow effect of the metal deposited on the semiconductor does not solve the problem of the photoactive contacts. It has been found that, when considering materials with nanometric thickness, the depletion regions associated with Schottky barriers can extend laterally several microns away from the metal contact edge [76,116], which means that photoactive Schottky barriers are to be expected even if the metal has been evaporated on top of a TMDC.

Figure 3.6.a–d shows different *J–V* curves of device A146 measured in the four–wire configuration that confirms the potential of the MoS_2 van der Waals homojunction as photovoltaic device, proving that it can reach V_{OC} values of, at least, 1.02 V. The output voltage is hindered by Schottky barriers present at the contacts and, although we can eliminate their effect on the V_{OC} by illuminating only the pn junction and measuring with a four–wire configuration, the Schottky barriers still degrade the FF of device A146, and consequently, its efficiency. As in device A122 from Figure 3.4, the metal/semiconductor junctions work electrically as a photoactive diode arranged in the opposite orientation to the pn junction. Hence, the current that can be extracted is limited by the rectifying nature of the contacts, and the photocurrent generated at the Schottky junctions. In Figure 3.6.a, the whole chip is illuminated obtaining a V_{OC} of 0.73 V. In Figure 3.6.b, when blocking the light at the p–side of the device, the V_{OC} increases to 0.80 V, as the contribution of the diode at the p–side is eliminated. In Figure 3.6.c, when eliminating the effect of the n–side, V_{OC} increases to 0.92 V, but at the same time, the lack of illumination on the n–side is accentuating the rectifying effect of the Schottky contact as the *J–V* curve starts to be limited in current. This phenomenon jeopardises the FF and the short–circuit current density (J_{SC}) because of the resistive effect of the contact. Finally, in Figure 3.6.d, when light only impinges the pn junction, the real voltage of the pn junction is obtained, which is 1.02 V. This yields a W_{OC} of 0.27 V for an illumination of 4 W/cm^2, a larger value than previously reported homojunctions [31,112,113]. If the Schottky barriers were completely removed, the device would be theoretically characterised by the red dashed curve depicted in each panel of Figure 3.6. According to this curve, the PCE could be around 6 % in such a simple unoptimised structure, rendering the use of MoS_2 homojunctions a promising approach to TMDC–based photovoltaics.

The V_{OC} of 1.02 V achieved in device A146 sets a record on voltage output provided by a TMDC–based structure and our experimental result is encouragingly close to the radiative limit. Only a similar value of V_{OC} has been reported by Liu et *al.* [95]. Still, it was achieved for a monolayer device (which has a larger band gap) under a gate voltage of -50 V. This result unveils the potential of TMDCs, and particularly substitutionally doped MoS_2, for the development of highly efficient, ultrathin and ultralight weight photovoltaic devices. We have published this result along with further discussions about MoS_2 homojunctions in the Nanoenergy journal [75] and the Photovoltaic Specialist Conference (47th PVSC) [76].

The comparison of Figure 3.6.b and c illustrates that, in device A146, the n–Schottky barrier is more rectifying than the p–Schottky barrier. According to the Schottky–Mott rule, this is expected because the WF of Ni (5.15 eV) [115] is closer to the valence band maximum energy of bulk MoS_2 (5.6 eV) [24] than to the conduction band minimum energy (4.3 eV) [24]. However, the real height of the Schottky barrier cannot be precisely estimated only from the WF because the metal evaporation triggers band structure changes in TMDC and leads to Fermi–level pinning [103,104,117–120]. During the evaporation process, metal atoms are deposited at high temperatures on the surface of the semiconductor. This process can induce structural defects at the surface such as vacancies or clusters that generate MIGS at the interface metal/semiconductor creating the CNL. Then, ohmic contacts to TMDCs cannot be achieved by evaporating metal with well–aligned WF, requiring more sophisticated strategies to unlock the potential of MoS_2 homojunctions.

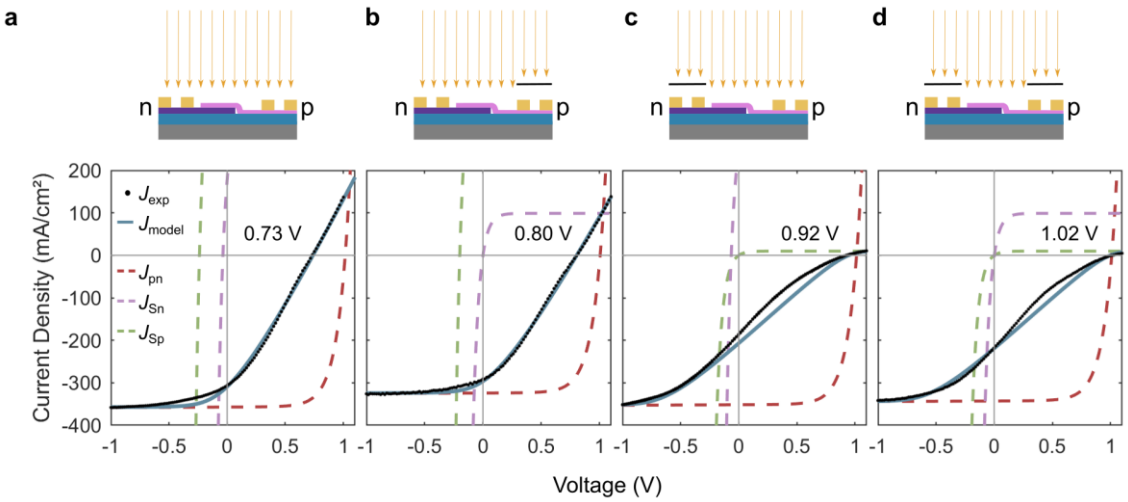

Figure 3.6. High photovoltage in a MoS_2 homojunction solar cell A146. (a–d) Schematics and J–V characteristics under different illumination conditions with a light source of 4 W/cm², showing a maximum V_{OC} of 1.02 V. Solid black dots show experimental values and a blue line for the modelled fit. The dashed curves represent the modelled contributions from the MoS_2 homojunction (red) and the contacts (green and purple). The irradiance level is the same in all cases, but the illuminated region is modified using a diaphragm.

3.5.4. Electrical model of the device

Solar cells are commonly modelled using the Shockley circuit model for a diode along with a current source that represents the photogenerated current of the device. However, the modelling *J–V* curves of solar cells as device A146 is more complex because metal/semiconductor contacts cannot be approximated to a simple series resistance. To characterise the MoS_2 van der Waals homojunction device with non–ideal contacts, we use the equivalent circuits depicted in Figure 3.7.

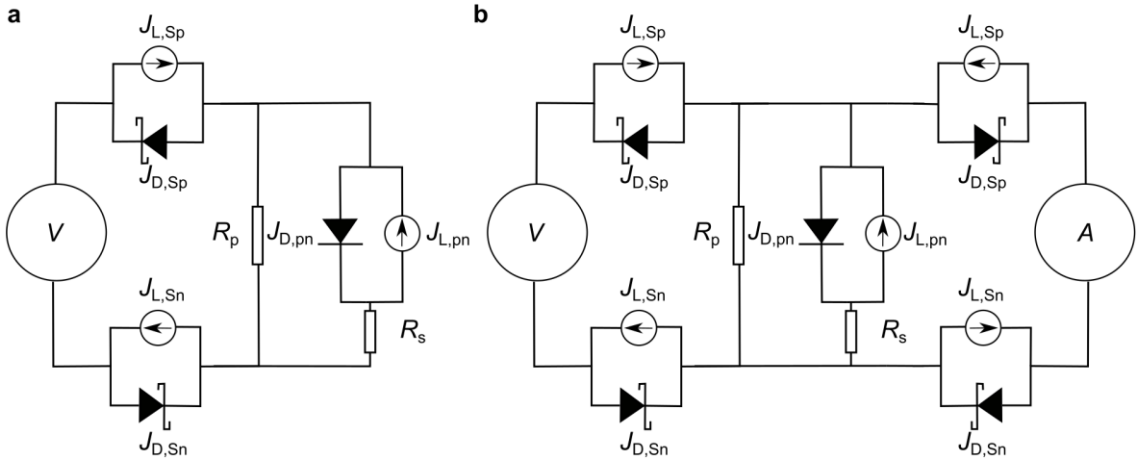

Figure 3.7. Equivalent circuit model of the MoS_2 homojunctions when measured in two–wire (a) and four–wire (b) configuration. The n–MoS_2/p–MoS_2 junction generates under illumination a current $J_{L,\,pn}$. The Schottky contacts generate, when illuminated, a current $J_{L,\,Sp,}$ and $J_{L,\,Sn}$.

The electrical circuit consists of three photovoltaic elements, each one represented as a combination of a constant current source (photogeneration) and a diode (recombination): the MoS_2 homojunction, which generates a photocurrent $J_{\mathrm{L,pn}}$; the Schottky at the n–contact, which generates a photocurrent $J_{\mathrm{L,Sn}}$; and the Schottky at the p–contact, which generates a photocurrent $J_{\mathrm{L,Sp}}$. The respective dark currents of the diodes are $J_{\mathrm{D,pn}}$, $J_{\mathrm{D,Sn}}$ and $J_{\mathrm{D,Sp}}$.

The three dark currents are modelled using the Shockley equation as:

$$J_{D,\mathrm{pn}} = J_{0,\mathrm{pn}} \exp\left(\frac{qV}{n_{\mathrm{pn}} k_B T(K)} - 1\right) \tag{3.3}$$

$$J_{\mathrm{D,Sn}} = J_{0,\mathrm{Sn}} \exp\left(\frac{qV}{n_{\mathrm{Sn}} k_B T(K)} - 1\right) \tag{3.4}$$

$$J_{\mathrm{D,Sp}} = J_{0,\mathrm{Sp}} \exp\left(\frac{qV}{n_{\mathrm{Sp}} k_B T(K)} - 1\right) \tag{3.5}$$

where $J_{0,xx}$ is the reverse saturation current of the respective diode, n_{XX} the ideality factor of the diode, q the electron charge, k_B the Boltzmann constant and $T(K)$ the temperature. In all calculations, temperature is 298 K. The diodes that represent the metal contacts are arranged in opposite direction to the pn junction, so the current that can be extracted from the pn junction is limited by the reverse current of the diodes allocated at the contacts.

R_P is the shunt resistance of the device, which is constant for all measurements on device A146. R_S is the linear series resistance introduced by the semiconductors that form the pn junction. R_S depends strongly on the illumination level and it decreases when light impinges the regions around the junction and the metal contacts. The n– and p–flakes are degenerately doped, so the illumination dependence of the R_S could be caused by the existence of depleted regions. The origin of these depleted regions could be related to different reasons as doping effects caused by the presence of debris and contamination, the lateral extension of the depleted regions of the contacts, and the interactions with the substrate properties. Thus, the series resistance increases when the device is in dark conditions. This effect by itself would improve the FF with the illumination intensity, but as it is observed in Figure 3.6.c., the tendency is just the opposite. The degradation of FF while increasing the illumination power is caused by the increasing voltage drop at the Schottky diodes, becoming larger and counteracting the improvement in the linear series resistance. The series resistance effects on the FF in device A146, including both, the linear component and especially the non–linear component, are strong enough to affect the measured J_{SC} value.

The interplay of R_P and R_S in the circuit model enables the reduction of the V_{OC} by the effect of R_S. In simple solar cell circuits, the R_S is in series with the current meter and there is no voltage drop at the R_S when the measured current is zero. In this model R_P and R_S are interconnected in a way that R_S can induce a reduction in the photovoltage, even under open–circuit conditions. V_{pn}^{*} is defined as the voltage drop across the junction itself, then:

$$V_{\mathrm{pn}} = V_{\mathrm{pn}}^{*} + \left(J_{\mathrm{L,pn}} - J_{\mathrm{D,pn}}\right) \cdot R_{\mathrm{S}} \qquad (3.6)$$

is the resistively–reduced junction voltage. The second term of the Equation (3.6) is negative because $J_{\mathrm{L,pn}}$ is negative. V_{pn} also equals the voltage across R_P. In current devices, the difference between V_{pn}^{*} and V_{pn} is very small, but the experimental curves cannot be fitted consistently using a different interconnection between R_P and R_S. The measured V_{OC} is then:

$$V_{\mathrm{OC}} = V_{\mathrm{pn}} - V_{\mathrm{Sn}} - V_{\mathrm{Sp}} \tag{3.7}$$

Table 3.1 resumes the fitting parameters of the *J*–*V* curves of A146 from Figure 3.6. The changes in J_{SC} in the experimental curves are caused by slight differences in the amount of stray light when the position of the diaphragm is modified. The current density values from Table 3.1 are obtained using the overlapping area of each junction. In real conditions, the areas spread beyond the overlapping area, so the value of the area used in the modelling is just an approximation [76,103,116]. Additionally, when a bias is applied, the space charged region (SCR) spreads or shrinks vertically and/or laterally altering the amount of photocurrent and dark current. This behaviour is related to the fact that TMDC–based devices are ultrathin, unlike conventional devices, and the volume of the SCR represents a large portion of the device. Hence, to accurately model of the device, it would be necessary the implementation of a voltage–dependent $J_{\mathrm{L,pn}}$ and $J_{0,\mathrm{pn}}$ parameters. Nevertheless, the good agreement between the experimental results and the modelled curves in Figure 3.6 indicates that the approximation of constant SCR volume and constant junction area is valid, although it results in a high apparent ideality factor for the pn junction.

The fitting of all curves in Figure 3.6 uses a constant ratio between the photocurrent produced by each Schottky contact and the photocurrent produced by the pn junction. The average width of the MoS_2 region that produces photocurrent around the metal edge can be estimated from this ratio. Considering that the photocurrent density at the Schottkys is similar to the pn junction, the width of the photogenerating region is estimated to be ~6 μm around the n–contact and ~ 4 μm around the p–contact.

Table 3.1. Modelling parameters used for A146 in Figure 3.6.

R_p ($\Omega \cdot cm^2$)	2093
R_s ($\Omega \cdot cm^2$)	(74.6 (in the dark) 0.5 (illuminated with 4W/cm²)
n_{np}	3.8
n_{Sn}	2.0
n_{Sp}	2.0
$J_{0,np}$ (mA/cm²)	0.012
$J_{0.Sn}$ (mA/cm²)	9
$J_{0,Sp}$ (mA/cm²)	327
A_{np} (µm²)	182
A_{Sn} (µm², under metal)	216
A_{Sp} (µm², under metal)	95
$J_{L.Sn}$ / $J_{L.pn}$	1.65
$J_{L.Sp}$ / $J_{L.pn}$	0.7

3.5.5. Electrical characterisation of other MoS_2 homojunctions solar cells

The model from Figure 3.7 was used to fit the *J–V* characteristics of other MoS_2 homojunctions. Until this point, we have modelled the electrical behaviour of MoS_2 homojunctions with non–ideal Schottky contacts and we have proved their photoactivity. The photoactive behaviour of the contacts does not only reduce the voltage output of the device, but it also may hinder the growth of the V_{OC} when increasing the illumination of the solar cell. This may explain the pinning effect observed in some of the devices reported in the literature [25,33,34,93]. Analysing again the *J–V* characteristics of device A146, Figure 3.5.c illustrates that device A146 is apparently not pinned. However, the posterior device characterisation demonstrates that the Schottky contacts are not eliminated. Hence, the apparent absence of pinning results from the larger growth of the photovoltage provided by the pn junction than the photovoltage subtracted by the contacts. This is a consequence of the non–deterministic nature of the device fabrication method, and it means that this problem is not solved.

The pinning effect of the V_{OC} is also observed upon increasing the light concentration on devices with similar architecture. Figure 3.9.a (inset) shows device A189. The structure of device A189 is a MoS_2 homojunction on a h–BN layer placed on a glass substrate. The metal contacts are made of Cr/Au and are deposited on the semiconductors just like in device A146. Figure 3.9.a illustrates the J–V curves corresponding to the measurements between pads allocated on the same flake. The J–V curves reveal the presence of photoactivity at the p–flake contact. Interestingly the Cr/n–MoS_2 contact shows an ohmic behaviour despite the thermal deposition of Cr onto the semiconductor. These curves were measured under an equivalent illumination of 4W/cm² showing V_{OC} at the p–side of nearly 0.1 V. Figure 3.9.b illustrates the J–V curves of A189 measured between the inner contacts of the pn junction, under illumination by a 522 nm green laser at varying levels of intensity in our green laser set–up described in Chapter 2. Despite the high photocurrent, the V_{OC} is found to be pinned at 0.68 V. The higher illumination level does not increase the V_{OC} of A189 because of the counteracting effect of the photoactivity at the p–contact which is strong enough to pin the V_{OC} of the whole device.

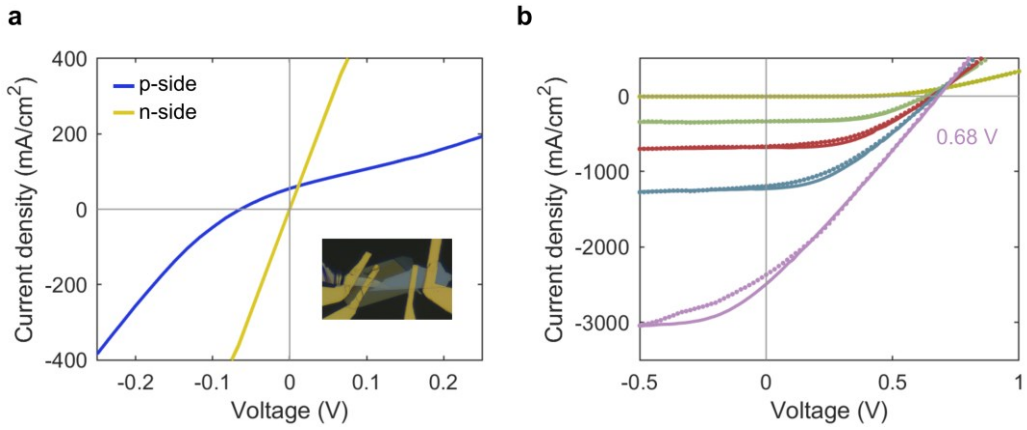

Figure 3.8.(a) J–V characteristics of the contacts of A189 under an illumination of 4 W/cm² (inset: micrograph of the device). (b) J–V characteristics of A189 for various illumination intensities. The modelled curves have been calculated using the model from Figure 3.7.a.

When parametrising the fitting curves of device A189 from Figure 3.8, we found that the use of a variable shunt resistance was necessary to match the curves for different illuminations. Shunt resistance refers to the resistance that is present in parallel with the photovoltaic device in a solar cell. This variable shunt resistance may be caused by a bias–dependent collection efficiency. This phenomenon appears

in solar cells with a relevant contribution of the SCR to the photocurrent. SCR has some nanometres of thickness, which is negligible in conventional solar cells. However, as we mentioned in the discussion about the circuit model in Subsection 3.5.4, in ultrathin TMDC solar cells, SCR occupies a considerable fraction of the volume of the solar cells. When the junction is biased (it's made more negative) the extension of the SCR increases. Since the photocurrent collection in the SCR is more efficient than in the neutral regions, when the SCR occupies a greater portion of the volume of the device, the photocurrent increases. That is why in the *J–V* curve it is appreciated a bias–dependent J_L value, that grows for negative biases. The model from Figure 3.7 does not consider the change in the width of the SCR as the complexity of the model would be increased because the variation of the SCR also takes place at the Schottky contacts. The effect of the SCR on the electrical modelling of the devices will be analysed deeply in Chapter 6.

Table 3.2. Modelling parameters used for A189 in Figure 3.8.

R_p ($\Omega \cdot cm^2$)	639 (Level of illumination 1) 63.9 (Level of illumination 2) 31.95 (Level of illumination 3) 13.85 (Level of illumination 4) 6.39 (Level of illumination 5)
R_s ($\Omega \cdot cm^2$)	0.49 (Level of illumination 1) 0.17 (Level of illumination 2) 0.15 (Level of illumination 3) 0.13 (Level of illumination 4) 0.11 (Level of illumination 5)
n_{np}	2.4
n_{Sn}	2.0
n_{Sp}	2.0
$J_{0,np}$ (mA/cm^2)	0.013
$J_{L,np}$ (mA/cm^2)	5.4 (Level of illumination 1) 366.19 (Level of illumination 2) 751.17 (Level of illumination 3) 1361.51 (Level of illumination 4) 3333.31 (Level of illumination 5)
A_{np} (μm^2)	230
$J_{L.Sn}$ / $J_{L.pn}$	0
$J_{L.Sp}$ / $J_{L.pn}$	0.9

Figure 3.8.a–c shows an example of fitting using the two–wire configuration which corresponds to another device identified as A156. This device is a MoS_2 homojunction placed on two pre–patterned gold contacts on a glass substrate. The reason to fabricate a device using a glass substrate is related to the measurements of EQE. We found that in devices using Si/SiO_2 substrates such as A146 and A189, the substrate can induce a photogating effect that results in incorrect interpretations of the measurement. This effect can be especially problematic when determining the indirect band gap of MoS_2.

In this case, the reduced size of the flakes impedes the total blockage of the light at the metal/semiconductor contacts. However, differences in the V_{OC} are distinguishable when the light impinges different parts of device A156. In this case, a lower V_{OC} (0.51 V) is obtained in comparison to device A146 from Figure 3.5. The reduced V_{OC} obtained could be explained by a higher recombination current. The poorer performance of this device may be explained by different reasons. We found that stacking materials on glass substrates is much more difficult than on Si/SiO_2 possibly related to the substrate surface. Besides, the substrate may induce doping effects that alter the electrical properties of the semiconductors. Additionally, the fabrication process of the devices is a non–deterministic procedure that may be affected by multiple variables. Among them, are the irregular shape and thickness of the flakes, the possible anisotropy of the original crystals, or the contamination of the semiconductor during the fabrication process. This results in difficulties in obtaining devices with the same characteristics despite following the same fabrication steps. Although this device shows a lower V_{OC}, its series resistance is lower in dark conditions. This could be explained by the fact that the flakes were deposited over pre–patterned contacts, so induced defects related to thermal deposition processes are avoided although Schottky contacts are still present.

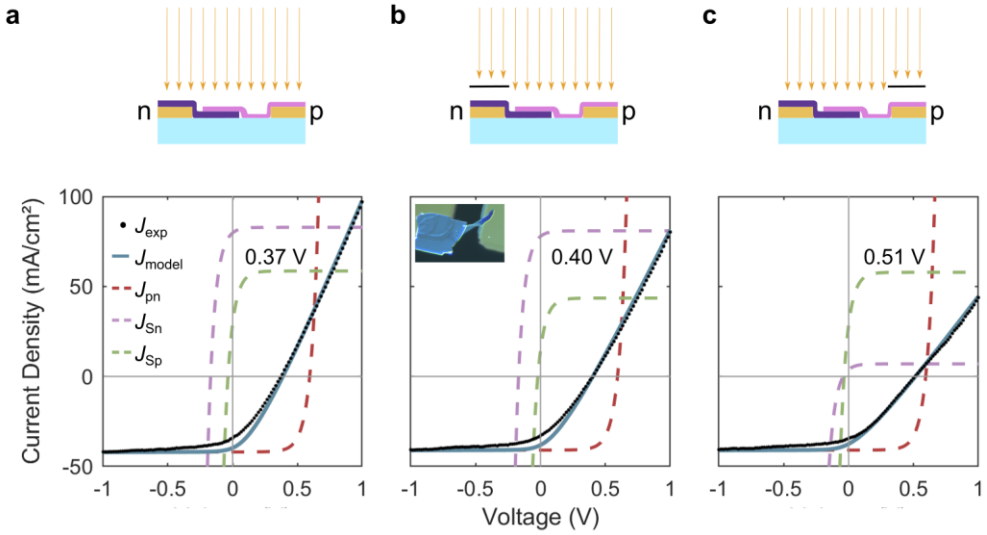

Figure 3.9. Schematics and J–V characteristics of A156 for various illumination conditions (a–c) (inset (b), micrograph of the device). The light source is a halogen lamp with an intensity approximately of 600 mW/cm². Note that blocking the light on both sides is not possible due to the smaller device size. The modelled curves have been calculated using the model from Figure 3.7.a.

Table 3.3. Modelling parameters used for A156 in Figure 3.9.b.

R_p (Ω·cm²)	234.2
R_s (Ω·cm²)	7.91 (in the dark) 4.98 (light on the n–side) 3.37 (light on the p–side) 2.83 (whole chip illuminated)
n_{np}	2.2
n_{Sn}	2.0
n_{Sp}	2.0
$J_{0,np}$ (mA/cm²)	40.8
A_{np} (µm²)	293
$J_{L.Sn}$ / $J_{L.pn}$	1.8
$J_{L.Sp}$ / $J_{L.pn}$	0.7

3.5.6. Quantum efficiency of MoS_2 homojunctions

MoS_2 homojunctions show a high V_{OC} which is limited by the characteristics of the contacts. Still, to obtain a significant PCE, the photogenerated current must be high enough. The spectral response of devices can be obtained from their EQE. Figure 3.10.a shows the micrograph of device A156 whose J–V curves were modelled in Figure 3.9. The thickness of each layer was measured with AFM, obtaining 12 nm for p–MoS_2:Nb and 262 nm n–MoS_2:Fe, comprising a pn junction area of 293 μm^2.

Figure 3.10.b shows the EQE of device A156 along with the calculated absorptance of the structure. The absorptance is determined using our optical model which calculates optical properties of multilayered structures. A deeper description of the working principle of this model is detailed in Chapter 4. The absorptance of the device is split into three contributions, the p–material (3.5 nm), the SCR (16.5 nm), and the n–material (254 nm). The SCR thickness was calculated using the total depletion approximation [121] and the doping levels $3.0 \cdot 10^{19}$ and $7.5 \cdot 10^{18}$ cm^{-3} were estimated from the characterisation of doped bulk MoS_2 samples. To calculate the thickness of the SCR, first we determine the $V_{built-in}$:

$$V_{built-in} = k_B \cdot T(K) \cdot \mathrm{Ln}\left(\frac{N_D \cdot N_A}{{n_{int}}^2}\right) \quad (3.8)$$

where n_{int} is the intrinsic carrier concentration of the material, N_D is the number of donor species in the n–material and N_A is the number of acceptor species in the p–material. In both cases each one approximates to the carrier population of each material. Hence, the width of the SCR can be calculated:

$$w_{SCR} = x_P + x_n \quad (3.9)$$

where x_p and x_n are the thickness of the neutral zones in the p–material and the n–material which are calculated as:

$$x_n = \sqrt{\frac{2\varepsilon\varepsilon_0 V_{built-in} N_A}{eN_D(N_D+N_A)}} \quad (3.10)$$

$$x_p = \sqrt{\frac{2\varepsilon\varepsilon_0 V_{built-in} N_D}{eN_A(N_D+N_A)}} \quad (3.11)$$

where ε is the relative dielectric constant of MoS_2 and ε_0 is the dielectric constant of vacuum.

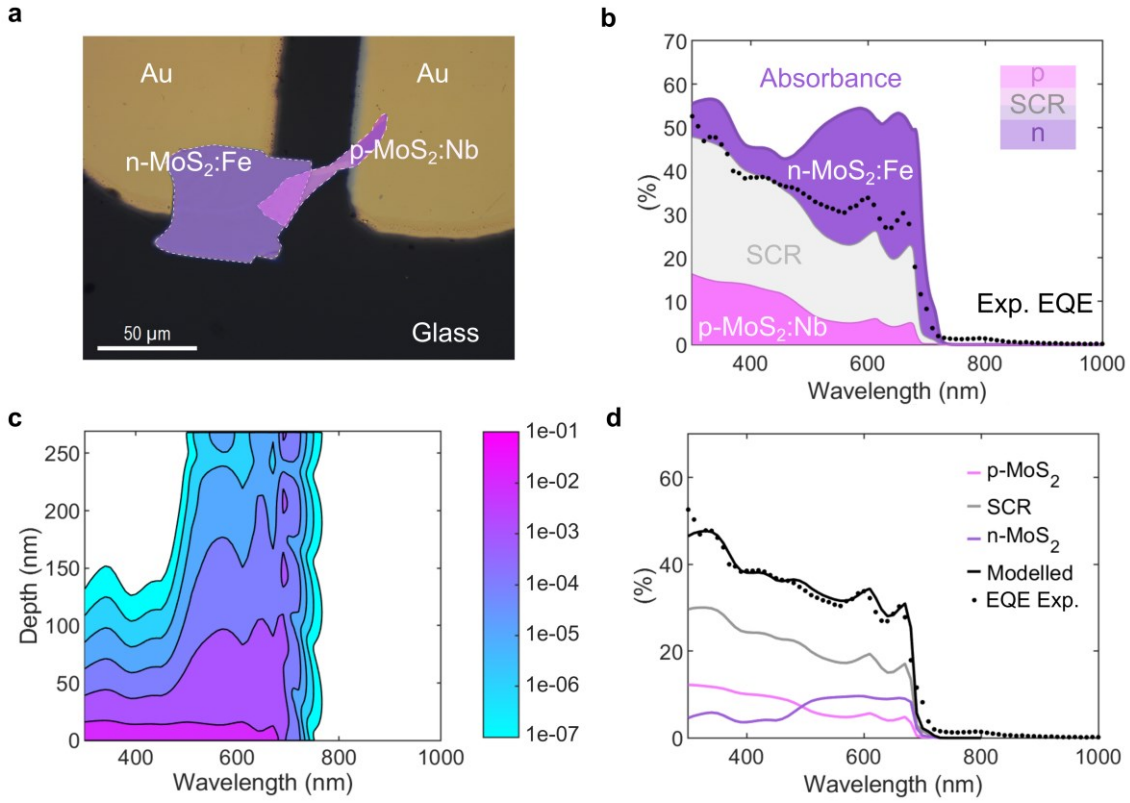

Figure 3.10. (a) Device A156 micrograph. (b) Calculated absorption spectra for our MoS_2 on glass device and comparison to experimental EQE data. (c) Modelled absorption profile of device A156. (d) Modelled EQE.

From Figure 3.10.b it can be deduced that the measured EQE accounts approximately for the sum of the p–material and SCR contributions, while the neutral part of the n–material has a substantially lower contribution to the photogeneration. This implies that a higher quality of the p–material over the n–material is preferred. Note that the experimental EQE curve presents two peaks at the wavelength of 600 nm and 660 nm which correspond to the Van Hove singularities [15,23].

The integration of the EQE over the AM1.5G solar spectrum results in a total J_{SC} of 6.6 mA/cm². To estimate the range of improvement of this value, we compare it to the integration of the theoretical absorbance over the same spectrum, which is 10.0 mA/cm². This yields a collection efficiency of 66% weighted over the range of interest. Both, the experimental and theoretical values of the J_{SC} are far from the values that MoS_2 could provide according to its band gap. This fact suggests the existence of considerable losses that can be explained by the reflection of light at the surface of MoS_2. Thus, another possible way to improve light collection is by implementing an anti–reflective layer (ARL) that minimises reflectance losses.

Further strategies to improve absorption can be used, as the reduced thickness of the absorbent layers enables the apparition of light interference effects. The optimisation of the absorption in MoS_2 homojunctions is beyond the scope of the present Chapter, but it will be deeply analysed in Chapter 4 and Chapter 5.

The resulting experimental EQE curve was fitted using the mathematical model developed by Zehender et *al.* [122]. This model uses the diffusion equations of the pn junction along with the optical parameters calculated with our optical model. The absorption profile presented in Figure 3.10.c is converted into a continuous function to solve a series of differential equations numerically instead of analytically. The solutions of the model are obtained by fitting the sum of a polynomial function and an exponential function to the continuous function of Figure 3.10.c. Equations are solved for the non–depleted regions of both, the p–side, and the n–side. When considering the SCR, we assume that all photons absorbed in this region generate charge carriers that are extracted from the device.

Figure 3.10.d shows the output from the model which yields the electrical contribution of each part of device A156, and the model parameters are compiled in Table 3.4. From this result, we can determine that carrier generation takes place in a narrow section of the device. The whole p–material contributes to carrier generation while the largest part of the n–material is inactive. The estimated diffusion length values show that most of the recombination occurs at the n–material. This suggest that n–material layer needs to be optimised to improve carrier collection. The minority carrier mobility in each material is estimated from the majority carrier mobility. We estimate a surface recombination velocity on the p–material of 800 cm/s, which is high taking into account that layered materials show theoretically self–passivated surfaces. This value is however difficult to predict for two reasons, first, the elevated reflectance of the material and the reduced thickness of the p–layer yield a small contribution to the EQE of device A156.

Table 3.4. Fitting parameters from EQE modelling.

Thickness of neutral zone p–material (nm)	3.5
Thickness of neutral zone n–material (nm)	249
Thickness of SCR (nm)	16.5
p–material minority carriers mobility ($cm^2/V \cdot s$)	0.5
n–material minority carriers mobility ($cm^2/V \cdot s$)	0.1
p–material carrier population (cm^{-3})	$3 \cdot 10^{19}$
n–material carrier population (cm^{-3})	$7.5 \cdot 10^{18}$
Diffusion length p–material (nm)	6
Diffusion length n–material (nm)	16
Carrier lifetime p–material (ps)	28
Carrier lifetime n–material (ps)	990
Surface recombination velocity p–material (cm/s)	800

The modelling of the EQE curves is a multiparametric optimisation process wherein various factors exert a comparable influence on the resultant curve. This is the case of the diffusion length and the surface recombination. A large diffusion length raises the amount of charge carriers that can be collected consequently increasing the EQE. Increasing the surface recombination reduces the amount of charge carriers that can be collected. In this case, it has an accentuated effect depending on the layer. High surface recombination on the top layer will reduce the EQE at the shorter wavelengths, as those wavelengths are absorbed at the most superficial level of the pn junction. By contrast, a high surface recombination at the bottom layer will diminish the carrier conversion of the longer wavelengths.

In device A156, the surface recombination velocity in the n–material cannot be estimated because the thickness of the n–layer is larger than its diffusion length, hence using large values of this parameter in the model would not produce significant changes in the modelled curve. Furthermore, the reduced thickness of the p–material complicates the accurate estimation of the diffusion length and surface recombination within this layer, as adjustments to either parameter yield comparable modifications to the modelled curve. The determination of both parameters results from a process of optimisation where several combinations of both parameters are tested. In this case, the internal quantum efficiency (IQE) is

the target curve, derived from the experimental EQE and the theoretical device reflectance computed through our optical model following the next expression:

$$IQE(\lambda) = \frac{EQE(\lambda)}{1-Reflectance(\lambda)} \quad (3.12)$$

Figure 3.11 shows multiple plots where the effect of varying the diffusion length (L_e) and the surface recombination (S_e) of the p–material is evaluated along with the IQE of device A156. The modelling confirms that both parameters have a similar impact on the modelled curves. However, surface recombination requires to exceed 500 cm/s to start having a little effect on the curve morphology. The results suggest that L_e is between 4 and 10 nm, and S_e is not larger than 1000 cm/s. Although the estimation of cell parameters is challenging, especially evaluating the surface recombination, this modelling provides initial insights into the characteristics of MoS_2 solar cells and it underscores their impact on both, IQE and EQE curves.

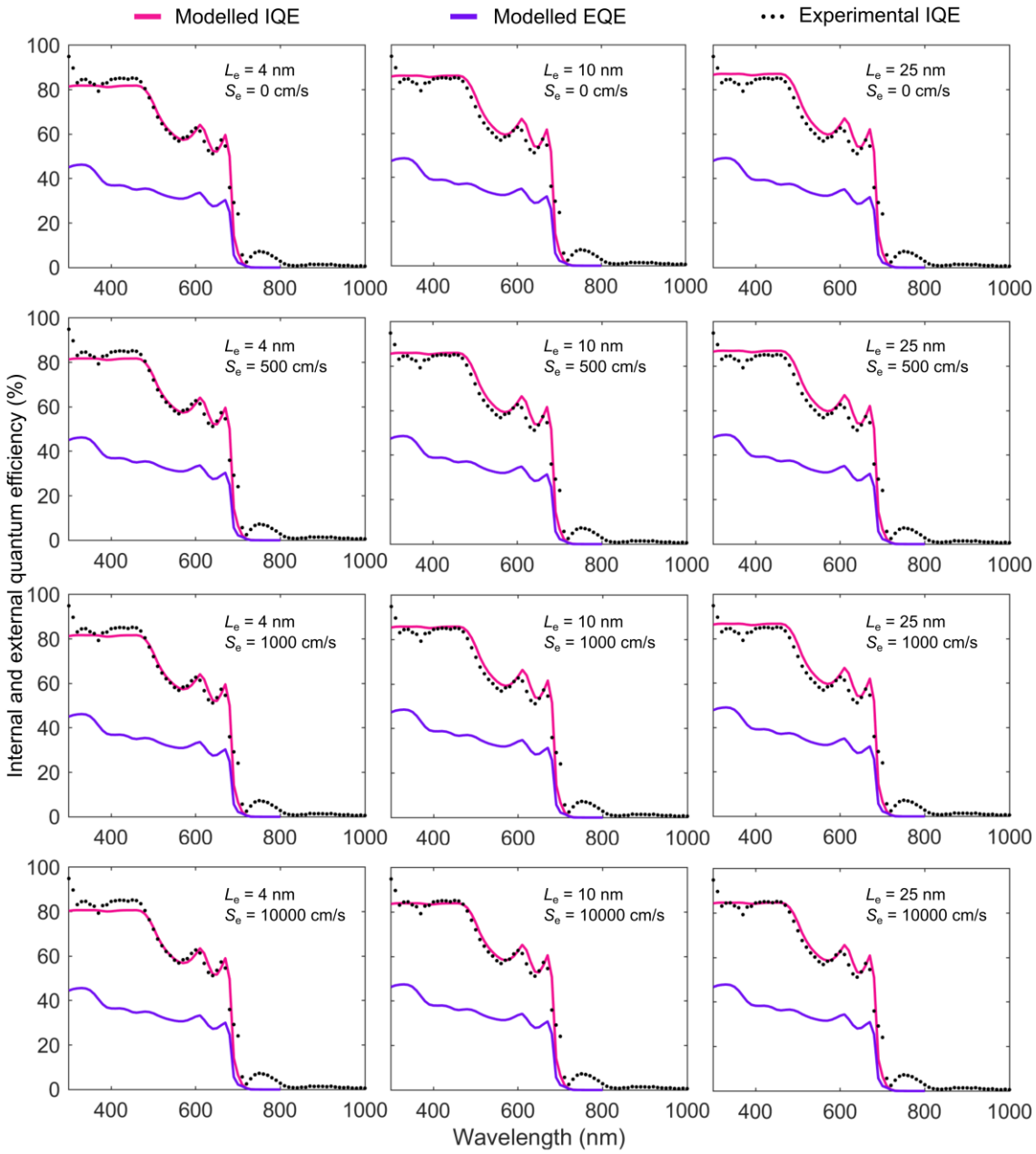

Figure 3.11. Effect of surface recombination and diffusion length on the modelled IQE and EQE of device A156.

3.6. Summary

A TMDC solar cell based on a MoS_2 homojunction produced through substitutional doping exhibits the highest yet reported V_{OC} in a photovoltaic van der Waals TMDC structure, 1.02 V under broadband illumination with 4 W/cm^2. This corresponds to a W_{OC} value of 0.27 V, to be compared to 0.16 V calculated for an ideal, and fully radiative device under the same illumination. Nevertheless, this V_{OC} is only observable if the photogeneration in the Schottky barriers present at the TMDC/metal interfaces is avoided, and the performance of the device is severely hindered by the poor quality of the TMDC/metal contacts.

The *J*–*V* characteristics of the MoS_2 homojunctions have been modelled using an equivalent circuit model, where the photoactive behaviour of the contacts is simulated using Shockley diodes that are inversely arranged with respect to the pn junction. The constraints on the V_{OC} of the device, the series resistance, and the FF have been modelled extracting the parameters of the pn junctions. The electrical model reveals the important impact that the non–ideal behaviour of the metal/semiconductor contacts has on the behaviour of the MoS_2 homojunctions, not only reducing the output voltage but also severely degrading the FF.

Although it has been tried to improve the quality of the metal/semiconductor contacts, the strategy of metal evaporation on the semiconductor was not successful. Metal deposition induces defects at the interfaces making the obtention of ohmic contacts unattainable by just material selection. Moreover, the expansion of the depleted regions beyond the interface aggravates this problem. This implies that a new fabrication strategy is required to avoid defective contacts and to minimise the performance losses related to their quality. Nevertheless, the impact of the non–ideal contacts has been quantified and modelled with an equivalent circuit model.

EQE measurements and modelling demonstrate the strong light interaction of MoS_2–based devices, which is characterised by the coupling effect of the layered structure known as Van Hove singularities. This results in enhanced absorption at the wavelengths of 600 nm and 660 nm. The experimental EQE has been modelled using the carrier transport equations of the pn junction along with an optical model to determine light absorption. The results of modelling determine that the carrier generation takes place at the most superficial levels of the device. This result implies that devices could reduce their thickness to tens of nanometres without hampering carrier generation. However, the light absorption of the device

is still not optimised, requiring a new design of the device structure to improve light absorption where an ARL must be added to increase the photogeneration. The optimisation of MoS_2–based structures will be addressed in Chapter 5, where we will use our optical model to optimise the light absorption of thinner devices.

The results presented in this Chapter confirm the potential of TMDCs, particularly substitutionally doped MoS_2, for developing highly efficient, ultrathin, and ultralight–weight photovoltaic devices. The issues that may hinder the achievement of competitive efficiencies have been successfully identified and quantified. From the analysis of the J–V curves and the EQE, we outline the next steps to realise high efficiency, which are the elimination of the Schottky barriers at the metallic contacts, the implementation of an anti–reflection coating and possibly an optical cavity, and the improvement of the radiative efficiency of the n–doped flake. The resolution of those concerns will boost the performance of TMDC–based solar cells and approach to the PCE levels already achieved by other emerging technologies.

Chapter 4

Optical modelling of TMDC devices

4.1. Introduction

The performance of solar cells is not only determined by the electrical properties of the materials forming the device but also by their optical properties. The maximum current a solar cell can provide is limited by the number of photons it can absorb. This maximum current depends on the material bandgap and its absorption coefficient. While the bandgap determines the minimum energy of the photons that can be absorbed, the absorption coefficient determines how far the photons of a particular wavelength can penetrate a material before being absorbed. Hence, the thickness of the semiconductor required in a solar cell to absorb an acceptable number of photons depends on the value of the absorption coefficient of the material.

TMDCs show an elevated absorption coefficient compared to conventional materials used in photovoltaic devices. This large absorption coefficient is directly related to Van Hove singularities of van der Waals structures that result in absorption peaks in the visible range [15,23]. Because of these structural properties, TMDCs show strong electronic transitions that enhance light absorption in both, monolayered and multilayered structures. Owing to their elevated absorption coefficients, devices employing TMDCs can attain noteworthy optical absorption levels, even when operating at thicknesses below 100 nanometers. The superior optical absorption of TMDCs in comparison to conventional materials is illustrated in Figure 5.1. In these slender devices, the thickness significantly dictates the occurrence of optical phenomena capable of altering the optical properties of the structure.

Modelling light absorption in such ultrathin structures requires the consideration of multiple reflections and it may also require considering the effect of light coherence throughout the structure. Each layer can be treated as coherent or incoherent depending on the thickness of the layer, its refractive index and its roughness. Light coherence plays an important role in the optical characteristics of ultrathin devices, as absorptance can be enhanced because of light interference

effects [123]. Furthermore, modelling TMDC–based structures is more challenging than other materials. Although TMDCs show outstanding optical properties, they show a high optical anisotropy. Hence, the values of the refractive index and extinction coefficient in the plane of the TMDC layer differ substantially from the values in the direction perpendicular to the layers. Finally, the fabrication processes of large–area TMDCs do not often result in homogeneous material layers requiring the introduction of artefacts to approach the real behaviour of the device.

In this Chapter, we present a complete optical model used to evaluate the optical parameters of TMDC–based structures. The model is derived from a mathematical formalism based on the transfer–matrix algorithm which was described by Centurioni [124]. In our work we have developed this formalism further to introduce all the particularities found in TMDC structures (optical anisotropy of TMDC, light interference and heterogeneous layers). The introduction of optical anisotropy is crucial to accurately evaluate TMDC layers, and the modelling of heterogeneous structures provide a reliable evaluation of TMDCs layers fabricated through large–area fabrication processes [20]. The model developed here has been implemented in a Matlab homemade software and it will be used in Chapters 5 and 8 for the optical design of TMDC–based structures. Also, the results obtained with this model have been used to simulate our experimental results in Chapters 3 and 7. This optical model can be used in conjunction with another tool that determines the spectral power distribution (SPD) and the angle of incidence of the light beam to determine the light power absorption of the TMDC–based devices in realistic cases (see Chapter 7). For this purpose, a mathematical algorithm has been created that accounts for the direct and diffuse absorption of light, especially considering the difficulties in providing a correct estimation of the diffuse absorption.

For a comprehensive reading, the first two sections of this Chapter offer a short review of the concepts of light coherence and interference, which are fundamental to understanding the following sections. In Section 4.4 our optical model is described in detail, including aspects specifically developed for the characteristics of TMDC devices in Subsections 4.4.3 and 4.4.4. Finally, in Section 4.5 we present the tools developed to quantify the light absorbed by a TMDC device considering a set of operation conditions (location, orientation, and time).

4.2. Light coherence

Light coherence refers to the degree to which the phases of different waves of light are correlated. A coherent light source emits waves that have a fixed phase relationship with each other, meaning that the crests and troughs of the waves line up perfectly. When analysing light coherence, it must be considered spatial and temporal coherence.

- Spatial coherence refers to the degree to which the waves of light are correlated in space. A light source with high spatial coherence emits waves that maintain their phase relationship over a large distance, meaning that they do not spread out and interfere with each other. The spatial coherence of a light source depends on the size of the source and the wavelength of the light it emits. A small source size and a long wavelength lead to high spatial coherence, while a large source size and a short wavelength lead to low spatial coherence.
- Temporal coherence refers to the degree to which the waves of light are correlated in time. A light source with high temporal coherence emits waves that maintain their phase relationship over a long period, keeping the frequency and wavelength of the light constant over time. The temporal coherence of a light source depends on the spectral width of the light it emits. A narrow spectral width corresponds to high temporal coherence, while a broad spectral width corresponds to low temporal coherence.

When considering ultrathin structures, light coherence is a key factor, as the existence of constructive interferences is essential to achieve high optical absorption. Although the Sun is a spatially incoherent source of light, the sunlight is coherent as stated by the van Cittert–Zernike theorem [125]. This mathematical theorem demonstrates that the wavefront of a spatially incoherent source appears mostly coherent at long distances from the emitter. Hence, the coherence of the light propagating through a structure will depend mainly on the characteristics of the medium inside which light propagates.

When considering the propagation of light through a material, light flux remains temporally coherent if the length that the flux passes through is shorter than the coherence length defined in Equation (4.1):

$$L = \frac{c}{n_i \cdot \Delta f} \tag{4.1}$$

where c is the light speed constant, n_i is the refractive index of the medium, and Δf is the bandwidth of the light source in frequency units. This implies that the longitudinal coherence length of the sunlight is ~ 0.4 – 0.6 μm in air. Note that, coherence length depends inversely on the refractive index of the material, then, to keep the light coherence, the thickness of the material layers must be shorter than the coherence length of sunlight in the air. In the case of TMDCs such as MoS_2, the refractive index is high (~ 5), so the coherence length is shorter (~ 100 nm).

Light spatial coherence is not only affected by the characteristics of the source but also by the topography and the homogeneity of the layers that are crossed by the light. The presence of defects such as discontinuities, pores, or roughness would scatter the light negatively affecting the spatial coherence of the light beam. According to Carniglia et *al.*, the coherence of the transmitted light inside a semitransparent medium can be modelled using the roughness of its surface, its refractive index, and the wavelength of the incident light [126]. The fraction of light that is scattered and loses coherence can be calculated with Equation (4.2):

$$T_d = T_0(1 - exp[-(2\pi\sigma_c|n_0 - n_i|/\lambda)^2]) \tag{4.2}$$

where T_d is the fraction of transmitted light that loses coherence, T_0 is the fraction of transmitted light, σ_c is the root mean square (RMS) roughness square mean of the surface, n_0 is the refractive index of the incident medium, n_i is the real part of the refractive index of the medium and λ is the wavelength of the light. If T_d is low in comparison to T_0, it can be assumed the spatial coherence of the incident light is not lost. Light coherence implies that interference phenomena can occur inside layers.

4.3. Light interference

Light interference takes place when the crests and troughs of the incident light wave are lined with the crest and troughs of the reflected waves at the interfaces of an ultrathin layer. Figure 4.1.a shows a schematic of a slab of MoS_2 on an Al_2O_3 substrate. When a light beam impinges the slab, there is a fraction of light that is reflected and another transmitted. The value of these fractions can be calculated using the Fresnel equations. Then, part of the transmitted beam will be reflected at the interface between MoS_2 and Al_2O_3. When the value of the thickness d of the slab is of the order of magnitude of the wavelength of the incident light, both reflected beams can interfere creating a Fabry–Perot (FP) interference (see Figure 4.1.b). The interference of both beams depends on the difference in the optical path between them which is defined by:

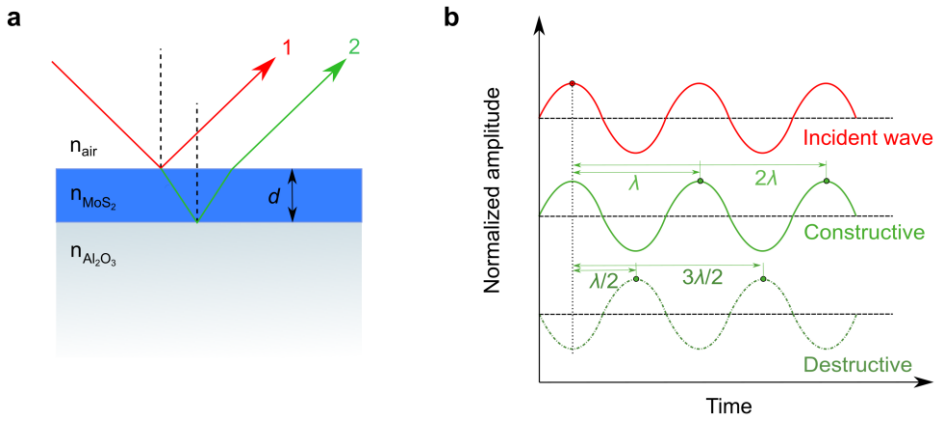

Figure 4.1. (a) Device schematic and interferences of reflected light. (b) Constructive and destructive interference schematic.

$$\Delta x = L_2 - (L_1 - \frac{\lambda}{2}) \tag{4.3}$$

where L_1 is the optical path of beam one and L_2 is the optical path of beam two. Note that half of the wavelength of the beam one must be deducted because the light coming from a lower refractive index material introduces a π phase shift in the reflected beam. As beam two reflects at the interface MoS_2/Al_2O_3 and the refractive index of Al_2O_3 is lower than the refractive index of MoS_2, there is no phase shift of the reflected beam two.

The amount of light that the MoS_2 slab absorbs, can be enhanced when beams one and two in Figure 4.1.a interfere destructively. The difference between L_2 and L_1 is equal to the thickness of the MoS_2 multiplied by the cosine of the propagation angle θ inside the layer, multiplied by two and the refraction index of MoS_2 (n_{MoS_2}):

$$\Delta x = 2n_{MoS_2} d \cos\theta - \frac{\lambda}{2} \tag{4.4}$$

Figure 4.1.b shows the conditions of constructive and destructive interference of the reflected light. The condition of constructive interference is that the difference in the optical path between both beams, is an integer multiple of the wavelength. Then, implementing this condition in Equation (4.4), it is obtained:

$$m\lambda = 2n_{MoS_2} d \cos\theta \tag{4.5}$$

where m is an integer number.

By contrast, there will be a destructive interference if the difference in the optical path between two beams equal to the wavelength multiplied by an integer number minus 0.5. Then, implementing this condition in Equation (4.4), it is obtained:

$$(m - \tfrac{1}{2})\lambda = 2n_{MoS_2} d \cos\theta \tag{4.6}$$

However, these equations are only accurate when considering a non–absorbing material. Traditionally, FP interference has been mostly studied for transparent materials whose extinction coefficient is zero. When considering a lossy media interference is evaluated using Equation (4.7) given by Llorens et *al.* [127] :

$$d = \mathrm{Re}\left(\frac{m\lambda}{2(n_i + ik_i)} - \frac{\lambda i}{2\pi(n_i + ik_i)} ln\left(\frac{n + ik_i + 1}{n + ik_i - 1}\right)\right) \tag{4.7}$$

where n_i is the refractive index and k_i the extinction coefficient of the material slab, and m (integer) is the interference order.

This equation yields a zeroth order of interference ($m = 0$) which is a consequence of the lossy characteristics of the material, and which is of enormous interest for ultrathin photovoltaic devices but has not been widely used yet. It has been described conceptually by Kats et *al.* [123] and Llorens et *al.* [127,128]. They have found that it can be very significant in the context of materials exhibiting a pronounced extinction coefficient and it can be substantially amplified by the presence of a metallic layer beneath the semiconductor slab. For this purpose, the metal must have finite optical conductance, thereby enabling the optimisation of the phase–shift in the reflection at the interface [123]. The substantial optical attenuation within the highly absorbent materials, coupled with the

corresponding non–trivial phase–shifts at the interface, results in a pronounced resonant behaviour within layers that are significantly thinner than the wavelength of light. The zeroth–order interference phenomenon will be exploited in our TMDC solar cell designs presented in Chapter 5 to enable high light absorption in extremely thin TMDC absorbers.

4.4. Optical modelling

In this section, we present the optical model that we have implemented in the form of a Matlab program to perform all optical calculations required in this Thesis. The model is derived from the transfer–matrix method described by Centurioni [124]. It is based on the implementation of Fresnel equations through a multilayer structure and considers the internal reflection and interference effects. The model supposes plain and homogeneous layers for all the calculations (except in Subsection 4.4.4). Our model includes several features that simplify the calculations especially when considering tilted illumination avoiding the use of complex numbers for the propagation angle through each layer. Moreover, it provides a complete analysis of any multilayered structure using algorithms to calculate not only coherent or incoherent structures, but also mixing both coherent and incoherent layers to evaluate partially coherent structures. Finally, our model allows the calculation of optical absorption including anisotropic materials by the definition of an equivalent refractive index depending on the light angle of propagation in a specific layer.

4.4.1. Coherent layers

Figure 4.2 depicts a schematic of a multilayer structure composed of m layers. The whole structure is surrounded by air. The positive direction is assigned to the flux moving from left to right. The evolution of the light flux passing through the structure can be described using the transfer–matrix formalism defined by:

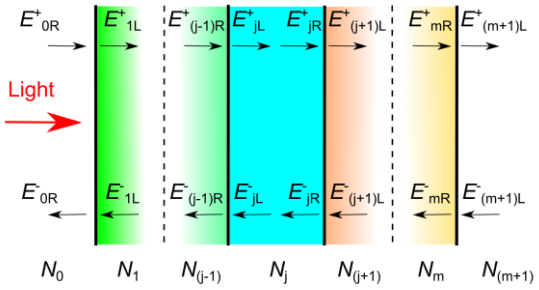

Figure 4.2. Schematic of the transfer–matrix method formalism for coherent layers.

$$\begin{bmatrix} E^{+}{}_{0R} \\ E^{-}{}_{0R} \end{bmatrix} = S \begin{bmatrix} E^{+}{}_{(m+1)L} \\ E^{-}{}_{(m+1)L} \end{bmatrix} \tag{4.8}$$

$E^{+}{}_{0R}$ is the electric field associated to the light flux propagating in the positive direction and $E^{-}{}_{0R}$ in the negative direction. These are the electric fields just before the first interface, and $E^{+}{}_{(m+1)L}$ refers to the electric field at the last interface in the positive direction. The electric field at both extremes of the structure is correlated to the two–dimensional matrix S defined by:

$$S = I_{0,1} L_1 I_{1,2} \dots L_m I_{m,m+1} \tag{4.9}$$

where $I_{j,j+1}$ defines the wave propagation through the interface between the layers j and $j+1$, and L_j defines the light flux through the layer j. When considering s–polarised light, the mathematical expression of $I_{j,j+1}$ is defined by:

$$I_{j,j+1} = \frac{1}{2\gamma_j} \begin{bmatrix} \gamma_j + \gamma_{j+1} & \gamma_j - \gamma_{j+1} \\ \gamma_j - \gamma_{j+1} & \gamma_j + \gamma_{j+1} \end{bmatrix} \tag{4.10}$$

The value of γ_j is defined by:

$$\gamma_j = \sqrt{N_j^2 - N_0^2 \sin(\theta)^2} \tag{4.11}$$

where N_j is the complex refractive index of the layer j, N_0 is the refractive index of the incident media, and θ is the angle of incidence of the light. The condition of Equation (4.11) is valid when $\mathrm{Re}(\gamma_j) > 0$ and $\mathrm{Im}(\gamma_j) \geq 0$. The γ_j value is derived from the Snell law, and its use in Equation (4.10) is analogous to the use of the Fresnel coefficients.

L_j is defined by:

$$L_j = \begin{pmatrix} e^{-i\gamma_j \frac{2\pi}{\lambda} d_j} & 0 \\ 0 & e^{i\gamma_j \frac{2\pi}{\lambda} d_j} \end{pmatrix} \tag{4.12}$$

where d_j is the thickness of the layer and λ is the wavelength of the incident light.

To calculate the value of the electric field at each layer, first, we define the boundary conditions of the system. We assume that light only impinges the structure at the right side, so ${E^-}_{(m+1)L} = 0$. Normalising the incident electric field ${E^+}_{0R} = 1$, then the Equation (4.8) can be redefined as:

$$\begin{bmatrix}1\\ r\end{bmatrix} = S\begin{bmatrix}t\\ 0\end{bmatrix} \tag{4.13}$$

where r is the front reflectance coefficient and t is the front transmittance coefficient of the whole structure. The values of each coefficient can be extracted solving Equation (4.13), resulting in:

$$t = \frac{1}{S_{11}} \tag{4.14}$$

$$r = \frac{S_{12}}{S_{11}} \tag{4.15}$$

From these values, it can be obtained all the optical coefficients R, T and A, which are respectively the reflectance, the transmittance, and absorptance of the whole structure:

$$R = |r|^2 \tag{4.16}$$

$$T = \frac{\mathrm{Re}(\gamma_{m+1})}{\gamma_0}|t|^2 \tag{4.17}$$

$$A = 1 - R - T \tag{4.18}$$

Note that until this point, s–polarised light (or transverse electric mode TE) has been considered. However, an equal contribution of the p–polarised light (or transverse magnetic mode TM) must be considered to define the absorption of unpolarised light. The formalism for p–polarised light is nearly the same as s–polarised light but now it is based on the propagation of the magnetic field, and this only implies modifications in the terms of Equations (4.10) and (4.17). When considering p–polarisation, $I_{j,j+1}$ is expressed as:

$$I_{j,j+1} = \frac{1}{2\,\gamma_j/N_j^2}\begin{bmatrix}\gamma_j/N_j^2 + \gamma_{j+1}/N_{j+1}^2 & \gamma_j/N_j^2 - \gamma_{j+1}/N_{j+1}^2\\ \gamma_j/N_j^2 - \gamma_{j+1}/N_{j+1}^2 & \gamma_j/N_j^2 + \gamma_{j+1}/N_{j+1}^2\end{bmatrix} \tag{4.19}$$

and T is now defined as:

$$T = \frac{\mathrm{Re}\left(\frac{\gamma_{m+1}}{N_{m+1}^2}\right)}{\frac{\gamma_0}{N_0^2}}|t|^2 \tag{4.20}$$

Then, the resultant reflection and transmission coefficient is the average of s–polarised and p–polarised modes.

Once the coefficients r and t are obtained, we calculate the value of the electric or magnetic field at each interface from an expression analogous to Equation (4.13):

$$\begin{bmatrix} E^{+}{}_{jL} \\ E^{-}{}_{jL} \end{bmatrix} = S_j{}' \begin{bmatrix} t \\ 0 \end{bmatrix} \tag{4.21}$$

where $S_j{}'$ is the transfer–matrix that includes all the terms from the material j to the last layer of the device:

$$S_j{}' = L_j I_{j,j+1} \dots L_m I_{m,m+1} \tag{4.22}$$

Equation (4.21) is valid for s–polarisation. For p–polarisation we consider the magnetic field instead of the electric field in Equation (4.21).

To calculate the value of the light absorbed by each layer, we evaluate the variation of the Poynting vector at each interface. The Poynting vector is a mathematical construct used in physics to describe the directional flow of energy in an electromagnetic field. The resulting vector points in the direction of energy flow, and its magnitude gives the power per unit area passing through that interface. The value of the electric and the magnetic field at each interface can be calculated from the result of Equation (4.21) for s–polarised light and p–polarised light, respectively:

$$\text{TE: } \begin{bmatrix} E_{j-1,j} \\ Z_0 H_{tj-1,j} \end{bmatrix} = \begin{bmatrix} 1 & 1 \\ -\gamma_j & \gamma_j \end{bmatrix} \begin{bmatrix} E_{jL}^{+} \\ E_{jL}^{-} \end{bmatrix} \tag{4.23}$$

$$\text{TM: } \begin{bmatrix} H_{j-1,j} \\ \frac{E_{tj-1,j}}{Z_0} \end{bmatrix} = \begin{bmatrix} 1 & 1 \\ \frac{\gamma_j}{N_j^2} & -\frac{\gamma_j}{N_j^2} \end{bmatrix} \begin{bmatrix} H_{jL}^{+} \\ H_{jL}^{-} \end{bmatrix} \tag{4.24}$$

where Z_0 is the vacuum impedance.

From the results of these equations, the value of the Poynting vector is obtained according to:

$$\text{TE: } P_{j-1,j} = \frac{1}{2}\text{Re}(-E H_t^*) = \frac{1}{2Z_0}\text{Re}\left(\gamma_j^*\left(E_{jL}^{+} + E_{jL}^{-}\right)\left(E_{jL}^{+*} - E_{jL}^{-*}\right)\right) \tag{4.25}$$

$$\text{TM: } P_{j-1,j} = \frac{1}{2}\text{Re}(E_t^* H^*) = \frac{1}{2Z_0}\text{Re}\left(\frac{\gamma_j}{N_j^2}\left(H_{jL}^{+} - H_{jL}^{-}\right)\left(H_{jL}^{+*} + H_{jL}^{-*}\right)\right) \tag{4.26}$$

From the Poynting vector, the fraction of light absorbed by a layer is obtained from the difference of the Poynting vector values at the two interfaces of the layer:

$$\text{TE: } A_j = \frac{P_{j-1,j} - P_{j,j+1}}{P_{inc}} = \frac{1}{\gamma_0} \text{Re}\left(\gamma_j^* \left(E_{jL}^+ + E_{jL}^-\right)\left(E_{jL}^{+*} - E_{jL}^{-*}\right)\right) \tag{4.27}$$

$$\text{TM: } A_j = \frac{P_{j-1,j} - P_{j,j+1}}{P_{inc}} = \frac{n_0^2}{\gamma_0} \text{Re}\left(\frac{\gamma_j}{N_j^2}\left(H_{jL}^+ - H_{jL}^-\right)\left(H_{jL}^{+*} + H_{jL}^{-*}\right)\right) \tag{4.28}$$

For unpolarised light, the absorption of each layer is the average of the sum of the absorption for TE and TM modes.

4.4.2. Mixed coherent and incoherent layers

When considering incoherent layers, the formalism used for coherent layers can be applied but adding some corrections. The incoherent formalism is simpler in the sense that electric and magnetic fields are treated only with their module, as no interference phenomena occur when layers are incoherent. However, the model becomes more complex when some of the layers of the structure are treated as coherent and others are treated as incoherent. In this case, a multilayer structure can be ideally divided into incoherent layers and packets of coherent layers as depicted in Figure 4.3. Each packet of coherent layers can be modelled as an incoherent interface. Assuming a packet of m coherent layers as in Figure 4.2, it can be defined as an incoherent interface characterised by the matrix $\bar{I}_{i',i'+1}$ which is obtained from the transfer–matrix of the coherent packet calculated with Equation (4.9). The resultant expression is defined by:

$$\bar{I}_{i',i'+1} = \begin{bmatrix} |S_{11}|^2 & -|S_{12}|^2 \\ -|S_{21}|^2 & \frac{|\det \boldsymbol{S}|^2 - |S_{12}S_{21}|^2}{|S_{11}|^2} \end{bmatrix} \tag{4.29}$$

Using Equation (4.29) the multilayer structure can be treated as a pile of incoherent layers whose transfer–matrix is defined by:

$$\bar{S} = \bar{I}_{0',1'}\bar{L}_{1'}\bar{I}_{1',2'} \ldots \bar{L}_{m'}\bar{I}_{m',m'+1} \tag{4.30}$$

where $\bar{L}_j$ is defined by:

$$\bar{L}_j = \begin{pmatrix} \left|e^{-i\gamma_j \frac{2\pi}{\lambda} d_j}\right|^2 & 0 \\ 0 & \left|e^{i\gamma_j \frac{2\pi}{\lambda} d_j}\right|^2 \end{pmatrix} \tag{4.31}$$

Note that the $\bar{I}_{j',j'+1}$ can be calculated for a packet of coherent layers or just an incoherent interface.

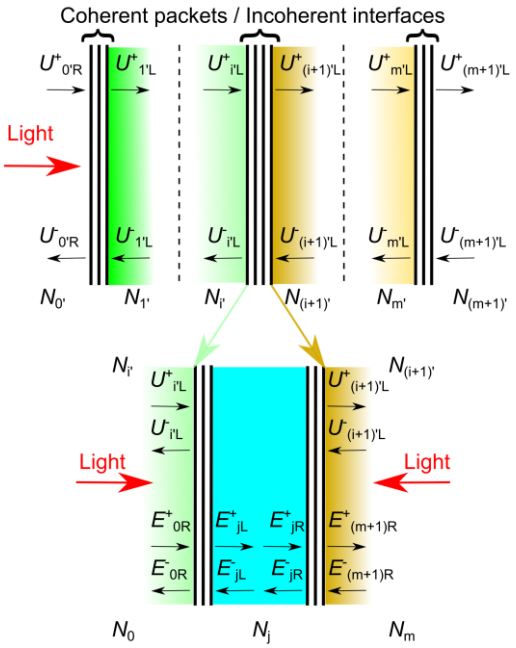

Figure 4.3. Schematic of the formalism for mixed coherent and incoherent layers.

From this point, the whole multilayered structure is treated as a pile of incoherent layers. When considering incoherent layers, instead of evaluating the variations of the electric field E, it is evaluated the evolution of its amplitude square $U = |E|^2$. To calculate the value of U at the interface i', the next equation is used:

$$\begin{bmatrix} U^+_{i'R} \\ U^-_{i'R} \end{bmatrix} = \overline{S_{i'}}' \begin{bmatrix} U^+_{(m+1)'L} \\ U^-_{(m+1)'L} \end{bmatrix} \tag{4.32}$$

where $\overline{S_{i'}}'$ is defined by:

$$\overline{S_{i'}}' = \bar{L}_{i'} \bar{I}_{i',i'+1} \dots \bar{L}_{m'} \bar{I}_{m',m'+1'} \tag{4.33}$$

(Note that Equation (4.32) can be used when calculating the magnetic field for either s–polarised or p–polarised light).

As at the right–hand side there is not incident light, hence $U^-_{(m+1)'L} = 0$, Equation (4.32) can be solved with the values of the incoherent transfer–matrix:

$$\begin{bmatrix} U^+_{i'R} \\ U^-_{i'R} \end{bmatrix} = \overline{S_{i'}}' \begin{bmatrix} \frac{1}{\bar{s}_{11}} \\ 0 \end{bmatrix} \tag{4.34}$$

As the resultant structure is made of incoherent layers, then there is no interference among the light beams inside the structure and the energy flux at the interface coming from the right side and the left side can be calculated separately for both s–polarisation and p–polarisation using the following equations:

$$\text{TE: } \begin{bmatrix} P^{+}{}_{i',i'+1} \\ P^{-}{}_{i',i'+1} \end{bmatrix} = \overline{S_{i'}}' \begin{bmatrix} \frac{1}{\bar{s}_{11}} \\ 0 \end{bmatrix} \cdot \frac{Re(\gamma_i)}{Re(\gamma_0)} P_0 \tag{4.35}$$

$$\text{TM: } \begin{bmatrix} P^{+}{}_{i',i'+1} \\ P^{-}{}_{i',i'+1} \end{bmatrix} = \overline{S_{i'}}' \begin{bmatrix} \frac{1}{\bar{s}_{11}} \\ 0 \end{bmatrix} \cdot \frac{Re\left(\frac{\gamma_i}{N_i{}^2}\right)}{Re\left(\frac{\gamma_0}{N_0{}^2}\right)} P_0 \tag{4.36}$$

The resultant energy flux at each interface is the difference between the energy flux coming from the right and the energy flux coming from the left:

$$P_{i',i'+1} = P^{+}{}_{i',i'+1} - P^{-}{}_{i',i'+1} \tag{4.37}$$

With these expressions, it is possible to calculate the light absorption at the incoherent layers, but the question that arises is how to calculate the energy flux and hence light absorption at the coherent layers of the structure. Until this point, the coherent layers have been treated as incoherent interfaces. To calculate the energy flux at each layer, we use the coherent layer formalism for each packet of coherent layers considering the boundary conditions imposed in the partially coherent structure as depicted in Figure 4.3. First, it is considered the light coming from the left side, so an expression similar to Equation (4.21) is obtained:

$$\begin{bmatrix} E^{+}{}_{jL} \\ E^{-}{}_{jL} \end{bmatrix} = S_j{}' \begin{bmatrix} \frac{1}{s_{11}} \\ 0 \end{bmatrix} E^{+}{}_0 \tag{4.38}$$

In this case, $E^{+}{}_0$ is the electric field at the left of the coherent packet, and its value can be obtained from:

$$E^{+}{}_0 = \left\{ (1 \quad 0) \cdot \overline{S_{i'}}' \cdot \begin{bmatrix} \frac{1}{s_{11}} \\ 0 \end{bmatrix} \right\}^{1/2} \tag{4.39}$$

where $\overline{S_{i'}}'$ is the transfer–matrix of incoherent layers from the coherent packet that is being analysed until the last layer of the structure, and S is the transfer–matrix of the coherent layers that forms the packet.

Now it is considered the light coming from the right side, which is more complex as in this case, the reflected component must be considered:

$$\begin{bmatrix} E^{+}{}_{jL} \\ E^{-}{}_{jL} \end{bmatrix} = S_j{}' \begin{bmatrix} -\frac{s_{12}}{s_{11}} \\ 1 \end{bmatrix} E^{+}{}_{(m+1)L} \tag{4.40}$$

Where $E^{+}{}_{(m+1)L}$ is defined by:

$$E^{+}{}_{(m+1)L} = \left\{ (0 \quad 1) \cdot \bar{L}_{i'+1} \overline{S_{i'+1}}' \cdot \begin{bmatrix} \frac{1}{s_{11}} \\ 0 \end{bmatrix} \right\}^{1/2} \tag{4.41}$$

These expressions are analogous to the calculation of the magnetic field in the case of p–polarised light. Then, using the Equations from (4.23) to (4.28) we calculate the light absorption at each coherent layer in a partially coherent structure.

4.4.3. Introducing optical anisotropy

TMDC materials show anisotropic electric and optical properties because of their layered structure. To accurately evaluate the optical properties of TMDC structures we have implemented an specific formalism that accounts for optical anisotropy. Figure 4.4.a shows a schematic of a TMDC layer with a tridimensional coordinates system. Using these coordinates as a reference, we define the in–plane properties (in the plane *xy*) and the out–of–plane properties (normal to the surface, parallel to the *z* axis). The difference between in–plane and out–of–plane optical properties has an important impact on the absorptance of TMDCs as these materials show a considerable difference in the value of their refractive index between both orientations. For instance, MoS_2 almost does not absorb light when propagates in the in–plane [129]. Therefore, it is crucial to consider optical anisotropy when modelling the optical behaviour of TMDC–based devices.

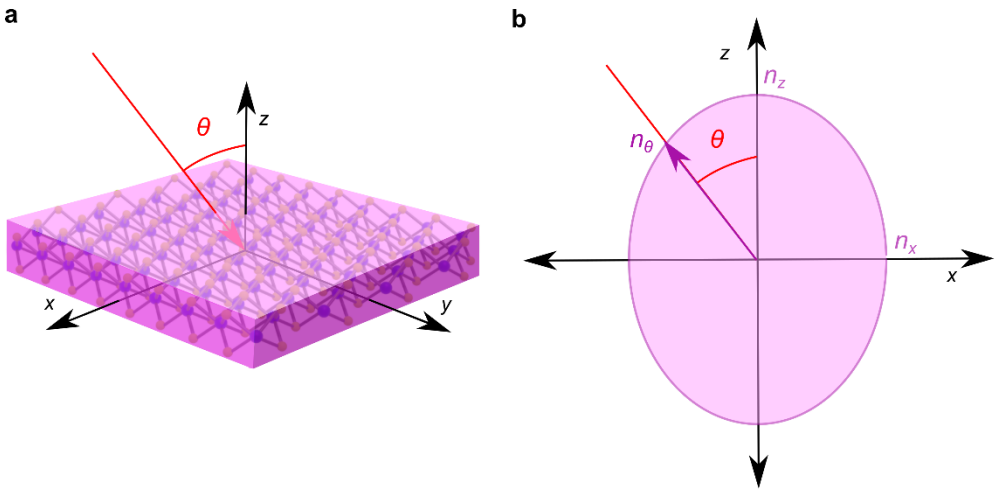

Figure 4.4. (a) Schematics of a TMDC layer with main reference axes. (b) Refractive index ellipsoid of a TMDC.

To accurately model the optical properties of TMDCs, we determine the refractive index of the material in the direction of light propagation. The refractive index of a material is derived from its electrical permittivity which can be represented as a second–rank tensor. Hence, the optical properties of the material can be defined

by the index ellipsoid as illustrated in Figure 4.4.b, which is a geometric construction which concisely represents the refractive index of a material, as functions of the orientation of the wavefront. The index ellipsoid accomplishes the following expression:

$$\frac{x^2}{{N_x}^2} + \frac{y^2}{{N_y}^2} + \frac{z^2}{{N_z}^2} = 1 \tag{4.42}$$

Where N_x, N_y and N_z are the complex refractive index in the main orientations of the material and x, y and z are the coordinates. In TMDCs there is in–plane index $N_x = N_y$ and out–of–plane index N_z. Hence using the index ellipsoid, we can obtain the refractive index N_θ in any arbitrary direction:

$$\frac{1}{{N_\theta}^2} = \frac{\sin^2\theta}{{N_x}^2} + \frac{\cos^2\theta}{{N_z}^2} \tag{4.43}$$

Note that this equation is used for the complex refractive index, hence there is the real part and the imaginary part which correspond to the effective value of the extinction coefficient k_θ.

The optical anisotropy of TMDCs involves the recalculation of the refractive index depending on the angle of propagation inside the layer. However, the angle of propagation is calculated according to the Snell Law which depends on the refractive index of the material. We implement an optimisation routine that considers the correlation between both parameters estimating them correctly. This routine consists of an algorithm that starts by considering the effective refractive index of the TMDC as the out–of–plane value to calculate the propagation angle and then uses this angle to recalculate the effective refractive index. The calculation is repeated until each parameter converges.

4.4.4. Light absorption in heterogeneous TMDC layers

Until this point, we have described the mathematical formalism to calculate the optical properties of plain and homogeneous multilayer structures. Nevertheless, the fabrication techniques may not always produce perfectly layers made of atomic monolayers of TMDCs stacked in a uniform orientation. In some cases, the TMDC slabs are made of multiple microscopical crystals of TMDC with a random distribution. This could be the case of fabrication processes based on the deposition of MoS_2 from microcrystals of material in a liquid suspension [20]. In this case, it is not accurate to consider the TMDC layer as a coherent and homogeneous layer.

To model such structures, first, we must treat every TMDC layer as incoherent. Then, we consider a distribution of the TMDC crystals inside the layer. We define a reference system whose z axis coincides with the normal direction of the surface of the TMDC slab. This can be defined as the macroscopic reference system with respect to which the angle of incidence is defined. At the microscopic level, each crystal of TMDC has its own z' axis normal to its surface, and each crystal has a certain orientation with respect to the macroscopic reference system as illustrated in Figure 4.5.

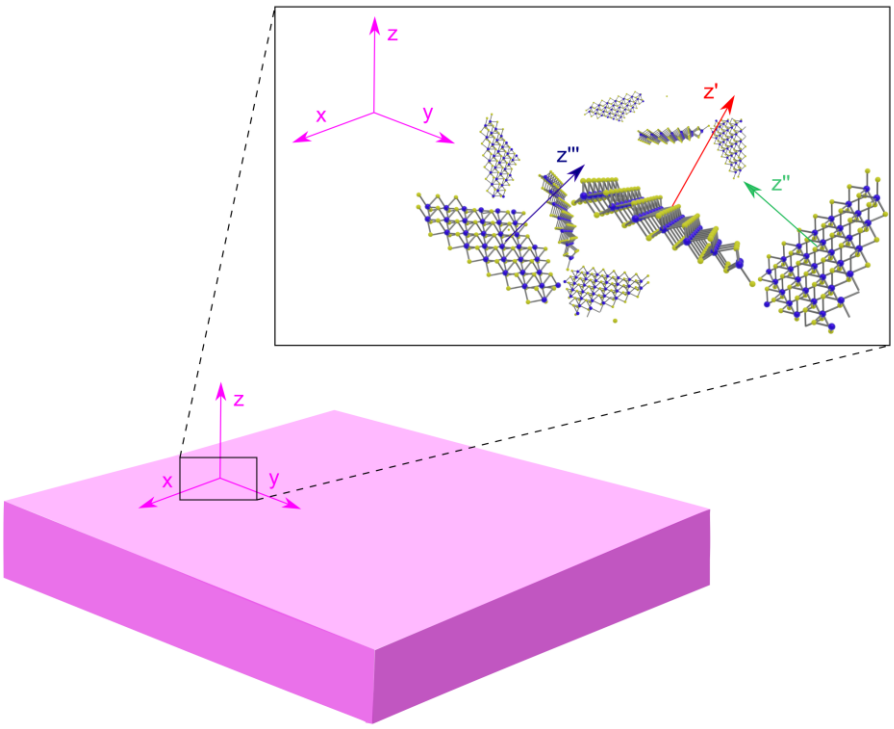

Figure 4.5. Schematic for the calculation of optical properties in heterogeneous layers.

To calculate the optical properties of the slab, we consider that all the crystals in the slab have the same orientation so light impinges the slab with an angle θ' which depends on the incidence angle of the light and the relative orientation of the crystals to the macroscopic reference system of the slab. We repeat the calculation for every possible value of θ' from 0^{o} to 90^{o} and the results are weighted over a normal distribution that represents the probability of a crystal of TMDC to be placed in a specific orientation. So, every optical property can be described with the following expression:

$$P(\lambda) = \sum_{\theta'=-90}^{90} P(\lambda,\theta') \cdot \frac{1}{\sigma\cdot\sqrt{2\pi}} \cdot exp\left(-\frac{(\theta'-\mu)}{2\sigma^2}\right) \cdot CFN(\mu,\sigma)^{-1} \quad (4.44)$$

where $P(\lambda,\theta')$ is the calculated property (absorptance, reflectance or transmittance) for an orientation angle θ', σ is the standard deviation of the distribution, μ is the angle of the main orientation of the crystals, and $CFN(\mu,\sigma)$ is a correction factor which is calculated with the following equation:

$$CFN(\mu,\sigma) = \int_{-90}^{90} \frac{1}{\sigma\cdot\sqrt{2\pi}} \cdot exp\left(-\frac{(\theta'-\mu)}{2\sigma^2}\right) d\theta' \quad (4.45)$$

This factor is used to consider only the angles between -90 and 90 in the normal distribution and to correct the integration value of the curve of probability between both values. Note that it is possible to customise the distribution of the semiconductor crystals to increase the weight of certain orientations in the overall calculation. Alternatively, a random distribution could be assumed where all possible orientations have the same probability.

4.5. Evaluation light absorption of a device with realistic position and orientation

The model developed in Section 4.4 provides the value of the optical absorption, transmission, and reflection of any multilayered structure. However, evaluating the optical behaviour of any device under certain operation conditions involves also considering the spectral characteristics of the incident light, such as its SPD and angle of incidence. The SPD is a characteristic of any light source, and when considering the Sun as the source, its SPD depends on the geographical coordinates of the reference point and the time of the day. Solar position in the sky and the incidence angle of the light beam at a certain date and hour are determined using the equations from Kalogirou [130]. We use the result from these equations as input to calculate the incident SPD on the evaluated structure using the equations from Bird and Riordan [131]. These equations model the direct and diffuse irradiance for cloudless atmospheres. From the AM0 solar spectrum, the equations apply different corrections related to the atmosphere composition (Rayleigh scattering, aerosol absorption, ozone and water vapour absorption) and the position of the Sun.

Once it is obtained the direct and diffuse SPD, the next step is to determine the absorbed power of the TMDC structure. The power absorption of the direct

irradiance is easily modelled by introducing the SPD calculated from the equations of Bird and Riordan, and its incidence angle provided by Kalogirou equations, but when considering diffuse irradiance, we cannot define an incident angle. To accurately compute the contribution of the diffuse irradiance we implement a model that considers the angular acceptance of the structure into the interaction with the diffuse spectrum. Angular acceptance is defined as the absorptance of a structure depending on the angle of incidence.

Figure 4.6 shows a schematic of our calculation method for the overall diffuse power absorption for a vertical surface computing the angular acceptance of the structure. We assume that the diffuse irradiance is perfectly distributed on a semisphere that resembles the sky with a radius R large enough to consider the TMDC structure a point O. For the scope of the Thesis, we consider that the TMDC structures are placed vertically, because these materials will be proposed for the development of semitransparent solar windows as we will see in Chapter 8. Hence, given a vertical surface, we can define points on the sky semisphere where the angle α between the z axis and the segment $\overline{OP}$ is constant. Then, the irradiance provided by these points is calculated by multiplying the surface revolution integral (dark blue surface) and the diffuse irradiance distribution:

$$Ir(\alpha) = \frac{Ir_{diffuse}}{4\pi R^2} \int_{R\cdot\sin\alpha}^{R\cdot\sin(\alpha+\nexists\alpha)} 2\pi \cdot f(y) \cdot \sqrt{1+[f'(y)]^2}\,dy \qquad (4.46)$$

where $f(y)$ is defined as:

$$f(y) = \sqrt{R^2 - y^2} \qquad (4.47)$$

Solving the Equation (4.46) the expression of the diffuse irradiance is obtained for a certain angle α:

$$Ir(\alpha) = \frac{1}{2} \cdot Ir_{diffuse} \cdot (\sin(\alpha + \Delta\alpha) - \sin\alpha) \qquad (4.48)$$

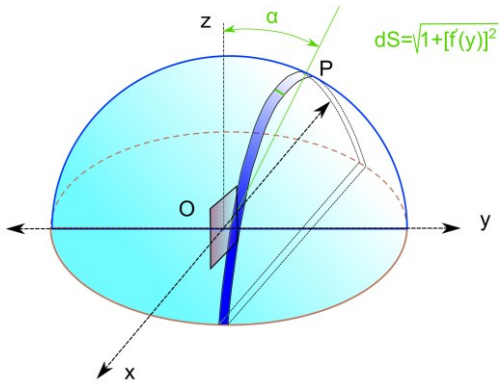

Figure 4.6. Schematic of the modelling of diffuse irradiance.

Equation (4.48) is the fraction of diffuse irradiance that can be considered to impinge the surface of the structure with a certain angle. Hence, to calculate the overall diffuse power absorption (DPA), this expression must be weighted along the absorptance of the structure for any angle of incidence.

$$DPA(\lambda) = \frac{\int_0^{\frac{\pi}{2}} A(\alpha,\lambda)\cdot Ir(\alpha)\cdot d\alpha}{Ir_{diffuse}} \qquad (4.49)$$

Note that the value of diffuse power absorption is obtained as a function of the wavelength and an equivalent expression can be used to evaluate the reflectance and the transmittance.

4.6. Summary

The characterisation of TMDC–based structures require the development of specialised tools for accurately assessing their optical properties. Key challenges include addressing the partial coherence inherent to these structures, accounting for interference effects, and the impact of the anisotropic refractive index of TMDCs. These challenges have been encompassed within a versatile model adaptable for characterising any kind of multilayered structure.

The assessment of light coherence involves evaluating conditions that enable material slabs to exhibit coherence, reliant upon the coherence length of sunlight within the material and its morphological characteristics. Moreover, the anisotropic features of TMDCs are pondered by calculating the effective refractive index of the material according to the angle of light propagation inside the material. Then, the transfer–matrix model is adapted to evaluate partially coherent multilayered structures. This model has been also adapted to evaluate heterogeneous structures that consider the limitations of the fabrication processes of TMDCs.

Finally, a model to calculate the SPD of the incident light is implemented. The results of this model serve as inputs for the optical model to evaluate light absorption in realistic cases. Direct absorption evaluation is straightforward, while accurate consideration of diffuse absorption necessitates specific procedures to account for the angular acceptance of TMDC–based structures. Diffuse absorption is modelled by assuming a uniform distribution of diffuse light in a semisphere that resembles the sky and considering the illumination from sections of that semisphere with a specific angle orientation to a reference point. The models developed herein hold significant relevance for subsequent chapters, as they provide crucial results for the theoretical characterisation of all devices and structures presented in this Thesis.

Chapter 5

Design of TMDC 1D optical cavities with strong light absorption

5.1. Introduction

TMDCs show absorption coefficients that overcome any material used in conventional solar cells. This feature enables the possibility of achieving ultrathin structures with a thickness unattainable by conventional technologies. The possibility of assembling multilayer TMDC–based devices with nanometric thickness can boost light absorption by the amplification of interference effects. Interference appears when the thickness of the material has similar dimensions to the wavelength of the incident light. This leads to the possibility of designing simple 1D nanocavities that achieve high optical absorption [123] without requiring complex light–trapping strategies used in other ultrathin film approaches.

Despite the exceptional optical properties exhibited by TMDCs, the attainment of a high level of optical absorption is not straightforward. An important drawback is the high reflectance observed in TMDCs which can be attributed to the elevated values of their refractive indices. To address this matter, we design a 1D nanocavity where the different layers interplay boosting light interference effects that provide large optical absorption while lowering the layer thicknesses. Therefore, the design of structures based on TMDCs entails not only the optimisation of thickness but also a judicious selection of the materials that improve the light absorption of TMDCs. This selection concerns not only the optical characteristics of the materials but also how TMDCs can be effectively integrated into solar cell configurations.

The analysis of the optical absorption of MoS_2 homojunctions presented in this Chapter have been published in Optics Express journal [132]. The light absorption of the modelled structures is calculated using the optical model developed in Chapter 4. Different MoS_2–based structures are presented where optical absorption is enhanced using 1D optical cavities. These designs increase the

absorption of MoS_2–based devices from 50% to over 80% of the incident light. We found that up to 87% of the photons contained in the 300–700 nm range of the AM1.5G spectrum can be absorbed employing a 1D nanocavity made of MoS_2 absorbers as thin as 10 nm sandwiched between h–BN layers and an Ag reflector. This high broadband absorption in these nanocavity structures enhances absorption by amplifying the zeroth FP interference mode, providing the highest light absorption with the lowest material requirements.

5.2. TMDCs as absorber materials in solar cells

TMDCs are characterised by an elevated absorption coefficient that enables a high absorption even in few nanometre–thick slabs of the material. Figure 5.1 shows the absorption coefficient of two of the most studied TMDCs, MoS_2 and WSe_2, along with the conventional materials used for solar cells. This absorption coefficient is considerably higher in the case of the MoS_2 considering the visible range. The outstanding optical properties of MoS_2 were first described by Mak et *al.* [15] identifying the strong light–matter interactions and the dependence of the band gap energy on the number of stacked layers. Among the properties described by Mak, there is the transition from an indirect (1.29 eV) to a direct (1.9 eV) band gap energy when approximating the monolayer limit, the presence of absorption peaks at visible wavelengths, and the strong photoluminescence of monolayers.

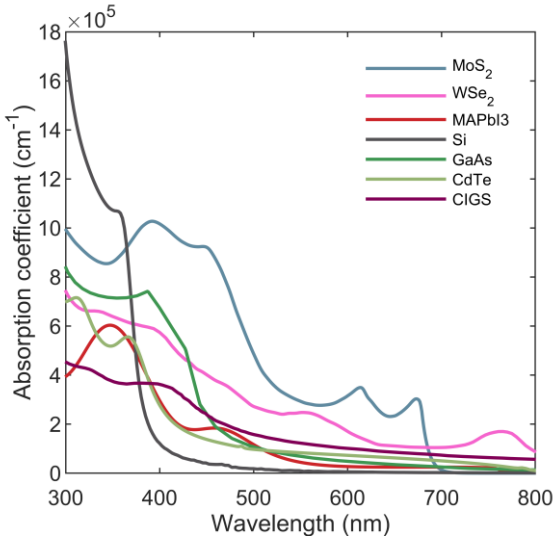

Figure 5.1. Absorption coefficient versus wavelength for different semiconductors typically used in solar 109 cells. Values have been extracted from the following references: MoS_2 [133], WSe_2 [134], MAPbI3 [135], Si [136], GaAs [136], CdTe [137], and CIGS [138].

The extraordinary light absorption found in TMDCs is related to their electronic structure. The strong light–matter interaction is explained by the calculation of the density of states. These calculations reveal pronounced peaks within the visible spectrum, attributed to Van Hove singularities. Van Hove singularities come from the interactions between the orbitals of the transition metal and the chalcogen atom that leads to absorption peaks [23].

The outstanding optical properties of TMDCs enable the possibility of assembling devices using ultrathin absorbers, opening a pathway to a new generation of thin and flexible devices. Considering the current thin–film technologies, it is dominated by the use of direct bandgap semiconductors such as III–V materials, CdTe, or CIGS allow for high efficiencies with lower absorber thickness between 1 and 4 µm [139]. However, despite this thickness reduction, there is not a decisive decrease in the fabrication cost with respect to silicon. Further thinning of photovoltaic devices would be desirable to reduce material consumption, to lower the economic and energetic cost of fabrication, and to produce low–weight and flexible devices that can expand the field of application of photovoltaics (building integrated, vehicle powering, wearable devices, etc.). However, severe device thinning presents some challenges [139]. The reduction to extremely thin laminae of conventional semiconductors turns them transparent and fragile, and their electronic properties become dominated by surface recombination. Recently, various works have tried to solve these issues and have presented progress.

Ultrathin GaAs–based devices featuring a 205–nanometre–thick absorber with a PCE of 19.9% [140], or alternatively, a 260–nanometre–thick absorber with a PCE of 22.35% [141], have been documented in the literature. It is noteworthy that, for reference purposes, the current record PCE for thicker GaAs devices stands at 29.1% [8]. The operation of these ultrathin devices hinges upon the implementation of intricate light–trapping strategies, such as the utilisation of nanostructured mirrors or plasmonic grids. In a distinct approach, Steenhoff et *al.* have employed an exceedingly slim absorber, measuring only 13 nanometres in thickness, composed of amorphous Ge, resulting in the production of a solar cell that aligns with cost–effective manufacturing and attains a PCE of nearly 4% [142].

TMDCs, such as MoS_2, are currently garnering attention as a potential means to transition from the conventional thin–film technologies operating within the 1–4 µm thickness range to a thinner regime of < 100 nm, all while obviating the necessity for intricate light–trapping techniques. The layered crystalline structure inherent to TMDCs affords the capability to isolate thin laminae, even down to the monolayer limit, which exhibits chemical and mechanical stability. Notably, these laminae present minimal surface recombination due to the absence of dangling bonds on their surfaces, thanks to their self–passivated nature. Devices can be readily assembled by bringing them into physical contact at room temperature, forming van der Waals structures, and nanosheet deposition from solution is also a viable approach [42]. Another advantage of TMDCs is the reduction of material usage owing to the extreme thinness of the devices. Furthermore, the reserves of Mo or W in the Earth's crust are larger than the reserves of materials such as Cd, Te, or In, which are used in conventional thin–film approaches [22]. Consequently, layered TMDC semiconductors emerge as natural candidates to produce ultrathin crystalline absorbers, potentially contributing to cost reduction through low–temperature fabrication.

The strong optical response of TMDC–based devices has been reported in the literature. Photodiodes at the ultimate thickness limit of two monolayers have been demonstrated with these materials (total absorber thickness ~1 nm) [27,28,30,91]. To enhance light absorption and facilitate current transport, an intermediate thickness range on the order of several nanometres has been investigated. This research encompasses solar cells composed of various combinations of TMDCs like MoS_2, $MoSe_2$, ReS_2, $ReSe_2$, WS_2, and WSe_2 [31,32,34,143]. Different strategies have been proposed to augment absorptance in

TMDC–based devices. For instance, the introduction of an Al_2O_3 adlayer has been shown to enhance the EQE of a WSe_2–based photodetector by 30% under monochromatic illumination at 410 nm [144]. The influence of a back metallic layer on the absorptance of photodetectors and solar cells constructed from thin layers of WSe_2, WS_2, and MoS_2 has also been documented, revealing exceptionally high peak absorbances [25,32]. Additionally, the incorporation of metallic nanoparticles has been reported to elevate the EQE of TMDC absorbers to approximately 30% under monochromatic illumination [145]. Nevertheless, for photovoltaic applications, a high broadband absorptance is imperative. To this end, the integration of monolayer TMDCs into photonic crystal nanocavities has been shown to enhance broadband absorptance at visible wavelengths, resulting in average EQEs on the order of 50% across the visible spectrum [145–147].

5.3. Considerations about the application of the optical model to TMDC structures

To model TMDC–based ultrathin solar cells, we consider a multilayer structure with homogeneous layers and plain and parallel interfaces. This assumption is consistent with the current fabrication processes of the materials that consist of the spin–coating of a solution of nanosheets and posterior annealing. This low–cost fabrication approach has proven to have very precise thickness control and homogeneity across 6" wafers for MoS_2 layers as thin as 2 nm [20]. The refractive indexes of each material used in the modelled structures are extracted from Refs. [133,134,148–151]. We suppose that the optical properties of MoS_2 are not affected by the doping within the dopant concentration range of interest, then the pn junction is modelled as a single MoS_2 slab using the refractive index of the pristine material. Nonetheless, it is well–established that differences exist between the values of n and k in monolayer and few–layer specimens in comparison to their bulk counterparts. It has been demonstrated that the attainment of bulk properties occurs precisely when the specimen reaches a thickness of 13 atomic layers in the instance of MoS_2 (~ 8 nm) [81] or 8 atomic layers in the case of h–BN (~ 3 nm) [83]. However, there is a large scattering in the published values of n and k for monolayer and few–layer MoS_2 which is even larger than the differences between bulk and monolayer values [80,81,152]. Then, we have used the bulk optical constant for all the calculations in this Thesis.

Figure 5.2 depicts the schematic structure of conventional thin–film solar cells (Figure 5.2.a) and the proposed structures for TMDC–based solar cells. When considering TMDC–based solar cells, there are two possible morphologies. Figure 5.2.b shows a structure where the pn junction is deposited directly over a metal layer which works as an electrical contact and back mirror. This design offers the possibility of enhanced absorptance through the aforementioned interference effects, especially for the lowest thickness [32,123,128]. Figure 5.2.c shows a structure where the pn junction is deposited over an insulant transparent substrate with embedded metal fingers that work as metallic contacts. This design may be useful in the fabrication of semitransparent devices and avoid shunting problems related to possible layer discontinuities in ultrathin layers fabricated through low–cost techniques.

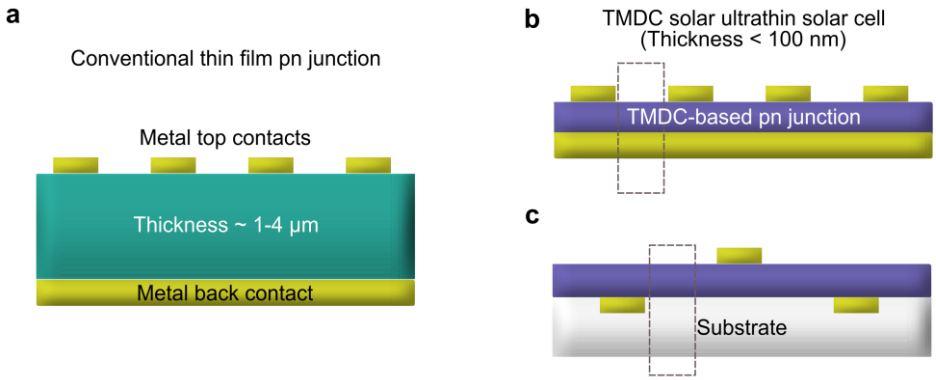

Figure 5.2. Illustration of the transition from thin–film (a) to TMDC–based ultrathin technologies (b) and (c).

For every calculation in this Chapter, we assume the light beam is assumed to be incident perpendicular to the surface, and when giving values of absorptance. The structure modelled is the section marked with a dashed rectangle in Figure 5.2.b and Figure 5.2.c. Then, the effect of the shadowed zones of the hypothetical solar cell is not considered. However, it is considered possible to add top layers on the absorbent that work as ARL.

5.4. Results

5.4.1. Absorptance of a MoS_2 slab on a transparent substrate

Here we calculate the absorptance of a MoS_2 layer on a transparent substrate (see scheme depicted in Figure 5.3.a). The election of the substrate is sapphire (Al_2O_3), but the results are generally applicable for any transparent substrate with a thickness of some hundreds of micrometres. When the calculations are repeated considering a glass substrate as a low–cost option, almost identical values are obtained. In Figure 5.3.b absorptance spectra for various thicknesses of MoS_2 are presented. The features depicted in this plot pose challenges in terms of interpretation due to the merging of interference maxima with excitonic absorption peaks associated with Van Hove singularities (the MoS_2 extinction coefficient exhibits two excitonic peaks at 620 and 680 nm). It is observed that, even for a thickness as modest as 60 nm, absorptance values within the range of 0.5 are attained, with the enhancement attributed to the presence of an interference maximum occurring at a wavelength of approximately 580 nm.

The interference effects are easier to identify in Figure 5.3.c. where the absorptance of a slab of MoS_2 is modelled for incoming light of different wavelengths. The green crosses and red squares mark the position of the constructive and destructive interference resonances. These points are calculated using the $k = 0$ where Equations (4.5) and (4.6) from Chapter 4. In Chapter 4, Section 4.2, we have argued that Equations (4.5) and (4.6) were not accurate when considering a lossy media, then, the position of the resonances obtained with the exact calculation differs slightly from the position obtained, and most importantly, the exact calculation shows a clear M0 resonance which is not possible for $k = 0$. From this plot another interesting conclusion is extracted. The effect of interference in the absorptance spectrum of a slab is stronger at longer wavelengths. This behaviour is explained by the fact that shorter wavelengths require less thickness to be absorbed and those photons are extinguished before reaching the interface between semiconductor and substrate and then induce interference.

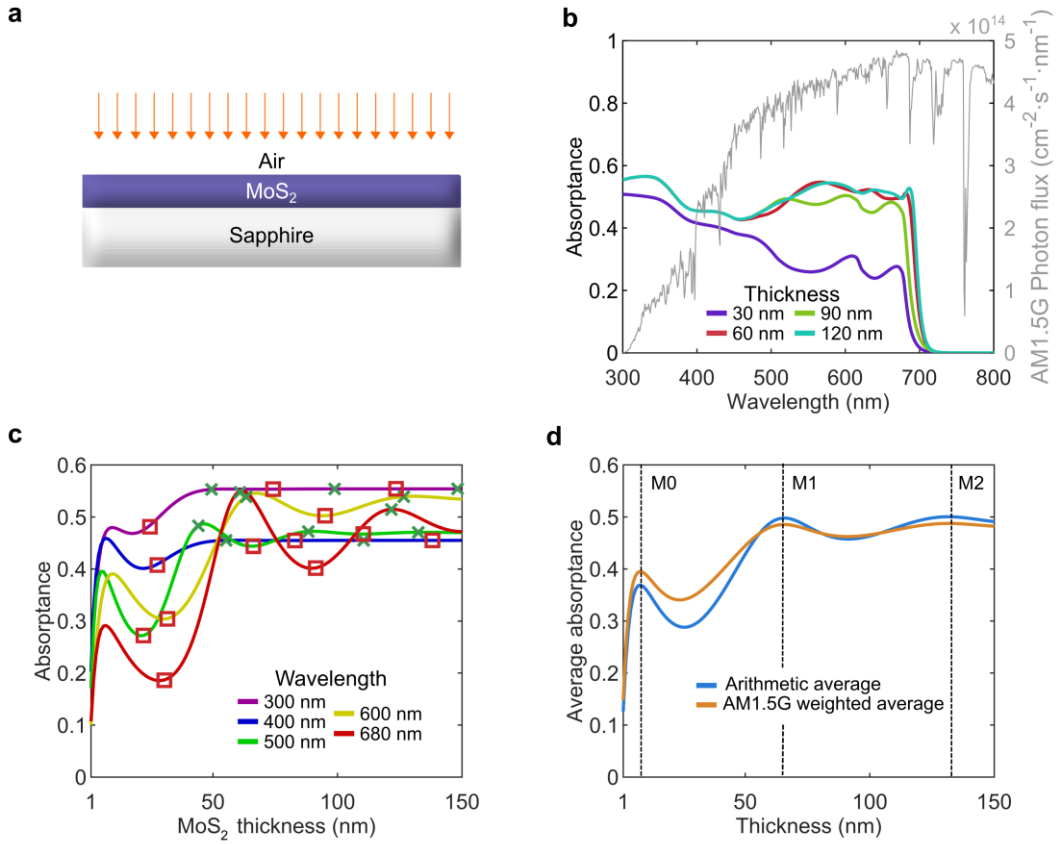

Figure 5.3. (a) Schematic of the MoS_2/sapphire structure. (b) Absorptance for different MoS_2 thicknesses. (c) Absorptance of a MoS_2 slab on sapphire as a function of MoS_2 thickness at different wavelengths. Green crosses (red squares) mark the constructive (destructive) interference resonances obtained with the $k = 0$ approximation. (d) Comparison between average absorptance (blue) and weighted absorptance with AM1.5G spectrum (orange). Vertical dashed lines mark the interference maxima M0, M1, and M2.

The position of the absorptance maxima depends not only on the spectral absorptance of the semiconductor but also on the incident spectrum. Figure 5.3.d shows average absorptance over the 300–700 nm range plotted as a function of the absorber thickness. It has been used two definitions of average: the plain arithmetic average (blue curve), and the AM1.5G–weighted average (orange curve), that is, the number of photons from the AM1.5G solar spectrum that are absorbed in the MoS_2 slab divided by the total number of photons of the AM1.5G spectrum with a shorter wavelength than the material band gap. The AM1.5G–weighted average reflects the fact that there are fewer photons in the short–wavelength range of the spectrum than in the long–wavelength range (see grey curve in Figure 5.3.b), and therefore, gives a more accurate estimation of the final photocurrent density in practical devices. Henceforth, when wavelength–

integrated absorptance values are presented in this Chapter, they are always referred to as the AM1.5G–weighted average.

In Figure 5.3.d, the absorptance of a MoS_2 slab on sapphire tends to stabilise at an approximately constant value of ~ 0.5 for thicknesses exceeding 100 nm. At this point, the transmission approaches zero, and the remaining 50% of incident light is lost because of reflectance. Through the integration of the product between absorptance and the AM1.5G spectrum, we estimate the photocurrent density provided by the structure. We found that the MoS_2 slab can yield a maximum photocurrent density of 10.03 mA/cm². For lower thicknesses, notable absorptance maxima are observed at 8 nm, 66 nm, and 132 nm, denoted as M0, M1, and M2, respectively. These peaks result from the zeroth–, first–, and second–order FP interference in the thin layer.

5.4.2. Absorptance of 1D cavities containing h–BN

Figure 5.3.d illustrates that the absorptance of MoS_2–based structures is limited to 50% of the incident spectrum. Such limitation is caused by the high refractive index of MoS_2 resulting in the reflection of half of the incident light. Therefore, the addition of an ARL is mandatory to minimise reflection losses. The material proposed for this purpose is h–BN for several reasons. First, its refractive index approximately equals the geometric mean between the refractive indices of MoS_2 and air over a wide range of the visible spectrum as depicted in Figure 5.4, which makes it a good candidate for the optical coupling of these two media. Also, it is common practice to use h–BN in combination with TMDCs (and graphene) due to the layered nature of h–BN. When these materials are stacked, the intermolecular forces of van der Waals nature come into play, maintaining the structural integrity of the surface at the atomic scale. The incorporation of h–BN layers into MoS_2 has also demonstrated to enhance its electrical transport characteristics because it encapsulates the material and protects it from surface–charge effects [153].

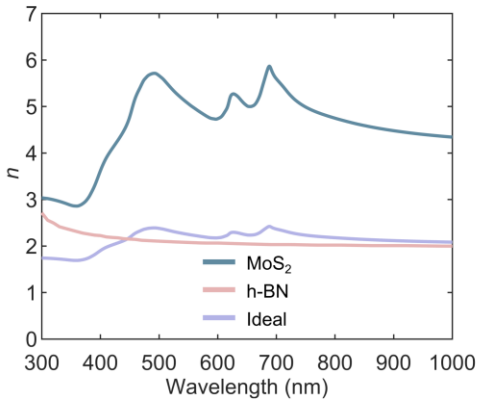

Figure 5.4. The refractive index of MoS_2 (from Ref. [133]), h–BN (from Ref. [151]), and an ideal antireflective material for MoS_2 (geometrical mean of the refractive indices of MoS_2 and air).

Figure 5.5.a illustrates a solar cell structure containing a MoS_2 absorber on a sapphire substrate, overlaid by an h–BN layer. Meanwhile, Figure 5.5.b presents the AM1.5G–weighted average absorptance as a function of both, h–BN and MoS_2 thickness. A substantial enhancement is observed in comparison to the MoS_2/sapphire configuration for the absorption maxima M1 and M2. The maximum absorptance reaches 0.84, yielding an estimated maximum photocurrent density is 17.20 mA/cm^2, attained at M2 for 120 nm of MoS_2 and 56 nm of h–BN. This signifies a remarkable 70% increase when contrasted to bare MoS_2. Figure 5.5.c shows the spectral absorptance for the two maxima M1 and M2. These outcomes surpass the results reported by Islam et *al.* [154] for MoS_2 absorbers under conventional antireflective coating materials (SiO_2, MgF_2, . . .) which is attributable to the more compatible refractive index of h–BN. However, it is noteworthy that the amplification of the zeroth FP mode is not as pronounced in the h–BN/MoS_2/sapphire structure, as evidenced in Figure 5.5.g. Detailed information regarding maximum absorptance values and optimal thicknesses for this and subsequent structures is compiled in Table 5.1.

Table 5.1. Optimum layer thicknesses, average absorptance (weighted over the 300 to 700 nm range of the AM1.G spectrum), and maximum photocurrent density under the AM1.5G spectrum for different MoS_2–based solar cell structures.

Structure	*Second top layer (nm)*	*Top layer (nm)*	*MoS_2 (nm)*	*Bottom layer (nm)*	*Absorptance*	*Max. photocurrent density (mA/cm^2)*
MoS_2/sapphire	–	–	8 66 132	–	0.40 (M0) 0.49 (M1) 0.49 (M2)	8.19 10.03 10.03
h–BN/MoS_2/sapphire	–	53 56	62 120	–	0.80 (M1) 0.84 (M2)	16.38 17.20
h–BN/MoS_2/Ag	–	32 53	10 69	–	0.87 (M0) 0.88 (M1)	17.81 18.01
h–BN/MoS_2/ sapphire/Ag	–	46 54	37 98	–	0.86 (M1) 0.87 (M2)	17.60 17.81
SiO_2/h–BN/ MoS_2/sapphire/Ag	37 31	34 44	38 98	–	0.87 (M1) 0.88 (M2)	17.81 18.01
h–BN/MoS_2/h–BN/Ag	–	31 52	10 57	1 48	0.87 (M0) 0.89 (M1)	17.81 18.22
Glass/ITO/MoS_2/Ag	-	61 80	11 71	–	0.88 (M0) 0.82 (M1)	18.01 16.79

The enhancement of the M0 interference mode requires a substrate material capable of inducing an optimum phase shift at the rear interface [123]. Figure 5.5.d presents a structure with h–BN on the top and an optically thick Ag layer as substrate. Figure 5.5.e illustrates the average absorption of this configuration. The metallic layer functions as a reflector, elevating the average absorption of M1 from 0.84 to 0.88. Most notably, M0 experiences substantial amplification achieving an

absorptance of 0.87 for an extremely thin configuration (MoS_2 10 nm, h–BN 32 nm). The integration with the AM1.5G spectrum yields a maximum photocurrent density of 18.01 mA/cm^2 for M2 and 17.81 mA/cm^2 for M1. It is worth mentioning that thinner absorbers are generally preferred in practical devices due to the diminishing efficiency in the collection of photogenerated carriers with increasing thickness. However, other factors, such as lateral series resistance, may justify a design within the thickness range of M1. Figure 5.5.f depicts the spectral absorbance of this structure at the M0 and M1 maxima. In the M0 case, the monochromatic absorptance at λ = 399 nm reaches a remarkable value of 0.97, and if the device was used under a UV–rich spectrum, such as the AM0, the average absorption of the M0 structure would likely surpass that of the M1 structure. In Figure 5.5.g the amplification of the M0 mode in the h–BN/MoS_2/Ag architecture is noticeable.

In Figure 5.6.a, we have replaced Ag in the schematic of Figure 5.5.d by Al. The AM1.5G–weighted absorptance contour map from Figure 5.6.b reveals fewer promising results specially concerning the zeroth–order FP: M0 exhibits an absorptance of only 0.77, and M1 reaches 0.85. Figure 5.6.c depicts the absorptance profiles of each maximum. This discrepancy arises because, in the case of Ag, reflection at the rear interface is maximised due to its reduced value of refractive index in the wavelength range above 350 nm, a condition not met by Al.

The presence of the resonance effects depends on several parameters such as the wavelength, the thickness of the layer, and the refractive index of the materials. When considering lossy materials ($k > 0$), and reflective metals, the M0 resonance appears because of the non–trivial (not equal 0 or π) phase shift produced at the MoS_2 surfaces. This allows the total phase accumulation in the slab, which is the sum of the interface and propagation phase shifts, to reach approximately 0 for a very small slab thickness [123,127,128]. The large extinction coefficient of Al in comparison to Ag results in a larger phase shift at the interface, making the M0 mode appear at a slightly larger MoS_2 thickness. Although Al performs better than Ag at some thicknesses and shorter wavelengths, in general terms, the Ag back mirror produces a higher average absorptance.

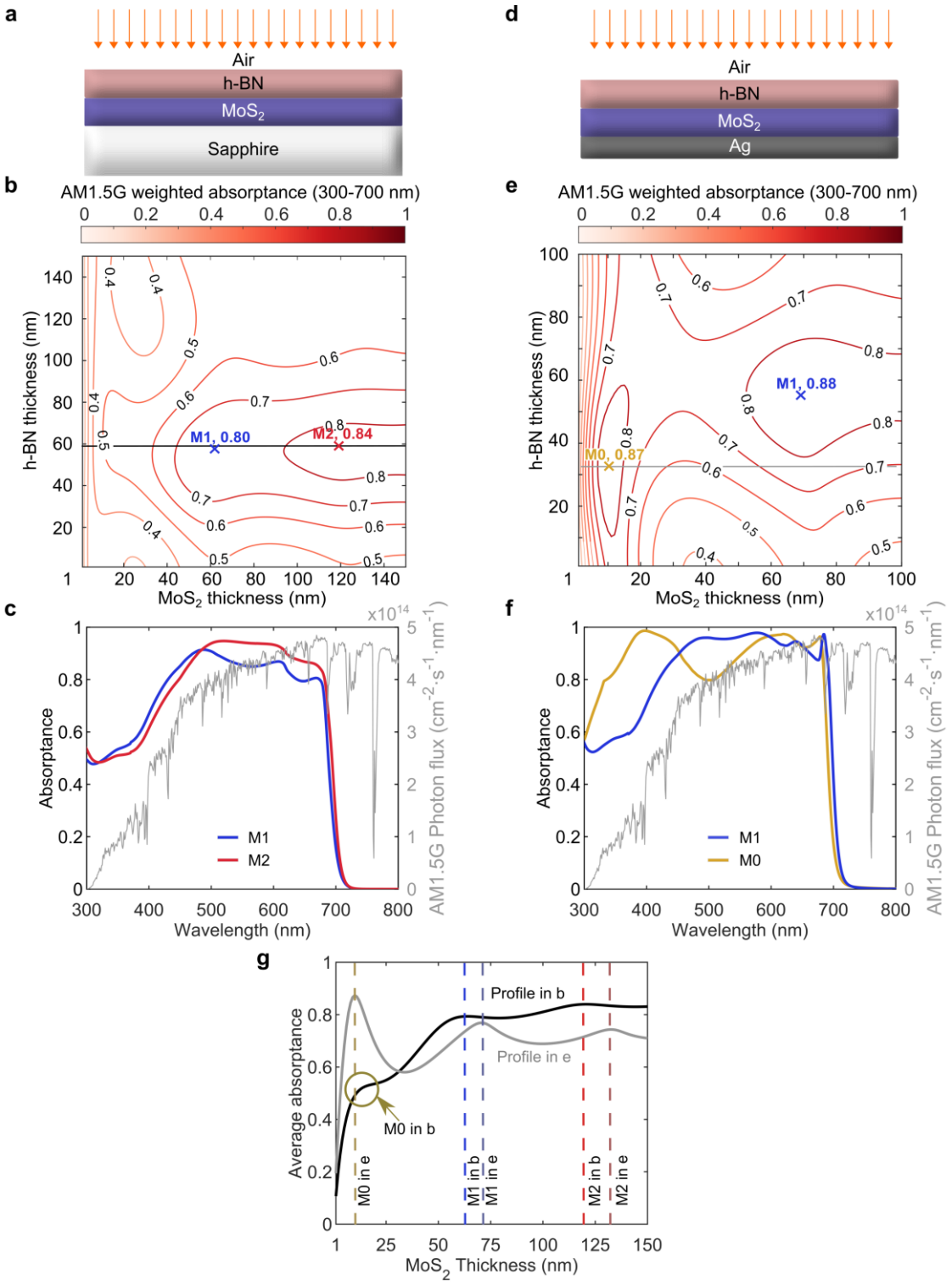

Figure 5.5. (a) Schematic of h–BN/MoS_2/sapphire structure. (b) AM1.5G–weighted absorptance as a function of h–BN and MoS_2 thicknesses in the structure in (a). (c) Spectral absorptance for the optimal cases M1 (blue) and M2 (red). (d) Schematic of h–BN/MoS_2/Ag structure. (e) AM1.5G–weighted absorptance as a function of h–BN and MoS_2 thicknesses in the structure in (d). (f) Spectral absorptance for optimal cases of (e) M0 (yellow) and M1 (blue). (g) AM1.5G–weighted absorptance for a constant h–BN thickness and variable MoS_2 thickness extracted from the maps in (b) and (c). The black (grey) curve corresponds to the black (grey) horizontal line in map (b) (e). The optimum layer thicknesses and average absorptance for the curves in (c) and (f) can be found in Table 5.1.

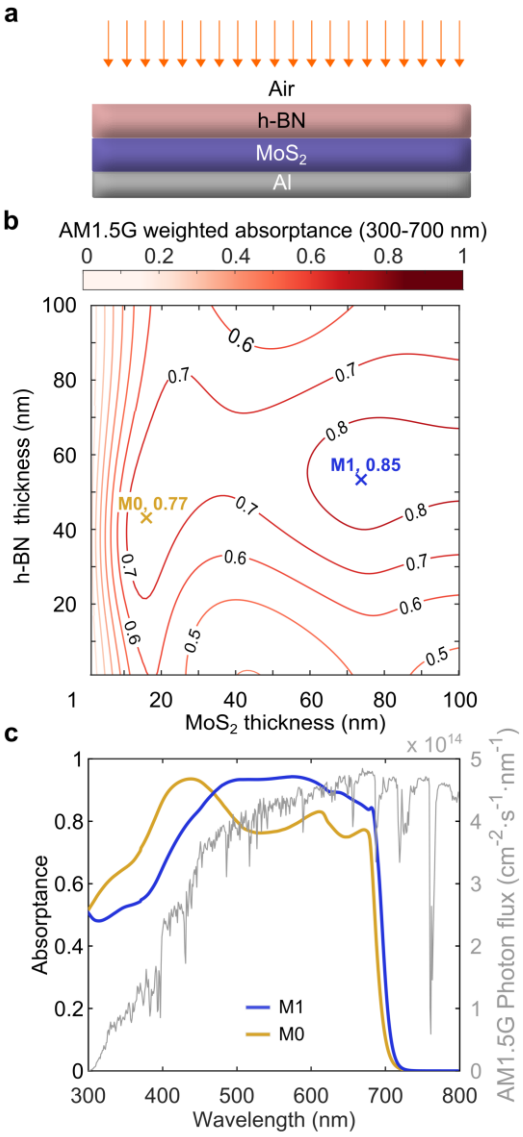

Figure 5.6. (a) Schematic of h–BN/MoS_2/Al structure. (b) AM1.5G–weighted absorptance map as a function of h–BN and MoS_2 thicknesses of structures in (a). (c) Spectral absorptance for optimal cases of (b) M0 (yellow) and M1 (blue).

5.4.3. Absorptance of structures containing h–BN and back mirror

Some practical applications require the use of non–conductive substrates as in the schematic presented in Figure 5.2.c. Figure 5.7.a depicts a new configuration where the reflector is placed at the back of the transparent sapphire substrate. Figure 5.7.b illustrates the average absorptance contour map as in the previous figure. The introduction of the rear mirror to the transparent substrate results in an enhancement of the absorptance concerning the h–BN/MoS_2/sapphire case (Figure 5.5.(a)–(c)) to reach 0.86 (M1) and 0.87 (M2) and it also shifts the optimum

MoS_2 thickness to lower thickness values: 37 (M1) and 98 nm (M2). Consequently, a maximum photocurrent density of 17.81 mA/cm² for M2 and 17.60 mA/cm² for M1 is achieved. However, it should be noted that these outcomes are slightly inferior to those observed in the h–BN/MoS_2/Ag scenario (Figure 5.5.(d)–(f)), and most crucially, the M0 peak is absent in this design. In this structure, the reflected and transmitted components at the interfaces fail to generate the required phase accumulation in a MoS_2 slab with thickness below $\lambda/4n$. Therefore, with this architecture it does not seem possible to fabricate an efficient device based on a MoS_2 absorber in the 10 nm thickness range.

One possible option for enhancing the performance of the h–BN/MoS_2/sapphire/Ag structure is the addition of a second ARL to create a graded refractive index transition. The choice of material for this second layer is broader than for the first layer since it will not be deposited onto the absorber, thereby not compromising its surface quality or electrical performance. Figure 5.7.d depicts a schematic of the solar cell structure featuring a top SiO_2 ARL and Figure 5.7.e illustrates the weighted absorptance for varying thicknesses of h–BN and MoS_2. For each point of the map, the thickness of the SiO_2 layer has been optimised. Comparable results can be obtained when considering MgF_2 instead of SiO_2. This design yields a slightly elevated absorptance relative to the single antireflective layer configuration: M1 reaches 0.87, and M2 achieves 0.88, matching the performance of the h–BN/MoS_2/Ag stack.

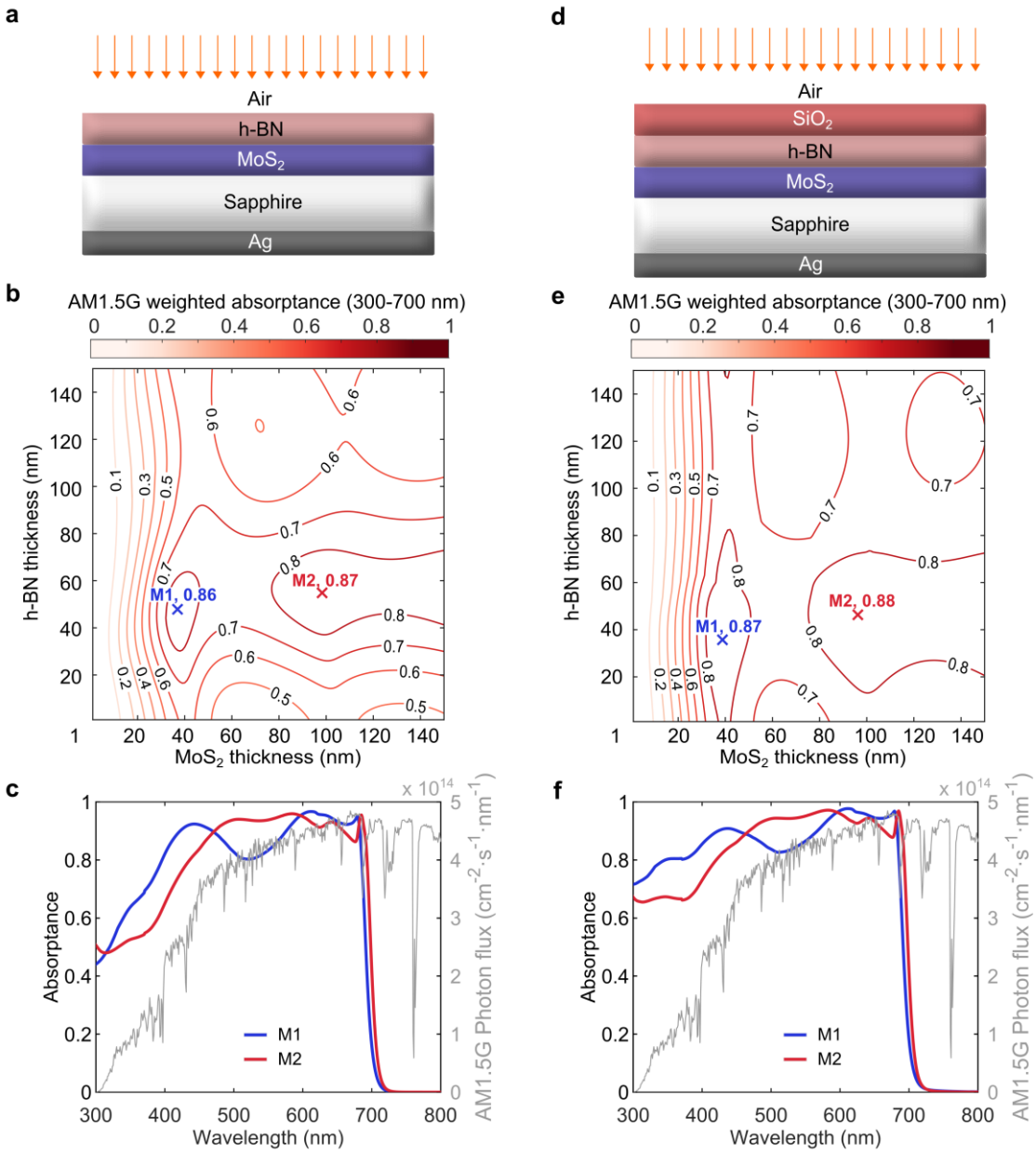

Figure 5.7. (a) Schematic of h–BN/MoS_2/sapphire/Ag structure. (b) AM1.5G–weighted absorptance as a function of h–BN and MoS_2 thicknesses of structure in (a). (c) Spectral absorptance for the optimal cases of (b) M1 (blue) and M2 (red). (d) Same structure as in (a) with the addition of a SiO_2 top layer. (e) AM1.5G–weighted absorptance as a function of h–BN and MoS_2 thicknesses of structure in (d) for the optimal thickness of SiO_2. (f) Spectral absorptance for the optimal cases of (f) M1 (blue) and M2 (red). The optimised layer thicknesses and average absorptance for the curves in (c) and (f) can be found in Table 5.1.

The spectral absorbance in Figure 5.7.f indicates that the improvement primarily occurs in the UV–blue region. The addition of a second antireflective layer exerts a notable impact in this spectral range because the refractive index of h–BN does not optimally match the MoS_2 refractive index below λ = 450 nm (see Figure 5.4). However, it is noteworthy that the AM1.5G spectrum exhibits a low photon flux in the UV–blue region, which accounts for the limited enhancement in the overall averaged absorptance. In space applications where the spectrum includes a more significant UV component, this fine tuning of the absorptance spectrum through the addition of a second antireflective layer may hold greater significance.

From Figure 5.7 it can be concluded that the design featuring a thick transparent substrate between the MoS_2 absorber, and the metallic mirror matches the performance of the cavity design only when the MoS_2 thickness exceeds 30 nm. For thinner absorbers, this design is interesting if it implies the facilitation of the fabrication process, an improvement of electrical properties, or cost reduction. From a purely optical perspective, for very thin structures (zeroth–order FP), the performance is inferior to that of the h–BN/MoS_2/Ag design, especially considering that the loss of interference effects cannot be fully rectified by enhancing antireflection through a double–layer configuration, at least for terrestrial applications.

Intriguingly, replacing Ag with Al as a low–cost alternative as in the design from Figure 5.8.a featuring a thick transparent substrate does not lead to a drastic reduction in absorptance. Figure 5.8.b depicts the AM1.5G–weighted absorptance contour map of the h–BN/MoS_2/sapphire/Al structure yielding and average absorptance of 0.82 for M1 and 0.86 for M2, and Figure 5.8.c shows the absorptance profile of each maximum. The lower differences in this structure in comparison to the designs where the back reflector is placed directly behind the absorber are explained by the weak interference effects and the absence of M0 in the thick transparent substrate configuration.

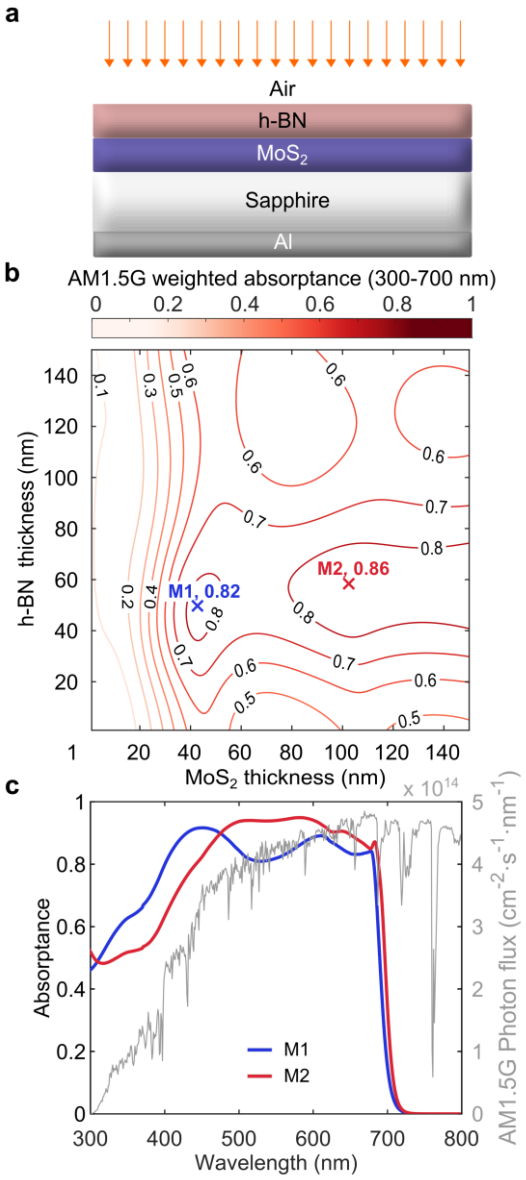

Figure 5.8. (a) Schematic of h–BN/MoS_2/sapphire/Al structure. (b) AM1.5G–weighted absorptance as a function of h–BN and MoS_2 thicknesses of structure in (a). (c) Spectral absorptance for the optimal cases of (b) M1 (blue) and M2 (red).

5.4.4. Absorptance of 1D cavities with double h–BN or ITO

Now we consider a similar structure to the one shown in Figure 5.5.d but placing an intermediate h–BN layer between the MoS_2 absorber and the metallic mirror, transforming the cavity into a quasi–symmetrical cavity as illustrated in Figure 5.9.a. Figure 5.9.b displays the contour map of AM1.5G–weighted absorptance. The thickness of the bottom h–BN layer has been optimised at each point on the map. Within this cavity structure, the M0 aligns with that observed in the h–

BN/MoS_2/Ag cavity, achieving an average absorptance of 0.87 and a maximum photocurrent density of 17.81 mA/cm² for a 10 nm–thick MoS_2 absorber. The respective optimal thicknesses of the h–BN layers in this arrangement are 31 nm (top) and 1 nm (bottom). This structure facilitates the encapsulation of the MoS_2 absorber, enhancing the mitigation of back surface recombination while preserving the amplification of the zeroth–order mode.

If we perform the same calculations for the h–BN/MoS_2/h–BN/Al cavity from Figure 5.9.d lower average absorptance is obtained. The AM1.5G–weighted absorptance contour map from Figure 5.9.e reveals that the presence of an h–BN bottom layer expands the range of thicknesses where absorptances higher than 0.7 can be attained. However, the improvement of the M0 is not as higher as in the case of the Ag back reflector just like in the case of the simple 1D cavity. Figure 5.9.f illustrates the absorptance profiles for each maximum of the h–BN/MoS_2/h–BN/Al cavity. It is observable the difference between the M0 maxima of the Ag and Al cavity as Al shows a poorer absorptance of the wavelength range between 550 and 700 nm.

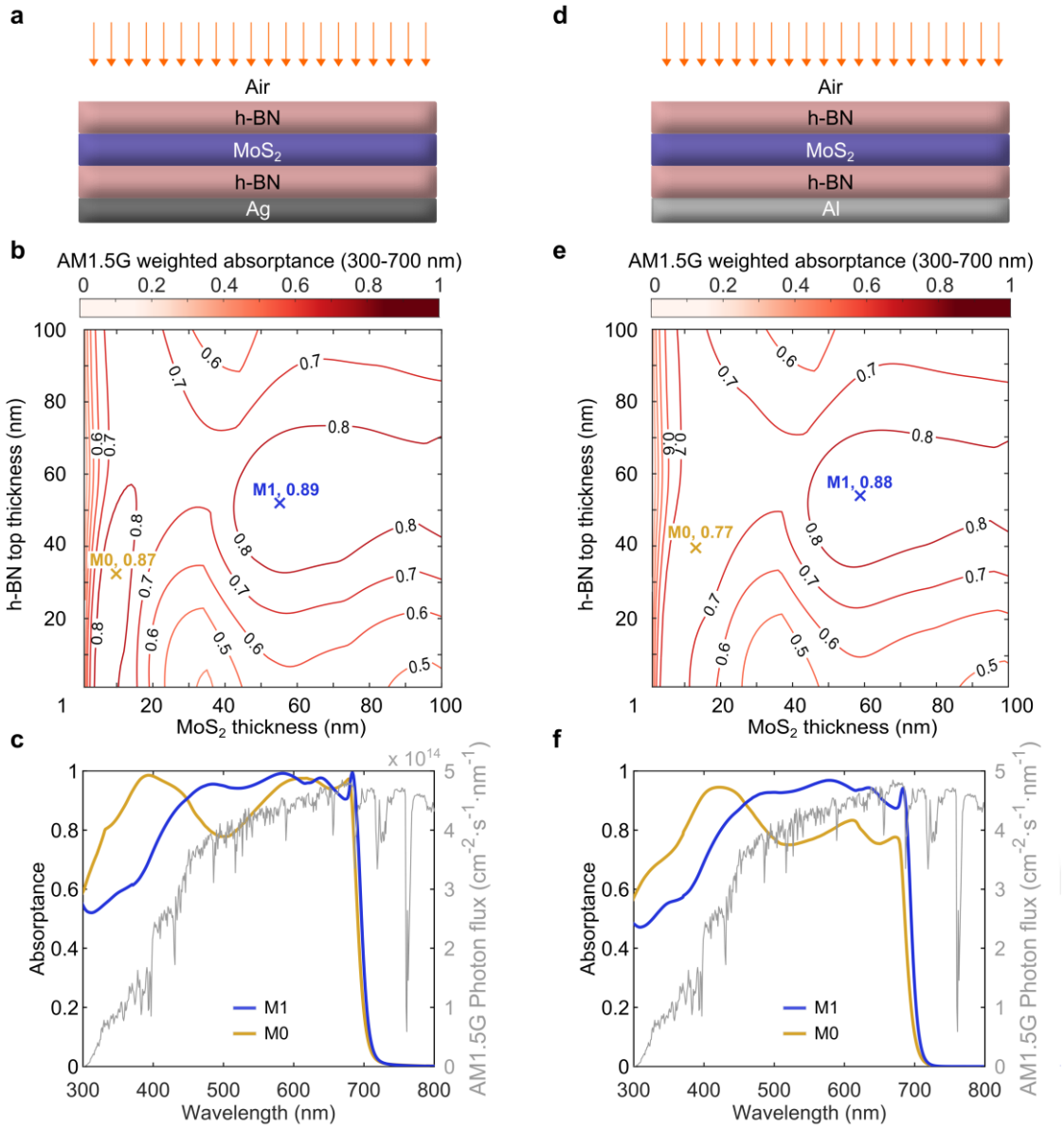

Figure 5.9. (a) Schematic of h–BN/MoS_2/h–BN/Ag structure. (b) AM1.5G–weighted absorptance as a function of h–BN–top layer and MoS_2 thicknesses of structure in (a). The thickness of the h–BN–bottom layer has been optimised at each point in the map. (c) Spectral absorptance for optimal cases of (b) structure M0 (yellow) and M1 (blue). (d) Schematic of h–BN/MoS_2/h–BN/Al structure. (e) AM1.5G–weighted absorptance as a function of h–BN–top layer and MoS_2 thicknesses of structure in (d). The thickness of the h–BN–bottom layer has been optimised at each point in the map. (f) Spectral absorptance for optimal cases of (e) structure M0 (yellow) and M1 (blue). The optimum layer thicknesses and average absorptance for the curves in (c) can be found in Table 5.1.

Furthermore, for non–optimal MoS_2 thicknesses surrounding the M0 maximum, the cavity with a bottom h–BN layer exhibits superior performance. Particularly, very thin MoS_2 absorbers benefit from this architecture. A 4–nm–thick MoS_2 slab achieves an absorptance of 0.81 when embedded in an h–BN sandwich structure,

comprising a 1–nm–thick top layer and a 26–nm–thick bottom layer. In contrast, without a bottom layer, it only reaches an absorptance of 0.59, even with an optimised top h–BN layer of 32 nm. This underscores the significance of the double h–BN cavity structure, especially when operating at the ultrathin limit.

We have illustrated that the introduction of a thick transparent substrate between the MoS_2 absorber and the mirror results in the disappearance of the M0 resonance (Figure 5.7.b). However, the addition of a transparent ultrathin layer that positions the absorber at the nanometric distance of the mirror reinforces the resonance. It does not augment the M0 maxima for an optimum MoS_2 thickness, but it broadens the M0 resonance peak. As shown by Kats et *al.*,[123] when light impinges from a strongly absorbing medium (k of the order of n) onto a lossy metal, the reflection phase shift is not restricted to be π and can, in principle, take any value. This phenomenon allows for phase accumulation at the reflective interface, leading to the resonance M0 at much smaller thicknesses than $\lambda/2n$. These findings indicate that the introduction of a nanometric transparent layer between the absorber and the metal adds a new degree of freedom to modulate the optical path of the interfering waves, thereby optimising absorptance for suboptimal absorber thickness. Janisch et *al.* [155] have shown a comparable effect in a MoS_2 monolayer placed onto an Al substrate, reporting an enhancement in the absorption at λ = 450 nm from 0.23 to 0.67 when a 45–nm–thick Al_2O_3 layer is deposited between the monolayer and the metal.

The inclusion of a bottom h–BN layer in the cavity exerts a noteworthy impact on the M1 interference peak. The maximum absorbance attains 0.89, marking the highest value among the structures examined in this Chapter, accompanied by a maximum AM1.5G photocurrent density of 18.22 mA/cm². Remarkably, M1 is achieved with only 57 nm of MoS_2, when both the top and bottom h–BN layers are 52 nm and 48 nm, respectively. This implies that the MoS_2 thickness at M1 can be reduced by approximately 40% compared to all prior cases while simultaneously enhancing absorptance. Additional calculations for a double h–BN cavity structure with an Al back mirror yield similar results for the M1 resonance but a less favourable performance for the M0 resonance (see Figure 5.9.f).

It is challenging to anticipate, at this point, which of the two maxima, M0 or M1, may be better suited for practical applications. This uncertainty arises because the potential impact on the ultimate device cost of reducing the thickness beyond 100 nm remains unclear. When considering such extreme thinness, the utilisation of semiconductor materials may have minimal influence on the overall cost.

Nonetheless, it is plausible to foresee certain indirect advantages and disadvantages associated with diminishing the thickness to such extreme values. For instance, ultrathin devices with a thickness of approximately 10 nm will necessitate a shorter minority carrier diffusion length compared to a 100–nm–thick device. Therefore, it can be reasonably expected that the fabrication parameters may become more relaxed for extremely thin devices, potentially leading to a reduction in cost. For example, the annealing time and temperature of solution–processed MoS_2 layers [20] could be reduced. Conversely, an extremely thin absorber introduces heightened lateral series resistance and elevates the complexity of establishing electrical contacts during the fabrication process. These factors are likely to result in more costly processing procedures.

Figure 5.10.a presents the last studied configuration. In this case, the MoS_2 occupies the space between an ITO top contact on glass and a substantially thick Ag back contact. This configuration is interesting as it resembles numerous contemporary low–cost photovoltaic devices founded on organic or perovskite absorbers. Once again, it is assumed that the MoS_2 absorber features a pn junction, obviating the need for hole and electron–selective contact layers.

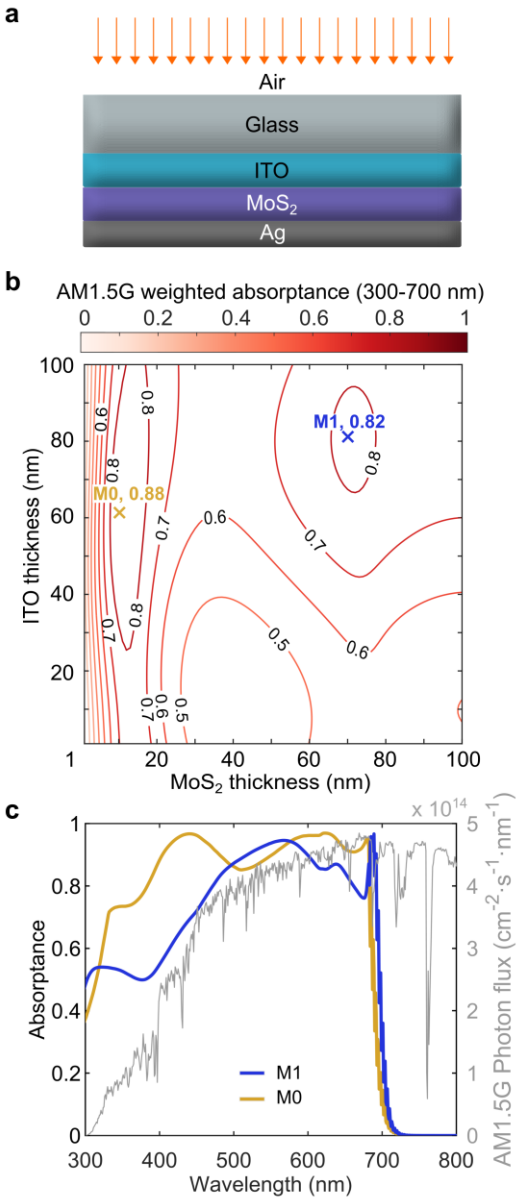

Figure 5.10. (a) Schematic of glass/ITO/MoS_2/Ag structure. (b) AM1.5G–weighted absorptance map as a function of ITO and MoS_2 thicknesses of structures in (a). (c) Spectral absorptance for optimal cases of (b) M0 (yellow) and M1 (blue). The optimised layer thicknesses and average absorptance for the curves in (c) can be found in Table 5.1.

The outcomes are indeed promising, Figure 5.10.b reveal a notable M0 resonance characterised by an average absorptance of 0.88 and a maximum photocurrent density of 18.01 mA/cm² for a MoS_2 thickness of 11 nm. It is noteworthy that in this case, M0 surpasses M1 with a clearly higher absorptance of the blue region of the visible spectrum (see Figure 5.10.c). This value slightly surpasses that attained with the h–BN cavities, although the M1 resonance in this case is relatively weaker at 0.82. However, it is imperative to exercise caution in interpreting these findings,

as the practical surface roughness of the glass and ITO layer will dictate the extent to which the condition of coherence can be upheld.

5.4.5. Effect of lower cost reflectors

Until this point, we have presented different structures that enhance the absorption of MoS_2–based solar cells using different approaches where the absorptance of the MoS_2 is optimised. In this Chapter, both Ag and Al have been studied as back reflectors, and Ag has shown better results, especially at the thinnest structures whose absorptance relies on the characteristics of the M0 resonance. Although Ag provides better results than Al, the question that arises is if it is worth this increase in absorptance when it implies higher fabrication costs and higher supply chain risks.

Ag is widely used in the photovoltaic industry as a conductive material to extract the photogenerated current because of its electrical compatibility with silicon. However, Ag is a relatively expensive material and it is estimated that the current projections of photovoltaic capacity additions may result in Ag shortage in the forthcoming years [156]. Apart from resource depletion (that could lead to price volatility) the usage of Ag poses concerns about its recycling (Ag is not always efficiently recovered and recycled from discarded solar panels, leading to potential waste and lost resources). Aiming to reduce fabrication costs and consumption of Ag, silicon solar cell manufacturers are currently trying to optimise their contact–printing techniques.

Our 1D optical cavity designs for TMDC solar cells work best when they contain an Ag back layer. However, in the context of the current concern for Ag scarcity, these designs may not seem realistic for industrial deployment. In this section we will calculate what is the minimum amount of Ag required to make the 1D optical cavities work and will compare it to the amount of Ag present in state–of–the–art silicon photovoltaic modules.

Taking as reference the consumption of Ag in a conventional monocrystalline silicon solar cells, the dimensions of the Ag fingers that contact the semiconductor are 50 μm–wide and 10 μm–high [157]. The distance between metal fingers is 2 mm, yielding a cross–sectional area of Ag of 2500 μm^2 per linear centimetre of solar cell. In the previous sections of this Chapter, for all the calculations where the use of a rear mirror has been involved, it has been assumed a mirror thickness of 100

nm. This yields a cross–sectional area of 1000 μm² per linear centimetre of Ag required in MoS_2–based structures, 40% of the Ag used in silicon solar cells. This result indicates that the development of MoS_2 solar modules could potentially reduce the amount of Ag used per square meter with respect to the current silicon technology.

A possible way to reduce even further the usage of Ag in MoS_2–based solar cells would be to implement a metallic bilayer as depicted in Figure 5.11.a. Figure 5.11.b shows the AM1.5G–weighted absorptance of three different thicknesses of MoS_2 slabs depending on the thickness of the Ag layer with an additional 1000 nm–thick layer of Al (dotted line) and without it (dashed line). The results indicate that it would be possible to reduce the thickness of Ag even to 5 nm in the case of the 15 nm–thick absorber. Therefore, using a combination of Al and Ag as a back reflector could help to reduce even more the usage of Ag keeping the absorptance levels unaltered. Our calculations predict that it would be theoretically possible to create TMDC–based solar cells with only the 2% of the Ag required by the silicon solar cell industry. (to around 50 nm) without hampering the absorptance of the device.

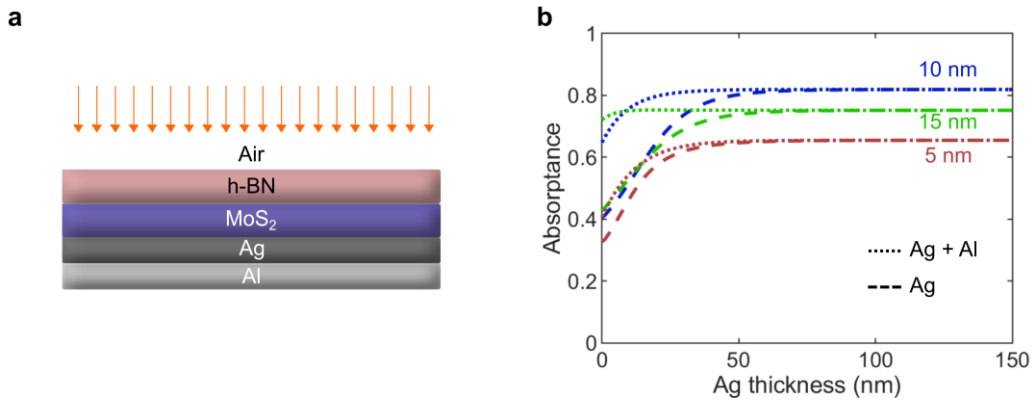

Figure 5.11. (a) Schematic of h–BN/MoS_2/Ag/Al structure. (b) AM1.5G–weighted absorptance for a device with 5, 10 and 15 nm of MoS_2 depending on the thickness of the Ag layer.

5.4.6. Comparison to other thin solar cells

Table 5.2 provides a compilation of experimental results pertaining to various solar cell technologies. In each case, a device representative of the current state–of–the–art for extremely thin absorbers within that specific technology has been selected. Additionally, it incorporates the highest photocurrent density result attained in our study for an ultrathin MoS_2 solar cell, which stands at 18.2 mA/cm² for a 57–

nm–thick absorber. This value surpasses the J_{SC} produced by the flexible ultrathin perovskite device (with a thickness of 350 nm) [158]. Furthermore, it is comparable to the photocurrent density observed in silicon solar cells, despite the significantly narrower band gap of Si and the thickness of the Si absorber being 830 nm, further enhanced by its integration within a nanophotonic structure. The CIGS and CdTe devices exhibit moderately larger short–circuit current densities, associated with absorbers measuring 260 nm and 700 nm in thickness, respectively. Lastly, the GaAs device exhibits a notably higher photocurrent density of 24.6 mA/cm². However, it is essential to acknowledge that in the case of GaAs, the absorber is 205 nm thick, yet the overall epitaxial structure measures 1.5 μm in thickness and incorporates an Ag nanostructured back mirror. This complexity makes direct comparisons with low–cost alternatives challenging.

Although the efficiency of MoS_2–based structures have not been assessed in the present Chapter, the results provided by our model forecast that MoS_2 solar cells could provide equivalent optical performance to already consolidated technologies in the ultrathin regime. Moreover, MoS_2 solar cells could be attained using a thickness unachievable by conventional technologies offering potential material savings and cost reductions.

Table 5.2. Comparison between TMDC–based solar cells and other ultrathin solar cells.

Technology	*Efficiency (%)*	*Short–circuit current density (mA/cm²)*	*Absorber thickness (nm)*
Si [159]	8.6	19.7	830
GaAs [140]	19.9	24.6	205
CIGS [160]	8.1	21.0	360
CdTe [161]	11.2	21.7	700
Perovskite [158]	14	17.3	350
Modelled MoS_2 devices	–	18.2 17.8	57 10

5.5. Summary

The broadband absorption of ultrathin MoS_2–based solar cell structures has been modelled, proposing several optical designs for a prototype of solar cells. The results of the modelled structures show that solar cells based on MoS_2 display optical properties that make this material attractive for energy harvesting applications. These optical properties are tightly related to the Van Hove singularities of TMDCs that enhance optical absorption at wavelengths of the visible range, achieving high optical absorptance even in the few–layer regime.

It has been demonstrated that just by adding an optimised top layer of h–BN (a layered material that is known to improve the surface properties of TMDCs) of 120 nm, a MoS_2 slab supported by a transparent substrate can absorb 84% of the photons contained in the 300–700 nm range of the AM1.5G spectrum. For a 1D cavity design containing a MoS_2 absorber as thin as 10 nm, the average absorption in this spectral range reaches 87%. This is achieved by exploiting the zeroth–order FP resonance and amplifying it in a cavity containing an Ag reflector and one or two layers of h–BN. Such improvement is even more remarkable as h–BN is compatible and easily added to TMDC–based structures.

FP resonance and light coherence are key factors when considering ultrathin devices, as they are the principles on which these devices rely to achieve high absorptance. Hence, when fabricating TMDC–based devices, and especially when the thickness of the absorber is very thin, it is mandatory to ensure the homogeneity and the quality of each layer to maintain light coherence over the photoactive part of the device. Otherwise, the performance of ultrathin devices could be severely affected. These cavities structures require the use of Ag as a back reflector that could in theory increase the fabrication costs of these devices. However, it has been demonstrated that these structures require even less Ag than conventional silicon solar cells and the Ag usage can be reduced even more by combining the use of Ag and Al as reflectors without hampering optical absorptance.

In future solar cell fabrication, a preferred cavity architecture can be chosen from the ones proposed here to match the MoS_2 thickness that optimises the electronic performance of the device. For extremely thin MoS_2 slabs, between 1 and 9 nm thick, the h–BN/MoS_2/h–BN/Ag cavity gives the highest absorption, whereas from 10 nm on, a more compact h–BN/MoS_2/Ag cavity gives similar results. For absorbers ≥ 30 nm an h–BN/MoS_2/sapphire/Ag architecture can also produce very

high absorption. In all three structures, a moderate MoS_2 thickness between 60 and 100 nm can also lead to ~90% average absorptance associated with the first–order FP resonance. Finally, it has been further shown that it is possible to enhance the monochromatic absorption in 10–nm–thick MoS_2 to 0.98. These results demonstrate that the light absorption of ultrathin solar cells based on nanometric TMDC absorbers can compete with established technology just with the aid of very simple 1D cavity structures. Moreover, these promising results are achievable reducing considerably the amount of Ag needed in comparison to conventional silicon solar cells. The lower usage of Ag in TMDC–based devices will offer a competitive advantage in future commercial devices.

Chapter 6

Electrical characterisation of TMDCs

6.1. Introduction

The outstanding properties of TMDCs discovered in the recent years have attracted even more interest in material characterisation. Electrical properties of TMDCs, especially MoS_2, have been the subject of study in numerous recent publications, particularly since the discovery of the properties of these materials in the monolayer regime [15,23]. For instance, the use of MoS_2 in transistors is an example of an application where monolayer devices are gaining momentum, reporting elevated mobilities up to 200 $cm^2/V \cdot s$ in MoS_2–based devices [162].

TMDCs optoelectronic properties allow for a wide range of applications based on devices with nanometric thickness. The reduction of the thickness of the devices to the nanometric scale offers some advantages. Among them, there are potential cost savings related to lower material consumption or the lower recombination rates that could lead to better electric performance in solar cell devices. Nevertheless, the development of such devices encounters challenges because of the extreme semiconductor thinness. Employing such thin material layers renders them highly vulnerable to surface effects caused by any substance in contact with them. Interactions with substrates, metallic contacts, and even the atmosphere can significantly impact device properties and compromise their functionality.

Characterisation of TMDCs electrical properties involves determining parameters such as resistivity and carrier density, as well as understanding how surrounding media affect their properties. Multiple publications analyse the functioning of TMDC–based devices without taking into consideration that their behaviour may be affected by the underlying substrate or the presence of moisture or debris. The environment and the substrates can induce changes in the properties of the TMDCs for example depleting the carrier population of the material. Hence, to perform an accurate characterisation of the materials, it is important to quantify the impact of the surrounding environment on the measured parameters.

This Chapter presents the results of the characterisation of substitutionally doped MoS_2 samples of different thicknesses and different doping levels. The aim is not

only to analyse the properties of MoS_2 but also to quantify how these properties are altered by external factors. Electrical characterisation is done using the Van der Pauw method [54,163]. This method determines the resistivity of lamellae of arbitrary shape which is ideal for samples fabricated by mechanical exfoliation. Combined with a Hall effect characterisation, it also allows the measurement of the carrier concentration and mobility. Apart from the Van der Pauw method, samples are characterised using KPFM, a technique that provides a surface characterisation of a material to map its work function and its topography. We have performed a series of thickness–dependent Van der Pauw measurements that reveal a non–negligible effect of the substrates on the properties of the materials analysed which becomes more influential as the thickness of the devices is lowered. In particular, we have found an n–doping effect of common substrates used in TMDC–based devices along with a strong thickness–dependence of resistivity of MoS_2. On the other hand, KPFM characterisation will show a depletion effect on the TMDC surface exposed to air, which is more noticeable in lightly doped materials. The quantification of the substrate/environment related effects allows us to provide an accurate characterisation of the materials tested.

6.2. Interactions of TMDCs with the environment

In Chapter 3 we already showed an example of how placing one thin lamella of TMDC in direct contact with another material can produce a strong effect on its electrical properties. TMDCs properties may also be affected by the underlying substrates. Charge accumulation has been reported in intrinsic MoS_2 layers inducing n–doping of the material when it is deposited on SiO_2 substrates [164,165]. The effect of substrates is assessed by comparing measurements, such as photoluminescence, between freestanding materials and transferred materials. The n–doping effect induced by SiO_2 substrates has been observed in other TMDC materials as well [166]. Another possible doping agent to be considered is moisture which has been reported to cause an even higher n–doping effect than the substrates [166]. Doping effects could alter the carrier density of the TMDCs, depleting the material and degrading its electrical properties.

Another surface effect, previously discussed in Chapter 3, is the formation of Schottky barriers at the metal/semiconductor interfaces, due to the disparity between the electronic affinity of the semiconductor and the metal WF. In such

cases, it has been reported that the depleted regions related to the Schottky barriers can expand or constrain depending on the voltage applied [167]. As in the case of the pn junction mentioned above, this depletion region appears in all kinds of semiconductors, but in 2D or quasi–2D semiconductors they are especially relevant because their thickness is comparable to that of the semiconductor. Indeed, such behaviour enables the possibility of developing gate–tuneable devices where the position of the bands of the semiconductor can be modified by changing the gate voltage [23,29,91,168]. In some cases, if the material is thin enough, its electrical properties could be completely distorted by the synergic effect of the substrate and the electrical contact. In that case, the experimental measurements will differ considerably from the expected values.

The influence of substrates or the surrounding atmosphere becomes increasingly significant as the TMDC material becomes thinner. Approaching the monolayer regime raises a challenge, as there is only one layer of atoms that can be affected by any material or substance underneath and over the layer. For instance, MoS_2 monolayers have exhibited n–type [15] and p–type [169] behaviour depending on the characteristics of the substrate where the material is placed. Although increasing the thickness reduces the susceptibility of the TMDC to surface effects, this does not mean that they cannot have an impact on the performance of the device as some features depend on the surface properties. For instance, when a slab of p–doped material is placed over a substrate that induces n–doping, the nearest layers to the substrate become depleted while the remaining layers are unaffected. Thus, when analysing the resistivity of the material, the depleted thickness must be considered to accurately assess this property. In this Chapter we will show that by performing Van der Pauw measurements on a series of samples of different thicknesses it is possible to characterise both the bulk electrical properties and the surface effects in TMDCs.

6.3. Van der Pauw method for TMDC–based devices

Conventional measurements of resistivity and Hall coefficient of flat samples involve the use of a standard geometry known as Hall bar (see Figure 6.1.a), which generally consists of a large channel with four perpendicular electrical contacts (two at each side). During the measurement, current flows through the long channel while measuring the potential difference between the other four contacts. From this geometry, it is possible to measure the resistivity of a semiconductor, its carrier population, and its mobility.

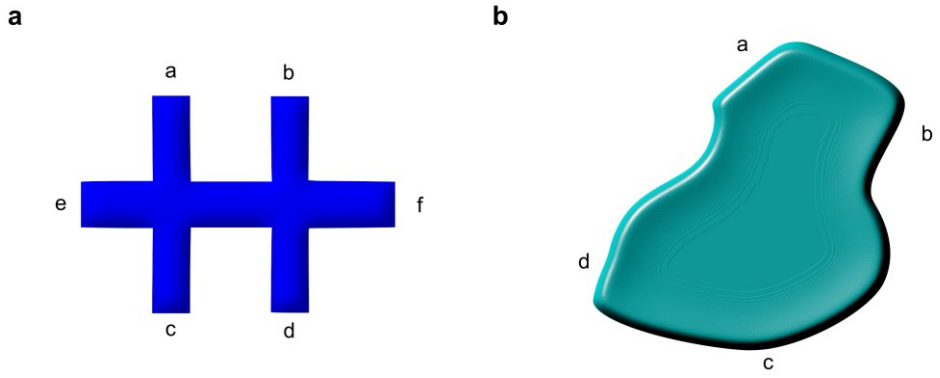

Figure 6.1. (a) Hall bar geometry. (b) Irregular lamella sample.

The resistivity is obtained from the coefficient between the difference of potential between the contacts placed parallel (a to c and b to d) and the injected current in the long channel (e to f). This measurement then is multiplied by the width of the long channel, and the thickness of the sample, and divided by the distance between contacts to determine the resistivity of the material.

Measurement of the carrier population and mobility is related to the Hall effect. The Hall effect is a phenomenon that describes the behaviour of electric charges in the presence of a magnetic field. When charges flow through a material, and there is a perpendicular magnetic field, a measurable voltage difference, known as the Hall voltage, develops across the conductor. This is explained by the Lorentz force which causes a deflection of the charges in a direction that is perpendicular to the plane defined by the original current lines and the magnetic field, creating an accumulation of charges on a side and a depletion on the opposite side. Hall voltage is obtained by measuring the voltage between two contacts that are perpendicular

to the long channel while applying a magnetic field that is perpendicular to the surface of the sample (see Figure 6.1.a).

The utilisation of the Hall bar geometry may not always be feasible. In situations involving devices based on mechanically exfoliated TMDCs, the process of isolating layers leads to irregularly shaped lamellae with areas that barely reach some square micrometres. In certain cases, the Hall bar geometry could potentially be achieved by employing photolithography in conjunction with reactive etching processes to modify the shape of the lamella. However, the unavailability of the Hall bar geometry does not impede the measurement of the resistivity and Hall coefficient of TMDCs.

In 1958, L.J. Van der Pauw proposed a method to measure the resistivity and the Hall coefficient of lamellae with an arbitrary shape as in Figure 6.1.b [54]. The applicability of the method described by Van der Pauw relies on a mathematical theorem. Suppose a semi–infinite lamella as in Figure 6.2 of thickness d where a current I is injected at points M flowing with radial symmetry. The current flow at M generates an electric field that can be calculated using the Ohm's Law:

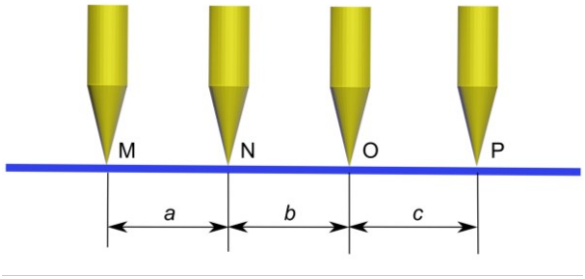

Figure 6.2.Schematic for Van der Pauw demonstration.

$$E = \rho \cdot J \tag{6.1}$$

where ρ is the resistivity of the material and J is the current density on the lamella that can be determined with the following expression:

$$J = \frac{I}{\pi \cdot d \cdot r} \tag{6.2}$$

where r is the distance from the point where current is injected into the material. This electric field generates a potential difference between the points O and P according to the following expression:

$$V_P - V_O = -\int_O^P E \cdot dr \tag{6.3}$$

Substituting Equations (6.1) and (6.2) in (6.3):

$$V_P - V_O = -\int_O^P \frac{\rho \cdot I}{\pi \cdot d \cdot r} \cdot dr \tag{6.4}$$

Solving Equation (6.4), the potential difference is obtained as expression dependent on the distance between the contact points:

$$V_P - V_O = -\frac{\rho \cdot I}{\pi \cdot d} \cdot Ln\left(\frac{a+b+c}{a+b}\right) \tag{6.5}$$

Note that this potential difference is caused only by the current injected at M. Now, it is considered the potential difference caused by the current extracted at N, note that in this case the current has the opposite sign than in the point M:

$$V_P - V_O = \frac{\rho \cdot I}{\pi \cdot d} \cdot Ln\left(\frac{b+c}{b}\right) \tag{6.6}$$

To calculate the overall potential difference, it is applied the superposition principle, and the resistance $R_{MN,OP}$ is obtained by dividing the potential difference with the injected current. This yields the following expression of the resistance:

$$R_{MN,OP} = \frac{\rho}{\pi \cdot d} \cdot Ln\left(\frac{(a+b)\cdot(b+c)}{b\cdot(a+b+c)}\right) \tag{6.7}$$

The same argument can be applied to calculate $R_{NO,PM}$ from the measured potential difference between M and P, when a current is applied between N and O:

$$R_{NO,PM} = \frac{\rho}{\pi \cdot d} \cdot Ln\left(\frac{(a+b)\cdot(b+c)}{a\cdot c}\right) \tag{6.8}$$

As the expressions (6.7) and (6.8) are equivalent:

$$\exp\left(\frac{-\pi \cdot R_{MN.OP} \cdot d}{\rho}\right) + \exp\left(\frac{-\pi \cdot R_{NO.PM} \cdot d}{\rho}\right) = \frac{a\cdot c + b\cdot(a+b+c)}{(a+b)\cdot(b+c)} \tag{6.9}$$

The right term in Equation (6.9) is equal to 1, yielding the equation of Van der Pauw where the only unknown variable is ρ.

This equation applies to the case of a finite lamella. Considering a lamella of material and four electrical contacts as depicted in Figure 6.1.b, we can define $R_{ab,cd}$ as the ohmic resistance measured resulting from dividing the potential difference between a and b by the current that flows from c to d. Then, the resistivity of the material can be extracted from the next expression:

$$\exp\left(\frac{-\pi \cdot R_{ab.cd} \cdot d}{\rho}\right) + \exp\left(\frac{-\pi \cdot R_{bc.da} \cdot d}{\rho}\right) = 1 \tag{6.10}$$

The Hall mobility of the sample is measured by evaluating the change of the resistance $R_{bd,ac}$ when applying a magnetic field perpendicular to the sample. When charges move in a magnetic field, there is a deviation of the current lines related to the Lorentz force which causes an additional potential difference to build up, which is equal to:

$$\Delta V = \frac{\mu_H \cdot B \cdot I \cdot \rho}{d} \tag{6.11}$$

where B is the value of the magnetic field applied. Dividing the voltage increment between the applied current it is obtained the change in the resistivity, so the Hall mobility μ_H can be calculated from:

$$\mu_H = \frac{d \cdot \Delta R_{bd,ac}}{B \cdot \rho} \tag{6.12}$$

The use of the Van der Pauw method implies some prerequisites to obtain reliable measurements. First, the thickness of the sample must be homogeneous. Second, the lamella must be continuous, meaning that it must be free of any hole or discontinuity. Finally, contacts should be sufficiently small and be placed at the borders (note that the mathematical description assumes point contacts). The two first requisites are easily accomplished when considering TMDCs lamellae produced by mechanical exfoliation, but the problem comes when considering the metallic contacts. The size of the TMDCs lamellae obtained by mechanical exfoliation is in the range between 5 to 500 μm^2, so it becomes difficult to develop electrical contacts sufficiently small in comparison to the size of the lamella. This implies that measurements of TMDC samples using the Van der Pauw method will always have an error because of the non–ideal geometry of the contacts.

Errors related to Van der Pauw characterisation can be estimated numerically. The accurate estimation of the errors related to the non–ideal geometries of both contacts and the TMDC layer is beyond the scope of the present Chapter, as it will require an analysis of how the different geometries of samples affect the error calculation. However, we provide a rough estimation of the errors using the equations defined by Van der Pauw for a disk–shaped sample [163]. The error calculation depends on geometric dimensions of the samples, so we use the most conservative dimensions to not underestimate the error and to provide a reliable approximation.

Figure 6.3 shows a schematic of the typical geometry of a TMDC sample employed for Van der Pauw characterisation along with the geometrical parameters utilised in error calculation. We define D as the smaller distance between two contacts of

the sample. For each contact, we define d_1 as the length of the section of the sample edge overlapped with the metallic contact (red–dotted line), and d_2 as the distance between the edge of the sample overlapped on the contact and the tip of the metallic contact (purple–dashed line). These dimensions are then applied in the Van der Pauw equations for error calculation of disk–shaped samples [54], considering three scenarios: a non–punctual contact of length d_2 at the perimeter (Equations 6.13 and 6.16), a non–punctual contact which penetrates a length d_3 into the sample (Equations 6.14 and 6.17), and a punctual contact which is made at a distance d_3 from the sample border (Equations 6.15 and 6.18).

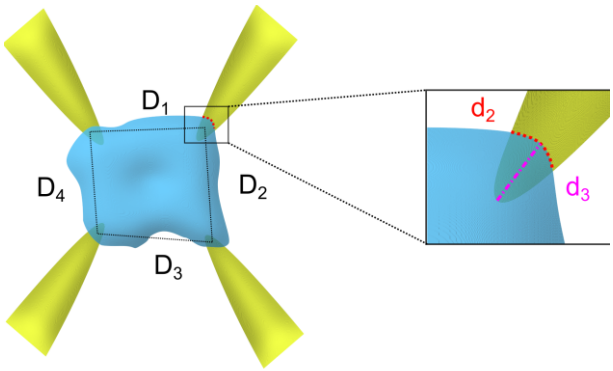

Figure 6.3. Schematic of dimensions definition for calculation of errors in Van der Pauw measurements.

$$\frac{\Delta\rho}{\rho} = \frac{{d_2}^2}{16 \cdot D^2 \cdot \ln(2)} \tag{6.13}$$

$$\frac{\Delta\rho}{\rho} = \frac{{d_3}^2}{4 \cdot D^2 \cdot \ln(2)} \tag{6.14}$$

$$\frac{\Delta\rho}{\rho} = \frac{{d_3}^2}{2 \cdot D^2 \cdot \ln(2)} \tag{6.15}$$

$$\frac{\Delta R_H}{R_H} = \frac{2 \cdot d_2}{\pi^2 \cdot D} \tag{6.16}$$

$$\frac{\Delta R_H}{R_H} = \frac{4 \cdot d_3}{\pi^2 \cdot D} \tag{6.17}$$

$$\frac{\Delta R_H}{R_H} = \frac{2 \cdot d_3}{\pi \cdot D} \tag{6.18}$$

R_H is the Hall coefficient which is obtained from the Equation (6.19):

$$R_H = \frac{\Delta R_{bd,ac} \cdot t}{B} = \frac{1}{n_c \cdot e} \tag{6.19}$$

where t is the thickness of the sample, n_c is the carrier density of the material and e is the charge of the electron.

To determine which expression fits better in the calculation of the error, there are two possible considerations. If the TMDC has a conductance comparable to the metal, it can be assumed that current flow uses the whole area of contact between metal and semiconductor. Hence, the error can be defined approximately as the sum of Equations 6.13 and 6.14 for the resistivity, and Equations 6.16 and 6.17 for the Hall coefficient. By contrast, if the conductance of the semiconductor is very low in comparison to the metal, current flows from the metal into the semiconductor in a region near the tip of the contact, which is a case that approximates Equations 6.15 and 6.18. In the cases presented in this Chapter, both errors are calculated, and the larger value is considered as the error of the sample.

6.4. Kelvin–probe force microscope (KPFM)

KPFM is a non–contact variant of AFM whereby the WF of the surfaces can be measured at atomic and molecular levels. This technique is based on the works about the parallel plate capacitor done by Lord Kelvin in 1898 [170], but it was in 1932 that Zisman was able to measure the contact potential difference of dissimilar metals [56]. The measurement of the Kelvin bias and the topography of the samples can be done simultaneously, as shown primarily by Lü et *al.* in 1999 [55]. During the measurement, the KPFM tip and the sample are electrically connected, generating an electron flux between the sample and tip that equalises their Fermi levels [56]. As a result of this, a V_{CPD} appears between the sample and the tip. This V_{CPD} is equal to the difference between the WF of the tip, which is known, and the surface potential of the sample. Figure 6.4.a shows the schematic of the KPFM setup. The tip is placed at a cantilever which oscillates over the sample. An infrared (IR) light beam impinges the cantilever which moves in the vertical direction because of the interaction forces between the tip and the surface. These displacements deflect the IR beam and are detected by a position–sensitive diode which provides an electrical signal to measure the topography of the sample.

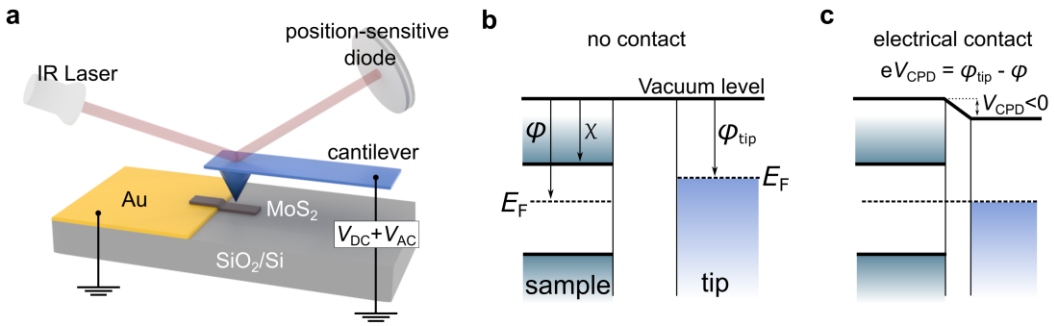

Figure 6.4. (a) Schematic of the experimental setup used in KPFM measurements. Band diagram of sample and tip: (b) when they are far away and (c) during KPFM measurement.

KPFM can be used to probe the band offsets of TMDC heterojunctions [57,58,171–173]. These measurements were based on the measurement of the surface potential of the materials forming a heterojunction. Surface potential provides an indirect measurement of the Fermi level of materials, thus the $V_{built-in}$ of a pn junction can be estimated. Besides, the values of the surface potential change depending on the illumination conditions, reducing the potential difference between the materials forming the pn junction and giving an insight into how the device J–V characteristics would perform [57,58]. However, the experimental values of the surface potential difference are underestimated in comparison to the V_{OC} recorded [171]. This is explained by the fact that KPFM measures surface properties, and therefore those properties may be affected by the presence of contaminators or adsorbates [174]. Despite this limitation, KPFM is a powerful tool for surface characterisation and it can be used to calculate the width of the depletion region in lateral junctions [171,173].

6.5. Results

In this Chapter, we measure samples made of substitutionally–doped and pristine MoS_2 with different doping levels using the Van der Pauw method. Samples are obtained by mechanical exfoliation of fresh crystals and deposited on pre–patterned metal contacts using a PDMS stamp. Measured crystals comes from different providers. P+–MoS_2, p–MoS_2 B and n–MoS_2 were growth by CVT by Prof. Der–Yuh Lin from Changua University of Education, while p–MoS_2 A and pristine MoS_2 are from HQ Graphene. Two substrates are used for the samples, SiO_2/Si, and sapphire (Al_2O_3). For each sample, the measurement error related to the non–ideality of the sample geometry is calculated using the Equations from Section 6.3. The measurement of the samples is done with the equipment described in Chapter 2. For each measurement, the value of the magnetic field is the same (0.55 T) achieved with a neodymium alloy magnet.

6.5.1. Conductance of depletion effect of the substrates on MoS_2

Figure 6.5.a shows a micrograph which is a representative example of the devices that we have used for Van der Pauw characterisation of MoS_2. Which metal is used for the contacts depends on the doping type in the MoS_2. We use Cr for n–doped MoS_2, Pt for p–MoS_2, and Au for pristine MoS_2. The election of the metal for the contacts is done according to the metal WF to obtain ohmic contacts following the Schottky–Mott rule. Several samples of two different p–doped MoS_2 (A and B) are characterised using the Van der Pauw method. Henceforth, the material with the higher dopant level will be referred to as p^+–MoS_2 and those with a lower dopant level as p–MoS_2 A (from HQ Graphene) and p–MoS_2 B (from Der–Yuh Lin). Figure 6.5.b and Figure 6.5.c present results for different samples of the p^+–MoS_2 and p–MoS_2 A, respectively. The graphs show how in both cases the sheet conductance of MoS_2 increases proportionally to the thickness of the devices. This is explained by the increase of material section available to transport the current. Hence, the thicker the slab is, the easier the current flows through it. The resistivity of the material can be then extracted from the inverse of the slope in Figure 6.5.b and Figure 6.5.c.

The layered structure of TMDCs may induce an elevated anisotropy of the properties, as each layer is bonded by Van der Waals forces, while atoms in the same plane are joined by covalent bonds. The different nature of in–plane and out–of–plane cohesive forces may result in poorer out–of–plane electrical properties.

However, the measurements in Figure 6.5.b(c) fit well to a straight line, which means that the current tends to flow through the whole section of the device and therefore, the difference between in–plane and out–of–plane conductance does not have a significant effect in samples with these doping levels, thickness range and aspect ratio.

From the van de Pauw measurements we conclude that the heavily doped p^+–MoS_2 material has a low resistivity of $3.7 \cdot 10^{-3}$ $\Omega \cdot cm$, which correspond to a carrier concentration of $1.4 \cdot 10^{20}$ cm^{-3} and a carrier mobility of 12 $cm^2/(V \cdot s)$. Such a high value means that this semiconductor is degenerately doped. This is consistent with a non–significant carrier depleted thickness at the surfaces in this material (the straight line in Figure 6.5.b virtually crosses the (0,0) point). In fact, when approaching the few–layer regime, it is still possible to obtain non–depleted samples with a clear ohmic behaviour. For instance, it has been possible to measure ohmic *I*–*V* characteristics in a sample with a thickness of 5 nm. Note that the slope of the sheet conductance is not affected by the substrate on which the sample is placed because it depends only on bulk properties.

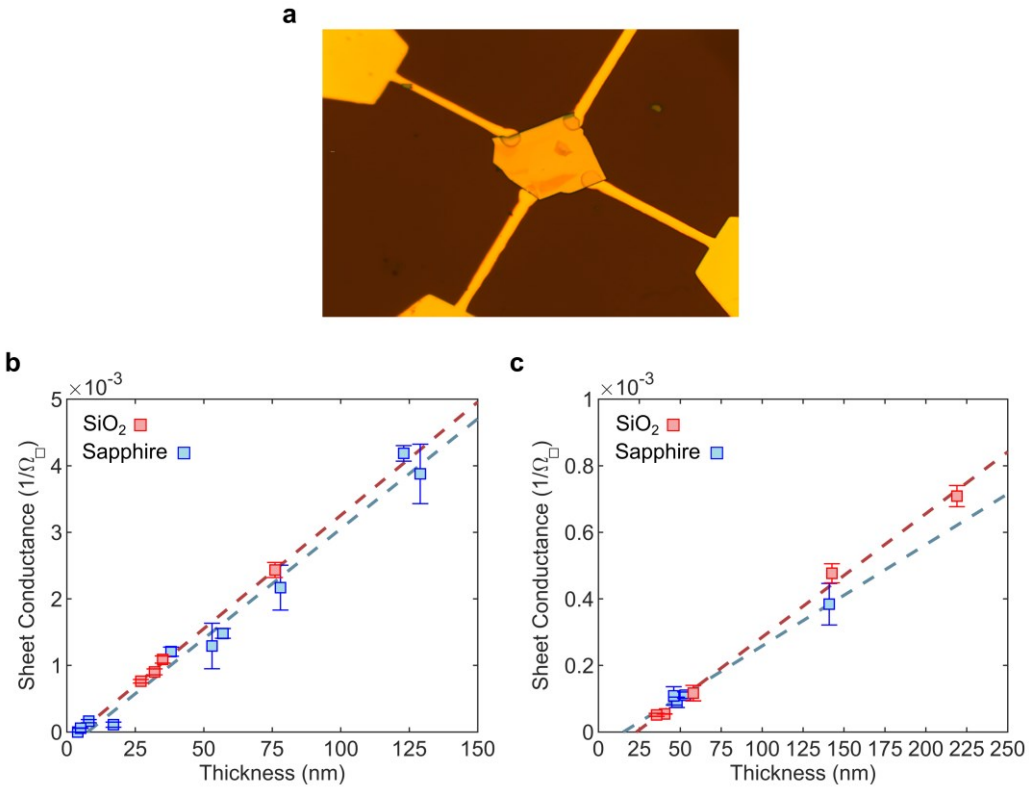

Figure 6.5. (a) Micrograph of a device used for Van der Pauw characterisation. (b) Sheet conductance of p+–MoS_2. (c) Sheet conductance of p–MoS_2 A.

Figure 6.5.c shows the sheet conductance of the material p–MoS_2 A which has according to our measurements a higher resistivity ($2.6 \cdot 10^{-2}$ Ω·cm) and lower doping level ($4.7 \cdot 10^{18}$ cm^{-3}) than p^+–MoS_2. The carrier mobility in this case is 53 $cm^2/(V \cdot s)$, higher than for the p^+–MoS_2, which is consistent with a lower doping level. In this case, we identify a thickness value of depleted material, around 23 nm for the case of SiO_2 and 17 nm for the case of sapphire. A more accurate determination of the depleted thickness would require more data. Nonetheless, this result proves that p–MoS_2 A may be affected by a depletion effect that could be attributable to the environment and underlying substrate. When samples thinner than the thinnest point presented in Figure 6.5.c have been measured, non–ohmic curves have been obtained. This result has an important impact as it demonstrates that thickness–related measurements, such as carrier population, cannot be done considering the real thickness of the sample, but the effective thickness of it. This effective thickness would be the real thickness of the slab minus the depleted thickness.

Depletion effects can result in the malfunction of a pn junction made of ultrathin TMDCs. The depletion effect in TMDCs is observable when measuring the *I*–*V* curve of a slab. Figure 6.6 shows two samples made of material p–MoS_2 B with a measured carrier population of $1.2 \cdot 10^{18}$ cm^{-3} on a SiO_2/Si substrate. According to Figure 6.5.c, layers with a thickness lower than 23 nm will be depleted for a material with a higher doping level. We have measured each layer thickness through AFM in Figure 6.6.c(d) obtaining for the device from Figure 6.6.a 34 nm and for the device from Figure 6.6.b 19 nm. Figure 6.6.e illustrates the *I*–*V* curve of each device. Although the thickness difference between both samples is not very large, the difference in conductivity is quite significant. This difference can only be explained by the whole depletion of the device from Figure 6.6.b while the device from Figure 6.6.a is thicker enough to maintain an effective section of the slab not depleted.

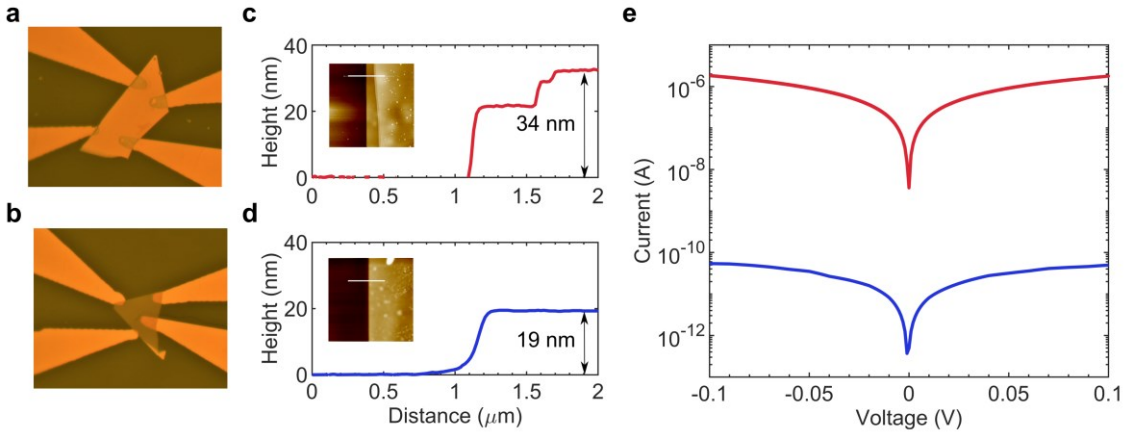

Figure 6.6. (a–b) p–MoS_2 B layer deposited on Pt contacts on a SiO_2/Si substrate. (c–d) AFM characterisation. (e) *I–V* characteristics of both devices.

The depletion of thin TMDC slabs compromises, for instance, the reliability of the ultrathin devices presented in Chapter 5, whose performance relies on the amplification of the zeroth–order interference maxima, and which is only achievable in the range of a few tens of nanometers. Then special care is needed when combining the absorber and substrate. For instance, avoiding the contact between p–doped materials and n–dopant substrates, or using clean, neutral insulant materials as h–BN [165].

Measurement of p–MoS_2 specimens revealed a n–doping surface effect induced by the substrates in the case of SiO_2 and sapphire which is congruent with the results presented in the literature [164,165]. Figure 6.7 shows the sheet conductance on n–doped MoS_2 slabs on a sapphire substrate. In this case, the measured sheet conductance values do not seem to increase too much despite increasing the thickness. This weak dependency is related to the low measured doping level, which is $3.60 \cdot 10^{17}$ cm^{-3} a resistivity of $3.9 \cdot 10^{-1}$ $\Omega \cdot cm$ and a mobility of 75 $cm^2/(V \cdot s)$. We cannot find an extrapolation that provides an estimation of the depleted thickness suggesting that the substrate is not inducing a depletion effect on the semiconductor which would be explained by the expected n–doping effect of the substrate observed in p–MoS_2 samples. Contrarily, in this case we could estimate an approximate charge accumulation caused by the substrate of $5 \cdot 10^{-6}$ $\Omega_{\square}^{-1}$. This result is consistent with the depletion effect observed in the p–MoS_2.

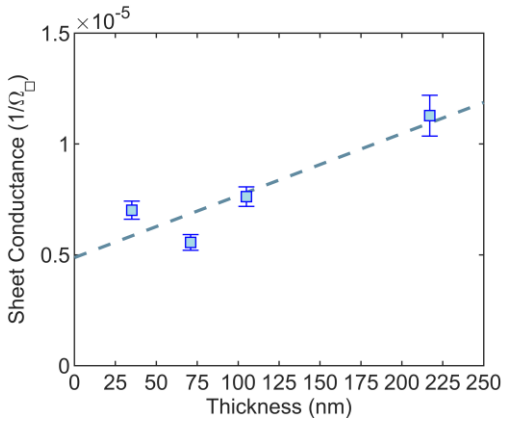

Figure 6.7. The sheet conductance of n–MoS_2 samples deposited on sapphire substrates.

6.5.2. Carrier density and mobility measurements

Table 6.1 shows the value of the parameters measured by the method of Van der Pauw for different types of MoS_2. Figure 6.8 shows the results of the Van der Pauw characterisation. Carrier density is calculated considering the effective thickness of the sample, in other words, the non–depleted or active thickness of the MoS_2 slab. It must be mentioned that measurements of pristine MoS_2 may not be very reliable, as the *I–V* characteristic of the device does not show completely ohmic contacts in either of the contacts. The values of the p–MoS_2 were successfully measured, making it possible to determine the depleted thickness of the material. In the case of the n–MoS_2 we found a charge accumulation caused by the substrate. The measurements reveal the n–doping effect of the substrates used which is in agreement with the findings published in the literature [164,165].

The measured values of carrier density of the samples differs from the nominal doping values. In the case of p–MoS_2 and n–MoS_2 from prof Der–Yuh Lin, the nominal doping values for these materials were $3.0 \cdot 10^{19}$ and $7.5 \cdot 10^{18}$ cm^{-3} for p– and n– material respectively [75]. The variance between the nominal and experimental values stems from the intricacies inherent in CV) fabrication process. Parameters such as temperature and gas concentration dictate the efficacy of semiconductor doping by influencing the quantity of atoms capable of effectively doping the material. Furthermore, improper positioning of dopant atoms may impede charge flow, thereby diminishing semiconductor mobility. Consequently, it can be inferred that the process of Fe–doping to achieve n–type MoS_2 is inherently more challenging than Nb–doping.

Table 6.1. Summary of the Van der Pauw characterisation for different materials.

Material	*Carrier density (cm^{-3})*	*Mobility ($cm^2/(V\,s)$)*	*Resistivity (Ω cm)*
p+–MoS_2	$(1.4 \pm 0.5) \times 10^{20}$	12 ± 4	$(3.7 \pm 0.5) \times 10^{-3}$
p–MoS_2 A	$(4.7 \pm 1.5) \times 10^{18}$	53 ± 18	$(2.6 \pm 0.2) \times 10^{-2}$
p–MoS_2 B	$(1.2 \pm 0.3) \times 10^{18}$	95 ± 36	$(5.4 \pm 0.6) \times 10^{-2}$
n–MoS_2	$(3.6 \pm 0.9) \times 10^{17}$	75 ± 18	$(3.9 \pm 0.2) \times 10^{-1}$
pristine MoS_2	$(5.5 \pm 1.5) \times 10^{16}$	93 ± 25	1.21 ± 0.06

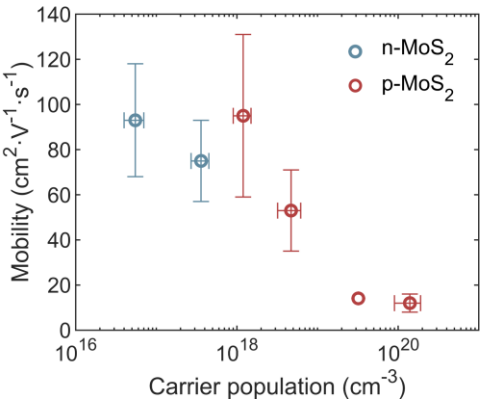

Figure 6.8. Carrier density and mobility of tested materials. The point without error bars was extracted from Ref. [41].

6.5.3. KPFM measurements of MoS_2

Until this point, we have discussed the possible effect that the underlying substrate could have on the electrical characteristics of TMDCs. Nevertheless, the resultant depletion of a material can stems from the concomitant impact of the substrate, the surrounding atmosphere or the presence of contamination on the surface of the material. We evaluate the effect on the surface of MoS_2 through KPFM characterisation. For these measurements, material slabs must be sufficiently thick in order to prevent the alteration of the measurement induced by the substrate. KPFM measurement output can be used to determine the WF of the semiconductors at their surface. It can be extracted from the measurement of V_{CPD} and the WF value for Au. The WF values for Au reported in the literature vary from 4.9 to 5.5 eV [24,115,175]. We have perform the fabrication of the samples, and the KPFM characterisation was done by Mónica Luna and Micaela Rodríguez Peña from Instituto de Micro y Nanotecnología CSIC.

To characterise the materials, we have deposited MoS_2 flakes with a PPC stamp onto a Si/SiO_2 substrate with pre–patterned Au contacts. From each flake is obtained a topographical image (Figure 6.9.a, c) and the surface V_{CPD} (Figure 6.9.b, d). The materials characterised were pristine MoS_2, p–MoS_2 B and n–MoS_2. Figure 6.9.e shows the statistical distribution of the measurements for each material. The measurements are referenced to the V_{CPD} of Au. Comparing the difference between

the mean value for p–MoS_2 and n–MoS_2, we obtain that a pn junction made of these materials has a $V_{built-in}$ of 0.86 V. This value limits the V_{OC} under illumination conditions. However, we will see in Chapter 7 that this value is underestimated.

As explained in Section 6.4, KPFM measurements provide information about the material surface, not its bulk properties. The underestimated value of the $V_{built-in}$ as well as the dispersion of the measurements of the surface potential recorded may be explained by the alteration of the material lattice at the surface [174]. Moreover, it has been argued that surface defects along with defect–chemistry–related variations in the local stoichiometry of the MoS_2 can modify the properties of MoS_2 [176]. This effect is observable in the different V_{CPD} values recorded in Figure 6.9.b. Traps in the oxide layer or defects at the oxide–semiconductor interface may cause the difference between the observed and expected values. Some references develop models to eliminate the effect of the surface and extract bulk doping values from the KPFM measurements like Baumgart et *al.* [177].

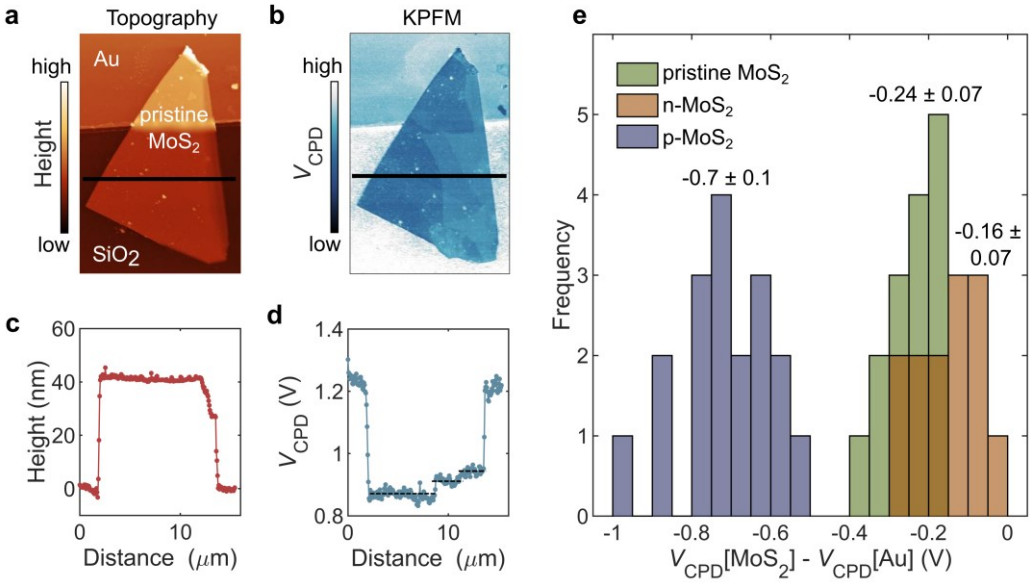

Figure 6.9. (a) Topographic image of pristine MoS_2 flake, and (b) V_{CPD} image taken simultaneously. (c) Topographic profile and (d) V_{CPD} profile along the black lines marked respectively in (a) and (b). Each profile has been averaged over ten neighbouring lines. (e) Histogram of V_{CPD} measured on different samples of p–doped, pristine, and n–doped MoS_2 (all values are referenced to the V_{CPD} of Au measured on the same sample). As it is observed in (b) different regions of a sample can present a different V_{CPD}, and in that case, all the values have been included in the histogram.

6.6 Summary

TMDCs electrical characteristics have been measured using the Van der Pauw method. Van der Pauw method has been proven to be a strong tool for the characterisation of TMDC–based devices. Nevertheless, there are still some points that need to be improved as the accurate calculation of geometrical errors. When performing Van der Pauw characterisation, it is necessary to consider how the substrate and the environment can affect the properties of the material and perform the specific correction to determine the parameters of each sample. We have conducted thickness–variable measurements to discern between bulk and surface effects on the electrical properties of TMDCs. The determination of parameters becomes more challenging as the carrier density of the semiconductor is lower because of the low conductance and the difficulties in obtaining ohmic contacts with the materials.

Samples made of MoS_2 with different doping levels have been characterised by identifying an n–doping effect of substrates such as SiO_2 and sapphire which is concordant with the effects reported in the literature. The depleted thickness of a p–doped MoS_2 has been estimated by the extrapolation of its sheet conductance dependence on the thickness of the material. The value of the depleted thickness depends on the carrier density of the material and can reach values around 20 nm for a carrier density of $4.7 \cdot 10^{18}$ cm^{-3}. Such value may suppose a non–negligible fraction of the total volume of an ultrathin slab, and it can have an important impact on the properties of the devices. We estimate that sapphire substrates induce a n–doping effect with a charge accumulation of $5 \cdot 10^{-6}$ $\Omega_{\square}^{-1}$.

KPFM of MoS_2 samples revealed the surface properties of the materials and why the performance of the devices can be strongly affected by the presence of defects, and discontinuities on the surface. Although KPFM does not accurately measure bulk properties, it may be useful to understand problems involving surface effects such as the obtention of ohmic contacts to MoS_2. The differences between the V_{CPD} from the n–MoS_2 and the p–MoS_2 is lower than the expected values discernible from the V_{OC} obtained in experimental pn junctions. This is explained by the band bending of semiconductor related to surface defects.

The results of this Chapter reveal the importance of substrate selection and device architecture. The electrical properties of ultrathin slabs could be severely hampered if materials are not correctly protected from the effects of the surrounding environment. These results must be considered when TMDC–based electronic devices approach the few–layer regime, as their properties may be no longer governed by the intrinsic characteristics of the material.

Chapter 7

MoS_2 solar cell with Fermi–level pinning free contacts and anti–reflection BN layer

7.1. Introduction

In Chapter 3, we have presented a proof–of–concept device based on a MoS_2 homojunction made of substitutionally doped crystals. This device yielded an extraordinarily high V_{OC} of 1.02 V for an indirect band gap material (1.3 eV), one of the highest values reported in Van der Waals solar cells [75]. However, light–energy conversion in that device was limited by two issues. On the one hand, the bad quality of the metallic contacts resulted in the presence of photoactive Schottky contacts that drain the photovoltage produced by the pn junction and reduce its FF. On the other hand, the high refractive index of MoS_2 causes elevated reflection losses, limiting the photogenerated current. In Chapter 5, we have demonstrated numerically that the absorptance of a MoS_2 slab is approximately limited to 50 % over the visible spectrum [132]. As a result of both factors, the PCE of MoS_2–based solar cells could not reach a sufficiently high value to be used in commercial applications.

The presence of Schottky contacts between metal and semiconductor is one of the main problems related to TMDC–based solar cells [178], and the obtention of ohmic contacts to these devices is not an easy task. Many factors can affect the properties of the materials forming the pn junction and the processes of contact fabrication to TMDC have not been completely developed. The key factors to obtain ohmic contacts to these materials are related to the selection of suitable metals depending on the semiconductor and how metal and semiconductor are contacted. This requires establishing new strategies to fabricate the metallic contacts as the methods employed in conventional devices may not be appropriate to TMDCs.

Apart from the issues related to the contacts in TMDC–based solar cells, the energy conversion is limited by the optical properties of the materials. Despite its large absorption coefficient, the high values of the refractive index of TMDCs lead to considerable optical losses because of reflection, [129,133] hence, an ARL is required. The use of ARL raises questions about the ideal material for this purpose.

TMDC–based devices are mostly incompatible with common ARL materials as they are deposited using methods that endanger the integrity of the absorbers. Therefore, new deposition methods and new materials for ARL are necessary to improve the light absorption of TMDC devices without hampering their electrical properties.

In this Chapter, we present a MoS_2 solar cell in which the problems beforementioned have been minimised by using a new fabrication process for the contacts and by improving light absorption. As device A146 from Chapter 3, this device is made of substitutionally Fe–doped (n–type) MoS_2 combined with substitutionally Nb–doped (p–type) MoS_2 to form a 120 nm–thick pn junction. To achieve low resistance ohmic contacts, we have developed a photolithography process based on the use of two resist that yields flawless and spotless contact surfaces made of metals with suitable WF (Cr for the n–contact and Pt for the p–contact), and we have used a heavily doped p–MoS_2 as a p–contact layer.

We have encapsulated the device using an h–BN layer, added to the structure to minimise reflection at the front surface and to improve the electrical properties of the device. The device exhibits (3.8 ± 0.2)% PCE and 57.1% FF under the AM1.5G spectrum; it also presents a maximum V_{OC} of 0.87 V under concentrated light and a maximum EQE of 0.98 at the excitonic peak. The results of this Chapter are condensed in [179]. We also highlight the importance of controlling the doping in the bulk and at the interfaces to take a new step in the maturity of this emerging solar cell technology. This PCE value may seem small if compared to PCE values of more mature technologies. However, is one of the highest values reported to this date for TMDC–based solar cells and sets the first step towards higher efficiencies.

7.2. Previous attempts at MoS_2 solar cells

Solar cells based on transition metal dichalcogenides have attracted significant attention as ultrathin and flexible alternatives to conventional III–V photovoltaic devices, but they suffer from low efficiencies. The most common approach towards these cells is based on heterostructures combining different TMDCs [23,25,27,28,34,93,180–182]. Among them, the most studied structure is MoS_2/WSe_2 heterostructure. When creating MoS_2/WSe_2 heterostructures, the use of monolayers is appealing as they show a larger band gap and hence a better electronic configuration. However, light–energy conversion of the monolayer–

based devices is limited because of the lack of light absorption. The first reported MoS_2/WSe_2 monolayer heterojunction barely reaches a J_{SC} of 1 mA/cm² [27]. Furchi et *al.* reported a MoS_2–WSe_2 heterostructure based on monolayers with reasonable electric parameters but reduced PCE (0.2%) under a halogen lamp and EQE (1.5%) [28]. The limited absorption of monolayer devices suggests that multilayer TMDCs are more suitable for energy harvesting applications despite their lower band gap. Thus, multilayer MoS_2/WSe_2 heterostructures display lower V_{OC} but larger J_{SC} and EQE than monolayer structures. One example is the device presented by Ahn et *al.*, which showed a V_{OC} of 0.32 V but a PCE of approximately 0.66% under a led lamp of 620 nm and 41.4 mW/cm² [34]. One of the best results for a MoS_2/WSe_2 heterostructure reported in the literature was presented by Wong et *al.* with a vertical heterostructure achieving a PCE of 3.4 % under a monochromatic laser illumination of 633 nm and 740 mW/cm² [25].

The natural n–type behaviour of MoS_2 [88] is one of the reasons to use them in heterostructures, but it also can be used to create devices based on Schottky junctions. The photovoltaic behaviour and the use of MoS_2 in Schottky–based solar cells were firstly reported in the '80s by Fortin and Sears [183]. They were able to realise a MoS_2/Cu Schottky junction measured under a white light illumination of 60 mW/cm² whose efficiency did not surpass 1% at 120 K. More recently, Shanmugam et *al.* fabricated Schottky–barrier solar cells based on multilayer MoS_2, using ITO and Au contacts [184]. The working principle of these devices relies on the presence of an ohmic contact of the intrinsic MoS_2 to an ITO layer and a Schottky contact to Au. MoS_2 slabs were grown by CVD and then transferred into the contacts. PCE values reported were 0.7 % for a 110 nm–thick device and 1.8 % for a 200 nm–thick device. Apart from MoS_2, other TMDCs have been successfully used in Schottky–based devices. One example is the WSe_2, where PCE has been increased by surface passivation [96], and that to this date has one of the highest values of PCE for TMDC–based devices (5.1%) [35].

In the emerging technology of TMDC–based solar cells, the research on electric doping is allowing to advance from heterojunction–based devices [23,25,27,28,34,93,180–182] where the maximum V_{OC} is determined by the natural band offset between two pristine materials, to homojunctions where V_{OC} is determined by the bandgap of the material [29,31,75,112,113,185]. For example, in bulk MoS_2/WSe_2 heterojunctions, the band offset is ~ 0.4 eV (~ 0.7 eV in monolayer heterojunctions), whereas the $V_{built-in}$ in a sufficiently doped homojunction can approach the bandgap energy (E_G), which is 1.3 eV in bulk MoS_2

(1.9 eV for monolayers) [15,24,110]. An example of MoS_2 homojunction is obtained by plasma–induced doping. In this process, the semiconductor is exposed to a plasma of O_2, SF_6, or CHF_3 to induce a p–doping effect on the material. As plasma only affects the surface, not the whole material is doped, creating a pn junction. Wi et *al.* [31] explored the use of different plasmas to create MoS_2 homojunctions. Once the pn junction was already achieved, it was transferred onto an Au substrate that contacts the p–doped surface, while the non–treated surface is contacted with ITO. This structure achieved a PCE of 2.8% under the illumination of the AM1.5G standard spectrum. The PCE obtained in plasma–doped MoS_2 homojunctions depends on the thickness of the semiconductor, obtaining optimal results at 120 nm, while thicker devices have a lower PCE. The results reported by Wi are obtained not only because of the doping effect of plasma but also because of the good quality of contacts. The interface between ITO and untreated n–type MoS_2 is expected to be a quasi–ohmic contact, because the WF of intrinsic MoS_2 (Φ_n-MoS_2 ~ 4.6 eV) is very close to that of ITO (Φ_{ITO} ~ 4.4–4.5 eV) [186], and the WF of CHF_3 plasma–treated (or p–doped) MoS_2 layers is estimated to be $\Phi_{p\text{-}MoS2}$~5.3 eV that is close to the WF of Au (Φ_{Au} ~ 5.1 eV). Therefore, an Au/p–doped MoS_2 interface would be likely a quasi–ohmic contact with a very shallow Schottky barrier.

Substitutional doping of MoS_2 [41] enables the possibility of obtaining doped crystals that could be later combined in homojunctions using mechanical exfoliation. The photovoltaic effect of substitutionally doped MoS_2 homojunctions has been demonstrated, but the reported devices showed a pinned V_{OC} that does not surpass 0.6 V even with increasing illumination, and a poor PCE around 0.5% [112,113]. The reasons that explain such performance are the adverse effects caused by the Schottky barriers at the metal/semiconductor interface that were described in Chapter 3, and the excessive reflectance of MoS_2 described in Chapter 5. In Chapter 3, we have demonstrated the potential of the MoS_2 pn junctions achieving a V_{OC} of 1.02 V under an equivalent illumination of 40 suns, and we modelled how the defective contacts jeopardised the performance of the device [75]. However, it was not possible to obtain ohmic contacts and light absorption was limited. By solving these problems, it would be possible to boost the performance of MoS_2–based solar cells.

7.3. Band alignment of doped MoS_2/metal contacts

The achievement of ohmic contacts to semiconductors is a key step to obtain a perfectly functioning solar cell. In Chapter 3, we have explained the problems related to the realisation of ohmic contacts to TMDCs. The presence of the CNL at the interface metal/semiconductor results in a strong pinning factor and the impossibility of realisation of ohmic contacts to MoS_2 by simply approaching the Schottky–Mott rule [101–103,178,187]. Nonetheless, TMDCs are characterised by clean and almost free–defect surfaces whereupon they should not show such a strong pinning factor. There are different theories about the possible origin of CNL in TMDCs but there is no consensus about this problem. The possible origin of the Fermi–level pinning in TMDCs may be related to the presence of defects caused by the fabrication process of the devices.

Recently, it has been demonstrated the possibility of eliminating the Fermi–level pinning in MoS_2–based structures by optimising the process whereby MoS_2 and metal are contacted [95]. Thermal deposition processes where metal is evaporated directly onto semiconductors may alter the surfaces of semiconductors, breaking the continuity of the material lattice. This could not be problematic in conventional semiconductors as their surface is a defect in itself, but in the case of TMDCs, thermal deposition would damage severely the semiconductor. Liu et *al.* [95] achieved contacts between MoS_2 and different metals that accomplish the Schottky–Mott rule by transferring the metal contacts onto the semiconductor using a PDMS stamp. This was tested by measuring the Schottky–barrier height for different devices and compared to the Schottky–barrier height achieved when metal is evaporated directly onto the semiconductor. Indeed, Liu measured a pinning factor of 0.1 when metals are evaporated directly onto the semiconductors, a result that has been reported in previous publications [101–103,187]. The findings of Liu demonstrate that the metal/TMDC contacts can follow the Schottky–Mott rule by transferring the metal contacts onto clean semiconductor surfaces. Hence, following an equivalent fabrication process would enable the obtention of ohmic contacts by the selection of an adequate metal for contacting both, n–type and p–type material by their WF. We proposed a fabrication process that has been introduced in Chapter 2, transferring the semiconductors to pre–patterned metal contacts. These contacts have been deposited using a double resist photolithography process that will be explained in Subsection 7.5.2.

7.4. Result and Discussion

7.4.1. Improving metal/MoS_2 contacts

In Chapter 3, we have presented a MoS_2 homojunction with a V_{OC} of 1.02 V (device A146) that surpasses the values reported in the literature for devices with similar characteristics [75]. Nonetheless, the PCE of device A146 was limited by the nature of the metal/semiconductor contacts. The presence of Schottky photoactive diodes at the interface between metal and semiconductor increases the resistance of the device and hampers the FF while reducing the V_{OC}. These Schottky diodes may be related to the difference between the WF of the metal and the band structure of the semiconductor, but as we mentioned in Chapter 6, Section 6.3, and explained in Chapter 3, it is mainly caused by the presence of a CNL at the interface of the contact. The origin of the CNL can be associated with the rupture of the layers at the surface of the semiconductor during the metal deposition process. As a result of the presence of the CNL, it would be impossible to reach an ohmic contact by only matching the metal WF with the position of the conduction band for n–type semiconductors or the position of the valence band for p–type semiconductors.

Figure 7.1 depicts the difference between the metal deposition onto a MoS_2 layer and the transference of the MoS_2 layer to an already–formed metal pad. In Figure 7.1.a, which presents the process of contact fabrication of device A146 from Chapter 3, metal atoms projected onto the MoS_2 surface during the thermal deposition process break the lattice of the semiconductor generating defects. These defects will be responsible for the CNL that pins the Fermi level and causes the formation of Schottky contacts independently of the pair metal/semiconductor selected. By contrast, the scheme from Figure 7.1.b is analogous to the process described by Liu et *al.* [95] that prevents the formation of defects at the interface between metal and semiconductor but in this case, it is the semiconductor that is transferred instead of the metal. This process provides contacts that approach the Schottky–Mott rule solving the Fermi–level pinning issue. Moreover, our method is simpler and more economic than the metal–transfer process proposed by Liu because the exfoliation and transference of semiconductors is more straightforward than the fabrication and transference of the metal contacts.

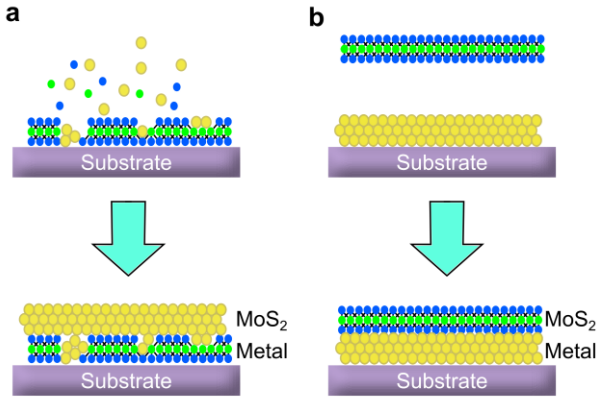

Figure 7.1. Deposition process of metal and MoS_2. (a) Metal deposition onto previously placed MoS_2. (b) MoS_2 was transferred onto a pre–patterned metal pad.

In device A146 presented in Chapter 3, metal contacts were directly evaporated onto the semiconductor as they would block the incident light and theoretically prevent photogeneration at the metal/semiconductor interface. However, this praxis does not eliminate the Schottky contact, and we proved that the photoactive zone of the Schottky contact expands beyond the area of contact between metal and semiconductor [167]. Hence, the only feasible structure for a well–functioning MoS_2 device must have the semiconductors deposited on pre–patterned metals. The process of fabrication of these pre–patterned contacts is not trivial as the shape and morphology of the contacts can conditionate the characteristics of the metal/semiconductor interface. The feasibility of the method presented in Figure 7.1.b relies on the obtention of smooth and clean surfaces of metal contacts where the semiconductors can bend and fold adapting to the shape of the metal pad.

The previous process of contact fabrication was based on the use of a negative photoresist, AZ1512 HS. This resit was spun over the surface of the substrate at 3000 rpm and baked at 100ºC for two minutes. After the baking, the substrate was exposed selectively to ultraviolet light to create a specific pattern over the photoresist. The exposed photoresist was removed with a developer (AZ 400K), the metal was deposited, and the remaining photoresist was cleaned off with organic solvents (acetone). Although this method is suitable for conventional solar cells, it produces defects that are critical for TMDC–based devices. During the deposition process, the metal accumulates at the edges of the pads resulting in defective borders as shown in Figure 7.2.a. The semiconductor flakes cannot adapt to the steep edges of the metallic pads (see Figure 7.2.b), and they encounter the metal only at a few points generating hot spots. These hot spots degrade the device under

the current flow because of the current concentration and semiconductors can eventually burn.

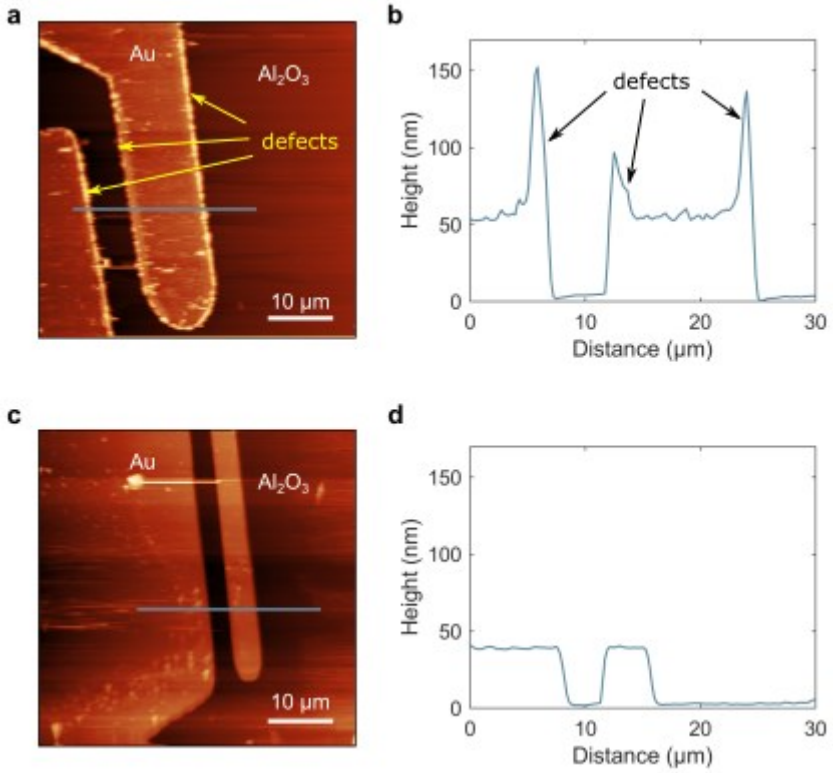

Figure 7.2. AFM characterisation comparing single layer resist and bilayer resist fabrication processes. (a) Topography scan on pre–patterned contacts fabricated with single–layer resist. (b) Profile along the blue line shown in (a). (c) Topography scan on pre–patterned contacts fabricated with bilayer resist. (d) Profile along the blue line shown in (c).

The accumulation of leftover material caused by photolithography is avoided by adding a step to the fabrication process which consists of using a second photoresist. The previously mentioned A1512HS is used as the top resist and the LOR7B is the bottom one. LOR7B is spun and baked at 180ºC for three minutes and after that, AZ1512HS is spun and baked at 100ºC for two minutes. LOR7B resist shows more sensitivity to the light so that, when both are exposed, it is affected in a larger area developing an undercut once both resists are removed with a developer. This undercut allows the metal to deposit under the top photoresist without sticking to the borders of the pattern (Figure 7.2.c). The flawless result of the double photoresist process is appreciable when comparing the AFM profiles of two metallic contacts created either by simple photolithography or by bilayer photolithography presented in Figure 7.2.b and d respectively. In Figure 7.2.b the

accumulation of metal at the border results in steep edges, which force the flakes to bend excessively to follow the morphology of the pads. Note that the size of the edges in this case is between 40 and 100 nm which is indeed the range of thicknesses of the semiconductors used in the devices. In Figure 7.2.d the bilayer resist process produces smoother borders that allow the semiconductor to perfectly stick to the metal surface.

Finally, the choice of metals to contact each material depends on the band gap of the semiconductor. For the case of MoS_2, Pt, with a WF of 5.7 eV [115], is a good choice for contacting the p–type semiconductor (valence band maximum at 5.6 eV). On the other hand, the n–material requires a low WF metal (the conduction band minimum is at 4.2 eV). Cr is a good choice for this contact with a WF of 4.5 eV [115]. Note that, to ensure an ohmic contact with Cr, it is important to prevent oxidation of the metal, so once the contact has been fabricated, it must be stored under a protective atmosphere of N_2.

7.4.2. Improving light–absorption

MoS_2 shows an extraordinarily high absorption coefficient in comparison to the materials used in conventional solar cells. Such high absorption is related to its layered structure that yields strong absorption peaks caused by Van Hove singularities which was explained in Chapter 5 [15,23,188]. However, the light absorption of the devices is limited because of the high reflectance caused by the high refractive index of MoS_2. This involves the use of anti–reflective coatings essential to achieve at least the same absorbance levels as conventional technologies. Coatings used in conventional solar cells are not suitable for TMDC devices as deposition processes may introduce defects and doping at the interfaces altering severely the semiconductor lattice [103]. Different materials have been proposed to reduce light reflection in these devices. Al_2O_3 has been used as ARL, increasing the EQE by up to 30% under monochromatic illumination (410 nm) in WSe_2 devices [144,189]. H–BN is another possible candidate because of its insulating properties, refraction index values [151] and feasibility to be implemented in devices with the same techniques used to build TMDCs ultrathin solar cells [44,190]. In Chapter 5 we have discussed that, without an ARL, the average absorbance of any MoS_2–based structure would be limited to 50% except in case of enhanced interference in plasmonic structures [32]. This problem is nonetheless overcome adding a h–BN top layer that could theoretically increase the average absorbance to values over 80% of the incident light [132].

The effect of h–BN used as ARL has been tested experimentally. Figure 7.3.a–b illustrates the device A210 before and after the deposition of an h–BN top layer. Figure 7.3.c shows the effect of adding an h–BN in the J–V curves of A210. There is an increase in the value of the J_{SC} from 323 mA/cm^2 to 478 mA/cm^2 under a broadband illumination of 4 W/cm^2. This means an improvement of 48.5% in photogeneration by only adding the ARL. The thickness of the h–BN and MoS_2 layers was measured with AFM. The results were 30 nm for the h–BN layer, 45 nm for the p–MoS_2, and 60 nm for the n–MoS_2. According to the absorptance maps presented in Chapter 5, a 105 nm–thick slab of MoS_2 would absorb approximately 47% of the AM1.5G solar spectrum. When adding a 30 nm–thick layer of h–BN, this weighted absorptance would increase to 68% being 44.7% higher than the case of not covered MoS_2. Note that in the case of device A210, the illumination source is a halogen lamp with an equivalent illumination to 4 W/cm^2 whose spectra is different from the AM1.5G used to evaluate the absorptance in Chapter 5. Nevertheless, the increase in photogenerated current observed experimentally is consistent with the expected increase in absorptance predicted by the optical model.

The J–V curve shown in Figure 7.3.c indicates that the addition of h–BN not only increases the photogenerated current but also increases the V_{OC}. This improvement is explained by the effect of surface passivation of the h–BN that reduces surface carrier recombination. Although TMDCs have inert, self–passivated surfaces [42], in real conditions their surfaces host a moderate density of defects [108]. This effect of surface passivation and V_{OC} improvement has been reported in other TMDC–based solar cells showing similar improvements in the values of the V_{OC} [96].

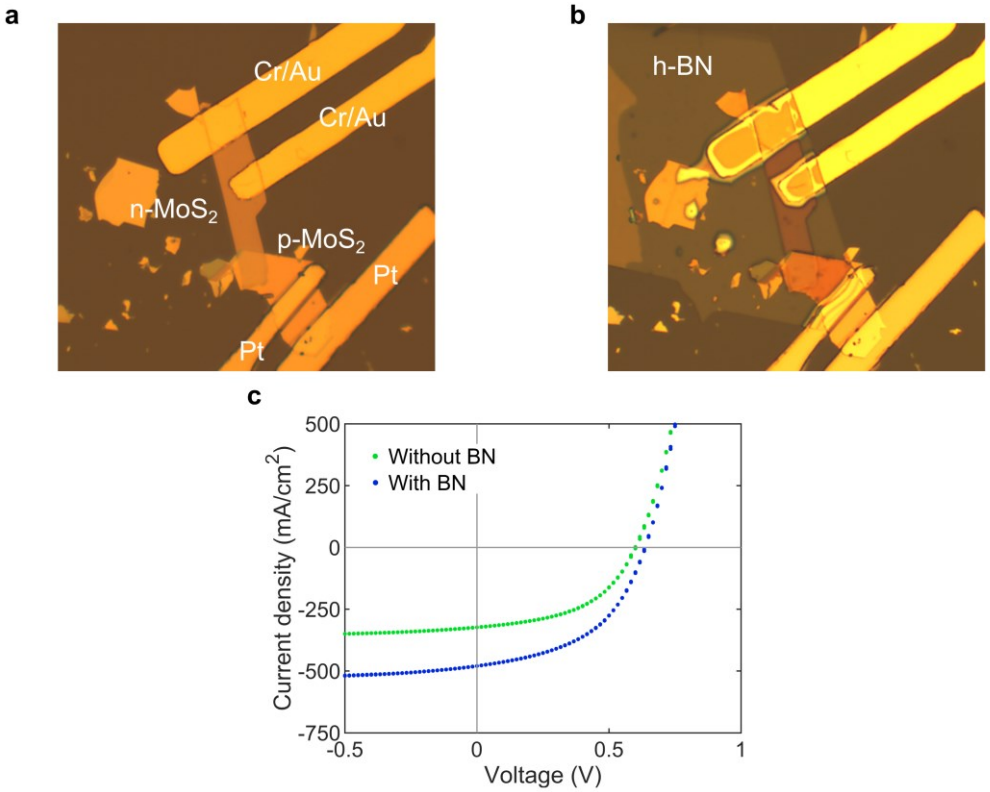

Figure 7.3. Micrographs of the MoS_2 homojunction device A210 before (left) and after (right) depositing the h–BN flake. (b) *J–V* curves of device A210 under broadband light with 4 W/cm² power density, before (green) and after (blue) placing the h–BN.

7.4.3. MoS_2 solar cell with a 3.82% PCE

The champion device of the MoS_2–based Van der Waals device is A339, and it follows the scheme depicted in Figure 7.4.a. A339 consists of three flakes of MoS_2 with different doping levels, n–MoS_2 (Fe doped), p–MoS_2 (Nb–doped), and p^+–MoS_2 (doped as p–MoS_2 but with a larger concentration). There are two reasons to add the p^+–MoS_2 layer. Firstly, the doping level of the p–MoS_2 of this device is $6.6 \cdot 10^{17}$ cm^{-3} and it does not guarantee an ohmic hole contact as we observed in previous attempts of the MoS_2 homojunctions. Secondly, the use of a heavily doped contact material ($1.4 \cdot 10^{20}$ cm^{-3}) improves contact resistance. The electrodes are pads made of Pt (p–contact) and Cr (n–contact) which have been pre–deposited on a SiO_2 (290 nm)/Si substrate by sputtering and thermal evaporation, respectively. The surface of the metal pads is homogeneous and spotless thanks to the double photolithography process explained in Subsection 7.4.1. The whole device is encapsulated using a larger slab of h–BN. Every crystal has been exfoliated from bulk samples. The h–BN is commercial (from HQ Graphene) and the MoS_2 has

been synthesised by the CVT process by [41]. Device A339 is fabricated using a PPC–covered silicone stamp following the process described in Chapter 2, Subsection 2.2.3. The pn junction is formed by the overlap of the p and n crystals whose junction area is 51 ± 2 μm². Figure 7.4.a illustrates a schematic of the structure of device A339.

Figure 7.4.b shows the *J*–*V* characteristics of device A339 under the AM1.5G spectrum produced by our Xe–lamp solar simulator with irradiance adjusted to 100 mW/cm² using a calibrated silicon solar cell. We measure a J_{SC} of 15.8 mA/cm², the V_{OC} is 0.43 V and the FF 57.1%. The PCE at the maximum power point at one–sun illumination is (3.8 ± 0.2)%, where the uncertainty mostly comes from the accuracy in the determination of the area. This value is one of the highest values reported to date in Van der Waals structures. Under the same illumination conditions, the highest PCE reported to date for a MoS_2 homojunction was 2.8% by Wi et *al.* [31].

Figure 7.4.c shows the topography image taken by AFM, and the thickness of the different crystals can be extracted from the AFM profiles from Figure 7.4.d. They are 67 ± 4 and 64 ± 4 nm for the p and n crystals, respectively, which means that the total thickness for light absorption is 131 ± 4 nm. For the case of a ~ 130 nm–thick MoS_2 structure, the required thickness to minimise reflection is between 50 and 70 nm according to the modelled structures in Chapter 5. The thickness of the BN layer in this device is 62 ± 4 nm which fits into the calculated range.

The *J*–*V* curves of device A339 were modelled using the Shockley equation of the diode but introducing an internal series resistance and considering the effects of the SCR in the current generation. The internal series resistance induces a voltage drop even in short–circuit conditions and it is associated with the current flow within the MoS_2 layers. The effect of the SCR is considered in this model because the width of the SCR is in the same range of thicknesses of the semiconductor layers. The intricacies of the model will be elucidated in Subsection 7.4.4. Figure 7.4.e illustrates the dark *J*–*V* curve of device A339 alongside *J*–*V* curves acquired under broadband illumination with power densities corresponding to 12 and 20 suns. An increment in V_{OC} is discernible with escalating illumination intensity. Each curve is denoted by open circles representing the experimental data, while the solid line denotes the fit derived from the circuital model. Table 7.1 compiles the values of the modelled parameters pertaining to device A339.

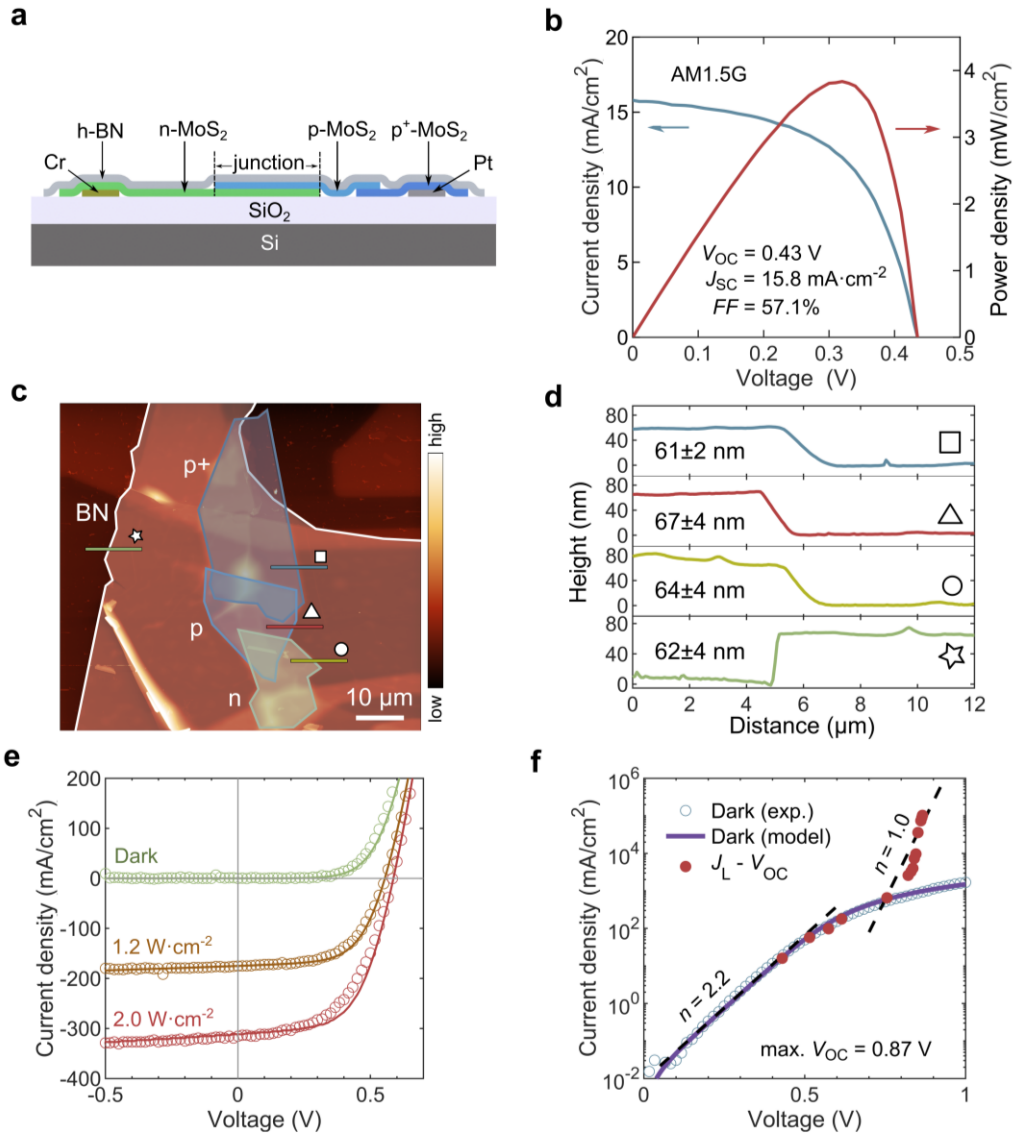

Figure 7.4. (a) Cross–section schematic of the MoS_2 homojunction solar cell A339. (b) *J*–*V* characteristic measured under illumination with the AM1.5G solar spectrum (100 mW/cm²) using a solar simulator (blue line) and corresponding power density–voltage curve (red line). (c) Topographic AFM image of device A339; the different flakes have been coloured for clarity. The horizontal lines mark the locations at which height profiles have been measured. (d) Height profiles of MoS_2 and BN flakes extracted from (c). (e) *J*–*V* curves were taken in the dark and under two different irradiances with a broadband source (halogen lamp); open circles are experimental data and solid lines fittings to the theoretical model. (f) Dark *J*–*V* curve plotted in logarithmic scale; open circles are experimental data, and the solid line is modelled data. The solid red circles are experimental (J_L – V_{OC}) pairs measured under different illumination power densities using a laser set–up from Subsection 2.3.1 (wavelength 525 nm). The two dashed black lines mark the slope in the regions with ideality factors 2.2 and 1.

Table 7.1. Parameters of device A339 extracted from the fitting of the dark *J–V* curve and illumination curves plotted in Figure 7.4.e and Figure 7.4.f. We have used a circuital model that combines an exponential expression for the pn junction (with ideality factor n and inverse saturation current density J_0) with resistive components. The latter includes a parallel resistance (R_p) and two series resistances: one associated with the current flow in the junction area ($R_{s,int}$) and the second one associated with the current flow to the metal contacts ($R_{s,ext}$).

n_2	2.2
J_{02} (mA/cm^2)	$8.9 \cdot 10^{-3}$
R_p ($\Omega \cdot$cm^2)	$3.1 \cdot 10^4$
$R_{s,int}$ ($\Omega \cdot$cm^2)	0.09
$R_{s,ext}$ ($\Omega \cdot$cm^2)	0.12

The FF of the *J–V* curves depicted in Figure 7.4.b surpasses the values previously reported for van der Waals solar cells [23,31,184,191]. However, it remains low in comparison to established photovoltaic technologies like silicon (FF ~ 80%) or GaAs (FF > 80 %) solar cells. Various factors contribute to this FF disparity. Initially, the curves exhibit an apparent decline in R_p (observable as a higher slope at $V = 0$ V) with escalating illumination density. This decrement cannot be elucidated by an increase in the leakage current. Rather, the apparent decline of the R_p correlates with width of the SCR. The variation of the SCR width alters the photocarrier collection efficiency as the voltage rises due to diminishing the SCR width. This results in a voltage–dependent photogenerated current (J_L) which is characteristic in solar cells where the SCR significantly contributes to the photocurrent generation, such as certain chalcopyrite devices and p–i–n solar cells [192].

The FF is also diminished because of the series resistance of 0.21 $\Omega \cdot$cm^2. Although this value is better than for instance the value reported by Wong et *al.* [25] or the value reported in device A146 from Chapter 3, it still markedly impacts the FF. Our theoretical modeling suggests that reducing series resistance to zero could enhance FF under one–sun illumination from 57% to 66%. A third factor influencing the FF and V_{OC} of the device is the nature and extent of recombination. The ideality factor is $n = 2.2$ point the nonradiative recombination as the dominant mechanism probably situated in the pn junction SCR and/or at the junction perimeter. Van der Waals structures typically report ideality factors between 1.3 and 2.6 [25,28,31,34,96,180] while some references report values as

large as $n = 6.5$ [92]. Intriguingly, lower values have been documented for devices where a junction is induced on a MoS_2 monolayer or bilayer via gate doping ($n = 1.9$) [21] or chemical surface doping ($n = 1.6$) [171]. The minimum n value has been achieved in a Schottky–based device ($n = 1.1$) [95]. Despite potential ideality factor improvement avenues, the reported value represents a significant enhancement compared to device A146 presented in Chapter 3.

In Figure 7.4.f dark J–V curve of A339 is plotted in logarithmic scale to ease the visualisation of the $n \sim 2$ slope. The experimental data are represented together with the theoretical fit, using the parameters from Table 7.1. The red circles plotted in the same graph are (J_L, V_{OC}) pairs measured for different illumination densities using a laser (wavelength 525 nm) measured in the concentrated light setup explained in Chapter 3. Under high illumination conditions, the V_{OC} increases up to 0.87 V. Most publications concerning van der Waals junctions that encompass the V_{OC} evolution under high illumination densities show V_{OC} pinning [25,34,182]. Pinning can ensue from insufficient band offset at the junction, especially in heterojunction devices, or from the presence of photoactive Schottky diodes located at metal/semiconductor interfaces, as they counteract the photovoltage of the pn junction [75]. The high V_{OC} of device A339 compared to E_G (1.29 eV) corroborates that substitutional doping is a viable strategy for generating a large band offset (or $V_{built-in}$). Its measurement with light impacting the entire chip attests to contact quality and notably, the absence of photoactive Schottky barriers, which are associated with the Fermi–level pinning effect explicated in Chapter 3.

In conventional solar cells that follow the superposition principle, a plot of J_L as a function of V_{OC} facilitates visualisation of device recombination current measured from the (J_L, V_{OC}) pairs that follow the Shockley equation. Consequently, the $J_L - V_{OC}$ plot is equivalent to a dark curve plot in which the effect of R_s has been eliminated. Although device A339 does not strictly follow the superposition principle, Figure 7.4.f. illustrates certain general trends. Within the high voltage region of the slope of the recombination current density, an ideality factor $n \sim 1$ is identifiable.

7.4.4. *J–V* curves modelling

To model the *J–V* curves of A339 we use the equivalent circuit derived from the circuit of Shockley depicted in Figure 7.5. The circuit contains the following components: J_L is the photogenerated current density, J_d is the recombined current density (modeled by Shockley's exponential expression), $R_{s,int}$ and $R_{s,ext}$ represent the series resistance associated with the lateral flow of current inside the MoS_2 crystals and to the MoS_2/metal contacts, respectively, and R_p is the parallel resistance of the device. Applying Kirchhoff's laws, the circuit is solved numerically. In this equivalent circuit the $R_{s,int}$ induces a voltage drop even when the extracted current is zero. Therefore, the V_{OC} depends on $R_{s,int}$ and the device does not follow strictly the superposition principle of solar cells.

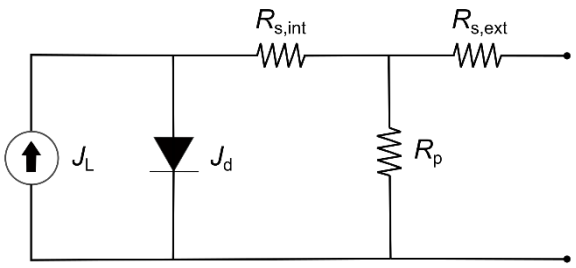

Figure 7.5. Equivalent electric circuit.

The modelling of the *J–V* curves of A339 must include additional features apart from the $R_{s,int}$. As discussed in Chapter 3, Section 3.5.2, in ultrathin solar cells the SCR occupies a significant portion of the total absorbing thickness. This will affect the value of the photogenerated current density because it will depend on the SCR width and hence a function of the applied voltage, $J_L(V)$. This produces a slope in the illumination *J–V* curves that resembles the effect of a low R_p, but in this case, the slope depends on the illumination density. Then, to calculate the J_L it is necessary to determine the thickness of the SCR. The SCR width (w_{SCR}) is the sum of the thicknesses of the depleted regions in the p and n sides using the total depletion approximation which is valid for abrupt junctions and non–degenerate materials [193]:

$$w_{SCR}(V) = x_P(V) + x_n(V) \tag{7.1}$$

These values are calculated as

$$x_n(V) = \sqrt{\frac{2\varepsilon\varepsilon_0 V_j(V) N_A}{eN_D(N_D+N_A)}} \tag{7.2}$$

$$x_p(V) = \sqrt{\frac{2\varepsilon\varepsilon_0 V_j(V) N_D}{eN_A(N_D+N_A)}} \tag{7.3}$$

where ε is the relative dielectric constant of MoS_2, ε_0 is the dielectric constant of vacuum and e is the electron charge. $V_j\,(V)$ is the height of the potential barrier of the pn junction, which depends on the applied bias and the $V_{built-in}$ of the pn junction:

$$V_j(V) = V_{built-in} - V \tag{7.4}$$

The $V_{built-in}$ mathematical expression was introduced in Equation (3.8) from Chapter 3. We consider no recombination at the SCR, so carriers photogenerated there contribute to J_L with a collection efficiency of 100%, while carriers photogenerated in the neutral zones contribute with a lower collection efficiency [192]. The J_L decreases because of the shrinking of the w_{SCR} as V increases. This effect is considered implementing a simple linear model, in which J_L is expressed by:

$$J_L(V) = J_{abs} \cdot (x_{SCR}(V) + (1 - x_{SCR}(V) \cdot CF) \tag{7.5}$$

where CF is the collection efficiency in the neutral zones, which is supposed to be a constant, neither dependent on V nor the illumination intensity. J_{abs} is the current density photogenerated at $V = 0$:

$$J_{abs} = J_{SC}^{exp} / (x_{SCR}(0) + (1 - x_{SCR}(0) \cdot CF) \tag{7.6}$$

where x_{SCR} is defined as the fraction of the total device thickness occupied by the SCR.

When evaluating the recombination current of the device, it is also considered the impact of the changes in the width of the SCR, using the following expression:

$$J_{02}(V) = J_{02} \cdot \frac{w_{scr}(V)}{w_{scr}(0)} \tag{7.7}$$

Figure 7.6.a shows the experimental J–V curves of A339 (open circles) and the fit (solid lines) obtained with the electrical model considering the $J_L(V)$ dependency, and Figure 7.6.b shows a fit with the same circuital model not considering the $J_L(V)$ dependency (assuming constant J_L). The effect is small, but it has an appreciable impact on the FF which is larger when increasing the illumination.

The J–V curves under these illumination levels are dominated by the $n \sim 2$ component. Hence, we can calculate the effect of $w_{SCR}(V)$ on the reverse saturation current density J_{02}. If J_{02} depends according to Equation (7.7) on w_{SCR}, the hypothesis that the origin of the $n \sim 2$ component is the SCR will be reinforced (and not, for instance, the perimeter of the junction). However, when implementing a $J_{02} = J_{02}(V)$ function in the model, the obtained fits (Figure 7.6.c) are practically indistinguishable from those in Figure 7.6.a. Therefore, we cannot determine the origin of the recombination processes in the device. Finally, Figure 7.6.d shows how the J–V would be in absence of series resistance. Improving the series resistance enhances the FF and PCE. However, the main improvement of the FF will come out from the obtention of ideality factors that approach the value of the already developed solar cell technologies.

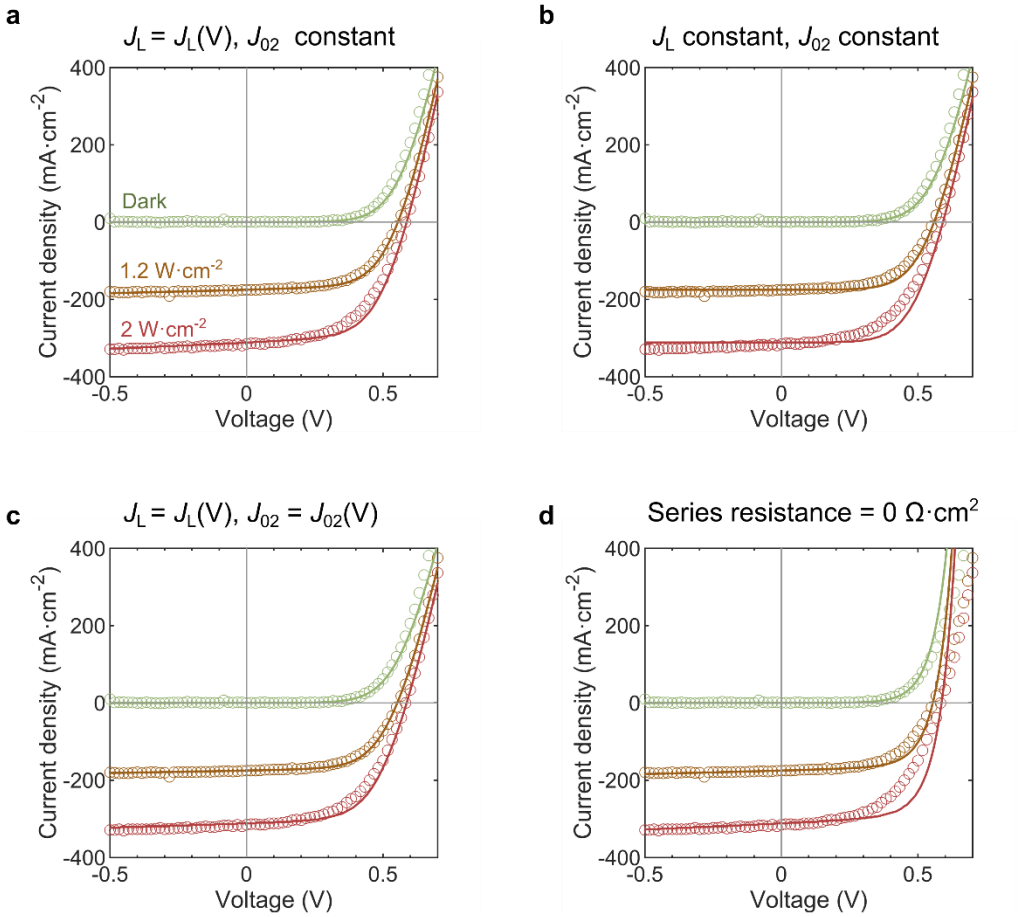

Figure 7.6. (a) Modelling of A339 J–V curves with J_{02} constant and J_L dependent on voltage. (b) Modelling with J_{02} and J_L constant. (c) Modelling with J_{02} and J_L dependent on voltage. (d) Modelling with J_{02} constant, J_L dependent on voltage and series resistance equal to 0 Ω·cm².

7.4.5. Experimental photocurrent maps

In device A339, we achieve an ohmic contact at the p–side introducing an additional junction between the heavily doped p^+–MoS_2 and p–MoS_2. However, this junction may add an extra component in the photocurrent generation. Hence, the measured PCE values may be overestimated because of the additional contribution of the pp^+ area. Besides, although the values of the *J–V* curves seem to be not affected by the existence of Schottky contacts at the metal/semiconductor interface, their presence cannot be discarded.

To ensure that there are no additional parasite effects related to the behaviour of the contacts or possible photogeneration at the pp^+ junction, we measure a photocurrent map of device A339. A 505 nm wavelength laser with a spot size of 10 μm^2 scans the surface of device A339 revealing which parts are contributing to the overall photocurrent production. Then, it is possible to identify a Schottky junction between metal and semiconductor, if there is photogeneration when the laser is impinging the metal/semiconductor junction [76]. Figure 7.7.a shows the micrograph of device A339, while Figure 7.7.d shows a photograph of device A342 which is a MoS_2 homojunction deposited on gold contacts. Figure 7.7.b,(e) shows the maps in short–circuit conditions of both devices where only the pn junction is contributing to the photogeneration. When we apply a direct bias of 0.3 V, in Figure 7.7.c there are no changes in the map of the p^+pn junction, only a slight reduction of the current recorded, expected because of the bias applied. However, in Figure 7.7.f it is observable that the Schottky junction p–MoS_2/Au is the blue zone inside the map.

The introduction of a photoactive component in the electrical model of Chapter 3 succeeded in replicating the effect of non–ideal contacts on the performance of MoS_2 homojunctions. The photocurrent measured in Figure 7.7.f demonstrates experimentally the presence of an opposite current to the pn junction and this Schottky junction encompasses an area larger than the area of contact metal/semiconductor, a behaviour that has been reported in literature by Mao et *al.* [167]. The expansion of the Schottky photoactive region beyond the contact may be explained by the growth of the carrier depletion region of the metal/semiconductor contact as the Schottky diode is reverse–biased when the pn junction is direct–biased [76].

The photocurrent maps demonstrate the absence of photoactive metal/semiconductor junctions in device A339 and inexistence of current

generation at the pp⁺ junction. The photoactive region is slightly bigger than the pn junction because of the spot size and the measurement conditions (step size), but the only photoactive area is the one defined by the p–flake and n–flake overlapping.

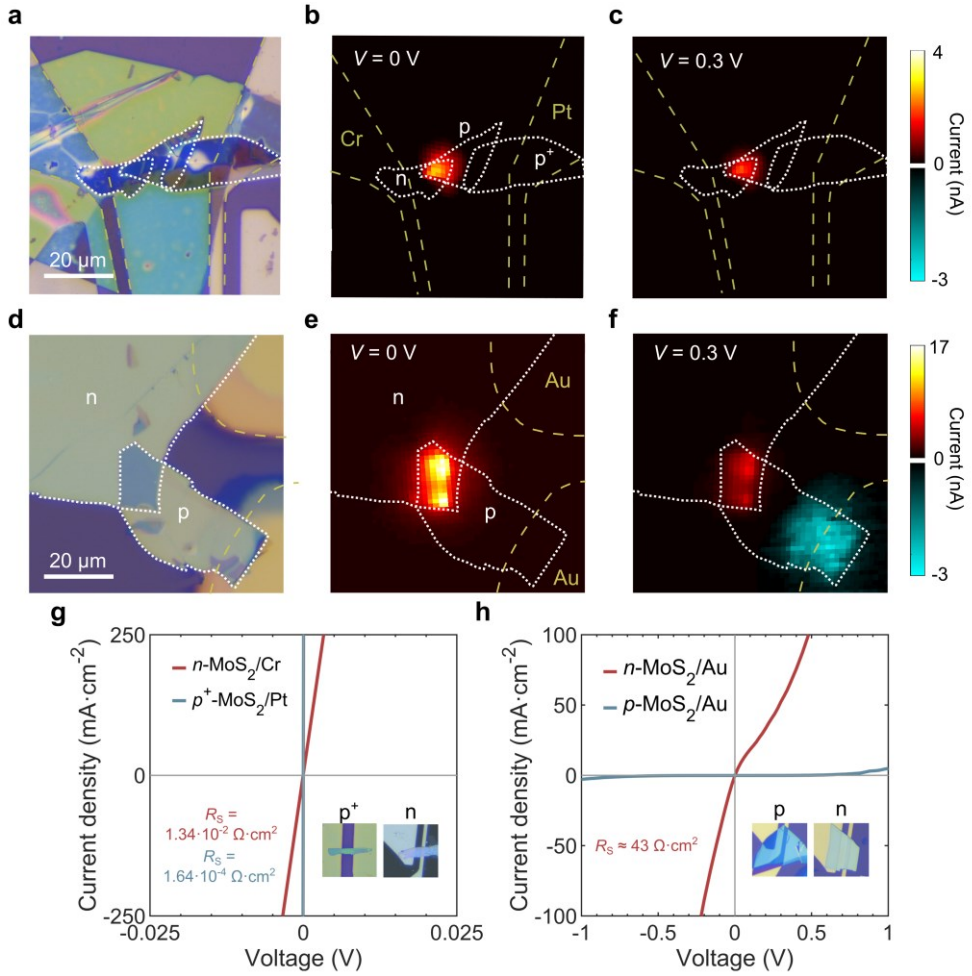

Figure 7.7. (a) A photograph of the device A339 (MoS_2 pn junction with Cr/n–contact and Pt/p⁺–contact). Spatial photocurrent maps of the device are shown in (a) with voltage bias between the Pt and Cr electrodes equal to (b) 0 V, and (c) 0.3 V. (d) Photograph of a MoS_2 pn junction with two Au electrodes (Device A342). Spatial photocurrent maps of the device shown in (e) with voltage bias between the two Au electrodes equal to (e) 0 V, and (f) 0.3 V. (g) *J*–*V* curves of p⁺–MoS_2/Pt (blue) and n–MoS_2/Cr (red) metal/semiconductor/metal junctions (the insets are photographs of the devices used in these measurements). Both curves show ohmic behaviour; the series resistance (*R*s) of the curves are given in the graph (in red for the n–contact and in blue for the p–contact). (h) *J*–*V* curves of p–MoS_2/Au (blue) and n–MoS_2/Au (red) metal/semiconductor/metal junctions (the insets are photographs of the devices used in the measurements). The blue curve shows a Schottky contact, and the red curve is quasi–ohmic.

Additionally, we have tested the behaviour of the metal/semiconductor contact placing a flake of each semiconductor, p^+–MoS_2, and n–MoS_2, onto pre–patterned contacts. We have use Pt for p^+–MoS_2 and Cr for n–MoS_2. Figure 7.7.g demonstrates that ohmic contacts have been achieved. The thicknesses of each flake measured with AFM are 24 nm for p^+–MoS_2 and 80 nm for n–MoS_2. Figure 7.7.h shows the *J*–*V* characteristics of p–MoS_2 and n–MoS_2 deposited on Au. Although the n–material shows a nearly ohmic curve, it is worse than to the Cr–contact presented in Figure 7.7.g. However, in the case of p–material, the rectifying contact marks the presence of a Schottky contact as observed in the photocurrent maps from Figure 7.7.f.

The experimental results of the photocurrent maps can be explained by the band diagram of each device depicted in Figure 7.8. For the scheme we use the electronic affinity of MoS_2 (4.3 eV) and its bulk band gap (1.3 eV) [24]. The WF of metals is 4.5 eV for Cr, 4.9 eV for Au, and 5.7 eV for Pt [175,194]. We calculate the position of Fermi levels in intrinsic MoS_2, n–MoS_2 and p–MoS_2 from the measured carrier population of each material and the values of the effective density of states in the conduction band (N_C) and in the valence band (N_V):

$$n_C = N_C \cdot exp\left(\frac{E_F - E_C}{k \cdot T}\right) \tag{7.9}$$

$$p_C = N_V \cdot exp\left(\frac{E_V - E_F}{k \cdot T}\right) \tag{7.10}$$

where n_C and p_C are the electron and hole density for either a n–semiconductor or a p–semiconductor measured experimentally, E_C is the position of the conduction band and E_V is the position of the valence band.

Table 7.2 compiles data from the literature and the calculated parameters according to the experimental and literature data. The surface properties of each material were measured with KPFM and are described in Chapter 6. The resultant band diagram for each material is presented in Figure 7.8.a–c. Figure 7.8.d shows the band diagram of device A339. We consider that p^+–MoS_2 is so doped that is degenerated and thus works as a metal. Note that the surface of the n–doped semiconductors is depleted according to the KPFM measurements revealing a possible p–doping effect of the atmosphere. The p^+–MoS_2 works as a contact layer for the p–MoS_2 assuring the ohmic contact. On the opposite side of the device, there is a small Schottky barrier at the chromium contact (0.02 eV), which is sufficiently small to be surpassed. In Figure 7.8.e, it is shown a pn junction between two gold

contacts as device A342. In this case, the height of the barriers causes the apparition of Schottky diodes in contact with both metals.

Table 7.2. Parameters involved in the band alignment of MoS_2 homojunctions and the interpretation of KPFM experiments:

	Values (eV) from literature	*Value (eV) used in this work to plot band diagrams*
Cr WF	4.5 ± 0.15 [115]	4.50
Au WF	4.9–5.5 [24] and references therein	4.90
Pt WF	5.65 ± 0.1 [115]	5.65
$PtIr_5$ [AFM tip] WF	4.86 [195]	not needed
MoS_2 χ	~ 4.3 [24] 4.38 [196] 4.45 [176]	4.40
MoS_2 pristine WF	4.4 – 5.3 [24] and references therein 5.04 [196]	4.59 in bulk (determined from Hall measurements) 5.14 at the surface (measured by KPFM)
n–doped MoS_2 WF	–	4.52 in bulk (determined from Hall measurements) 5.06 at the surface (measured by KPFM)
p–doped MoS_2 WF	–	5.61 in bulk (determined from Hall measurements) 5.60 at the surface (measured by KPFM)

Table 7.3 Parameters needed to calculate the position of the Fermi level, the width of the space charge region at the pn junction, and its built–in voltage from the carrier densities obtained in the Hall measurements.

MoS_2 dielectric constant (adim.)	11 (relative to vacuum) [197]
N_C (cm^{-3}) *	8.055×10^{19}
N_V (cm^{-3}) *	1.696×10^{19}
E_G (eV)	1.29 (from previous experiments [75])

* The effective densities of states at the CB (N_C) and the VB (N_V) have been calculated from the effective masses reported in Ref. [198] (assuming a degeneracy of 6 in the CB and 1 in the VB) [199,200].

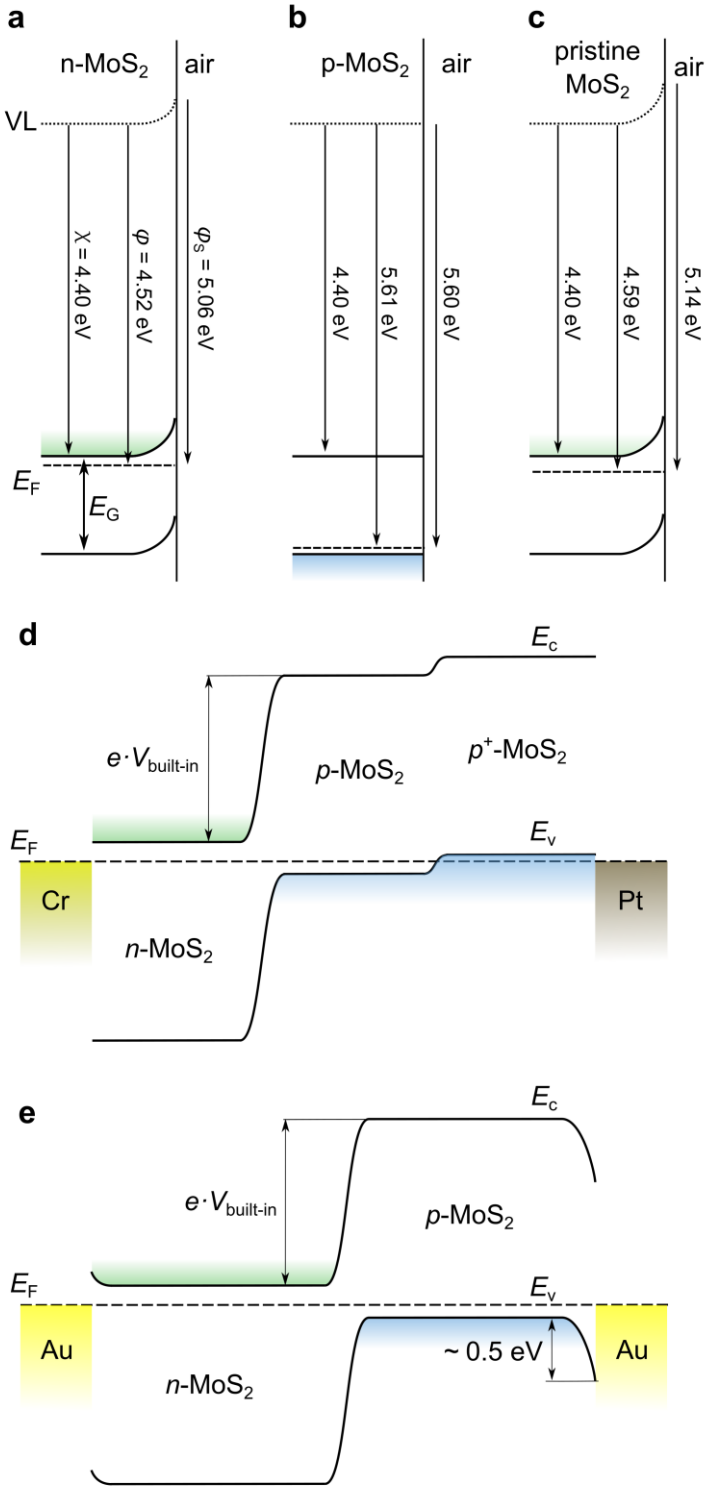

Figure 7.8. Band diagrams of (a) n–MoS_2, (b) p–MoS_2, and (c) pristine MoS_2 showing the region close to a surface exposed to air. (d) Band diagram of a MoS_2 pn junction with Cr at the n–contact and p+–MoS_2/Pt at the p–contact (this structure corresponds to device A339 in Figure 7.4 and Figure 7.7(a–c). (e) Band diagram of MoS_2 pn junction with gold electrodes at both contacts (this structure corresponds to device A342 in Figure 7.7(e–g). All diagrams have been drawn to scale in the energy axis using the electron affinity (χ), bulk WF (φ), and surface WF (φ_S) values that are compiled in Table 7.2.

7.4.6. Quantum Efficiency Measurements

The J–V characteristics of device A339 reveal that the problem related to the presence of Schottky contacts between MoS_2 and metals has been solved. The next step is the discussion about the photocurrent generated by the solar cell and optical absorption. As discussed in Chapter 4, the high value of the MoS_2 refraction index results in considerable optical losses. The addition of a h–BN ARL on device A339 as presented in Figure 7.9.a improves its J–V characteristics (see Figure 7.9.b). There is a noticeable increase in the photogenerated current as well as an improvement of the FF and V_{OC}, which goes from 0.6 V to 0.65 V. Besides, it is visible that series resistance decreases after the deposition of the h–BN layer. Such change could be explained by the characteristics of the fabrication process of the device, as the different flakes could not be perfectly in contact with the metal after their deposition. As a result of this, the addition of a top layer may help to improve those contacts and thus reduce the series resistance. The increase in the V_{OC} can be explained by the passivation effect of the h–BN on the surface of the MoS_2 which reduces the recombination current as in the case of device A210.

The absorption of the device is analysed using EQE measurements. As in the EQE measurements performed in Chapter 3, the absorbance of the device is split into three contributions from the three electrical regions of the device: SCR (63 nm), neutral part of the p–flake (36 nm), and neutral part of the n–flake (32 nm). The SCR thickness is calculated using the total depletion approximation [121] and the doping levels $6.6 \cdot 10^{17}$ and $7.4 \cdot 10^{17}$ cm^{-3} were measured with Van der Pauw. Figure 7.9.c–d, depicts how the SCR shrinks when applying a direct bias. Figure 7.9.e compares the experimental EQE of device A339 with the absorbance of a MoS_2 slab in a structure with the same thicknesses and architecture calculated with our model developed in Chapter 4.

We measured the thickness of the layers with AFM to simulate the same structure as the experimental device. We modelled a stack made of h–BN(62 nm)/MoS_2(131 nm)/SiO_2(290 nm)/Si(500 μm), splitting the MoS_2 into the zones neutral p, SCR, and neutral n. The EQE curve presents two peaks that approximate the maximum absorption at 630 and 675 nm of 0.98 and 0.93 respectively almost matching the theoretical values and which correspond to the Van Hove singularities of the material [15]. Absorption takes place mainly in the p–material, being the contribution of the n–neutral zone, the smallest of the zones considered. As in device a156 from Chapter 3, we notice the presence of the direct and indirect band

gap of MoS_2. Until 700 nm, optical absorption is dominated by the direct bandgap, and most of the total absorption is associated with it. The indirect bandgap is visible with an absorbance tail that extends until 900 nm. We estimate the photogenerated current of 15.91 mA/cm^2 integrating the EQE curve along with the AM1.5G solar spectrum. This value is concordant with the J_{ld} modelled for device A339 under an illumination equivalent to the AM1.5G solar spectrum (see Figure 7.4.b). Repeating the calculation with the calculated absorption profile, a J_{ld} of 19.94 mA/cm^2 is obtained. This yields an IQE of 79.8 % averaged over the range of interest.

Figure 7.9.f shows the EQE of A339 modelled using the mathematical model developed by Zehender et *al.* [122] which we used previously in Chapter 3, Subsection 3.5.3. The same assumptions as in Chapter 3 are made, as 100% efficiency in carrier collection at the SCR. Most of the photons are absorbed in the p–material, while absorption in the n–material is reduced. This suggests that it is possible to reduce the thickness of the n–layer to improve carrier collection without affecting light absorption. The excitonic peaks that are visible in the experimental curve could not be properly modelled. Results of modelling suggest an improvement of the surface recombination velocity in comparison to device A146 presented in Chapter 3, where surface recombination was estimated between 500 and 1000 cm/s. Nevertheless, as in Chapter 3, it is difficult to accurately estimate the exact value of surface recombination. The use of a lower doping level of the materials enables larger diffusion lengths improving carrier collection. Table 7.4 compiles the parameters used to fit the EQE curves.

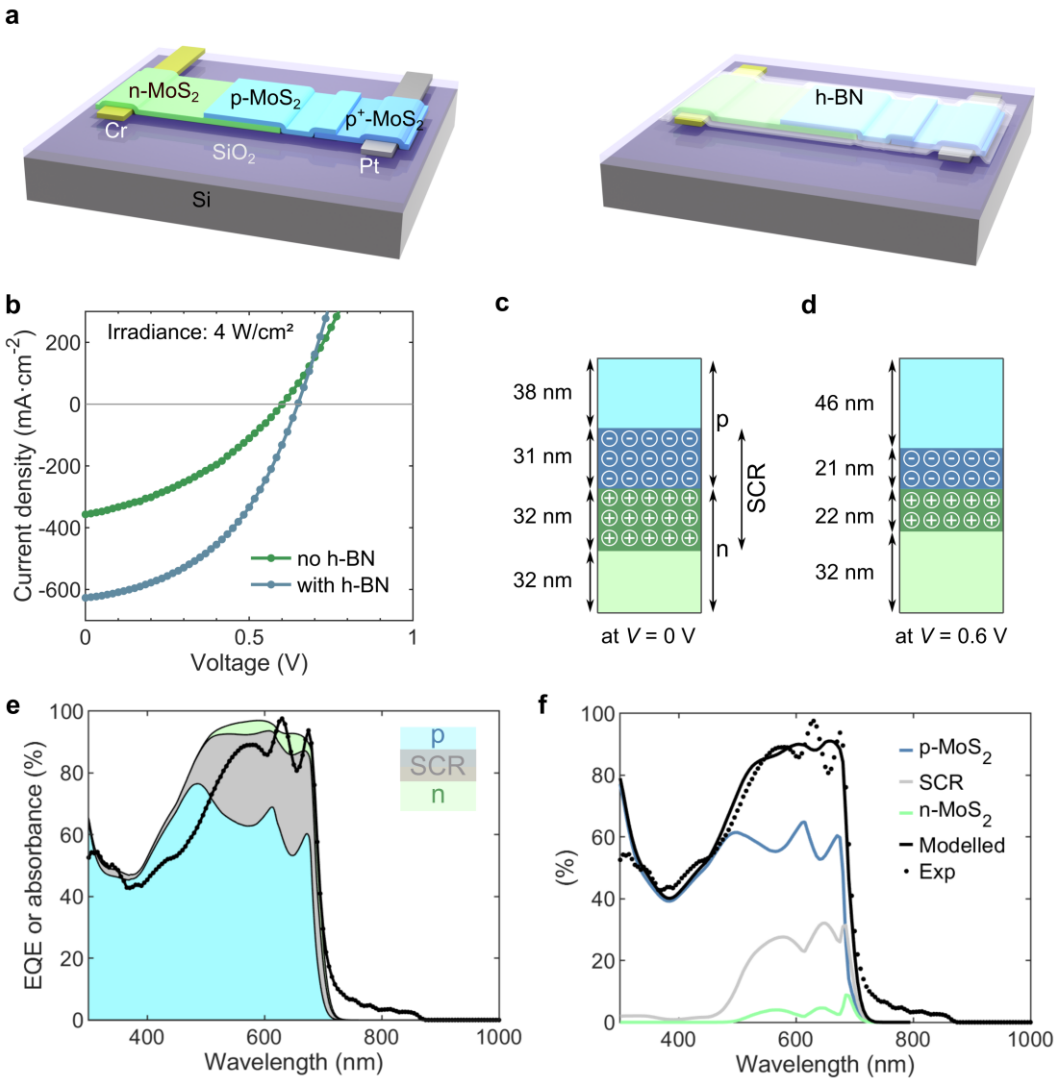

Figure 7.9. (a) Schematic of device A339 before and after BN deposition. (b) *J*–*V* curves taken under illumination from a broadband source (halogen lamp, irradiance 4 W/cm²) before (green dots) and after (blue dots) BN deposition. Cross–section schematics of the pn junction showing the calculated width of the space charge region (SCR) compared to the thickness of the p and n neutral regions: (c) when the junction is at $V = 0$ V, and (d) when it is at $V = 0.6$ V. (e) EQE measured after BN deposition (black line) compared to the calculated absorption for this structure; coloured areas represent the contribution of each device region to the total absorption. (f) Modelled EQE.

Table 7.4. Resulting parameters from EQE modelling.

Thickness of neutral zone p–material (nm)	36
Thickness of neutral zone n–material (nm)	32
Thickness of SCR (nm)	63
p–material minority carriers mobility ($cm^2/V \cdot s$)	7
n–material minority carriers mobility ($cm^2/V \cdot s$)	6
p–material carrier population (cm^{-3})	$6.6 \cdot 10^{17}$
n–material carrier population (cm^{-3})	$7.4 \cdot 10^{17}$
Diffusion length p–material (nm)	80
Diffusion length n–material (nm)	85
Carrier lifetime p–material (ps)	354
Carrier lifetime n–material (ps)	466
Surface recombination velocity p–material (cm/s)	200

7.5. Summary

It has presented a MoS_2 homojunction produced through substitutional doping whose efficiency of 3.82% and FF of 57.1% under a simulated light equivalent to the AM1.5G spectrum. This value surpasses the results previously reported in MoS_2 devices and it is one of the highest reported for TMDC–based devices.

To minimise the contact resistance and eliminate the Schottky barriers at the contact, it has been developed a specific process for contact fabrication that yields an optimal surface for semiconductor deposition. This fabrication process along with the use of tailored metal contacts according to the metal WF and the band structure of the semiconductor and the use of heavily doped materials enables the obtention of ohmic contacts to MoS_2.

The electrical contacts have been tested by measuring the J–V curves and photocurrent maps to discard the presence of photoactive Schottky contacts. The results reveal the absence of photoactive zones at the interfaces between metal and semiconductors, and J–V curves show a linear dependence verifying the obtention of ohmic contacts. However, the modelling of device A339 shows that further improvements are required to reduce the series resistance and to improve the ideality factor.

The presented devices yield a not pinned V_{OC} as it increases with the light input, being able to reach ~0.87 V under high concentration. Finally, the performance of

the MoS_2–based solar cells is boosted by implementing an ARL based on BN. This ARL allows the achievement of an elevated absorbance in the range between 500 and 700 nm approaching 100% of EQE at the excitonic peaks. Additionally, the h–BN helps to passivate the absorbent surface of the devices reducing carrier recombination.

The improvements applied to MoS_2 solar cells show that the performance of the devices can be enhanced considerably. However, there is still room for improvement in this technology. The next steps towards higher efficiencies are the improvement of the ideality factor, the reduction of the contact resistance, and the increase in the size of the devices

Chapter 8

Future applications of TMDC solar cells: semitransparent windows

8.1. Introduction

Solar photovoltaics is expanding in terms of the range of applications and installed capacity. Reports forecast an exponential growth of the photovoltaic industry which is boosted by the policies oriented to reduce the carbon intensity of industry, transport and buildings [1]. Solar photovoltaic devices are mainly used in flat opaque modules mostly made of monocrystalline silicon. Although the monocrystalline silicon solar module is a mature technology with reasonable PCE values (maximum of 24.4% [8]), it is not reliable that this technology will cover all the new capacity additions. Furthermore, the new concepts of photovoltaic devices such as curved or flexible modules cannot be achieved using conventional mono or polycrystalline silicon, opening the pathway to alternative materials.

Semitransparent solar cells are among the new photovoltaic concepts. Semitransparent solar cells are a technology that merges the benefits of light–to–electricity conversion and visible light transparency. This technology could be used in building integrated photovoltaics (BIPV) in windows and skylights within energy–sustainable buildings. The most extended form of BIPV is rooftop solar modules based on crystalline silicon. Nonetheless, technical reports emphasize that using façades and windows for generating power offers a convincing value proposition that supports potential market expansion [201]. Using façades to generate power will be crucial in the development of near–zero energy buildings [201–203], for instance by implementing semitransparent photovoltaic devices on the large area available in buildings with glazing curtain walls. Although BIPV still represents a small fraction of the PV market, global policies such as the European Directive 2010/31/EU will push forward to increase its market share [204]. Subsequently, the advancement of semitransparent solar cells emerges as an intriguing solution for BIPV, as they enable the ingress of natural light into a space, concurrently harnessing energy, and facilitating the controlled transmission of radiant heat and convective heat management.

The design of semitransparent solar cells is intricate but different motivations support the development of this technology. Sunlight provides a wide spectrum and an elevated power density, and its luminosity can be excessive for the human eye. Therefore, semitransparent photovoltaics can be used to control indoor illumination. Sunlight provides illumination levels that can reach over 100000 lux, a value that exceeds by far the European illumination regulations for buildings (200 or 500 lux in office buildings) [205]. Window designers regulate natural illumination and avoid extra heat offering solutions based on boosting the reflectance of windows. However, uncontrolled reflection, particularly from large buildings, may result in disruptive glares for pedestrians and drivers, which can lead to inconvenience and potential harm to vehicles and other objects on public roadways [206]. Furthermore, the concern regarding light reflection from buildings is escalating in the context of adapting cities to climate change. Light reflection from buildings may disrupt the thermal equilibrium of urban streets, causing the pavement to heat up and raising temperatures beyond comfortable levels during warm months [207]. This issue can be particularly problematic when using low–emissivity windows which are efficient for regulating the temperature inside the buildings but reflect especially near–IR radiation [208]. The implementation of semitransparent solar cells in the structure of windows would avoid reflectance–related issues as the excess of luminous power will be transformed into electrical power.

Designing solar cells to be used in semitransparent devices involves several challenges. Not all PV technologies are susceptible of achieving semitransparent arrangements. The thickness reduction of the devices of conventional technologies induces non–negligible performance losses [139], and their absorption profile yields transmitted spectrums that are not appealing to the human eye. A balance between the PCE and illumination is needed, as the improvement of one of both parameters involves the degradation of the other. In this context, TMDCs appear as a reliable solution for semitransparent applications, as they show a balanced absorption spectrum, and they can be assembled in slabs of nanometric thickness assuring semitransparency while generating power.

In this Chapter, we present a theoretical evaluation of how well TMDC–based devices can function as semitransparent solar cells. We evaluate two cases of TMDC–based semitransparent windows (MoS_2–based and WSe_2–based) whose structure is optimised to provide the largest PCE values while maintaining a proper indoor illumination level. The illumination properties are assessed in terms

of the amount of visible light that the window transmits, and the colorimetry of the transmitted spectrum. The indoor illumination conditions of an office are simulated using Blender software to show the effect of these semitransparent windows changing the chromaticity of the incident light. The potential energy savings related to the implementation of TMDC–based devices will be analysed using as a model example the Picasso Tower in Madrid, Spain. It is estimated that TMDC–based power–generating semitransparent windows could save in average up to 23.4% of the daily energy consumption in this case of study. This percentage rises to 32.9% when one third of the façade surface is covered with opaque modules made of the same TMDC. The main results presented in this Chapter have been compiled in [209].

8.2. State–of–the–art of semitransparent photovoltaics

Designing semitransparent solar cells presents a difficulty in balancing the need to produce power with the ability to transmit light effectively. Concerning semitransparent solar cells, technologies such as c–Si or amorphous Si have been traditionally used [204]. However, c–Si solar cells are not semitransparent. There are two main reasons why c–Si cannot reach semitransparency by reducing the thickness. Firstly the PCE values are severely hampered from over 20% in conventional cells to barely 4% in a 1 μm–thick device [210], and secondly, thin c–Si films develop a reddish hue because of absorption spectrum cut–offs in the visible light wavelength range [211]. Therefore, semitransparency in c–Si devices is only achieved by intercalating c–Si cells along transparent material. Nevertheless, the resulting patchy lighting is often not adequate for working environments. To solve this problem, it has been proposed the development of microhole–shaped light transmission windows on bare c–Si wafers. This solution shows a lab–scale PCE from 12.2% to 7.4% and associate transmittances of 20% and 50% [212]. The micro–drilled solar cells yield a transmitted light spectrally unaltered in comparison to the incident light but involves a complex fabrication process.

Amorphous Si solar cells, on the other hand, can be classified as semitransparent if the active layer permits some light to pass through, leading to flexible applications that can achieve a PCE of 5% and an average transmittance of 34% [213]. In addition to silicon, other technologies, such as inorganic, organic, dye–

synthesised, and hybrid perovskite, have emerged as viable candidates for these semitransparent applications. Organic photovoltaics offer the opportunity to tailor absorption spectra by absorbing IR frequencies imperceptible to the human eye, consequently preserving an almost unaltered visible light transmission spectrum. This feature has been accomplished in an organic–based device, yielding a PCE of 10.8% and an average light transmission of 45.7% [214]. For all these emerging technologies, the optimisation of the chromatic characteristics of the transmitted light is an important challenge [215].

Perovskite–based devices reported by Eperon et *al.* employ similar strategies to c–Si to achieve a balanced transmitted spectrum [216]. In this case, it is pointed out that dyes can be blended with the cell components to adjust the transmitted spectrum without adversely affecting the electrical properties of the device. However, dyes may absorb photons that will not be longer available for photoconversion. This technique is not limited to semitransparent devices; it can also be utilised to attain the desired aesthetic appearance of solar cells, mimicking natural elements such as rocks [215]. Colour tuning of perovskites and organic solar cells is an effective strategy to approach the target chromaticity coordinates of semitransparent devices, however, it is essential to acknowledge that dyes may degrade over time, thereby losing their properties. An alternative solution involves the use of dyed glass, serving as a colour–balancing layer to equalise the window light transmission, or using light filters to partially block a specific wavelength, although it results in an extra power loss.

The current methodologies for achieving semitransparent power–generating structures are characterised by their dependence on a blend of solar cell constituents in conjunction with supplementary materials aimed at facilitating either semitransparency or colour neutrality. Furthermore, conventional materials encounter difficulties in meeting the required thickness essential for the realisation of semitransparent structures. Consequently, an optimal semiconductor suitable for semitransparent purposes ought to exhibit a harmonised absorption of incident light, while concurrently enabling the fabrication of ultrathin structures that maintain semitransparency without compromising the electrical characteristics of the devices.

8.3. TMDC semitransparent devices

The requisites needed in semitransparent solar cells make TMDCs an innovative solution due to their appealing properties. These properties such as strong light–matter interactions or relative abundance in nature were explained in Chapter 5, Section 5.2 [15,22,23,123,145]. Concerning the use of TMDCs in semitransparent windows, the fabrication process of the layers is a positive feature. We proposed the structure illustrated in Figure 8.1.a as the architecture of the TMDC–based module wherein the solar cell is deposited between two ITO layers. For the sake of cost–efficiency, this structure would be built using solution–processed TMDC deposition on the front ITO/glass substrate with precise thickness control and homogeneity [20]. The TMDC slab represented in Figure 8.1 contains a pn junction implemented through substitutional doping [41,75]. As in commercial solar modules, it includes high transmittance glass on the front cover (low–iron glass quality), whereas the back glass is a conventional architectural glass (clear glass quality) [217]. Both glasses have a thickness of 3.2 mm. As is also customary in PV, the module is encapsulated using an insulant polymer (ethyl–vinyl acetate, EVA) of 0.45 mm. No ARL has been inserted in the structure because, as we have already shown for opaque devices elsewhere [132], the front ITO layer has a close–to–optimum refractive index to produce an antireflective effect when located onto a TMDC layer. This structure could be implemented in windows of large buildings as presented in Figure 8.1.b.

TMDCs are suitable for semitransparent applications because of their outstanding optical properties. Figure 8.1.c shows the absorptance of different material slabs weighted over the non–reflected fraction of the incident light. TMDCs show an absorption coefficient extraordinarily large. The light absorption in a self–standing slab of only 10 nm of MoS_2 or WSe_2 (left graph) is comparable to the absorption of 100 nm of conventional direct gap semiconductors (middle graph) or 1 μm of silicon (right graph). Another remarkable feature is the presence of strong absorption peaks thanks to the presence of Van Hove singularities [15,23]. These peaks raise the absorption in the vicinity of the band gap edge, producing a balanced absorption over the whole visible range that results in the presence of strong absorption peaks at the longer wavelengths of the visible spectrum. Conventional materials, by contrast, show a steep curve that results in an unbalanced absorption of the spectrum, which leads to a reddish transmitted spectrum if the device is thick enough to produce a significant photocurrent [211]. The device optimisation work presented here aims at exploiting this unique characteristic of TMDC

semiconductors to design colour–neutral power–generating windows. Moreover, these materials show comparable absorption values with ten times less material than conventional technologies, and one hundred times less material than c–Si, leading to potential material cost savings.

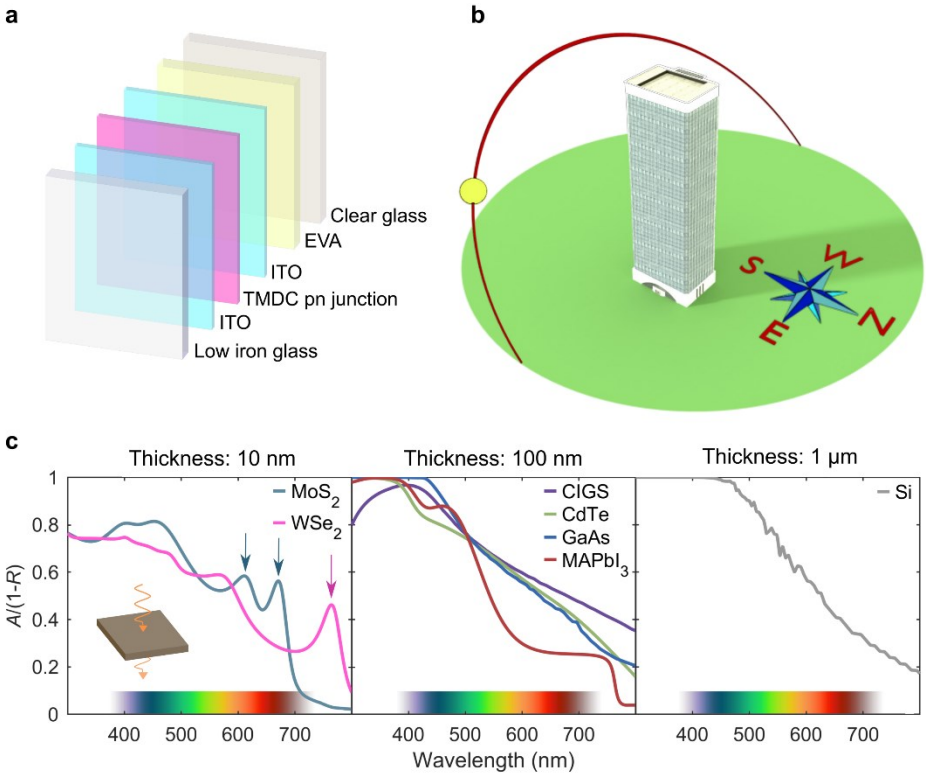

Figure 8.1. (a) Schematic of the layers in a TMDC–based power–generating semitransparent window. (b) Example of integration of semitransparent windows applied to the Picasso Tower in Madrid. (c) Absorbed light weighted over the non–reflected light of a single slab of different semiconductor materials (arrows point to the Van Hove singularities in TMDCs).

8.4. Designing considerations

When designing a power–generating semitransparent window, there is a trade–off between the amount of energy that the device can generate and the quality of the light flux that is transmitted to the interior of the building. The transmitted light flux can be evaluated using different parameters derived from its SPD. As figures of merit, we consider the average photopic transmission (APT), the chromaticity of transmitted light according to the CIE 1931 colour space, and the colour rendering index (CRI).

8.4.1. Average photopic transmission

The evaluation of the quality of the light flux implies not only attending to its SPD but also to how this light is perceived by the human eye. Under daylight conditions, the human eye perception is governed by the cone cells in the retina. These cone cells are most sensitive to medium–wavelength (green–yellow) light, approximately in the range of 555 to 575 nm. The perception of the human eye under these conditions can be described by the photopic function. This function describes how the sensitivity to light changes with different wavelengths. The photopic function is widely used in luminotechnics to design artificial light sources or to assess the performance of lighting systems and luminosity. It plays a crucial role in understanding how the human visual system perceives light under different conditions and forms the basis for designing lighting solutions that are both efficient and comfortable for human beings.

The APT is the percentage of transmitted light through a semitransparent structure weighted over the photopic function. This value is calculated using the following expression:

$$APT = \frac{\int SPD(\lambda)\cdot T(\lambda)\cdot \bar{y}(\lambda)\cdot d\lambda}{\int SPD(\lambda)\cdot \bar{y}(\lambda)\cdot d\lambda} \qquad (8.1)$$

where $SPD(\lambda)$ is the incident SPD, $T(\lambda)$ is the transmittance of the semitransparent window and $\bar{y}(\lambda)$ is the photopic function.

8.4.2. Chromaticity

The chromaticity of an SPD can be evaluated according to the CIE 1931 XYZ colour space. The CIE 1931 colour space was created in 1931 by the International Commission of Illumination from the works of Willian David Wright and John Guild conducted in the late 1920s [218]. This was the first quantitative link between the spectral distributions and the colours perceived by the human eye. In their experiment, an observer tried to replicate a test colour sample by mixing the light of three primary colours red, green and blue. Each visible colour was obtained by weighting the contributions of each primary colour defining them with a mathematical expression. From this experiment, it was defined the CIE 1931 RGB colour space. However, some of the test colours could not be obtained from the mixture of the primary light sources. This problem was solved by illuminating the test samples with one of the primary colours so the colour can be defined including a negative contribution of that primary colour. The use of a perception curve with

negative values is counterintuitive, so the RGB space was transformed using linear mathematical relationships into the XYZ space. In the CIE 1931 XYZ colour space, any colour can be obtained from a mixture of three imaginary colours, but also the original RGB space can be defined inside this space.

In both, the XYZ and the RGB colour space, all visible colours can be represented as a set of coordinates. This set of coordinates is obtained from the integration of the SPD with the CIE 1931 XYZ colour–matching functions (see Figure 8.2.a). These functions are related to the perception of the human eye of the colours red, green, and blue extracted for the RGB colour space but then transformed into the XYZ colour space to avoid negative coordinates. This formalism yields the tristimulus values that can be converted into coordinates in the CIE 1931 XYZ colour space (see Figure 8.2.b):

$$X = \int SPD(\lambda) \cdot \bar{x}(\lambda) \cdot d\lambda \tag{8.2}$$

$$Y = \int SPD(\lambda) \cdot \bar{y}(\lambda) \cdot d\lambda \tag{8.3}$$

$$Z = \int SPD(\lambda) \cdot \bar{z}(\lambda) \cdot d\lambda \tag{8.4}$$

The CIE XYZ colour space was designed so that the Y parameter is also a measure of the luminance of a colour and the colour matching function $\bar{y}(\lambda)$ is the photopic function previously used in Equation (8.1).

The chromaticity is then specified by the parameters x and y, which are derived from the tristimulus values:

$$x = \frac{X}{X+Y+Z} \tag{8.5}$$

$$y = \frac{Y}{X+Y+Z} \tag{8.6}$$

Note that it is possible to determine a third coordinate z using an equivalent expression to Equations (8.5) and (8.6). The resulting values of x and y provide the chromaticity coordinates of the evaluated light source according to the colour space illustrated in Figure 8.2.b.

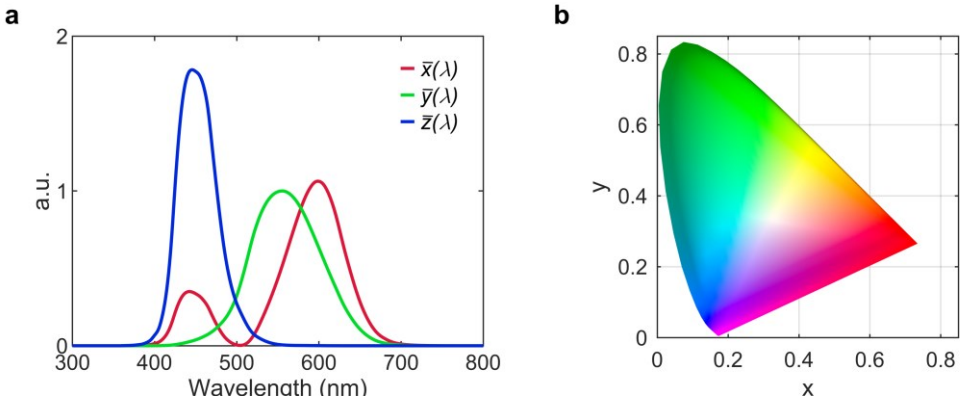

Figure 8.2. (a) XYZ colour matching functions. (b) CIE 1931 XYZ colour space.

8.4.3. Colour rendering index

The CRI is a quantitative measure of the ability of a light source to render faithfully the colour of an object. This parameter is presented as an index that measures the quality of a light source on a scale from 0 to 100. To determine the CRI of a light source it is compared to a reference illuminant according to the normative [219]. The calculation of the CRI involves several steps, but before describing the process of calculation it is necessary to define some concepts that are required to understand it properly.

When calculating the CRI, it is used as a reference illuminant. This illuminant has its SPD that can be found in the normative, but the selection of the illuminant depends on the characteristics of the tested light. An important parameter of the light is the colour correlated temperature ($CCT(K)$) which is defined as the temperature of the Planckian radiator whose perceived colour most closely resembles the light. $CCT(K)$ can be easily calculated from the coordinates in the CIE 1931 XYZ colour space using the McCamy approximation [220]:

$$n_C = \frac{(x-0.332)}{(y-0.186)} \tag{8.7}$$

$$CCT(K) = 437 \cdot {n_C}^3 + 3601 \cdot {n_C}^2 + 6861 \cdot n_C + 5517 \tag{8.8}$$

If the $CCT(K)$ of the tested light is higher than 5000 K, the reference illuminant chosen is the D65, which tries to represent average daylight and has a $CCT(K)$ of approximately 6500 K, but if $CCT(K)$ is lower, the reference illuminant is a black body radiator whose SPD is calculated according to the Planck's Law:

$$B_\lambda(\lambda, T) = \frac{2 \cdot h \cdot c}{\lambda^3} \cdot \frac{1}{exp\left(\frac{h \cdot c}{\lambda \cdot k_B \cdot T(K)}\right) - 1} \tag{8.9}$$

Although until this point it has been used the CIE 1931 XYZ colour space, to calculate the CRI it is necessary to change the colour space to CIE 1960 UCS by the following equations:

$$u = \frac{4 \cdot X}{X + 15 \cdot Y + 3 \cdot Z} \tag{8.10}$$

$$v = \frac{6 \cdot Y}{X + 15 \cdot Y + 3 \cdot Z} \tag{8.11}$$

After the transformation into the CIE 1960 UCS colour space, the calculation of the CRI involves the following steps:

- **Selection of test samples**: There are selected a set of 8 or 15 colour samples with a known reflectance spectrum. These samples cover a range of hues. The spectral reflectance of those test samples is tabulated.
- **Selection of reference illuminant**: It is selected according to the $CCT(K)$ value of the tested light. Note that to correctly evaluate the CRI, the distance between the coordinates of the tested light and the reference illuminant must not surpass a limit of $5.4 \cdot 10^{-3}$ units [219].
- **Measurement**: The test samples are evaluated under the reference illuminant and the tested light. It can be done mathematically by multiplying the SPD of the sources with the reflectance of each test sample and obtaining its coordinates in the CIE UVW colour space.
- **Colour Fidelity Calculation**: A set of colour rendering indices (R_i) is obtained from the distance of the test samples under the reference illuminator and the tested light.
- **CRI Calculation**: The average of all R_i measured for each sample is calculated to get the overall CRI value.

8.5. Modelling

8.5.1. Optical absorption modelling

The modelling of the absorptance of the power–window structures is done using the optical model developed in Chapter 4. In this case, we model our proposed structure for a module depicted in Figure 8.1.a. For this module, both glasses have a thickness of 3.2 mm. The structure includes the module encapsulation using an EVA layer of 0.45 mm. The solar cell is made of a homojunction of MoS_2 or WSe_2 contacted with ITO layers. It is considered the TMDC absorber and ITO layers as coherent. The thicker EVA and glass layers are considered incoherent.

In Chapter 4, Section 4.3, we discussed the reasons to consider a layer as coherent or incoherent depending on thickness and the roughness of the layers in the structure. EVA and glass layers are too thick to be treated as coherent but when considering the ITO and the MoS_2 layer, the coherent length of the sunlight is larger (coherent length ~ 250 nm for ITO and ~ 100 nm for MoS_2) than the thickness of each layer modelled. So the coherence of the ITO and the MoS_2 will depend on the roughness of each layer as predicted by Equation (4.2) described by Carniglia [126].

The roughness of ITO layers deposited on glass substrates varies according to the process of deposition. The parameter used to measure the roughness is the RMS roughness, and in the case of ITO, it ranges between 0.5 and 1.5 nm for the better cases [221,222] up to 18 nm for the worse cases [223]. The RMS roughness values of MoS_2 achieved in the solution–deposition process are small when considering thicknesses under 10 nm but increase considerably in thicker layers [20]. For instance, it is considered a structure with a MoS_2 solar cell 30 nm–thick which is made of two independent layers of 15 nm, corresponding to the p–MoS_2 and the n–MoS_2 that conform to the pn junction. In this case, the expected RMS roughness of each layer is 4 nm [20]. Considering an ITO roughness of 10 nm, it is possible to calculate the expected light scattering. Figure 8.3 represents the fraction of scattered light calculated according to the expression of Carniglia introduced in Equation (4.2) in Chapter 4 [126]. Results show that the scattered fraction of light barely surpasses the 5% of the incident light in the visible range, then, ITO and MoS_2 layers can be treated as coherent. Note that in the case of WSe_2, similar results of MoS_2 are expected.

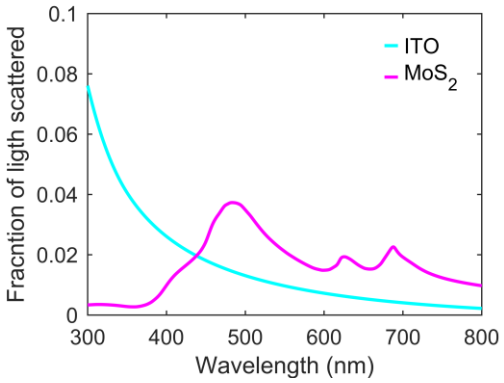

Figure 8.3. Fraction of scattered light for ITO and MoS_2 (15 nm–thick layers).

The refractive indexes and extinction coefficients have been taken from Refs. [129,217,224–226]. For the TMDCs, it is used the bulk optical constants, in opposition to few–layer values. The reason to use bulk constants is the scattering in the published values of refractive index for few–layer and monolayer MoS_2 as was argued in Chapter 5, Subsection 5.3.1.

8.5.2. Solar spectrum modelling

The SPD of the incident spectrum depends on the geographical coordinates of the reference point and the time of the day. The position of the Sun in the sky and the incidence angle are determined using the equations from Kalogirou [130] and the SPD impinging on the semitransparent window is determined using the equations from Bird and Riordan [131] as described in Chapter 4, Section 4.5. To evaluate the absorptance of the diffuse irradiation component we use our model explained in Chapter 4, Section 4.5.

8.5.3. Model to estimate photovoltaic generation

The conjunction of the optical model and the spectrum model allows the calculation of the light absorbed and transmitted for any structure at any moment of the day, date, and place in the world. The estimation of the *J–V* curve of a TMDC–based power–generating semitransparent window from the absorption of the solar cell is not straightforward, as the electrical behaviour of these devices is not completely understood yet. In this work, we have made an approximate estimation of the photogenerated power based on a set of assumptions. These assumptions include a realistic assessment of the series resistance because lateral electrical resistance is expected to by a limiting factor in this technology. The assumptions also include high–quality diode parameters, which can be reviewed once TMDCs devices are further developed in the future. First, it is considered that all the absorbed photons by the semiconductor are converted into electrons. Hence the photogenerated current is calculated following expression:

$$J_L = e \cdot \int SPD(\lambda) \cdot A(\lambda) \cdot d\lambda \qquad (8.12)$$

where $A(\lambda)$ is the spectral absorptance of the solar cell. Note that this calculation is done for both the direct and diffuse components.

To determine the parameters of the *J–V* curve, first, it is assumed a value of $n = 1$ for the ideality factor of the diode. Then, recombination current density is calculated using the Shockley equation in short–circuit conditions:

$$J_0 = \frac{J_L}{e^{\left(\frac{E_G - W_{OC}}{n \cdot k_B \cdot T(K)}\right)} - 1} \tag{8.13}$$

where J_L is calculated with Equation (8.12) when the incident light is the AM1.5G spectrum with normal incidence. The temperature is assumed to be 298 K. The W_{OC} is determined according to King et *al.* [68] depending on the bandgap of the semiconductor considered. King calculates the W_{OC} for a realistic semiconductor solar cell working in the radiative limit. For MoS_2, it is considered a W_{OC} of 0.43 V, and for WSe_2 0.42 V, which correspond to a V_{OC} value of 0.86 V and 0.79 V respectively.

Once the parameters of the diode have been determined, we can write the following $J(V)$ equation:

$$J(V) = J_0 \cdot \left(\exp\left(\frac{V - R_S \cdot J}{n \cdot k_B \cdot T(K)}\right) - 1\right) - J_L \tag{8.14}$$

where R_S is the effective series resistance of the device. The device has metal fingers that work as contacts which are separated a distance d and whose resistance is not considered (see Figure 8.4). R_S is calculated assuming that majority charge carriers move in the TMDC layers only in the direction perpendicular to the junction until they reach the ITO layers, where they travel laterally to reach the contacts. Therefore, R_S is determined by the sheet resistance of the ITO layers. Note that assuming some lateral transport in the TMDC layers would reduce the value of R_S with respect to our estimation. Then, to calculate the series resistance we evaluate the power dissipation in the ITO layer:

$$dP_{loss} = I^2 \cdot dR \tag{8.15}$$

where I is the current flowing through the ITO layer, which can be calculated as a function of the distance x to the fingers with the following equation:

$$I(x) = J \cdot w \cdot \left(\frac{d}{2} - x\right) \tag{8.16}$$

where w is the width of the solar cell. The differential of resistance can be determined with the following expression:

$$dR = R_{\square} \cdot \frac{dx}{w} \tag{8.17}$$

where $R_{\square}$ is the sheet resistance of the ITO. $R_{\square}$ is obtained assuming an ITO resistivity of $1.4 \cdot 10^{-4}$ Ω·cm, a value congruent with the resistance of ITO deposited on glass in literature [227–229].

Then, power loss is calculated by substituting in Equation (8.15) the terms of Equations (8.16) and (8.17).

$$P_{loss} = \int_0^{d/2} J^2 \cdot w^2 \cdot \left(\frac{d}{2} - x\right)^2 \cdot R_{\square} \cdot \frac{dx}{w} \tag{8.18}$$

Solving Equation (8.18):

$$P_{loss} = J^2 \cdot w \cdot R_{\square} \cdot \frac{d^3}{24} \tag{8.19}$$

On the other hand, the power loss can be expressed according to the following expression:

$$P_{loss} = I^2 \cdot R_{lumped} \tag{8.20}$$

where R_{lumped} is related to the effective series resistance of the device by the following equation:

$$R_s = R_{lumped} \cdot A_c \tag{8.21}$$

where A_c is the area of current collection for each finger, which is the width of the solar cell multiplied by half of the distance between fingers as each finger collects the current that flows through the area marked in red in Figure 8.4:

$$A_c = w \cdot \frac{d}{2} \tag{8.22}$$

R_{lumped} is calculated equalising Equations (8.19) and Equation (8.20) obtaining:

$$R_{lumped} = R_{\square} \cdot \frac{d}{6 \cdot w} \tag{8.23}$$

Substituting Equation (8.22) and Equation (8.23) in Equation (8.21), we obtain the value of the effective series resistance used in Equation (8.14):

$$R_s = R_{\square} \cdot \frac{d^2}{12} \tag{8.24}$$

Once the *J–V* curve of the device has been obtained, the photogenerated power density is calculated at the maximum power point.

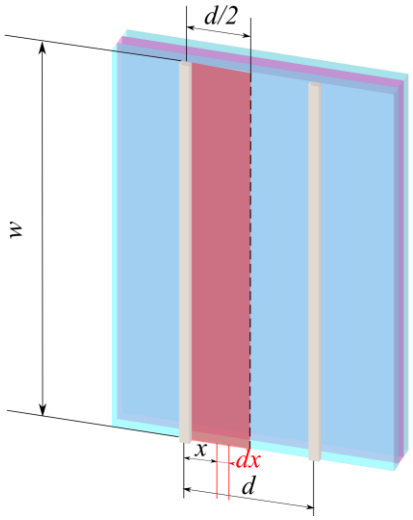

Figure 8.4. Schematic of the dimensions of the semitransparent TMDC device for series resistance calculation.

8.6. Results

8.6.1. Considerations

Semitransparent solar cells entail a balance between the electrical performance of the device and the quality of the transmitted spectrum. To achieve this balance, designers use different approaches and figures of merit to evaluate the quality of their devices. Most of the publications about semitransparent solar cells focus on the idea of colour neutrality of a transmitted spectrum. Colour neutrality is often defined as the resemblance between the CIE coordinates of the transmitted spectrum and a reference illuminant [212,215,216]. This reference illuminant is usually the D65, but lamps and lightbulb manufacturers offer a product range whose illumination characteristics differ from the D65 illuminant and are still considered natural illuminants. We have established an alternative condition for colour neutrality based on the proximity of the CIE coordinates of the SPD of the examined light to the Planckian locus. The Planckian locus is the path or locus that the colour of a black body radiator would take in the CIE colour space as the black body temperature changes.

The use of the Planckian locus as a reference to achieve a natural colour of a light source is comparable to the requisites established at the ANSI C78.377 standard, which was enveloped by the American National Standards Institute (ANSI) along with other associations to standardise the description of tints in LEDs and solid–state lighting. This standard sets eight quadrangles in the CIE colour space which contains the chromaticity coordinates of those points which are equivalent to a natural light source with a specific $CCT(K)$. The use of the ANSI C78.377 standard is usual for lightbulb manufacturers but it has been used in the evaluation of the chromatic characteristics of the transmitted spectrums of organic semitransparent photovoltaic cells [214].

The optimisation of TMDC semitransparent windows is done by trying to maximise the optical absorption while attending to the chromaticity characteristics of the transmitted spectrum. We implement a mathematical algorithm based on the optical model developed in Chapter 4. For a fixed device architecture (see Figure 8.1.a), low iron glass (3.2 mm)/ITO/TMDC/ITO/EVA(0.45 mm)/clear glass (3.2 mm), the algorithm determines for any thickness of TMDC, the optimal thickness of ITO that maximises absorptance while the chromaticity coordinates of the transmitted SPD remain at a maximum distance of $5.4 \cdot 10^{-3}$ units

from the nearest point in the Planckian locus in the CIE 1960 colour space, which is the maximum distance admissible by the CIE standard [219]. This means that the optimum layer structure is not necessarily the one that results in the highest possible absorption. The incident light SPD used in the optimisation is the AM1.5G solar spectrum with an incidence angle of 57º. The choice of this angle approximates average angle of incidence for a device in a vertical orientation along a day. Finally, when referring to any calculation of SPD for a specific date, SPD is calculated at the coordinates 40º 30' N, 3º 40' W which corresponds to Madrid, Spain.

8.6.2. Optimisation of structures

Figure 8.5.a(b) illustrates the absorptance of the TMDC solar cell (WSe_2 or MoS_2) within the module. Different solar cell thicknesses are presented from 3 to 55 nm. Each thickness depicted in the figure corresponds to a specific design scenario. The 3 nm window is the minimal achievable thickness using large–area fabrication techniques of TMDCs [20]. Conversely, the 11 nm window is the scenario in which a maximum absorptance is achieved for the MoS_2–based device owing to the zeroth–order absorption maxima in a resonant cavity [123]. In Chapter 5 we discussed that zeroth–order interference can be boosted using a back reflector [132]. Although, in the case of a semitransparent device zeroth–order interference is not amplified, the device maintains a reasonably high absorptance. For instance, the absorptance curve of 11 nm of MoS_2 even surpasses the curve of 30 nm from 550 nm. The 30 nm window characterises a possible maximum permissible thickness for a semitransparent application as absorptance is approximately half of the incident spectrum. In the case of WSe_2, it has been added a case 55 nm–thick that may lead to excessive light absorption for most applications, but the chromaticity of the transmitted light remains within the optimisation bounds. The optimised thickness values of the ITO layers are compiled in

Table 8.1.

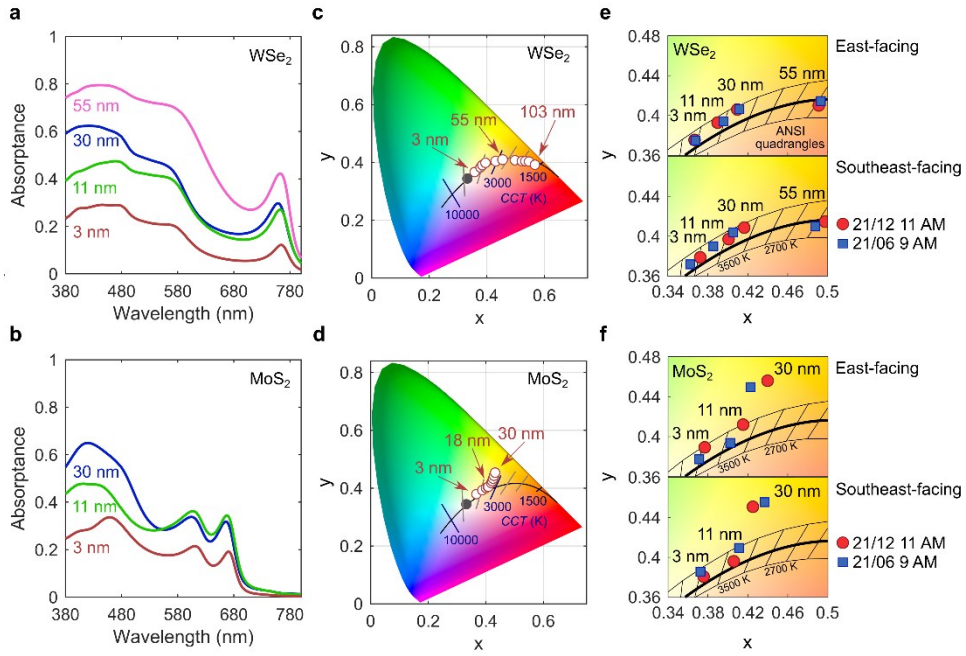

Figure 8.5. (a) (b) Absorptance of the solar cell in the module structure for different thicknesses of WSe_2 (MoS_2). (c) (d) CIE 1931 colour space with the AM1.5G transmitted spectrum of the module for different thicknesses of WSe_2 (MoS_2). The grey dot indicates the chromaticity coordinates of the AM1.5G. (e) (f) Partial CIE 1931 colour space and ANSI C78.377 quadrangles along with the transmitted spectrum for the structures from Fig 8.5.a(b) for the incident solar spectrum in Madrid at 11 a.m. on December 21st and at 9 a.m. on June 21st, and east–facing (E) and southeast–facing (SE) windows.

Table 8.1. Optimised layer thicknesses, for MoS_2 and WSe_2 semitransparent power–generating windows.

MoS_2 devices		
ITO top (nm)	***MoS_2 (nm)***	***ITO bottom (nm)***
161	3	154
152	11	150
150	30	145
WSe_2 devices		
ITO top (nm)	***WSe_2 (nm)***	***ITO bottom (nm)***
123	3	127
91	11	110
62	30	91
54	55	207

Figure 8.5.c(d) shows the CIE 1931 colour space and illustrates the chromatic characteristics of TMDC–based photovoltaic windows. White dots show how the chromaticity of the transmitted light changes when increasing the thickness of the semiconductor under the illumination of the AM1.5G spectrum. Inside the CIE colour space, it is depicted the Planckian locus along multiple representing points of the CIE colour space with the same $CCT(K)$. When increasing the thickness, the transmitted light shifts towards reddish tones. In the case of WSe_2–based structures, deviation from the Planckian locus is minimal. This indicates that the transmitted SPD of WSe_2–based semitransparent windows resembles that of a black body, which is a pleasant illumination for the human eye at any $CCT(K)$ and results practical for indoor illumination for $CCT(K)$ above 2700 K. It is remarkable that this is achieved without requiring the use of dyes or coloured glass that would complicate the structure of the window. An unacceptable deviation from the Planckian locus is only observed at 103 nm of WSe_2. In contrast, MoS_2–based structures deviate from the Planckian Locus once the TMDC solar cell thickness exceeds 18 nm. This can be explained by the difference in the band gap of both materials. While MoS_2 cannot absorb the longer wavelengths of the visible spectrum, WSe_2 does, so the absorptance is more balanced.

Figure 8.5.e(f) illustrates the chromaticity of the transmitted spectrums of the structures from Figure 8.5.a(b) in conjunction with the acceptable regions of chromaticity outlined by ANSI C78.377. In this case, the transmitted spectrums are computed for two distinct dates (December 21st at 11 AM and June 21st at 9 AM) and east– and southeast–facing arrangements using the models from Subsection 8.5.2. The selected dates represent the extreme cases of daylight, (winter and summer solstice) and optimal irradiation during the early hours of the day coinciding with the standard office schedule. The times refer to local time in Madrid, using UTC+02:00 in June and UTC+01:00 in December. Notably, the chromaticity coordinates of the transmitted light show similar deviations when considering AM1.5G as the illuminator under normal incidence. In addition, the chromaticity coordinates still fall within the area delimited by the ANSI–defined boundaries except for the 30 nm–thick MoS_2 window. Consequently, the 30 nm–thick MoS_2 window cannot be applied according to illumination standards [219]. However, cases such as 30 nm–thick MoS_2 may find a different application in architectures for aesthetic purposes, for instance, combining them with windows with different colours to create luminous effects or intentionally altering the perception of colours [230,231].

The chromaticity of the incident spectrum is shifted towards reddish tones by the effect of the TMDC–based semitransparent window, which causes an alteration of the colour perception that is acceptable if the chromaticity coordinates of the transmitted spectrum approach those of a black body radiator. However, the transmitted spectrum changes along with the SPD of the sunlight throughout the day, so that the window properties which may be acceptable at 9 AM can turn uncomfortable at some point of the day. We assess how chromaticity evolves during the day. Figure 8.6 depicts the evolution of the chromaticity of the incident and transmitted light on June 21st through an east–facing 30 nm–WSe_2 semitransparent window. The incident and transmitted chromaticity coordinates simultaneously move on the CIE chart as time passes, but at any moment of the day, the transmitted light still complies with the chromatic requirements of the ANSI standard. Note that, at 3 PM and 6 PM, direct sunlight does not illuminate the window. In circumstances where only diffuse illumination is present, it is foreseen, based on the location of the transmitted spectrum in the CIE colour space, that an observer situated behind the TMDC semitransparent glass would perceive the sky as possessing a white hue. To interpret Figure 8.6, it is possible to make the following analogy: indoor illumination with the solar spectrum is comparable to illumination with cold white LEDs, whereas illumination through TMDC–based power–generated windows is comparable to illumination with warm white LEDs. For reference, an incandescent bulb lab has a $CCT(K)$ of 2700K.

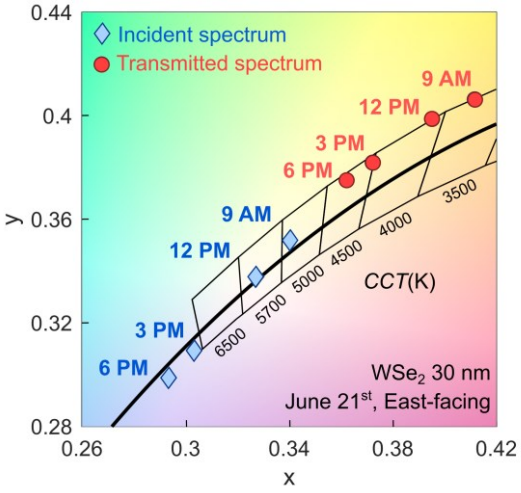

Figure 8.6. Partial CIE 1931 colour space and evolution of the incident and transmitted spectrum on the east–facing 30 nm–WSe_2 semitransparent windows on June 21st.

8.6.3. Average photopic transmission and colour rendering index evaluation.

The CIE colour space coordinates reveal the chromatic properties of the light source but do not give an insight into its brightness. Indeed, two different light sources may have the same coordinates in the CIE colour space, but one could be much brighter. Hence, a complete evaluation of the quality of the transmitted light requires to consider further parameters. The brightness of the transmitted light could be evaluated using the APT which determines the percentage of luminosity of the incident light that is transmitted through the semitransparent window. This parameter is widely used in the design of windows, for instance, concerning architectural glass, APT values above 60% look clear, and any value below 50% begins to look dark, coloured, and/or reflective [232]. Finally, the capacity of the light to faithfully render the colours is evaluated through the CRI. The acceptable values of the CRI depend on the lighting requirements of a room, but an 80 CRI is the general baseline for acceptable colour rendering. For places where colour appearance is particularly important for the ongoing work, a 90 CRI and above can be a reasonable value.

Table 8.2 shows the values of the CRI and APT for the transmitted spectrums illustrated in Figure 8.5.e(f). The 3 nm cases show higher values of ATP and CRI, and they could be used to provide clear illumination as ATP values surpass the threshold of 50%. The CRI values accomplish the highest requisites for colour rendering and these structures can be suitable for hospitals, textile factories, printing facilities, paint shops or any facilities where a high CRI is desirable. Thicker cases still provide an acceptable CRI, but ATP values indicate that transmitted light is beginning to get dark. These cases may be useful to reduce the excess of natural light brightness and heat instead of using light–blocking systems, which are common, for example, on west–facing facades of office buildings. The case of 30 nm–thick MoS_2 does not show CRI values matching the illumination standards, the deviation from the reference illuminant exceeds the aforementioned limit of $5.4 \cdot 10^{-3}$ units in the CIE 1960 UCS colour space [219]. Nonetheless, this structure can be used for other semitransparent applications such as coloured glass.

Table 8.2. CRI (dimensionless) and APT (percentage) of the transmitted light of different TMDC–based semitransparent power–generating windows on June 21st at 9 AM and December 21st at 11 AM with east–facing and southeast–facing façades.

	Thickness (nm)	*21st June, East*		*21st Dec. East*		*21st June, Southeast*		*21st Dec. Southeast*		*Type of illumination*
		CRI	**APT**	**CRI**	**APT**	**CRI**	**APT**	**CRI**	**APT**	
MoS_2	3	95.6	62.4	94.2	59.0	94.0	59.0	96.0	62.5	Clear
	11	92.9	31.2	90.6	31.8	90.2	31.7	93.4	31.1	Sun control
	30	–	15.4	–	15.8	–	15.7	–	15.5	Coloured
WSe_2	3	98.1	68.4	97.9	63.6	98.2	63.7	97.8	68.5	Clear
	11	95.7	43.7	95.7	41.7	96.1	41.7	95.2	43.7	Sun control
	30	93.7	24.0	93.3	22.8	93.8	22.8	93.2	24.0	Sun control
	55	83.9	14.9	82.4	13.1	82.8	13.1	83.6	15.0	Sun control

8.6.4. Angular acceptance of TMDC semitransparent windows

The architectural design and spatial orientation of the structure impose constraints on the precise placement of semitransparent windows or any BIPV application. Consequently, the angle at which incident light impinges semitransparent windows becomes notably inclined. In the formulation of semitransparent windows or the implementation of any BIPV system, it is more advantageous to optimise light absorption at an average angle of incidence rather than solely considering a perpendicular flux. Moreover, it would be advantageous that the structures maintain their absorptance even for very tilted incidence angles.

Figure 8.7.a(b) illustrates the variation in absorptance of the solar cell within the TMDC–based semitransparent module as the incidence angle changes. The structure was optimised for the average incidence angle during the day, resulting in a peak absorptance at 57º. Notably, the solar cell maintains its absorptance levels across various incident angles. It is worth mentioning that the reduction in

absorptance under sharply slanted incident light is primarily attributable to the front glass reflection. Solar cell manufacturers concentrate their efforts on mitigating reflection through the application of anti–reflective coatings or surface texturisation to achieve high absorptance, even at steep angles such as 80 degrees [233]. Nevertheless, in commercial applications involving encapsulated solar cells, the attainment of such high absorptance levels is unfeasible due to the intrinsic reflectance of the front glass, and these limitations are inherent to all types of solar modules.

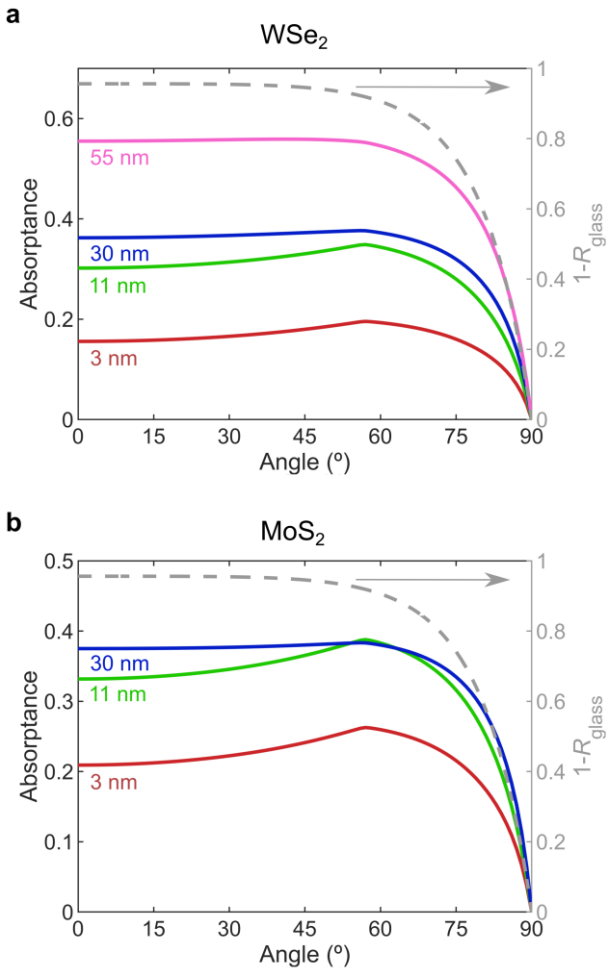

Figure 8.7. (a) (b) Angular acceptance of WSe_2 (MoS_2) module (left axis). In dashed grey, the fraction of light not reflected by the front glass (right axis).

8.6.5. Estimated power generation through TMDC semitransparent windows

Power generation through TMDC–semitransparent windows is calculated using the models explained in Section 8.5. Figure 8.8.a–d shows the resulting transmitted illumination flux, photocurrent, and estimated power for WSe_2 and MoS_2 semitransparent windows. The transmitted illumination flux is obtained from the product of the incident spectrum, the transmittance of the module, and the photopic function. The photocurrent generated is computed using Equation (8.12) and the photogenerated power is obtained from the current density–voltage curve of the device (Equation 8.14). The details about the calculation of these parameters were exposed in Subsection 8.5.3. The finger distance considered is 0.5 cm and the width of the fingers is 50 μm, which implies a shadow factor of 1% in the semitransparent devices. This value is so low that it is possible to neglect the effect of the fingers on the APT calculation. A more detailed calculation of the series resistance would probably allow a longer distance between fingers as TMDCs will present some degree of lateral transport and, therefore, the series resistance of the device would decrease.

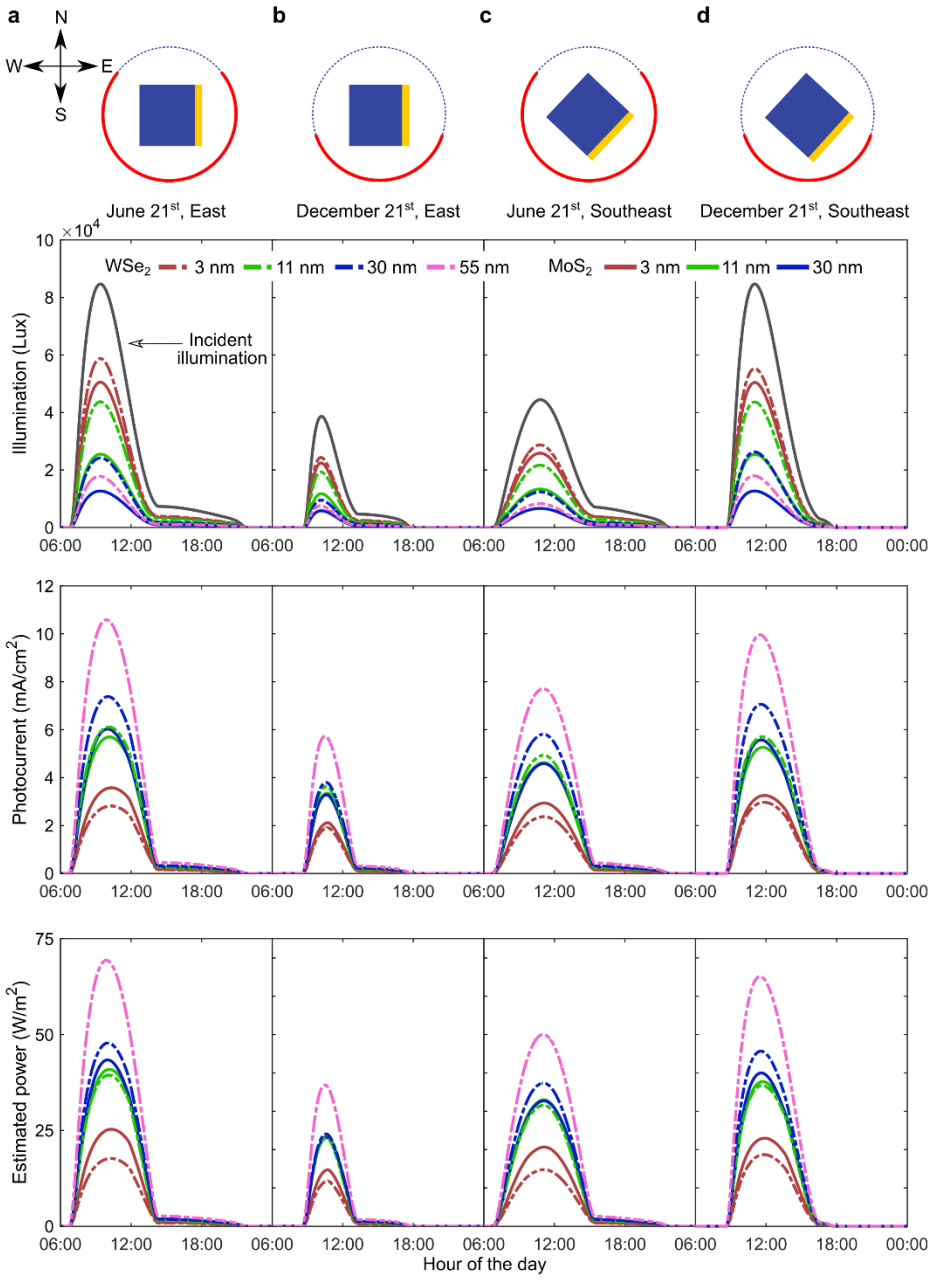

Figure 8.8. Transmitted illumination flux, calculated photocurrent, and estimated power density for MoS_2– and WSe_2–based semitransparent windows with different absorber thicknesses. (Left to right) (a) 21st June east–facing, (b) 21st December east–facing, (c) 21st June southeast–facing, (d) 21st December southeast–facing. Schematic of building orientation with the position of the module (yellow) and solar path (red).

Table 8.3 presents the outcome of the calculated daily energy output concerning the east– and southeast–facing façades on both June 21st and December 21st. The results indicate that, despite the light attenuation attributed to the semitransparent windows, the luminance level at the plane containing the window exceeds the 500 lux stipulated in the normative for office environments [205]. The

maximal energy production values are observed on June 21st in the case of the east–facing configuration. Nonetheless, the disparity in daily production between December and June is markedly more pronounced for the east–facing façade compared to the southeast–facing one. This implies that a southeast–facing arrangement would yield a more uniform production throughout the entire year. To select which is the optimal structure, it is distinguished between the different illumination levels provided according to Table 8.2. For clear windows, MoS_2–based windows demonstrate superior performance, exhibiting approximately 40% higher production on June 21st and 24% on December 21st compared to WSe_2. Conversely, in the context of sun control applications, WSe_2–based devices accommodate a broader range of admissible thicknesses than MoS_2, consequently resulting in higher power density output. The selection of the most suitable structure hinges on the consideration of admissible APT and CRI values, which are dependent on the building design and intended purposes. For instance, windows with lower ATP may find application in west–facing façades to mitigate glare disturbances at the end of the day when sunlight directly impacts the windows. The possibility of employing different window types within the same façade exists, as illumination levels may vary based on the floor of the building or the function of the illuminated area. For example, while standard office spaces necessitate 500 lux, corridors and passageways require less illumination.

Table 8.3. Energy density values of different TMDC–based semitransparent power–generating windows on June 21st and December 21st for east–facing and southeast–facing façades.

	Thickness (nm)	*Estimated daily power density production (Wh/m²)*				*Type of illumination*
		21st June, East	*21st Dec., East*	*21st June, Southeast*	*21st Dec. Southeast*	
MoS_2	3	127	41	111	110	Clear
	11	205	67	179	182	Sun control
	30	215	68	180	189	Coloured
WSe_2	3	91	33	81	90	Clear
	11	198	66	171	178	Sun control
	30	240	70	205	220	Sun control
	55	340	108	275	306	Sun control

8.6.6. Simulation of indoor Lighting conditions

The evaluation of various parameters thus far, encompassing chromaticity, ATP, and CRI, contributes to the establishment of a comprehensive dataset elucidating the features of illumination conditions provided by TMDC–based semitransparent windows. While these parameters prove valuable in characterising lighting, it is imperative to acknowledge that indoor illumination is additionally contingent upon the architectural attributes of the space. Nevertheless, a realistic image of the illumination conditions within a room can be attained through the merge of outputs from optical and spectral models, along with the utilisation of 3D creation software such as Blender. Using Blender, we create a scene of a standard office where windows have been substituted by TMDC–based semitransparent devices, and the illumination is mimicked using the tools provided by the software. These simulations have been conducted by Prof. Francisco Gómez–Campos (Universidad de Granada) using our input data.

To create the scene, we use the render engine Cycles. The scene consists of a building in which a set of office furniture was placed. Every material in the scene was a perfect white diffuse colour object. The windows were oriented to the east. The distance between the floor and the ceiling was set at 3.5 m. The furniture was placed at different distances from the windows to see the differences in lighting: a long table surrounded by chairs was placed 5 m away from the window and two desks were placed at 10 m from the window. An outdoor ground infinite plane was set to perfect black, and it was hidden in the rendered image, thus removing undesired effects in lighting like outdoor ground albedo or light coming from below the horizon in the absence of ground.

To simulate the illumination conditions, we have used two different light sources: a sun–type lamp for the direct light with the power corresponding to the integration of the spectrum irradiance and an RGB colour obtained from the tristimulus values XYZ computed from the transmission spectrum of the window, and an environment light using an emission node of strength value obtained from the diffuse transmission spectrum of the window. The colour of the sky in the images is directly obtained from those environment light RGB components and power conditions. The sun–type lamp orientation had two different configurations depending on the sun position at a specific date: azimuth=147.87º and elevation=19.07º (corresponding to December 21st, 11 a.m. local time, Madrid,

Spain) and azimuth=78.05º and elevation=22.95º (corresponding to June 21st, 9 a.m. local time, Madrid, Spain).

The emission node strength parameter is related to the power of the diffuse light source, but it needed to be calibrated because in Cycles that parameter is unitless. For calibration purposes, we use a perfect white diffuse colour plane with a sun–type light perpendicularly illuminating the object. A set of images is rendered changing the colour of the light in three rows: perfect red (R=1; G=0; B=0), perfect green (R=0; G=1; B=0) and perfect blue (R=0; G=0; B=1). In each case, a set of power values was swept (in W/m^2) and recorded the RGB values of the illuminated plane. The diffuse light was set to zero. In the second step, environmental light was used only in three rows again with the same colours and changing the value of the strength of the emission node, recording the RGB values of the illuminated plane. Then, we found the relation between the strength parameter and the direct light power, thus obtaining the equivalence of the strength parameter in W/m^2. Finally, the exposure was set to different values mimicking the adaptation of the pupil to different lighting conditions. The range of exposures was changed between 0.10 and 0.12.

Figure 8.9 shows the render result of Blender for the analysed cases of TMDC semitransparent windows in comparison to the use of common architectural glass. As it was predicted in Figure 8.5.e(f), the tonality of the transmitted light evolves from the white of the clear illumination cases to reddish and yellowish tones with the thickness of the TMDC layer. Clear structures almost do not show considerable differences when comparing them to the use of clear glass, proving that they provide optimal illumination conditions. The sun control cases show a darker tonality, but they still achieve a good illumination level according to the simulations. It is also observed how WSe_2–based devices can reach optimal illumination conditions even using the same thickness as MoS_2. While the window of 30 nm–thick WSe_2 appears as an acceptable case, the 30 nm–thick MoS_2 window has a yellowish tonality that does not resemble natural light.

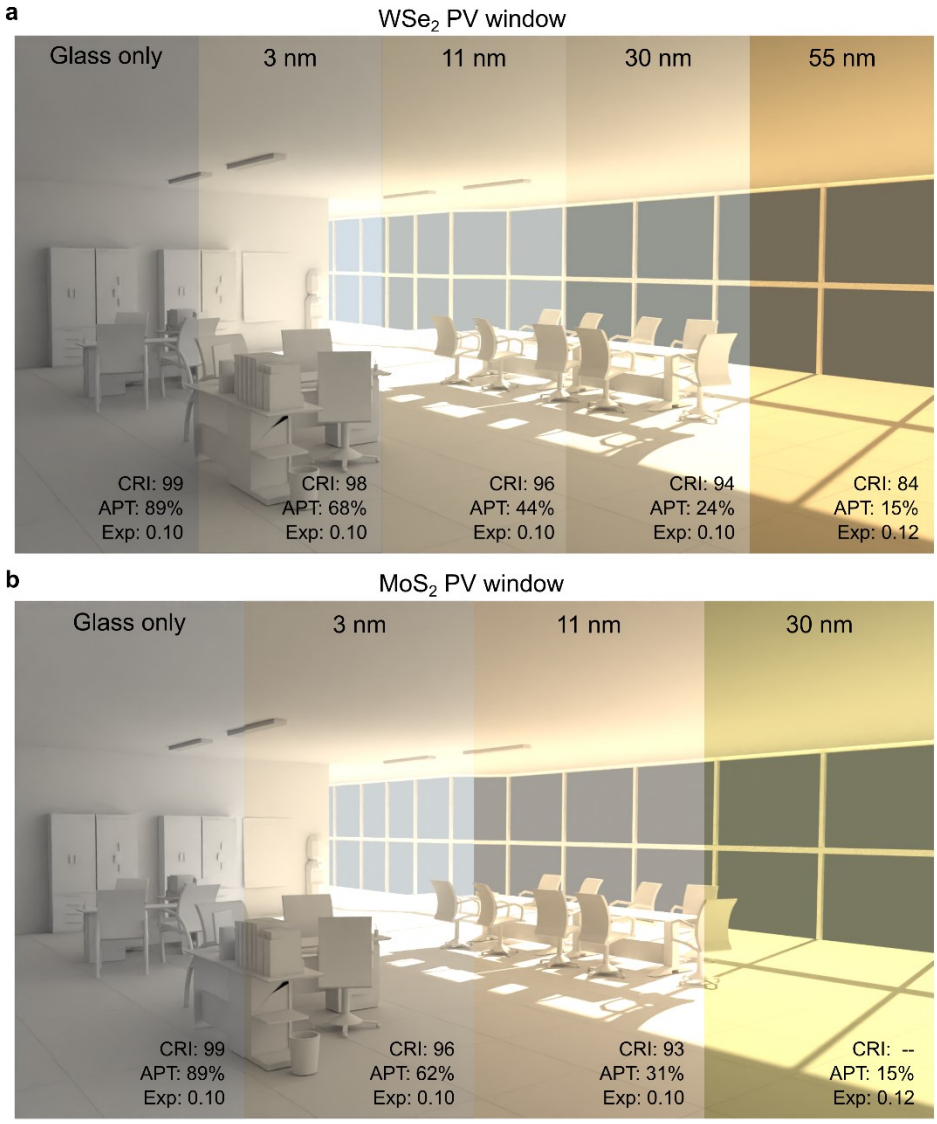

Figure 8.9. Simulation of the illumination inside an office with different cases of TMDC semitransparent windows for an east–facing façade on June 21st at 9 a.m. in Madrid, along with the CRI, the APT, and the level of exposition for each image. (a) WSe_2 PV windows and (b) MoS_2 PV windows.

8.6.7. Estimated power generation in TMDC opaque modules

TMDC semitransparent devices promise to be a reliable solution for power generation and illumination control. However, the TMDCs can be also used in opaque structures like standard solar modules. In Chapter 5, we discussed the advantages of the use of TMDCs in solar cells. Among them, there is the possibility of achieving maximum light absorptance with low material requirements and the opportunity to develop a range of flexible applications. Both characteristics are desirable concerning the BIPV prospectives as they would reduce fabrication costs

and adapt to the architectural elements of the buildings. When considering an entire building, it would be realistic that opaque structures were combined with semitransparent using the maximum area available. Hence, a building with TMDC semitransparent windows could integrate areas with TMDC opaque structures.

To estimate the power output of TMDC opaque modules, we use the same models employed for the semitransparent cases, but in this case, the thickness of the semiconductor layer is optimised to provide the maximum absorptance requiring the lowest amount of material Figure 8.10.a shows a schematic of the module structure. In this case, it has been added an aluminium layer that would work as a back reflector to improve absorptance. The back sheet marked in Figure 8.10.a can be made of encapsulant materials as EVA, but for our optical model does not interfere as is placed behind aluminium. Figure 8.10.b shows the optical absorptance of the solar cell inside the module and Figure 8.10.c–f illustrates the photocurrent and estimated power density output for the same cases analysed for semitransparent structures. The energy density yield values of each case are compiled in Table 8.4.

Table 8.4. Energy density production of different TMDC–based opaque power–generating modules on June 21st and December 21st for east–facing and southeast–facing façades.

	Thickness (nm)	*Estimated daily power density production (Wh/m²)*			
		21st June, East	*21st Dec. East*	*21st June, Southeast*	*21st Dec. Southeast*
MoS_2	123	415	129	329	377
WSe_2	72	490	155	381	452

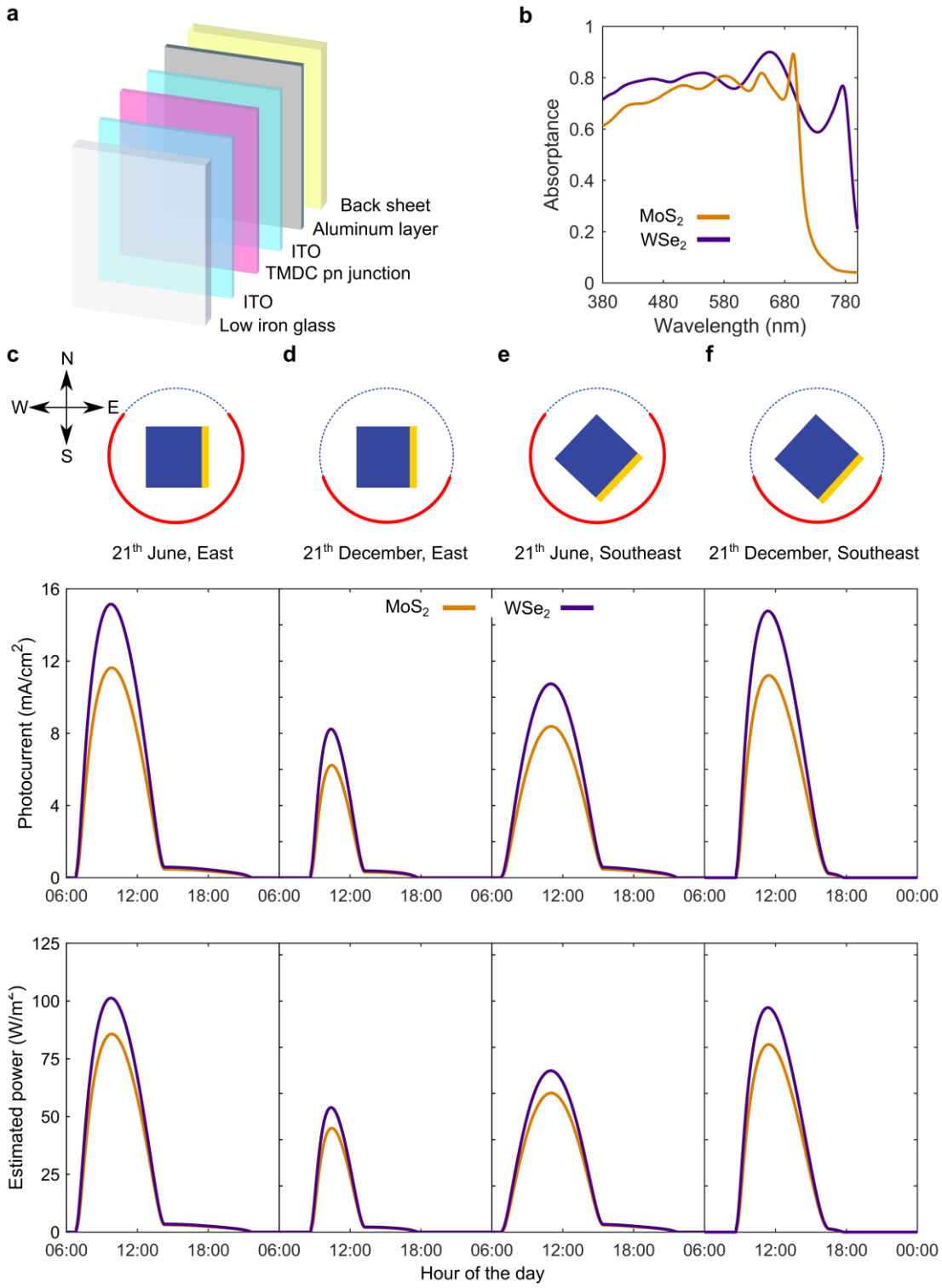

Figure 8.10. (a) Schematic of TMDC–based opaque module. (b) Absorptance of the solar cell inside the module structure. (Right to left) (c) 21st June east–facing, (d) 21st December east–facing, (e) 21st June southeast–facing, (f) 21st December southeast–facing. Schematic of building orientation with the position of the module (yellow) and solar path (red), calculated photocurrent and estimated power density.

8.7. Case of study: Picasso Tower

The purpose of BIPV is the implementation of solar photovoltaic devices that can supply the energy demand of buildings. In this sense, we consider the application of the evaluated TMDC–based structures in a real building. The building selected is the Picasso Tower, an office building located in Madrid, Spain, with coordinates 40º 24' N, 3º 42' W. The Picasso Tower is one of the most iconic buildings in the city. Designed by the Japanese architect Minoru Yamasaki, the building was erected in the 1980s, and it is placed in the heart of the financial centre of the Spanish capital city. The Picasso Tower has a height of 157 m and a base dimension of 49.6 x 37.7 m. The larger façades of the building are east–facing and west–facing. We have calculated the power consumption of this building using the estimation by CIBSE for general offices which is 95 KWh/m^2 per year [234]. The total office area of the tower is 71700 m^2 [235], resulting in an estimated daily consumption of 18.66 MWh.

To analyse the case of integration we suppose that the whole east–, south–, and west–facing façades of the building are covered by semitransparent TMDC–based windows for sun control, using the 11 nm–MoS_2 case and the 30 nm–WSe_2 case. These windows guarantee the minimum standardised illumination level of 500 lux [205] at the plane of the window even when there is no direct irradiance and provide optimal spectral characteristics according to the data presented in Table 8.2. Note that this analysis aims to provide insight into the feasibility of TMDC semitransparent structures, and not to study deeply a complex case of architectural integration. Therefore, we have neglected the shadow effect of the surrounding elements on the building, and we have considered the illumination conditions of a clear day with no clouds. This scenario resembles the schematic of Figure 8.1.b.

The daily energy output is 2.36 MWh for the MoS_2–based window on December 21st and 3.56 MWh on June 21st. The WSe_2 case shows a larger energy output, 2.97 MWh on December 21st and 4.36 MWh on June 21st. Although these values already represent a reasonable percentage of the overall energy consumption of the building, it is realistic to consider that one third of the façade is covered with opaque modules made of the same material. In this case, the overall energy production increases between 36 and 41% for MoS_2 and between 40 and 45% for WSe_2. As we have mentioned in Subsection 8.6.7, the integration of opaque

modules is a reliable solution, for example, for spaces between floors that contain electrical installations, ventilation ducts, etc.

The energy production of each façade varies depending on the date Figure 8.11 shows the energy production for each case on two dates and for each façade. East–facing and west–facing façades show a larger energy output in summer surpassing the output of the south–facing façade. Unlike rooftop modules, windows are usually in a vertical layout, and the elevated altitude of the sun at the central hours of the day in summer makes the incident angle on a vertical surface too steep. The conditions are different in December, where the incidence angle at the south–facing façade is less tilted. By contrast, production at east–facing and west–facing façades is lowered because of the azimuth angle at the dawn and the dusk. In the highest energy production case is achieved a production of 6.15 MWh per day which means 32.9% of the overall energy consumption of the building. If such value were achieved in every office building in Spain, it would be 11.6 TWh per year. This amount of energy represents 4.6% of the annual energy consumption in Spain during 2022 [236]. Table 8.5 compiles the data of the daily energy output for each case considered.

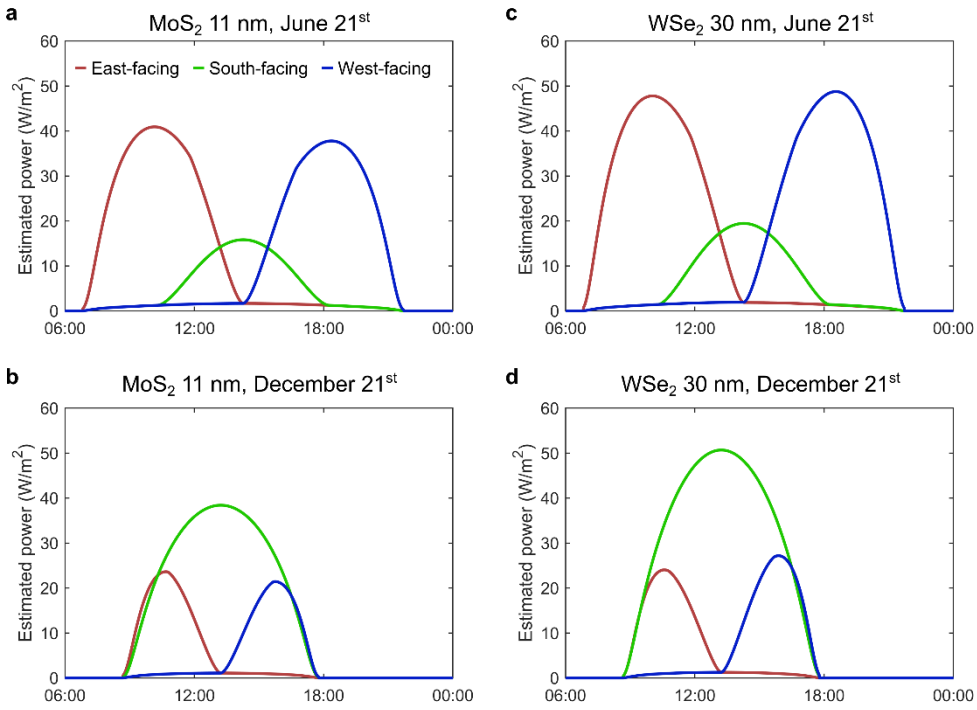

Figure 8.11. Energy density production of TMDC–based semitransparent power–generating windows in the Picasso Tower. (a) MoS_2 11 nm–thick on June 21st, (b) MoS_2 11 nm–thick on December 21st, (c) WSe_2 30 nm–thick on June 21st, (d) WSe_2 30 nm–thick on December 21st.

Table 8.5. Daily energy production and percentage over the building energy consumption for different solutions of sun control and sun control modules combined with opaque modules.

	Date	*Case 1: 100 % façade covered with semitransparent PV*		*Case 2: One third of the façade covered with opaque modules*	
		Energy production (MWh)	*% of energy consumption*	*Energy production (MWh)*	*% of energy consumption*
MoS_2	June 21st	3.56	19.1	4.85	26.0
	December 21st	2.36	12.7	3.31	17.7
WSe_2	June 21st	4.36	23.4	6.15	32.9
	December 21st	2.97	15.9	4.30	23.0

8.8. Summary

TMDC–based solar cells emerge as promising candidates for semitransparent applications owing to their layered structure, which enhances the absorption of specific wavelengths within the visible spectrum. Their layered configuration results in a well–balanced absorptance of visible light, a feature not attainable through conventional solar cell technologies. The performance of two TMDC–based power–generating semitransparent windows has been modelled, optimising their design to maximise energy production while ensuring the quality of transmitted light. In the analysis of two materials, MoS_2 and WSe_2, WSe_2 exhibits superior energy density production and accommodates a broader range of thicknesses without compromising the chromatic characteristics of transmitted light. Conversely, MoS_2 demonstrates enhanced performance when considering clear illumination as the desired scenario.

The energy yield of TMDCs has been evaluated as being able to reach up to 240 Wh/m^2 of power density generation in a WSe_2–based structure. These energy production values are achieved while maintaining optimal illumination conditions within buildings, characterised by a high CRI, appropriate APT, and acceptable luminosity values. The impact of incorporating TMDC semitransparent windows in a standard office setting has been assessed using Blender software. A faithful

representation of the layout of a standard office has been created and its illumination has been simulated using the output data from the optical and spectral modelling performed. The simulations reveal that the illumination conditions within the office meet the prescribed standards, with minimal deviation compared to the use of conventional clear glass windows.

The performance of TMDCs semitransparent structures has been evaluated in a realistic scenario using the Picasso Tower as a reference. The estimations indicate that the integration of TMDC–based power–generating semitransparent windows in this scenario could result in a substantial reduction of up to 23.4% in daily energy consumption. This percentage increases to 32.9% when semitransparent windows are coupled with opaque modules made from the same TMDCs. Although a further and more extensive analysis will be required, TMDC–based semitransparent windows exhibit significant potential for BIPV applications. The presented results prove that TMDCs could play a pivotal role in the decarbonisation of buildings and the path to clean energy production in the urban areas.

Chapter 9

Conclusions and future lines

9.1. Chapter 3: Large open–circuit voltage in a MoS_2 homojunction

MoS_2–based solar cells can reach high V_{OC} considering the band gap of the material. In this work this V_{OC} has surpassed the values of 1 V under concentrated light demonstrating the photoconversion potential of MoS_2 homojunctions even in non–optimised structures. The obtention of large V_{OC} in TMDC–based devices is limited because of the defective characteristics of the metal/semiconductor contacts. The presence of photoactive Schottky barriers induces photovoltage in the opposite direction to the photovoltage provided by the pn junction. Therefore, the resultant V_{OC} of the devices results from the difference between the pn junction and the Schottky contacts. By blocking the light incident on the contacts, the negative contribution on the V_{OC} of the contacts is eliminated, extracting the real photovoltage provided by the pn junction. However, although this photovoltage can be extracted, the rectifying nature of the Schottky contacts jeopardises the electrical characteristics of the devices and therefore their PCE.

The observed pinning effect in the V_{OC} of TMDC solar cells when increasing the illumination level is a consequence of the defective contacts. Although the pn junction provides a larger photovoltage when increasing illumination, the concurrent rise in the parasitic photovoltage at the contacts curtails the overall V_{OC} output yielded by the device. The pinning degree will depend on the features of each device, but it will always constrain the performance of the device under any illumination condition.

The obtention of ohmic contacts to TMDCs is an intricate problem as it not only depends on the properties of the metal and semiconductor chosen. The fabrication process of the contacts is a key aspect as any process that may damage the semiconductor will compromise the chance of achieving an ohmic contact. This issue is even more difficult to solve in TMDC–based devices because of the thinness of the material layers used. This feature hampers the use of the conventional

techniques employed in conventional materials to obtain ohmic contacts requiring customised design strategies to reach ohmic contacts to TMDCs.

Finally, the EQE characterisation shows that light absorption takes place in a narrow range of thicknesses. Although TMDCs exhibit a large absorption coefficient, its photogeneration is limited because of the high reflectivity. Hence, photogeneration could be potentially enhanced by the implementation of optical cavities that improve absorption through interference effects. To improve the light–energy conversion of these devices, we require the optimisation of the thickness of the semiconductor layers and the addition of new materials that could enhance their performance.

9.2. Chapter 4: Optical modelling of TMDC devices

The optical analysis of structures based on TMDCs necessitates the consideration of specific aspects inherent to these architectures. These particularities encompass the assessment of interference phenomena arising from light coherence and the anisotropic nature of TMDCs. Evaluation of interference effects is effectively accomplished through the utilisation of an optical model derived from the transfer–matrix method proposed by Centurioni. Incorporating the anisotropy of TMDCs entails using the refractive index values pertinent to the in–plane and out–plane directions, along with the expression for the index ellipsoid. The index ellipsoid determines the effective refractive index of the material at a given angle of propagation. It is pertinent to note that the developed model is not only pertinent to TMDC–based structures but also extends its applicability to any multilayered configuration where the refractive indices of each layer are known.

Using our optical model, we assessed the light absorption of the TMDC–based structures. To perform these calculations, it was necessary to implement the equations for solar position and SPD calculation. The absorption of direct light was easily evaluated introducing the angle of incidence. The absorption of diffuse light required the implementation of a model that considers the angular acceptance of the structures in the calculation of diffuse power absorption.

9.3. Chapter 5: Light absorption in TMDC devices

TMDC–based structures and especially MoS_2 show limited optical absorptance despite their strong absorption coefficients. This fact is mainly caused by their elevated values of refractive index that result in excessive reflectance. Therefore, it is necessary to implement device architectures that minimise reflection and enhance absorption to obtain well–performing solar cells.

It has been demonstrated that the utilisation of h–BN as ARL significantly enhances the absorptance of MoS_2–based devices. However, the enhancement of optical properties is not solely attributed to the inclusion of the ARL. The improvement in optical absorption achieved through the development of 1D nanocavities promises the development of a new concept of ultrathin solar cells. Within these structures, optimal absorptance is attained through the synergistic integration of the optical characteristics of TMDCs and the amplification of interference effects. The magnification of interference is contingent upon the structure of the devices and specific thickness values. The phenomena of interference maxima have been identified, denoting configurations that yield higher absorptance by intensifying interference effects.

The ultrathin characteristics of the TMDC layers in combination with the addition of metallic back reflectors and other layers contribute to increase optical absorptance to values up to ~90% of the AM1.5G spectrum in the visible range with minimal thickness requirements (~10 nm) by exploiting the zeroth–order FP resonance. The most remarkable feature is that such high absorptance levels are attainable without complex light–trapping strategies that would potentially increase the complexity and cost of the devices. Moreover, such thickness values are unattainable by conventional solar cell materials without unacceptable efficiency losses.

The elevated absorptance achieved in most of these ultrathin devices relies on the use of silver back reflectors, which may raise questions related to their cost in large–area devices. Nevertheless, theoretically, it has been demonstrated that the amount of silver required to fabricate these reflectors is minimal and can be even reduced when combining silver with lower–cost materials such as aluminium. Indeed, the amount of silver used in these structures is lower than the amount of silver used in conventional silicon solar cells.

9.4. Chapter 6: Electrical characterisation of TMDCs

TMDCs are sensible to the surrounding environment. The electric properties of the materials can be severely altered because of the effect of the materials in contact with the semiconductor and the atmosphere. These alterations are related to superficial effects that locally modify the carrier population of the TMDC and could even deplete the material completely.

Van der Pauw measurements are an effective procedure to determine the electric characteristics of TMDCs, but when performing material characterisation, it is important to balance the aforementioned environmental effects of the device to obtain reliable records. We have proved that the systematic Van de Pauw characterisation of samples with different thicknesses is useful to estimate the effect of the substrate on the properties of the TMDC as it can provide an approximation of the induced depleted thickness on a material layer. Results show that the substrates analysed, sapphire and SiO_2 induce an n–doping effect in agreement with the observations reported in the literature. Using the Van der Pauw method, it was possible to estimate the depleted thickness of p–MoS_2 samples and the charge accumulation induced by the sapphire substrate on n–MoS_2 samples. Nevertheless, this characterisation is incomplete as we have not quantified the effect of the environment on the surface, and the Van der Pauw measurements are affected by both substrate and atmosphere.

KPFM measurements reveal that not only the underlying substrates can alter the electrical properties, but also the surrounding atmosphere. Despite the scattering on the V_{CPD} values measured, it can be guessed that the atmosphere induces a p–doping effect on the surface of the materials. Moreover, the lower differences observed in the V_{CPD} measure between the p–material and the n–material of a pn junction in comparison to the experimental V_{OC} values recorded in experimental devices, suggest that the electrical characteristics of the materials in their surface differs from their bulk properties. This underlines the importance of the surface properties as they conditionate the performance of the devices.

9.5. Chapter 7: MoS_2 solar cell with Fermi–level–pinning–free contacts and anti–reflection–BN layer

The best MoS_2 homojunction solar cell reported in this work has a p^+pn structure and it has achieved a PCE of 3.82% and FF of 57.1% under a simulated light equivalent to the AM1.5G spectrum. To date, this is the highest PCE value ever reported for a MoS_2 homojunction ever reported and one of the highest values in TMDC–based solar cells. Such a result is the result of the device contact optimisation and the improvement of light absorption.

Contact optimisation has been achieved by improving the fabrication of contacts and a proper metal choice. The development of a double photoresist photolithography process along with the pick–up technique yields clean and almost defect–free surfaces that allow the approaching of the Schottky–Mott rule, avoiding the Fermi–level pinning effect and obtaining ohmic contacts. Moreover, the use of degenerately doped materials as a contact layer is a successful strategy to obtain ohmic contacts without introducing parasitic junctions.

Absorptance is improved by adding h–BN and optimising the thickness of the layers. The theoretical improvement in optical absorption by adding a h–BN ARL is demonstrated experimentally. Moreover, the addition of h–BN induces a passivation effect on the surface of the device as is observed in the increase of the V_{OC} before and after the ARL deposition. This also confirms that the material surfaces are not completely free of defects and can be altered by the surrounding environment.

Electrical properties of the device were successfully modelled showing the importance of the changes in the SCR width on the $J-V$ characteristics of the device. The results from the modelling show that in other to improve the PCE of MoS_2 homojunction solar cells, it is necessary to focus on the reduction of the ideality factor, and the improvement of the series resistance.

9.6. Chapter 8: Future applications of TMDC solar cells: Semitransparent windows

The increasing demand for electric energy is pushing the development of alternative ways to produce electricity. In this context, the implementation of semitransparent solar cells in BIPV is an interesting option where novel solar cell technologies may be applicable as conventional technologies struggle to accomplish the desired requirements. Concerning semitransparent applications, TMDCs are a plausible solution because of their outstanding optical properties of TMDC and the possibility of developing ultrathin devices.

While conventional materials show a steep absorptivity when reducing the thickness, TMDCs and especially WSe_2 have a balanced absorption through the whole visible spectrum thanks to the Van Hove singularities that raise the absorptance of these long wavelength photons. Therefore, it would be possible to implement TMDC semitransparent devices that maintain the colour neutrality of the transmitted spectrum assuring acceptable levels of APT and CRI according to the illumination standards.

The use of TMDCs semitransparent structures could be an interesting solution, especially for buildings with a large height/surface ratio such as skyscrapers. The potential energy yield of TMDCs could reach a value of 240 Wh/m^2 of power density generation while maintaining a high CRI, appropriate APT, and acceptable luminosity values within the building. We have assessed the visual impact of incorporating TMDC semitransparent windows in a standard office using Blender software. The simulations show minimal deviation in the chromatic characteristics of the transmitted light in comparison to the use of conventional clear glass windows.

We have estimated the potential energy savings in a realistic scenario using the Picasso Tower in Madrid as a reference. The implementation of TMDC–based power–generating semitransparent windows could provide 23.4% in daily energy consumption and up to 32.9% when semitransparent windows are coupled with opaque modules made from the same TMDCs. This is a rough estimation as we have simplified the optimisation problem not considering facts such as clouds, shadowing or the balance of the system of the installation, but the results still provide a reasonable high value of energy savings. Although TMDC devices are quite novel technology and it is still far from commercial applications, the

presented results prove that TMDCs could become an interesting option for developing systems for the decarbonisation of buildings.

9.7. Future lines of work

This Thesis presents one of the initial comprehensive research into the utilisation of TMDCs and especially MoS_2 in solar cell applications. Despite the limited depth of knowledge regarding the working principles of TMDC solar cells, numerous compelling arguments suggest that TMDCs could significantly contribute to the development of a novel generation of solar cell devices. Theoretical models anticipate that solar cells based on TMDCs may exhibit noteworthy performance, and initial experimental results show efficiency values that, while seemingly modest, are within the expected at the early stages of exploration. Indeed, comparable performance values were reported by established commercial technologies in their early stages of development, which themselves required extensive research and development over several years to achieve their current efficiency levels.

Although the journey towards the realisation of the first commercially viable TMDC–based device may be long, it has unmistakably commenced. The findings presented in this Thesis propose a series of avenues that may be pursued to address challenges associated with TMDC solar cells and facilitate the creation of devices with enhanced energy yield.

- Experimental devices presented in this Thesis were built at the microscopical level. The fabrication techniques employed here are only useful to create proof–of–concept devices. A huge step towards commercial cells would be the construction of macroscopical cells. Large TMDC substrates of some square inches have been already achieved. The combination of these fabrication methods along with effective doping schemes would allow the obtention of large solar cells. They do not only offer the advantage of easier characterisation but also it can be guessed that they could provide a better performance than microscopic devices.
- Chapters 3 and 7 manifest the importance of the electrical contacts to TMDCs in minimising losses during electric power extraction. The achievement of ohmic contacts relies on the proper selection of the binomial metal/semiconductor and a thorough fabrication process. Unlike conventional solar cells, TMDCs are not susceptible to undergo the standard

procedures to develop ohmic contacts requiring to pursuit of customised strategies. Band alignment is important in TMDC solar cells, and it has been shown that the use of heavily doped TMDCs also is an effective way to avoid the presence of Schottky contacts. Moreover, the results presented in Chapters 3 and 7 are limited by the high lateral series resistance, which is expected in ultrathin devices. Future TMDC solar cells could obtain ohmic and low–resistive contacts by the implementation of these heavily doped materials that require effective doping strategies. Besides, the fabrication of large–area devices would help to reduce lateral series resistance and improve the PCE values.

- Chapter 5 showed that TMDC ultrathin structures may show outstanding optical absorption with minimal thickness requirements. However, the enhancement of light absorption through interference effects (M0 interference maxima enhancement) may be a laborious task, especially because of the quality of the device layers, which must be homogeneous and flawless to allow interference to take place. It is necessary to underline that these ultrathin devices may show elevated absorption and theoretically optimised carrier collection because of their thinness, but the use of such ultrathin layers involves problems that need to be tackled. One example is materials carrier depletion as it was shown in Chapters 6. Another problem of ultrathin devices is the excessive lateral series resistance. Therefore, it would be advisable, at list in the first attempts to fabricate large are devices that TMDC solar cells try to approximate structures that maximise optical absorption at thicker devices (M1 interference maxima).
- Chapter 6 demonstrates that TMDCs, particularly when formed into layers just a few nanometres thick, exhibit sensitivity to their surrounding environment. Phenomena such as layer depletion must be prevented to ensure the functionality of devices. It is suggested that isolating materials as h–BN, be utilised. We have demonstrated that h–BN enhances carrier collection but also serves as a protective barrier against external factors for TMDCs.
- Chapter 8 presents an initial assessment of the potential application of TMDCs in semitransparent devices. Consistent with the aforementioned findings, the adoption of large–area fabrication techniques could facilitate the development of semitransparent structures. Consequently, the findings detailed in Chapter 8 can be corroborated through experimental investigations. These investigations should be directed towards determining the PCE of the devices alongside analysing the spectral characteristics of the transmitted light.

References

1. *World Energy Outlook 2022. License: CC BY 4.0 (Report); CC BY NC SA 4.0 (Chapter 3)* (International Energy Agency, 2022).
2. H. O. Pörtner, D. C. Roberts, M. Tignor, E. S. Poloczanska, K. Mintenbeck, A. Alegria, M. Craig, S. Langsdorf, S. Löschke, V. Möller, A. Okem, and B. Rama, *Climate Change 2022: Impacts, Adaptation and Vulnerability. Contribution of Working Group II to the Sixth Assessment Report of the Intergovernmental Panel on Climate Change* (Intergovernmental Panel on Climate Change, 2022).
3. S. Phillips and W. Warmuth, *Photovoltaics Report* (Fraunhofer Institute for Solar Energy Systems, ISE with support of PSE Projects GmbH, 2023).
4. *IEA, Change in Electricity Generation in the Stated Policies Scenario between 2021 and 2030* (International Energy Agency, 2022).
5. A. Richter, M. Hermle, and S. W. Glunz, "Reassessment of the Limiting Efficiency for Crystalline Silicon Solar Cells," IEEE Journal of Photovoltaics **3**(4), 1184–1191 (2013).
6. "Longi claims world's highest efficiency for silicon solar cells," https://web.archive.org/web/20240416093823/https://www.pv-magazine.com/2022/11/21/longi-claims-worlds-highest-silicon-solar-cell-efficiency/.
7. IEA, "Solar PV manufacturing capacity and production by country and region, 2021-2027," https://www.iea.org/data-and-statistics/charts/solar-pv-manufacturing-capacity-and-production-by-country-and-region-2021-2027.
8. M. A. Green, E. D. Dunlop, J. Hohl-Ebinger, M. Yoshita, N. Kopidakis, K. Bothe, D. Hinken, M. Rauer, and X. Hao, "Solar cell efficiency tables (Version 60)," Progress in Photovoltaics: Research and Applications **30**(7), 687–701 (2022).
9. K. S. Novoselov, A. K. Geim, S. V. Morozov, D. Jiang, Y. Zhang, S. V. Dubonos, I. V. Grigorieva, and A. A. Firsov, "Electric Field Effect in Atomically Thin Carbon Films," Science **306**(5696), 666–669 (2004).
10. M. Zeng, Y. Xiao, J. Liu, K. Yang, and L. Fu, "Exploring Two-Dimensional Materials toward the Next-Generation Circuits: From Monomer Design to Assembly Control," Chem. Rev. **118**(13), 6236–6296 (2018).
11. S. Manzeli, D. Ovchinnikov, D. Pasquier, O. V. Yazyev, and A. Kis, "2D transition metal dichalcogenides," Nat Rev Mater **2**(8), 1–15 (2017).
12. R. Lv, J. A. Robinson, R. E. Schaak, D. Sun, Y. Sun, T. E. Mallouk, and M. Terrones, "Transition metal dichalcogenides and beyond: synthesis,

properties, and applications of single- and few-layer nanosheets," Acc Chem Res **48**(1), 56–64 (2015).

13. R. G. Dickinson and L. Pauling, "The crystal structure of Molybdenite," J. Am. Chem. Soc. **45**(6), 1466–1471 (1923).
14. R. F. Frindt and A. D. Yoffe, "Physical Properties of Layer Structures: Optical Properties and Photoconductivity of Thin Crystals of Molybdenum Disulphide," Proceedings of the Royal Society of London. Series A, Mathematical and Physical Sciences **273**(1352), 69–83 (1963).
15. K. Mak, C. Lee, J. Hone, J. Shan, and T. Heinz, "Atomically Thin MoS_2 : A New Direct-Gap Semiconductor," Physical review letters **105**, 136805 (2010).
16. J. A. Wilson and A. D. Yoffe, "The transition metal dichalcogenides discussion and interpretation of the observed optical, electrical and structural properties," Advances in Physics **18**(73), 193–335 (1969).
17. Y. Zhan, Z. Liu, S. Najmaei, P. M. Ajayan, and J. Lou, "Large-Area Vapor-Phase Growth and Characterization of MoS_2 Atomic Layers on a SiO_2 Substrate," Small **8**(7), 966–971 (2012).
18. Y.-H. Lee, X.-Q. Zhang, W. Zhang, M.-T. Chang, C.-T. Lin, K.-D. Chang, Y.-C. Yu, J. T.-W. Wang, C.-S. Chang, L.-J. Li, and T.-W. Lin, "Synthesis of Large-Area MoS_2 Atomic Layers with Chemical Vapor Deposition," Advanced Materials **24**(17), 2320–2325 (2012).
19. J.-W. Chung, Z. R. Dai, and F. S. Ohuchi, "WS_2 thin films by metal organic chemical vapor deposition," Journal of Crystal Growth **186**(1), 137–150 (1998).
20. H. Yang, A. Giri, S. Moon, S. Shin, J.-M. Myoung, and U. Jeong, "Highly Scalable Synthesis of MoS_2 Thin Films with Precise Thickness Control via Polymer-Assisted Deposition," Chem. Mater. **29**(14), 5772–5776 (2017).
21. B. W. H. Baugher, H. O. H. Churchill, Y. Yang, and P. Jarillo-Herrero, "Optoelectronic devices based on electrically tunable p-n diodes in a monolayer dichalcogenide," Nat Nanotechnol **9**(4), 262–267 (2014).
22. W. M. Haynes, D. R. Lide, and T. J. Bruno, *Abundance of Elements in the Earth's Crust and in the Sea, CRC Handbook of Chemistry and Physics* (Taylor & Francis group, CRC Press, 2016), **97**.
23. L. Britnell, R. M. Ribeiro, A. Eckmann, R. Jalil, B. D. Belle, A. Mishchenko, Y.-J. Kim, R. V. Gorbachev, T. Georgiou, S. V. Morozov, A. N. Grigorenko, A. K. Geim, C. Casiraghi, A. H. C. Neto, and K. S. Novoselov, "Strong Light-Matter Interactions in Heterostructures of Atomically Thin Films," Science **340**(6138), 1311–1314 (2013).
24. R. Addou, S. McDonnell, D. Barrera, Z. Guo, A. Azcatl, J. Wang, H. Zhu, C. L. Hinkle, M. Quevedo-Lopez, H. N. Alshareef, L. Colombo, J. W. P. Hsu, and R. M. Wallace, "Impurities and Electronic Property Variations of Natural MoS_2 Crystal Surfaces," ACS Nano **9**(9), 9124–9133 (2015).

25. J. Wong, D. Jariwala, G. Tagliabue, K. Tat, A. R. Davoyan, M. C. Sherrott, and H. A. Atwater, "High Photovoltaic Quantum Efficiency in Ultrathin van der Waals Heterostructures," ACS Nano **11**(7), 7230–7240 (2017).

26. D. Jariwala, A. R. Davoyan, J. Wong, and H. A. Atwater, "Van der Waals Materials for Atomically-Thin Photovoltaics: Promise and Outlook," ACS Photonics **4**(12), 2962–2970 (2017).

27. C.-H. Lee, G.-H. Lee, A. M. van der Zande, W. Chen, Y. Li, M. Han, X. Cui, G. Arefe, C. Nuckolls, T. F. Heinz, J. Guo, J. Hone, and P. Kim, "Atomically thin p–n junctions with van der Waals heterointerfaces," Nature Nanotech **9**(9), 676–681 (2014).

28. M. M. Furchi, A. Pospischil, F. Libisch, J. Burgdörfer, and T. Mueller, "Photovoltaic effect in an electrically tunable van der Waals heterojunction," Nano Lett **14**(8), 4785–4791 (2014).

29. A. Pospischil, M. M. Furchi, and T. Mueller, "Solar-energy conversion and light emission in an atomic monolayer p-n diode," Nat Nanotechnol **9**(4), 257–261 (2014).

30. R. Frisenda, A. J. Molina-Mendoza, T. Mueller, A. Castellanos-Gomez, and H. S. J. van der Zant, "Atomically thin p–n junctions based on two-dimensional materials," Chem. Soc. Rev. **47**(9), 3339–3358 (2018).

31. S. Wi, H. Kim, M. Chen, H. Nam, L. J. Guo, E. Meyhofer, and X. Liang, "Enhancement of Photovoltaic Response in Multilayer MoS_2 Induced by Plasma Doping," ACS Nano **8**(5), 5270–5281 (2014).

32. D. Jariwala, A. R. Davoyan, G. Tagliabue, M. C. Sherrott, J. Wong, and H. A. Atwater, "Near-Unity Absorption in van der Waals Semiconductors for Ultrathin Optoelectronics," Nano Lett **16**(9), 5482–5487 (2016).

33. H. S. Lee, J. Ahn, W. Shim, S. Im, and D. K. Hwang, "2D WSe_2/MoS_2 van der Waals heterojunction photodiode for visible-near infrared broadband detection," Applied Physics Letters **113**(16), 163102 (2018).

34. J. Ahn, P. J. Jeon, S. R. A. Raza, A. Pezeshki, S.-W. Min, D. K. Hwang, and S. Im, "Transition metal dichalcogenide heterojunction PN diode toward ultimate photovoltaic benefits," 2D Mater. **3**(4), 045011 (2016).

35. K. Nassiri Nazif, A. Daus, J. Hong, N. Lee, S. Vaziri, A. Kumar, F. Nitta, M. E. Chen, S. Kananian, R. Islam, K.-H. Kim, J.-H. Park, A. S. Y. Poon, M. L. Brongersma, E. Pop, and K. C. Saraswat, "High-specific-power flexible transition metal dichalcogenide solar cells," Nat Commun **12**(1), 7034 (2021).

36. "Sapphire Substrates," https://web.archive.org/web/20240221144711/https%3A%2F%2Fwww.ossila.com%2Fproducts%2Fsapphire-substrates%3F_pos%3D1%26_sid%3D667f3d820%26_ss%3Dr.

37. "Polymethylglutarimide (PMGI) Resists | Kayaku Advanced Materials," https://web.archive.org/web/20240221145831/https%3A%2F%2Fkayakuam.

com%2Fwp-content%2Fuploads%2F2023%2F08%2FKAM-LOR-PMGI-Data-Sheet.8.21.23-final.pdf.

38. "Photoresist AZ 1512HS Photoresists MicroChemicals GmbH," https://web.archive.org/web/20240221150333/https%3A%2F%2Fwww.microchemicals.com%2Fproducts%2Fphotoresists%2Faz_1512_hs.html.

39. H. Schäfer, *Chemical Transport Reactions* (Elsevier, 2013).

40. S. Y. Wang, T. S. Ko, C. C. Huang, D. Y. Lin, and Y. S. Huang, "Optical and electrical properties of MoS_2 and Fe-doped MoS_2," Jpn. J. Appl. Phys. **53**(4S), 04EH07 (2014).

41. J. Suh, T.-E. Park, D.-Y. Lin, D. Fu, J. Park, H. J. Jung, Y. Chen, C. Ko, C. Jang, Y. Sun, R. Sinclair, J. Chang, S. Tongay, and J. Wu, "Doping against the Native Propensity of MoS_2: Degenerate Hole Doping by Cation Substitution," Nano Lett. **14**(12), 6976–6982 (2014).

42. A. K. Geim and I. V. Grigorieva, "Van der Waals heterostructures," Nature **499**(7459), 419–425 (2013).

43. R. Frisenda, E. Navarro-Moratalla, P. Gant, D. P. D. Lara, P. Jarillo-Herrero, R. V. Gorbachev, and A. Castellanos-Gomez, "Recent progress in the assembly of nanodevices and van der Waals heterostructures by deterministic placement of 2D materials," Chemical Society Reviews **47**(1), 53–68 (2018).

44. C. R. Dean, A. F. Young, I. Meric, C. Lee, L. Wang, S. Sorgenfrei, K. Watanabe, T. Taniguchi, P. Kim, K. L. Shepard, and J. Hone, "Boron nitride substrates for high-quality graphene electronics," Nat Nanotechnol **5**(10), 722–726 (2010).

45. G. F. Schneider, V. E. Calado, H. Zandbergen, L. M. K. Vandersypen, and C. Dekker, "Wedging Transfer of Nanostructures," Nano Lett. **10**(5), 1912–1916 (2010).

46. P. J. Zomer, S. P. Dash, N. Tombros, and B. J. Van Wees, "A transfer technique for high mobility graphene devices on commercially available hexagonal boron nitride," Applied Physics Letters **99**(23), 232104 (2011).

47. A. Castellanos-Gomez, M. Buscema, R. Molenaar, V. Singh, L. Janssen, H. S. J. van der Zant, and G. A. Steele, "Deterministic transfer of two-dimensional materials by all-dry viscoelastic stamping," (2014).

48. F. Pizzocchero, L. Gammelgaard, B. S. Jessen, J. M. Caridad, L. Wang, J. Hone, P. Bøggild, and T. J. Booth, "The hot pick-up technique for batch assembly of van der Waals heterostructures," Nat Commun **7**(1), 11894 (2016).

49. L. Wang, I. Meric, P. Y. Huang, Q. Gao, Y. Gao, H. Tran, T. Taniguchi, K. Watanabe, L. M. Campos, D. A. Muller, J. Guo, P. Kim, J. Hone, K. L. Shepard, and C. R. Dean, "One-Dimensional Electrical Contact to a Two-Dimensional Material," Science **342**(6158), 614–617 (2013).

50. M. A. Meitl, Z.-T. Zhu, V. Kumar, K. J. Lee, X. Feng, Y. Y. Huang, I. Adesida, R. G. Nuzzo, and J. A. Rogers, "Transfer printing by kinetic control of adhesion to an elastomeric stamp," Nature Mater **5**(1), 33–38 (2006).

51. K. L. Haley, J. A. Cloninger, K. Cerminara, R. M. Sterbentz, T. Taniguchi, K. Watanabe, and J. O. Island, "Heated Assembly and Transfer of Van der Waals Heterostructures with Common Nail Polish," Nanomanufacturing **1**(1), 49–56 (2021).

52. "Thorlabs - FDS1010 Si Photodiode, 65 ns Rise Time, 350 - 1100 nm, 10 mm x 10 mm Active Area," https://web.archive.org/web/20240221151420/https%3A%2F%2Fwww.thorlabs.com%2Fthorproduct.cfm%3Fpartnumber%3DFDS1010.

53. "RC18 Datasheet," https://web.archive.org/web/20240221151215/https%3A%2F%2Fsupport.atonometrics.com%2Fsupport%2Fsolutions%2Farticles%2F71000000463-rc18-datasheet.

54. L. J. Van der Pauw, "A method of measuring specific resistivity and Hall effect on lamellae of arbitrary shape," Philips Technical Review **20**(20), 220–224 (1958).

55. J. Lü, E. Delamarche, L. Eng, R. Bennewitz, E. Meyer, and H.-J. Güntherodt, "Kelvin Probe Force Microscopy on Surfaces: Investigation of the Surface Potential of Self-Assembled Monolayers on Gold," Langmuir **15**(23), 8184–8188 (1999).

56. W. A. Zisman, "A new method of measuring contact potential differences in metals," Review of Scientific Instruments **3**(7), 367–370 (1932).

57. Y. Almadori, N. Bendiab, and B. Grévin, "Multimodal Kelvin Probe Force Microscopy Investigations of a Photovoltaic WSe_2/MoS_2 Type-II Interface," ACS Appl. Mater. Interfaces **10**(1), 1363–1373 (2018).

58. M. J. Shearer, M.-Y. Li, L.-J. Li, S. Jin, and R. J. Hamers, "Nanoscale Surface Photovoltage Mapping of 2D Materials and Heterostructures by Illuminated Kelvin Probe Force Microscopy," J. Phys. Chem. C **122**(25), 13564–13571 (2018).

59. M. Moun, M. Kumar, M. Garg, R. Pathak, and R. Singh, "Understanding of MoS_2/GaN Heterojunction Diode and its Photodetection Properties," Sci Rep **8**(1), 11799 (2018).

60. J. Colchero, A. Gil, and A. M. Baró, "Resolution enhancement and improved data interpretation in electrostatic force microscopy," Phys. Rev. B **64**(24), 245403 (2001).

61. M. Luna, J. Colchero, and A. M. Baró, "Study of Water Droplets and Films on Graphite by Noncontact Scanning Force Microscopy.," The Journal of Physical Chemistry B **103**(44), 9576–9581 (1999).

62. P. J. de Pablo, J. Colchero, M. Luna, J. Gómez-Herrero, and A. M. Baró, "Tip-sample interaction in tapping-mode scanning force microscopy," Phys. Rev. B **61**(20), 14179–14183 (2000).

63. A. Gil, J. Colchero, J. Gómez-Herrero, and A. M. Baró, "Electrostatic force gradient signal: resolution enhancement in electrostatic force microscopy and improved Kelvin probe microscopy," Nanotechnology **14**, 332–340 (2003).

64. M. Luna, M. Barawi, S. Gómez-Moñivas, J. Colchero, M. Rodríguez-Peña, S. Yang, X. Zhao, Y.-H. Lu, R. Chintala, P. Reñones, V. Altoe, L. Martínez, Y. Huttel, S. Kawasaki, A. Weber-Bargioni, V. A. de la Peña ÓShea, P. Yang, P. D. Ashby, and M. Salmeron, "Photoinduced Charge Transfer and Trapping on Single Gold Metal Nanoparticles on TiO_2," ACS Applied Materials and Interfaces **13**(42), 50531–50538 (2021).

65. A. Minj, A. Cros, N. Garro, J. Colchero, T. Auzelle, and B. Daudin, "Assessment of Polarity in GaN Self-Assembled Nanowires by Electrical Force Microscopy," Nano Lett **15**(10), 6770–6776 (2015).

66. R. Boisgard, D. Michel, and J. P. Aimé, "Hysteresis generated by attractive interaction: oscillating behavior of a vibrating tip–microlever system near a surface," Surface Science **401**(2), 199–205 (1998).

67. I. Horcas, R. Fernández, J. M. Gómez-Rodríguez, J. Colchero, J. Gómez-Herrero, and A. M. Baro, "WSXM: A software for scanning probe microscopy and a tool for nanotechnology," Review of Scientific Instruments **78**(1), 013705 (2007).

68. R. R. King, D. Bhusari, A. Boca, D. Larrabee, X.-Q. Liu, W. Hong, C. M. Fetzer, D. C. Law, and N. H. Karam, "Band gap-voltage offset and energy production in next-generation multijunction solar cells," Progress in Photovoltaics: Research and Applications **19**(7), 797–812 (2011).

69. H. J. Snaith, "Perovskites: The Emergence of a New Era for Low-Cost, High-Efficiency Solar Cells," J. Phys. Chem. Lett. **4**(21), 3623–3630 (2013).

70. W. Shockley and H. J. Queisser, "Detailed Balance Limit of Efficiency of p-n Junction Solar Cells," Journal of Applied Physics **32**(3), 510–519 (1961).

71. B. M. Kayes, H. Nie, R. Twist, S. G. Spruytte, F. Reinhardt, I. C. Kizilyalli, and G. S. Higashi, "27.6% Conversion efficiency, a new record for single-junction solar cells under 1 sun illumination," in *2011 37th IEEE Photovoltaic Specialists Conference* (2011), pp. 000004–000008.

72. K. Yoshikawa, H. Kawasaki, W. Yoshida, T. Irie, K. Konishi, K. Nakano, T. Uto, D. Adachi, M. Kanematsu, H. Uzu, and K. Yamamoto, "Silicon heterojunction solar cell with interdigitated back contacts for a photoconversion efficiency over 26%," Nat Energy **2**(5), 1–8 (2017).

73. W. S. Yang, J. H. Noh, N. J. Jeon, Y. C. Kim, S. Ryu, J. Seo, and S. I. Seok, "High-performance photovoltaic perovskite layers fabricated through intramolecular exchange," Science **348**(6240), 1234–1237 (2015).

74. M. Saito, Y. Nakano, R. Hayase, N. Shida, T. Gotanda, S. Mori, H. Nakao, H. Oooka, and M. Hosoya, "Module Development for Organic Thin-Film Photovoltaics," 28th European Photovoltaic Solar Energy Conference and Exhibition 2236–2238 (2013).

75. S. A. Svatek, C. Bueno-Blanco, D.-Y. Lin, J. Kerfoot, C. Macías, M. H. Zehender, I. Tobías, P. García-Linares, T. Taniguchi, K. Watanabe, P. Beton, and E. Antolín, "High open-circuit voltage in transition metal dichalcogenide solar cells," Nano Energy **79**, 105427 (2021).

76. C. Bueno-Blanco, S. A. Svatek, D.-Y. Lin, C. Macías, M. García-Sánchez, M. H. Zehender, K. Watanabe, T. Taniguchi, P. García-Linares, and E. Antolín, "High open-circuit voltage MoS_2 homojunction - effect of Schottky barriers at the contacts," in *2020 47th IEEE Photovoltaic Specialists Conference (PVSC)* (2020), pp. 0324–0329.

77. M. Chhowalla, H. S. Shin, G. Eda, L.-J. Li, K. P. Loh, and H. Zhang, "The chemistry of two-dimensional layered transition metal dichalcogenide nanosheets," Nature Chem **5**(4), 263–275 (2013).

78. Y. Guo and J. Robertson, "Band engineering in transition metal dichalcogenides: Stacked versus lateral heterostructures," Appl. Phys. Lett. **108**(23), 233104 (2016).

79. E. Parthe, L. Gelato, B. Chabot, M. Penzo, K. Cenzual, R. Gladyshevskii, and L. Gmelin, *Gmelin Handbook of Inorganic and Organometallic Chemistry: TYPIX: Standardized Data and Crystal Chemical Characterization of Inorganic Structure Types.* (Spriger, 1993).

80. C. Hsu, R. Frisenda, R. Schmidt, A. Arora, S. M. Vasconcellos, R. Bratschitsch, H. S. J. Zant, and A. Castellanos-Gomez, "Thickness-Dependent Refractive Index of 1L, 2L, and 3L MoS_2, $MoSe_2$, WS_2, and WSe_2," Adv. Optical Mater. **7**(13), 1900239 (2019).

81. B. Song, H. Gu, M. Fang, X. Chen, H. Jiang, R. Wang, T. Zhai, Y.-T. Ho, and S. Liu, "Layer-Dependent Dielectric Function of Wafer-Scale 2D MoS_2," Advanced Optical Materials **7**(2), 1801250 (2019).

82. A. Castellanos-Gomez, J. Quereda, H. P. van der Meulen, N. Agraït, and G. Rubio-Bollinger, "Spatially resolved optical absorption spectroscopy of single- and few-layer MoS_2 by hyperspectral imaging," Nanotechnology **27**(11), 115705 (2016).

83. D. Wickramaratne, L. Weston, and C. G. Van de Walle, "Monolayer to Bulk Properties of Hexagonal Boron Nitride," J. Phys. Chem. C **122**(44), 25524–25529 (2018).

84. P. Lin, L. Zhu, D. Li, L. Xu, C. Pan, and Z. Wang, "Piezo-Phototronic Effect for Enhanced Flexible MoS_2/WSe_2 van der Waals Photodiodes," Advanced Functional Materials **28**(35), 1802849 (2018).

85. A. Chaves, J. G. Azadani, H. Alsalman, D. R. da Costa, R. Frisenda, A. J. Chaves, S. H. Song, Y. D. Kim, D. He, J. Zhou, A. Castellanos-Gomez, F. M. Peeters, Z. Liu, C. L. Hinkle, S.-H. Oh, P. D. Ye, S. J. Koester, Y. H. Lee, P.

Avouris, X. Wang, and T. Low, "Bandgap engineering of two-dimensional semiconductor materials," npj 2D Mater Appl **4**(1), 1–21 (2020).

86. L. Liu, S. Ryu, M. R. Tomasik, E. Stolyarova, N. Jung, M. S. Hybertsen, M. L. Steigerwald, L. E. Brus, and G. W. Flynn, "Graphene Oxidation: Thickness-Dependent Etching and Strong Chemical Doping," Nano Lett. **8**(7), 1965–1970 (2008).

87. D. C. Elias, R. R. Nair, T. M. G. Mohiuddin, S. V. Morozov, P. Blake, M. P. Halsall, A. C. Ferrari, D. W. Boukhvalov, M. I. Katsnelson, A. K. Geim, and K. S. Novoselov, "Control of Graphene's Properties by Reversible Hydrogenation: Evidence for Graphane," Science **323**(5914), 610–613 (2009).

88. H. Qiu, T. Xu, Z. Wang, W. Ren, H. Nan, Z. Ni, Q. Chen, S. Yuan, F. Miao, F. Song, G. Long, Y. Shi, L. Sun, J. Wang, and X. Wang, "Hopping transport through defect-induced localized states in molybdenum disulphide," Nat Commun **4**(1), 2642 (2013).

89. Q. Cheng, J. Pang, D. Sun, J. Wang, S. Zhang, F. Liu, Y. Chen, R. Yang, N. Liang, X. Lu, Y. Ji, J. Wang, C. Zhang, Y. Sang, H. Liu, and W. Zhou, "WSe_2 2D p-type semiconductor-based electronic devices for information technology: Design, preparation, and applications," InfoMat **2**(4), 656–697 (2020).

90. J.-B. Lee, Y. R. Lim, A. K. Katiyar, W. Song, J. Lim, S. Bae, T.-W. Kim, S.-K. Lee, and J.-H. Ahn, "Direct Synthesis of a Self-Assembled WSe_2/MoS_2 Heterostructure Array and its Optoelectrical Properties," Advanced Materials **31**(43), 1904194 (2019).

91. M. M. Furchi, F. Höller, L. Dobusch, D. K. Polyushkin, S. Schuler, and T. Mueller, "Device physics of van der Waals heterojunction solar cells," npj 2D Mater Appl **2**(1), 1–7 (2018).

92. R. Cheng, D. Li, H. Zhou, C. Wang, A. Yin, S. Jiang, Y. Liu, Y. Chen, Y. Huang, and X. Duan, "Electroluminescence and Photocurrent Generation from Atomically Sharp WSe_2/MoS_2 Heterojunction p–n Diodes," Nano Lett. **14**(10), 5590–5597 (2014).

93. N. Flöry, A. Jain, P. Bharadwaj, M. Parzefall, T. Taniguchi, K. Watanabe, and L. Novotny, "A $WSe_2/MoSe_2$ heterostructure photovoltaic device," Appl. Phys. Lett. **107**(12), 123106 (2015).

94. M. S. Choi, D. Qu, D. Lee, X. Liu, K. Watanabe, T. Taniguchi, and W. J. Yoo, "Lateral MoS_2 p–n Junction Formed by Chemical Doping for Use in High-Performance Optoelectronics," ACS Nano **8**(9), 9332–9340 (2014).

95. Y. Liu, J. Guo, E. Zhu, L. Liao, S.-J. Lee, M. Ding, I. Shakir, V. Gambin, Y. Huang, and X. Duan, "Approaching the Schottky-Mott limit in van der Waals metal-semiconductor junctions," Nature **557**(7707), 696–700 (2018).

96. E. McVay, A. Zubair, Y. Lin, A. Nourbakhsh, and T. Palacios, "Impact of Al_2O_3 Passivation on the Photovoltaic Performance of Vertical WSe_2 Schottky Junction Solar Cells," ACS Appl. Mater. Interfaces **12**(52), 57987–57995 (2020).

97. R. T. Tung, "The physics and chemistry of the Schottky barrier height," Applied Physics Reviews **1**(1), 011304 (2014).

98. J. Bardeen, "Surface States and Rectification at a Metal Semi-Conductor Contact," Phys. Rev. **71**(10), 717–727 (1947).

99. A. M. Cowley and S. M. Sze, "Surface States and Barrier Height of Metal-Semiconductor Systems," Journal of Applied Physics **36**(10), 3212–3220 (1965).

100. D. K. Schroder and D. L. Meier, "Solar cell contact resistance—A review," IEEE Transactions on Electron Devices **31**(5), 637–647 (1984).

101. S. Das, H.-Y. Chen, A. V. Penumatcha, and J. Appenzeller, "High performance multilayer MoS_2 transistors with scandium contacts," Nano Lett **13**(1), 100–105 (2013).

102. J. Kwon, J.-Y. Lee, Y.-J. Yu, C.-H. Lee, X. Cui, J. Hone, and G.-H. Lee, "Thickness-dependent Schottky barrier height of MoS_2 field-effect transistors," Nanoscale **9**(18), 6151–6157 (2017).

103. A. Allain, J. Kang, K. Banerjee, and A. Kis, "Electrical contacts to two-dimensional semiconductors," Nature Mater **14**(12), 1195–1205 (2015).

104. W. Liu, J. Kang, W. Cao, D. Sarkar, Y. Khatami, D. Jena, and K. Banerjee, "High-performance few-layer-MoS_2 field-effect-transistor with record low contact-resistance," in *2013 IEEE International Electron Devices Meeting* (2013), p. 19.4.1-19.4.4.

105. M. Amani, D.-H. Lien, D. Kiriya, J. Xiao, A. Azcatl, J. Noh, S. R. Madhvapathy, R. Addou, S. KC, M. Dubey, K. Cho, R. M. Wallace, S.-C. Lee, J.-H. He, J. W. Ager, X. Zhang, E. Yablonovitch, and A. Javey, "Near-unity photoluminescence quantum yield in MoS_2," Science **350**(6264), 1065–1068 (2015).

106. W. Zhou, X. Zou, S. Najmaei, Z. Liu, Y. Shi, J. Kong, J. Lou, P. M. Ajayan, B. I. Yakobson, and J.-C. Idrobo, "Intrinsic Structural Defects in Monolayer Molybdenum Disulfide," Nano Lett. **13**(6), 2615–2622 (2013).

107. H. Lu, A. Kummel, and J. Robertson, "Passivating the sulfur vacancy in monolayer MoS_2," APL Materials **6**(6), 066104 (2018).

108. H. Wang, C. Zhang, and F. Rana, "Surface Recombination Limited Lifetimes of Photoexcited Carriers in Few-Layer Transition Metal Dichalcogenide MoS_2," Nano Lett. **15**(12), 8204–8210 (2015).

109. H. Schmidt, F. Giustiniano, and G. Eda, "Electronic transport properties of transition metal dichalcogenide field-effect devices: surface and interface effects," Chem. Soc. Rev. **44**(21), 7715–7736 (2015).

110. J. Gusakova, X. Wang, L. Shiau, A. Krivosheeva, V. Shaposhnikov, V. Borisenko, V. Gusakov, and B. Tay, "Electronic Properties of Bulk and Monolayer TMDs: Theoretical Study Within DFT Framework (GVJ-2e Method)," physica status solidi (a) **214**(12), 1700218 (2017).

111. D. Kiriya, M. Tosun, P. Zhao, J. S. Kang, and A. Javey, "Air-Stable Surface Charge Transfer Doping of MoS_2 by Benzyl Viologen," J. Am. Chem. Soc. **136**(22), 7853–7856 (2014).

112. S. A. Svatek, E. Antolin, D.-Y. Lin, R. Frisenda, C. Reuter, A. J. Molina-Mendoza, M. Muñoz, N. Agraït, T.-S. Ko, D. P. de Lara, and A. Castellanos-Gomez, "Gate tunable photovoltaic effect in MoS_2 vertical p–n homostructures," J. Mater. Chem. C **5**(4), 854–861 (2017).

113. C. Reuter, R. Frisenda, D.-Y. Lin, T.-S. Ko, D. P. de Lara, and A. Castellanos-Gomez, "A Versatile Scanning Photocurrent Mapping System to Characterize Optoelectronic Devices based on 2D Materials," Small Methods **1**(7), 1700119 (2017).

114. D. Gu, S. K. Dey, and P. Majhi, "Effective work function of Pt, Pd, and Re on atomic layer deposited HfO_2," Applied Physics Letters **89**(8), 082907 (2006).

115. D. E. Eastman, "Photoelectric Work Functions of Transition, Rare-Earth, and Noble Metals," Phys. Rev. B **2**(1), 1–2 (1970).

116. Y. Yi, C. Wu, H. Liu, J. Zeng, H. He, and J. Wang, "A study of lateral Schottky contacts in WSe_2 and MoS_2 field effect transistors using scanning photocurrent microscopy," Nanoscale **7**(38), 15711–15718 (2015).

117. C. Kim, I. Moon, D. Lee, M. S. Choi, F. Ahmed, S. Nam, Y. Cho, H.-J. Shin, S. Park, and W. J. Yoo, "Fermi Level Pinning at Electrical Metal Contacts of Monolayer Molybdenum Dichalcogenides," ACS Nano **11**(2), 1588–1596 (2017).

118. W. J. Yu, Z. Li, H. Zhou, Y. Chen, Y. Wang, Y. Huang, and X. Duan, "Vertically stacked multi-heterostructures of layered materials for logic transistors and complementary inverters," Nature Mater **12**(3), 246–252 (2013).

119. C. M. Went, J. Wong, P. R. Jahelka, M. Kelzenberg, S. Biswas, M. S. Hunt, A. Carbone, and H. A. Atwater, "A new metal transfer process for van der Waals contacts to vertical Schottky-junction transition metal dichalcogenide photovoltaics," Science Advances **5**(12), eaax6061 (2019).

120. Y. Wang, J. C. Kim, R. J. Wu, J. Martinez, X. Song, J. Yang, F. Zhao, A. Mkhoyan, H. Y. Jeong, and M. Chhowalla, "Van der Waals contacts between three-dimensional metals and two-dimensional semiconductors," Nature **568**(7750), 70–74 (2019).

121. J. P. Colinge and C. A. Colinge, eds., "The PN Junction Diode," in *Physics of Semiconductor Devices* (Springer US, 2002), pp. 95–137.

122. M. H. Zehender, "Three-terminal heterojunction bipolar transistor solar cells = Células solares de tres terminales tipo transistor bipolar de heterounión," phd, E.T.S.I. Telecomunicación (UPM) (2022).

123. M. A. Kats, R. Blanchard, P. Genevet, and F. Capasso, "Nanometre optical coatings based on strong interference effects in highly absorbing media," Nat Mater **12**(1), 20–24 (2013).

124. E. Centurioni, "Generalized matrix method for calculation of internal light energy flux in mixed coherent and incoherent multilayers," Appl. Opt., AO **44**(35), 7532–7539 (2005).

125. A. R. Thompson, J. M. Moran, and G. W. Swenson, "Van Cittert–Zernike Theorem, Spatial Coherence, and Scattering," in *Interferometry and Synthesis in Radio Astronomy*, A. R. Thompson, J. M. Moran, and G. W. Swenson Jr., eds. (Springer International Publishing, 2017), pp. 767–786.

126. C. K. Carniglia, "Scalar Scattering Theory for Multilayer Optical Coatings," OE **18**(2), 104–115 (1979).

127. J. M. Llorens, J. Buencuerpo, J. M. Ripalda, and P. A. Postigo, "Amplification of the Zeroth Order Mode in Ultra-thin Layers," Journal of Green Engineering **5**(4), 71–82 (2015).

128. J. M. Llorens, J. Buencuerpo, and P. A. Postigo, "Absorption features of the zero frequency mode in an ultra-thin slab," Appl. Phys. Lett. **105**(23), 231115 (2014).

129. G. A. Ermolaev, D. V. Grudinin, Y. V. Stebunov, K. V. Voronin, V. G. Kravets, J. Duan, A. B. Mazitov, G. I. Tselikov, A. Bylinkin, D. I. Yakubovsky, S. M. Novikov, D. G. Baranov, A. Y. Nikitin, I. A. Kruglov, T. Shegai, P. Alonso-González, A. N. Grigorenko, A. V. Arsenin, K. S. Novoselov, and V. S. Volkov, "Giant optical anisotropy in transition metal dichalcogenides for next-generation photonics," Nature Communications **12**(1), 854 (2021).

130. S. A. Kalogirou, "Chapter 2 - Environmental Characteristics," in *Solar Energy Engineering (Second Edition)*, S. A. Kalogirou, ed. (Academic Press, 2014), pp. 51–123.

131. R. E. Bird, "A simple, solar spectral model for direct-normal and diffuse horizontal irradiance," Solar Energy **32**(4), 461–471 (1984).

132. C. Bueno-Blanco, S. A. Svatek, and E. Antolin, "High broadband light absorption in ultrathin MoS_2 homojunction solar cells," Opt. Express, OE **30**(23), 42678–42695 (2022).

133. A. R. Beal and H. P. Hughes, "Kramers-Kronig analysis of the reflectivity spectra of 2H-MoS_2, 2H-$MoSe_2$ and 2H-$MoTe_2$," J. Phys. C: Solid State Phys. **12**(5), 881–890 (1979).

134. A. R. Beal, W. Y. Liang, and H. P. Hughes, "Kramers-Kronig analysis of the reflectivity spectra of 3R-WS_2 and 2H-WSe_2," J. Phys. C: Solid State Phys. **9**(12), 2449 (1976).

135. L. J. Phillips, A. M. Rashed, R. E. Treharne, J. Kay, P. Yates, I. Z. Mitrovic, A. Weerakkody, S. Hall, and K. Durose, "Dispersion relation data for methylammonium lead triiodide perovskite deposited on a (100) silicon wafer using a two-step vapour-phase reaction process," Data Brief **5**, 926–928 (2015).

136. D. E. Aspnes and A. A. Studna, "Dielectric functions and optical parameters of Si, Ge, GaP, GaAs, GaSb, InP, InAs, and InSb from 1.5 to 6.0 eV," Phys. Rev. B **27**(2), 985–1009 (1983).

137. R. E. Treharne, A. Seymour-Pierce, K. Durose, K. Hutchings, S. Roncallo, and D. Lane, "Optical Design and Fabrication of Fully Sputtered CdTe/CdS Solar Cells," J. Phys.: Conf. Ser. **286**, 012038 (2011).

138. M. Gloeckler and J. R. Sites, "Band-gap grading in Cu(In,Ga)Se_2 solar cells," Journal of Physics and Chemistry of Solids **66**(11), 1891–1894 (2005).

139. I. Massiot, A. Cattoni, and S. Collin, "Progress and prospects for ultrathin solar cells," Nat Energy **5**(12), 959–972 (2020).

140. H.-L. Chen, A. Cattoni, R. De Lépinau, A. W. Walker, O. Höhn, D. Lackner, G. Siefer, M. Faustini, N. Vandamme, J. Goffard, B. Behaghel, C. Dupuis, N. Bardou, F. Dimroth, and S. Collin, "A 19.9%-efficient ultrathin solar cell based on a 205-nm-thick GaAs absorber and a silver nanostructured back mirror," Nat Energy **4**(9), 761–767 (2019).

141. J. Buencuerpo, T. E. Saenz, M. Steger, M. Young, E. L. Warren, J. F. Geisz, M. A. Steiner, and A. C. Tamboli, "Efficient light-trapping in ultrathin GaAs solar cells using quasi-random photonic crystals," Nano Energy **96**, 107080 (2022).

142. V. Steenhoff, M. Theuring, M. Vehse, K. von Maydell, and C. Agert, "Ultrathin Resonant-Cavity-Enhanced Solar Cells with Amorphous Germanium Absorbers," Advanced Optical Materials **3**(2), 182–186 (2015).

143. A.-J. Cho, S. D. Namgung, H. Kim, and J.-Y. Kwon, "Electric and photovoltaic characteristics of a multi-layer ReS_2/$ReSe_2$ heterostructure," APL Materials **5**(7), 076101 (2017).

144. A. Daus, C. J. McClellan, K. Schauble, J. C. Costa, R. W. Grady, L. Petti, G. Cantarella, N. Münzenrieder, and E. Pop, "Aluminum oxide as a dielectric and passivation layer for (flexible) metal-oxide and 2D semiconductor devices," in *Oxide-Based Materials and Devices XII* (International Society for Optics and Photonics, 2021), **11687**, p. 116871I.

145. X. Liu, T. Galfsky, Z. Sun, F. Xia, E. Lin, Y.-H. Lee, S. Kéna-Cohen, and V. M. Menon, "Strong light–matter coupling in two-dimensional atomic crystals," Nature Photon **9**(1), 30–34 (2015).

146. S. Wu, S. Buckley, A. M. Jones, J. S. Ross, N. J. Ghimire, J. Yan, D. G. Mandrus, W. Yao, F. Hatami, J. Vučković, A. Majumdar, and X. Xu, "Control of two-dimensional excitonic light emission via photonic crystal," 2D Mater. **1**(1), 011001 (2014).

147. X. Gan, Y. Gao, K. Fai Mak, X. Yao, R.-J. Shiue, A. van der Zande, M. E. Trusheim, F. Hatami, T. F. Heinz, J. Hone, and D. Englund, "Controlling the spontaneous emission rate of monolayer MoS_2 in a photonic crystal nanocavity," Appl. Phys. Lett. **103**(18), 181119 (2013).

148. I. H. Malitson, "Refraction and Dispersion of Synthetic Sapphire," J. Opt. Soc. Am., JOSA **52**(12), 1377–1379 (1962).

149. I. H. Malitson, "Interspecimen Comparison of the Refractive Index of Fused Silica," J. Opt. Soc. Am., JOSA **55**(10), 1205–1209 (1965).

150. M. J. Dodge, "Refractive properties of magnesium fluoride," Appl. Opt., AO **23**(12), 1980–1985 (1984).

151. G. Cappellini, G. Satta, M. Palummo, and G. Onida, "Optical properties of BN in cubic and layered hexagonal phases," Phys. Rev. B **64**(3), 035104 (2001).

152. G. A. Ermolaev, Y. V. Stebunov, A. A. Vyshnevyy, D. E. Tatarkin, D. I. Yakubovsky, S. M. Novikov, D. G. Baranov, T. Shegai, A. Y. Nikitin, A. V. Arsenin, and V. S. Volkov, "Broadband optical properties of monolayer and bulk MoS_2," npj 2D Mater Appl **4**(1), 21 (2020).

153. C. Yelgel, Ö. C. Yelgel, and O. Gülseren, "Structural and electronic properties of MoS_2, WS_2, and WS_2/MoS_2 heterostructures encapsulated with hexagonal boron nitride monolayers," Journal of Applied Physics **122**(6), 065303 (2017).

154. K. M. Islam, R. Synowicki, T. Ismael, I. Oguntoye, N. Grinalds, and M. D. Escarra, "In-Plane and Out-of-Plane Optical Properties of Monolayer, Few-Layer, and Thin-Film MoS_2 from 190 to 1700 nm and Their Application in Photonic Device Design," Adv Photo Res **2**(5), 2000180 (2021).

155. C. Janisch, H. Song, C. Zhou, Z. Lin, A. L. Elías, D. Ji, M. Terrones, Q. Gan, and Z. Liu, "MoS_2 monolayers on nanocavities: enhancement in light–matter interaction," 2D Mater. **3**(2), 025017 (2016).

156. B. Hallam, M. Kim, Y. Zhang, L. Wang, A. Lennon, P. Verlinden, P. P. Altermatt, and P. R. Dias, "The silver learning curve for photovoltaics and projected silver demand for net-zero emissions by 2050," Progress in Photovoltaics: Research and Applications **31**(6), 598–606 (2023).

157. H. Hannebauer, T. Dullweber, T. Falcon, X. Chen, and R. Brendel, "Record Low Ag Paste Consumption of 67.7 mg with Dual Print," Energy Procedia **43**, 66–71 (2013).

158. Y. Li, L. Meng, Y. (Michael) Yang, G. Xu, Z. Hong, Q. Chen, J. You, G. Li, Y. Yang, and Y. Li, "High-efficiency robust perovskite solar cells on ultrathin flexible substrates," Nat Commun **7**(1), 10214 (2016).

159. V. Depauw, C. Trompoukis, I. Massiot, W. Chen, A. Dmitriev, P. R. i Cabarrocas, I. Gordon, and J. Poortmans, "Sunlight-thin nanophotonic monocrystalline silicon solar cells," Nano Futures **1**(2), 021001 (2017).

160. O. Lundberg, M. Bodegård, J. Malmström, and L. Stolt, "Influence of the $Cu(In,Ga)Se_2$ thickness and Ga grading on solar cell performance," Progress in Photovoltaics: Research and Applications **11**(2), 77–88 (2003).

161. A. Gupta, V. Parikh, and A. D. Compaan, "High efficiency ultra-thin sputtered CdTe solar cells," Solar Energy Materials and Solar Cells **90**(15), 2263–2271 (2006).

162. B. Radisavljevic, A. Radenovic, J. Brivio, V. Giacometti, and A. Kis, "Single-layer MoS_2 transistors," Nature Nanotech **6**(3), 147–150 (2011).

163. L. J. Van der Pauw, "A method of measuring specific resistivity and Hall effect of discs of arbitrary shape," Philips Research Reports **13**(1), 1–9 (1958).

164. D. Sercombe, S. Schwarz, O. Del Pozo-Zamudio, F. Liu, B. J. Robinson, E. A. Chekhovich, I. I. Tartakovskii, O. Kolosov, and A. I. Tartakovskii, "Optical investigation of the natural electron doping in thin MoS_2 films deposited on dielectric substrates," Sci Rep **3**, 3489 (2013).

165. N. Scheuschner, O. Ochedowski, A.-M. Kaulitz, R. Gillen, M. Schleberger, and J. Maultzsch, "Photoluminescence of freestanding single- and few-layer MoS_2," Phys. Rev. B **89**(12), 125406 (2014).

166. Y. Yu, Y. Yu, C. Xu, Y.-Q. Cai, L. Su, Y. Zhang, Y.-W. Zhang, K. Gundogdu, and L. Cao, "Engineering Substrate Interactions for High Luminescence Efficiency of Transition-Metal Dichalcogenide Monolayers," Advanced Functional Materials **26**(26), 4733–4739 (2016).

167. D. Mao, T. Kananen, T. Li, A. Soman, J. Sinsky, N. Petrone, J. Hone, P. Dong, and T. Gu, "Bandwidth Limitation of Directly Contacted Graphene–Silicon Optoelectronics," ACS Appl. Electron. Mater. **1**(2), 172–178 (2019).

168. F. Wang, Z. Wang, K. Xu, F. Wang, Q. Wang, Y. Huang, L. Yin, and J. He, "Tunable GaTe-MoS_2 van der Waals p–n Junctions with Novel Optoelectronic Performance," Nano Lett. **15**(11), 7558–7566 (2015).

169. K. Dolui, I. Rungger, and S. Sanvito, "Origin of the n-type and p-type conductivity of MoS_2 monolayers on a SiO_2 substrate," Phys. Rev. B **87**(16), 165402 (2013).

170. Lord Kelvin, "V. Contact electricity of metals," The London, Edinburgh, and Dublin Philosophical Magazine and Journal of Science **46**(278), 82–120 (1898).

171. H.-M. Li, D. Lee, D. Qu, X. Liu, J. Ryu, A. Seabaugh, and W. J. Yoo, "Ultimate thin vertical p–n junction composed of two-dimensional layered molybdenum disulfide," Nat Commun **6**(1), 6564 (2015).

172. K. Chen, X. Wan, J. Wen, W. Xie, Z. Kang, X. Zeng, H. Chen, and J.-B. Xu, "Electronic Properties of MoS_2–WS_2 Heterostructures Synthesized with Two-Step Lateral Epitaxial Strategy," ACS Nano **9**(10), 9868–9876 (2015).

173. Z. Feng, B. Chen, S. Qian, L. Xu, L. Feng, Y. Yu, R. Zhang, J. Chen, Q. Li, Q. Li, C. Sun, H. Zhang, J. Liu, W. Pang, and D. Zhang, "Chemical sensing by band modulation of a black phosphorus/molybdenum diselenide van der Waals hetero-structure," 2D Mater. **3**(3), 035021 (2016).

174. X. Wang, J.-B. Xu, W. Xie, and J. Du, "Quantitative Analysis of Graphene Doping by Organic Molecular Charge Transfer," J. Phys. Chem. C **115**(15), 7596–7602 (2011).

175. G. N. Derry, M. E. Kern, and E. H. Worth, "Recommended values of clean metal surface work functions," Journal of Vacuum Science & Technology A **33**(6), 060801 (2015).

176. S. McDonnell, R. Addou, C. Buie, R. M. Wallace, and C. L. Hinkle, "Defect-Dominated Doping and Contact Resistance in MoS_2," ACS Nano **8**(3), 2880–2888 (2014).

177. C. Baumgart, M. Helm, and H. Schmidt, "Quantitative dopant profiling in semiconductors: A Kelvin probe force microscopy model," Phys. Rev. B **80**(8), 085305 (2009).

178. D. S. Schulman, A. J. Arnold, and S. Das, "Contact engineering for 2D materials and devices," Chem. Soc. Rev. **47**(9), 3037–3058 (2018).

179. C. Bueno-Blanco, S. A. Svatek, M. Rodríguez-Pena, D.-Y. Lin, M. Luna, A. Martí, and E. Antolin, "MoS_2 homojunction solar cell with Fermi-level-pinning-free contacts and antireflection BN layer," (to be published) (n.d.).

180. A. Varghese, D. Saha, K. Thakar, V. Jindal, S. Ghosh, N. V. Medhekar, S. Ghosh, and S. Lodha, "Near-Direct Bandgap WSe_2/ReS_2 Type-II pn Heterojunction for Enhanced Ultrafast Photodetection and High-Performance Photovoltaics," Nano Lett **20**(3), 1707–1717 (2020).

181. P. K. Sahoo, S. Memaran, F. A. Nugera, Y. Xin, T. Díaz Márquez, Z. Lu, W. Zheng, N. D. Zhigadlo, D. Smirnov, L. Balicas, and H. R. Gutiérrez, "Bilayer Lateral Heterostructures of Transition-Metal Dichalcogenides and Their Optoelectronic Response," ACS Nano **13**(11), 12372–12384 (2019).

182. A.-J. Cho, M.-K. Song, D.-W. Kang, and J.-Y. Kwon, "Two-Dimensional WSe_2/MoS_2 p–n Heterojunction-Based Transparent Photovoltaic Cell and Its Performance Enhancement by Fluoropolymer Passivation," ACS Appl. Mater. Interfaces **10**(42), 35972–35977 (2018).

183. E. Fortin and W. M. Sears, "Photovoltaic effect and optical absorption in MoS_2," Journal of Physics and Chemistry of Solids **43**(9), 881–884 (1982).

184. M. Shanmugam, C. A. Durcan, and B. Yu, "Layered semiconductor molybdenum disulfide nanomembrane based Schottky-barrier solar cells," Nanoscale **4**(23), 7399–7405 (2012).

185. J. Ye, X. Li, J. Zhao, X. Mei, and Q. Li, "A Facile Way to Fabricate High-Performance Solution-Processed n-MoS_2/p-MoS_2 Bilayer Photodetectors," Nanoscale research letters **10**, 454 (2015).

186. Y. Park, V. Choong, Y. Gao, B. R. Hsieh, and C. W. Tang, "Work function of indium tin oxide transparent conductor measured by photoelectron spectroscopy," Applied Physics Letters **68**(19), 2699–2701 (1996).

187. M. Abraham and S. E. Mohney, "Annealed Ag contacts to MoS_2 field-effect transistors," Journal of Applied Physics **122**(11), 115306 (2017).

188. M. Bernardi, M. Palummo, and J. C. Grossman, "Extraordinary Sunlight Absorption and One Nanometer Thick Photovoltaics Using Two-Dimensional Monolayer Materials," Nano Lett. **13**(8), 3664–3670 (2013).

189. C. R. Ryder, J. D. Wood, S. A. Wells, and M. C. Hersam, "Chemically Tailoring Semiconducting Two-Dimensional Transition Metal Dichalcogenides and Black Phosphorus," ACS Nano **10**(4), 3900–3917 (2016).

190. A.-J. Cho and J.-Y. Kwon, "Hexagonal Boron Nitride for Surface Passivation of Two-Dimensional van der Waals Heterojunction Solar Cells," ACS Applied Materials & Interfaces (2019).

191. M. Fontana, T. Deppe, A. K. Boyd, M. Rinzan, A. Y. Liu, M. Paranjape, and P. Barbara, "Electron-hole transport and photovoltaic effect in gated MoS_2 Schottky junctions," Sci Rep **3**, 1634 (2013).

192. A. Luque and Hegedus, Steven, eds., *Handbook of Photovoltaic Science and Engineering*, 2nd Edition (John Wiley & Sons, 2011).

193. G. Neudeck and G. W. Neudeck, *The PN Junction Diode* (Addison-Wesley, 1989).

194. P. J. Wass, D. Hollington, T. J. Sumner, F. Yang, and M. Pfeil, "Effective decrease of photoelectric emission threshold from gold plated surfaces," Review of Scientific Instruments **90**(6), 064501 (2019).

195. J. J. Kopanski, M. Y. Afridi, S. Jeliazkov, W. Jiang, and T. R. Walker, "Scanning Kelvin Force Microscopy For Characterizing Nanostructures in Atmosphere," AIP Conference Proceedings **931**(1), 530–534 (2007).

196. H. Kim and H. J. Choi, "Thickness dependence of work function, ionization energy, and electron affinity of Mo and W dichalcogenides from DFT and GW calculations," Phys. Rev. B **103**(8), 085404 (2021).

197. X. Chen, Z. Wu, S. Xu, L. Wang, R. Huang, Y. Han, W. Ye, W. Xiong, T. Han, G. Long, Y. Wang, Y. He, Y. Cai, P. Sheng, and N. Wang, "Probing the electron states and metal-insulator transition mechanisms in molybdenum disulphide vertical heterostructures," Nat Commun **6**(1), 6088 (2015).

198. H.-P. Komsa and A. V. Krasheninnikov, "Native defects in bulk and monolayer MoS_2 from first principles," Phys. Rev. B **91**(12), 125304 (2015).

199. J. Hong, C. Lee, J.-S. Park, and J. H. Shim, "Control of valley degeneracy in MoS_2 by layer thickness and electric field and its effect on thermoelectric properties," Phys. Rev. B **93**(3), 035445 (2016).

200. H. Peelaers and C. G. Van de Walle, "Effects of strain on band structure and effective masses in MoS_2," Phys. Rev. B **86**(24), 241401 (2012).

201. P. Bonomo, A. Chatzipanagi, and F. Frontini, "Overview and analysis of current BIPV products: new criteria for supporting the technological transfer in the building sector," VITRUVIO - International Journal of Architectural Technology and Sustainability (1), 67–85 (2015).

202. T. E. Kuhn, C. Erban, M. Heinrich, J. Eisenlohr, F. Ensslen, and D. H. Neuhaus, "Review of technological design options for building integrated photovoltaics (BIPV)," Energy and Buildings **231**, 110381 (2021).

203. B. Norton, P. C. Eames, T. K. Mallick, M. J. Huang, S. J. McCormack, J. D. Mondol, and Y. G. Yohanis, "Enhancing the performance of building integrated photovoltaics," Solar Energy **85**(8), 1629–1664 (2011).

204. B. Petter Jelle, C. Breivik, and H. Drolsum Røkenes, "Building integrated photovoltaic products: A state-of-the-art review and future research opportunities," Solar Energy Materials and Solar Cells **100**, 69–96 (2012).

205. "Light and lighting - Lighting of work places - Part 1: Indoor work places. UNE-EN 12464-1:2022," (2022).

206. R. Danks, J. Good, and R. Sinclair, "Assessing reflected sunlight from building facades: A literature review and proposed criteria," Building and Environment **103**, 193–202 (2016).

207. C. Hong, Y. Wang, Z. Gu, and C. W. Yu, "Cool facades to mitigate urban heat island effects," Indoor and Built Environment. **31**(10), 2373–2377 (2022).

208. M. Ichinose, T. Inoue, and T. Nagahama, "Effect of retro-reflecting transparent window on anthropogenic urban heat balance," Energy and Buildings **157**, 157–165 (2017).

209. C. Bueno-Blanco, S. A. Svatek, F. Gómez-Campos, and E. Antolin, "Photovoltaic windows based on ultrathin transition-metal dichalcogenides that produce natural light spectra," (to be published) (n.d.).

210. V. Depauw, Y. Qiu, K. Van Nieuwenhuysen, I. Gordon, and J. Poortmans, "Epitaxy-free monocrystalline silicon thin film: first steps beyond proof-of-concept solar cells," Progress in Photovoltaics: Research and Applications **19**(7), 844–850 (2011).

211. S. Wang, B. D. Weil, Y. Li, K. X. Wang, E. Garnett, S. Fan, and Y. Cui, "Large-Area Free-Standing Ultrathin Single-Crystal Silicon as Processable Materials," Nano Lett. **13**(9), 4393–4398 (2013).

212. K. Lee, N. Kim, K. Kim, H.-D. Um, W. Jin, D. Choi, J. Park, K. J. Park, S. Lee, and K. Seo, "Neutral-Colored Transparent Crystalline Silicon Photovoltaics," Joule **4**(1), 235–246 (2020).

213. R. Yang, C.-H. Lee, B. Cui, and A. Sazonov, "Flexible semi-transparent a-Si:H pin solar cells for functional energy-harvesting applications," Materials Science and Engineering: B **229**, 1–5 (2018).

214. Y. Li, X. Guo, Z. Peng, B. Qu, H. Yan, H. Ade, M. Zhang, and S. R. Forrest, "Color-neutral, semitransparent organic photovoltaics for power window applications," Proceedings of the National Academy of Sciences **117**(35), 21147–21154 (2020).

215. E. Pascual-San José, A. Sánchez-Díaz, M. Stella, E. Martínez-Ferrero, M. I. Alonso, and M. Campoy-Quiles, "Comparing the potential of different strategies for colour tuning in thin film photovoltaic technologies," Science and Technology of Advanced Materials **19**(1), 823–835 (2018).

216. G. E. Eperon, V. M. Burlakov, A. Goriely, and H. J. Snaith, "Neutral Color Semitransparent Microstructured Perovskite Solar Cells," ACS Nano **8**(1), 591–598 (2014).

217. M. Rubin, "Optical properties of soda lime silica glasses," Solar Energy Materials **12**(4), 275–288 (1985).

218. T. Smith and J. Guild, "The C.I.E. colorimetric standards and their use," Trans. Opt. Soc. **33**(3), 73 (1931).

219. "CIE Standard Illuminants for Colorimetry.ISO 10526:1999/CIE S005/E-1998.," (1999).

220. C. S. McCamy, "Correlated color temperature as an explicit function of chromaticity coordinates," Color Research & Application **17**(2), 142–144 (1992).

221. Y. Z. You, Y. S. Kim, D. H. Choi, H. S. Jang, J. H. Lee, and D. Kim, "Electrical and optical study of ITO films on glass and polymer substrates prepared by DC magnetron sputtering type negative metal ion beam deposition," Materials Chemistry and Physics **107**(2), 444–448 (2008).

222. D. Raoufi, A. Kiasatpour, H. R. Fallah, and A. S. H. Rozatian, "Surface characterization and microstructure of ITO thin films at different annealing temperatures," Applied Surface Science **253**(23), 9085–9090 (2007).

223. C. Guillén and J. Herrero, "Comparison study of ITO thin films deposited by sputtering at room temperature onto polymer and glass substrates," Thin Solid Films **480–481**, 129–132 (2005).

224. T. A. F. König, P. A. Ledin, J. Kerszulis, Mahmoud. A. Mahmoud, M. A. El-Sayed, J. R. Reynolds, and V. V. Tsukruk, "Electrically Tunable Plasmonic Behavior of Nanocube–Polymer Nanomaterials Induced by a Redox-Active Electrochromic Polymer," ACS Nano **8**(6), 6182–6192 (2014).

225. M. R. Vogt, H. Holst, H. Schulte-Huxel, S. Blankemeyer, R. Witteck, D. Hinken, M. Winter, B. Min, C. Schinke, I. Ahrens, M. Köntges, K. Bothe, and R. Brendel, "Optical Constants of UV Transparent EVA and the Impact on the PV Module Output Power under Realistic Irradiation," Energy Procedia **92**, 523–530 (2016).

226. B. Munkhbat, P. Wróbel, T. J. Antosiewicz, and T. O. Shegai, "Optical Constants of Several Multilayer Transition Metal Dichalcogenides Measured by Spectroscopic Ellipsometry in the 300–1700 nm Range: High Index, Anisotropy, and Hyperbolicity," ACS Photonics **9**(7), 2398–2407 (2022).

227. J. P. Zheng and H. S. Kwok, "Low resistivity indium tin oxide films by pulsed laser deposition," Applied Physics Letters **63**(1), 1–3 (1993).

228. S. Ishibashi, Y. Higuchi, Y. Ota, and K. Nakamura, "Low resistivity indium–tin oxide transparent conductive films. II. Effect of sputtering voltage on electrical property of films," Journal of Vacuum Science & Technology A **8**(3), 1403–1406 (1990).

229. R. N. Joshi, V. P. Singh, and J. C. McClure, "Characteristics of indium tin oxide films deposited by r.f. magnetron sputtering," Thin Solid Films **257**(1), 32–35 (1995).

230. M. Debije, "Better luminescent solar panels in prospect," Nature **519**(7543), 298–299 (2015).

231. V. V. Plotnikov, C. W. Carter, J. M. Stayancho, N. R. Paudel, H. Mahabaduge, D. Kwon, C. R. Grice, and A. D. Compaan, "Semitransparent PV windows with sputtered CdS/CdTe thin films," in *2013 IEEE 39th Photovoltaic Specialists Conference (PVSC)* (2013), pp. 0405–0408.

232. C. J. Traverse, R. Pandey, M. C. Barr, and R. R. Lunt, "Emergence of highly transparent photovoltaics for distributed applications," Nat Energy **2**(11), 849–860 (2017).

233. H. Savin, P. Repo, G. von Gastrow, P. Ortega, E. Calle, M. Garín, and R. Alcubilla, "Black silicon solar cells with interdigitated back-contacts achieve 22.1% efficiency," Nature Nanotech **10**(7), 624–628 (2015).

234. *Energy Benchmarks. CIBSE TM46: 2008.* (The Chartered Institution of Building Services Engineers, 2008).

235. "Torre Picasso - Ficha, Fotos y Planos," https://web.archive.org/web/20240308145246/https://es.wikiarquitectura.com/edificio/torre-picasso/.

236. *Informe Del Sistema Eléctrico 2022.* (Red Eléctrica de España, 2023).